THE IMPACT OF SPATIAL RESOLUTION ON RIPARIAN LEAF AREA INDEX MODELLING USING REMOTE SENSING

GORDON LOGIE
Bachelor of Science, University of Lethbridge, 2013

A Thesis
Submitted to the School of Graduate Studies
of the University of Lethbridge
in Partial Fulfillment of the
Requirements for the Degree

MASTER OF SCIENCE

Department of Geography
University of Lethbridge
LETHBRIDGE, ALBERTA, CANADA

THE IMPACT OF SPATIAL RESOLUTION ON RIPARIAN LEAF AREA INDEX MODELLING USING REMOTE SENSING

GORDON LOGIE

Date of Defence: April 25, 2016

Dr. Craig Coburn Supervisor	Associate Professor	Ph.D.
Dr. Lawrence Flanagan Thesis Examination Committee Member	Professor	Ph.D.
Dr. Karl Staenz Thesis Examination Committee Member	Professor	Ph.D.
Dr. Derek Peddle Thesis Examination Committee Member	Professor	Ph.D.
Dr. Tom Johnston Chair, Thesis Examination Committee	Associate Professor	Ph.D.

ABSTRACT

This thesis investigated the impact of differing sensor spatial resolutions on leaf area index (LAI) modelling. Airborne images along with ground measurements of LAI were acquired for riparian areas along the Oldman River in southern Alberta. Airborne images were spatially resampled to spatial resolutions between 18 cm and 500 m, and the Modified Simple Ratio (MSR) was calculated from the imagery. LAI regression models were created at each spatial resolution, and changes in the relationship between MSR and LAI were observed at each spatial resolution, as well as changes in the modelled LAI estimates. The relationship between MSR and LAI was scale invariant at spatial resolutions as low as 10 m, and only moderately changed until 30 m. MSR and predicted LAI gradually reduced as resolution coarsened further, with large changes occurred beyond 100 m. No relationship was evident between MSR and LAI at spatial resolutions coarser than 300 m.

ACKNOWLEDGEMENTS

I would like to thank my supervisor, Dr. Craig Coburn, for his mentorship during this journey. Craig consistently went above and beyond as a supervisor, allowing me the freedom to make this research my own, but providing the guidance needed to ensure it was the best it could be. I am incredibly grateful for his support and encouragement that allowed me to rise to this challenge.

I would also like to thank the rest of my committee members, Dr. Karl Staenz, Dr Derek Peddle, and Dr. Lawrence Flanagan, for their support, encouragement, and helpful suggestions.

I would like to acknowledge the Natural Sciences and Engineering Research Council (NSERC) and the NSERC CREATE AMETHYST program for their generous funding and support of my research. I would also like to thank the University of Lethbridge and the Alberta Terrestrial Imaging Centre (ATIC).

I thank all my friends and fellow graduate students who helped me maintain my sanity and made this a far more enjoyable experience than it would have otherwise been. Misery loves company, which is probably why graduate students become good friends. I would like to thank my office mate Peter Kennedy for countless stimulating conversations on topics from remote sensing to philosophy. I would also like to thank Colin Langhorn, Ariel Belsheim, Laurens Philipsen, and Charmaine Bonifacio, for all the great times and “spirited” games of Settlers of Catan.

I owe my gratitude to my family for their endless support and patience while I pursued this degree. I thank them for enduring my often foul moods and stress while I fought with this research. I would like to especially thank my mother, who has supported me by providing me with food and shelter through two degrees. I could not have asked for a better family, and I am ever grateful for having them in my life.

Last, but certainly not least, I want to thank my girlfriend Meagan. Thank you for your love, support, and understanding during this experience. I am continually thankful to have someone who supports my dreams and motivates me to be the best version of myself. Somehow she has managed to support me even from 14,000 kilometres away. I am looking forward to the next chapter in our lives together.

TABLE OF CONTENTS

LIST OF TABLES

LIST OF FIGURES

LIST OF SYMBOLS & ABBREVIATIONS

α	Woody-to-total leaf area ratio
ADC	Analog-to-Digital Converter
ASD	ASD response/reflectance
ASDσ	Normalized ASD response
ASDMax	Maximum ASD response
Cam	Camera response
CamMax	Maximum linearized camera response
Camσ	Intensity-adjusted camera response
CCD	Charge-Coupled Device
CMOS	Complementary Metal-Oxide-Semiconductor
CR	Canopy Reflectance
DBH	Diameter at Breast Height
DN	Digital Number
eLAI	Effective Leaf Area Index
ELC	Empirical Line Calibration
EMR	Electromagnetic Radiation
ET	Evapotranspiration
EVI	Enhanced Vegetation Index
F	F-statistic
fAPAR	Fraction of Absorbed Photosynthetically Active Radiation
FIR	Far Infrared
FWHM	Full Width at Half Maximum
γ	Needle-to-shoot area ratio
G	Green
GCP	Ground Control Point
GIS	Geographic Information System
GNDVI	Green Normalized Difference Vegetation Index
GSD	Ground Sampling Distance
HSNC	Helen Schuler Nature Centre
IMG	Airborne image reflectance
IMU	Inertial Measurement Unit
Int	Relative intensity value
λ	Wavelength
L	Soil adjustment factor
LAI	Leaf Area Index
$\overline{\text{LAI}}$	Average LAI
LAIactual	Ground-measured LAI
LAIerror	LAI prediction error
LAIpred	Predicted LAI
LUT	Lookup Table
LWIR	Longwave Infrared
m	metre(s)
μm	micrometre(s)
MAUP	Modifiable Areal Unit Problem
MCARI2	Modified Chlorophyll Absorption Ratio Index 2
MNF	Minimum Noise Fraction
MSAVI	Modified Soil Adjusted Vegetation Index
MSR	Modified Simple Ratio

MTVI2	Modified Transformed Vegetation Index 2
MWIR	Midwave Infrared
N	Sample size
NDVI	Normalized Difference Vegetation Index
NIR	Near Infrared
nm	nanometre(s)
OLI	Operational Land Imager
PAI	Plant Area Index
PSF	Point Spread Function
R	Red
RDVI	Renormalized Difference Vegetation Index
RGB	Red Green Blue
RMSE	Root-Mean-Square Error
S	Standard deviation
SAVI	Soil Adjusted Vegetation Index
SIFT	Scale Invariant Feature Transform
SLA	Specific Leaf Area
SMA	Spectral Mixture Analysis
SNR	Signal-to-Noise Ratio
SVI	Spectral Vegetation Index
SWIR	Shortwave Infrared
T	T-statistic
TRAC	Tracing Radiation and Architecture of Canopies
USGS	United States Geological Survey
UV	Ultraviolet
VIS	Visible
Ω	Clumping index

1. INTRODUCTION

An estimated 40,000 large dams and 800,000 small dams have been constructed on the world's rivers, intercepting almost two-thirds of the fresh water flowing to the oceans (Nilsson & Berggren, 2000). These dams provide a stable water supply for agricultural, municipal, and industrial use. An unfortunate consequence of river regulation is that river discharge patterns have been altered from those of the natural flow regime (Braatne et al., 2008; Nilsson & Berggren, 2000). Vegetation in riparian ecosystems have often been negatively impacted by these alterations, as these vegetation species are adapted to the natural river flow patterns (Brismar, 2002; Shafroth et al., 2002).

Riparian areas are located adjacent to water courses, serving as the transition zone between aquatic and terrestrial ecosystems (Gregory et al., 1991). These ecosystems are among the most diverse on the planet, and their importance to the biosphere is very high relative to their small spatial extent (Naiman et al., 1993). Healthy riparian vegetation contributes to water filtration, flood mitigation, and river bank stabilization, among many other benefits (Anbumozhi et al., 2005; Patten, 1998).

Cottonwood trees are found in many riparian areas, often acting as the cornerstone of the entire riparian ecosystem. Their roots help stabilize the river channel, allowing establishment of understory vegetation (Gom & Rood, 1999). The trees also provide shade and habitat for terrestrial and aquatic animals (Gom & Rood, 1999).

Riparian cottonwoods are in a state of decline along many major rivers, and alterations of the river flow regime by dams and other regulation mechanisms are implicated as the primary cause (Braatne et al., 2007; Howe & Knopf, 1991; Rood & Mahoney, 1990; Scott et al., 1999). These alterations include reductions in the amount

of annual river discharge, reductions in flooding, and alterations to the timing of river peak flows (Rood & Mahoney, 1990). The reduction of discharge has led to a lowering of the floodplain water table, causing moisture stress in the trees (Scott et al., 1999). Cottonwood seeds are released to coincide with high streamflow conditions in order to capitalize on moist sites scoured of vegetation (Rood et al., 2003). Reductions in flood events has resulted in fewer suitable sites available for seedling germination, while alterations of the timing of peak flows have led to cottonwood seedlings being released at suboptimal times, reducing their chances of survival (Rood et al., 2003). Climate change may exacerbate these problems in many areas, placing further strain on cottonwoods (Rood et al., 2008; Stromberg et al., 2010).

1.1 Riparian Cottonwoods in Southern Alberta

In the prairies of southern Alberta, Canada, agriculture dominates the landscape. The majority of crops in the region are irrigated to mitigate the risk of shortfalls in precipitation due to the semi-arid climate. Irrigation water is primarily drawn from a number of major rivers crossing the region, with much of it coming from the Oldman River, which flows through the city of Lethbridge, the main urban centre in the area.

Water from the Oldman River is heavily allocated. In 2006 almost 70% of the mean annual natural streamflow was allocated to agricultural, municipal, and industrial purposes (AMEC, 2009). Actual water consumption was less than half the allocated amount at 29% of mean annual flow (AMEC, 2009). Agricultural irrigation accounted for 83% of water allocations, and 88% of actual water consumption (AMEC, 2009). Water use on the river is forecast to increase by 27% to 40% over the 2006 amount by the year 2030, amounting to 36% to 40% of the mean annual river flow (AMEC, 2009). Irrigation is predicted to account for 75% of this increase.

Aside from supporting agricultural and municipal activities, the Oldman River supports a diverse and vibrant riparian ecosystem. Cottonwood trees, of the Genus Populus, are the major vegetation type. Three main species are represented along the river (*Populus deltoides*, *Populus augustifolia*, and *Populus balsamafera*), along with numerous interspecific hybrids. The Oldman River is of unique ecological significance, representing the only known area where the ranges of these three cottonwood species overlap to produce a tri-specific hybrid swarm (Floate, 2004).

Following the construction of a dam on the Saint Mary River, one of the Oldman River tributaries, a 48% reduction in cottonwoods was observed downstream of the dam (Rood & Heinze-Milne, 1989). While the same dramatic decline was not seen on the Oldman River following construction of the Oldman Dam in 1992, efforts are being made to ensure continued cottonwood health through sustainable flow management practices (Rood et al., 2005). Positive results have been shown when alternative flow management practices were implemented, with high cottonwood seedling recruitment and survival (Rood et al., 1998); however, quantitative measurements of the ecosystem response are necessary (Rood et al., 2005).

Riparian response can be assessed through monitoring vegetation biophysical parameters including the evapotranspiration (Nagler et al., 2005), leaf area index (Gray & Song, 2012), the concentration of foliage biochemicals including nitrogen and chlorophyll (Yoder & Pettigrew-Crosby, 1995), and the fractional cover of the vegetation (Xiao & Moody, 2005), among other measures.

1.2 Leaf Area Index

The leaf area index (LAI) is a key biophysical parameter and measure of foliage density. LAI is functionally linked to many key vegetation processes, and consequently, it is a necessary parameter for many climatic, vegetation, and

hydrologic models (Beck et al., 2006; Buermann et al., 2001; Moran et al., 1995; Sellers et al., 1997).

The LAI is related to evapotranspiration (ET), the sum of water evaporation from water bodies and the soil as well as water transpiration through the leaves of plants. ET can provide a measure of the water requirements of riparian vegetation (O'Keeffe & Davies, 1991). Changes in the rate of ET can also indicate moisture stress in the vegetation (Landsberg & Sands, 2011). Thus, monitoring ET is critical for assessment of the riparian response to alternative flow management strategies. Due to its important influence over the rate of ET, LAI is a required input parameter for many ET models (Glenn et al., 2007). Therefore, measures of LAI are important for assessing the water use requirements of riparian vegetation.

1.3 Remote Sensing for LAI Estimation

Ground-based measurements of LAI are costly, have a low spatial coverage, and scaling them up to estimate LAI at the landscape or regional scale is problematic (Zheng & Moskal, 2009). Remote sensing is capable of providing estimates of LAI over large areas, allowing regional or global-scale assessments of LAI (Zheng & Moskal, 2009).

Remote sensing is the derivation of information about the Earth's surface through measurements of electromagnetic radiation (EMR) using terrestrial, airborne, or space-borne sensors (Jensen, 2007). Differences in LAI are correlated with differences in the EMR reflectance of vegetation in particular spectral regions (Jordan, 1969). This correlation allows models to be constructed based on remote sensing data which can be used to estimate LAI. The ability to estimate LAI using remote sensing in this way has been exploited for many years to obtain regional and

global-scale estimates of LAI (Asrar et al., 1984; Chen et al., 2002; Colombo et al., 2003; Jordan, 1969; Myneni et al., 1997; Serbin et al., 2013; Turner et al., 1999).

To assess the LAI for all riparian areas along a river through ground measurements alone would be very difficult, if not impossible. Providing timely LAI estimates over multiple years to inform dam managers on riparian health would not be feasible; therefore, it is necessary to use remote sensing to provide LAI estimates. For this reason, the research in this thesis examined the use of remote sensing to provide operational monitoring of riparian LAI.

Implementation of a riparian LAI monitoring program requires selection of a remote sensor that possesses appropriate characteristics to satisfy the requirements of the project. Among the various sensor characteristics is the spatial resolution, which quantifies the amount of spatial detail in images acquired by the sensor.

1.4 Spatial Scale in Remote Sensing

Spatial scale refers to the amount of spatial detail in a measurement, map, or study. Depending on the scale of analysis, the objects, phenomena, and patterns under study can change (Gehlke & Biehl, 1934; Marceau, 1999; Openshaw & Taylor, 1979). Thus, determination of the appropriate spatial scale for measuring phenomena is a key issue in geographical studies.

In remote sensing, the issue of scale is related to the sensor spatial resolution. The spatial resolution is usually quantified using the ground sampling distance (GSD), the ground distance between the centres of adjacent picture elements (pixels) in a remotely sensed image (Woodcock & Strahler, 1987). The smaller the GSD, the greater the amount of resolvable spatial detail.

There are now many remote sensing systems available, offering a wide range of spatial resolutions. Satellite sensor spatial resolutions vary from sub-1 metre to

coarser than 1 kilometre. Airborne and unmanned aerial vehicle (UAV) platforms can also offer very high-spatial resolution data of just a few centimetres.

High-spatial resolution data are often desirable, as high-spatial resolution imagery can be spatially resampled to coarser spatial resolutions if required, while the opposite is not possible. However, achieving a high-spatial resolution requires tradeoffs, such as decreasing the spatial coverage or decreasing the spectral information content (Landgrebe, 2005; Schott, 2007). Therefore, care must be taken to select an appropriate spatial resolution for a desired study. An excessively high-spatial resolution may add no useful spatial detail, as the phenomena of interest are occurring at scales larger than the spatial resolution. In such cases, the use of a lower spatial resolution sensor is appropriate. However, use of a sensor with too low a spatial resolution risks sacrificing too much spatial detail, leading to inadequate characterization of the geographic phenomena being studied.

Figure 1.1 visually demonstrates the scale issue in remote sensing. The figure shows a false-colour infrared image of the same scene at three progressively coarser spatial resolutions. At the highest spatial resolution (18 cm) it is possible to spatially resolve individual trees, vehicles in the parking lot, and pathways through the site. At a resolution of 30 m small details are not resolvable, but it is still possible to separate vegetation, water, gravel bars, and asphalt from each other. At a spatial resolution of 250 m it is no longer possible to discern any spatial detail in the scene. However, a 250 m spatial resolution may perform well for separation of large areal extent land-cover types at a global scale, such as large lakes, cities, and forests.

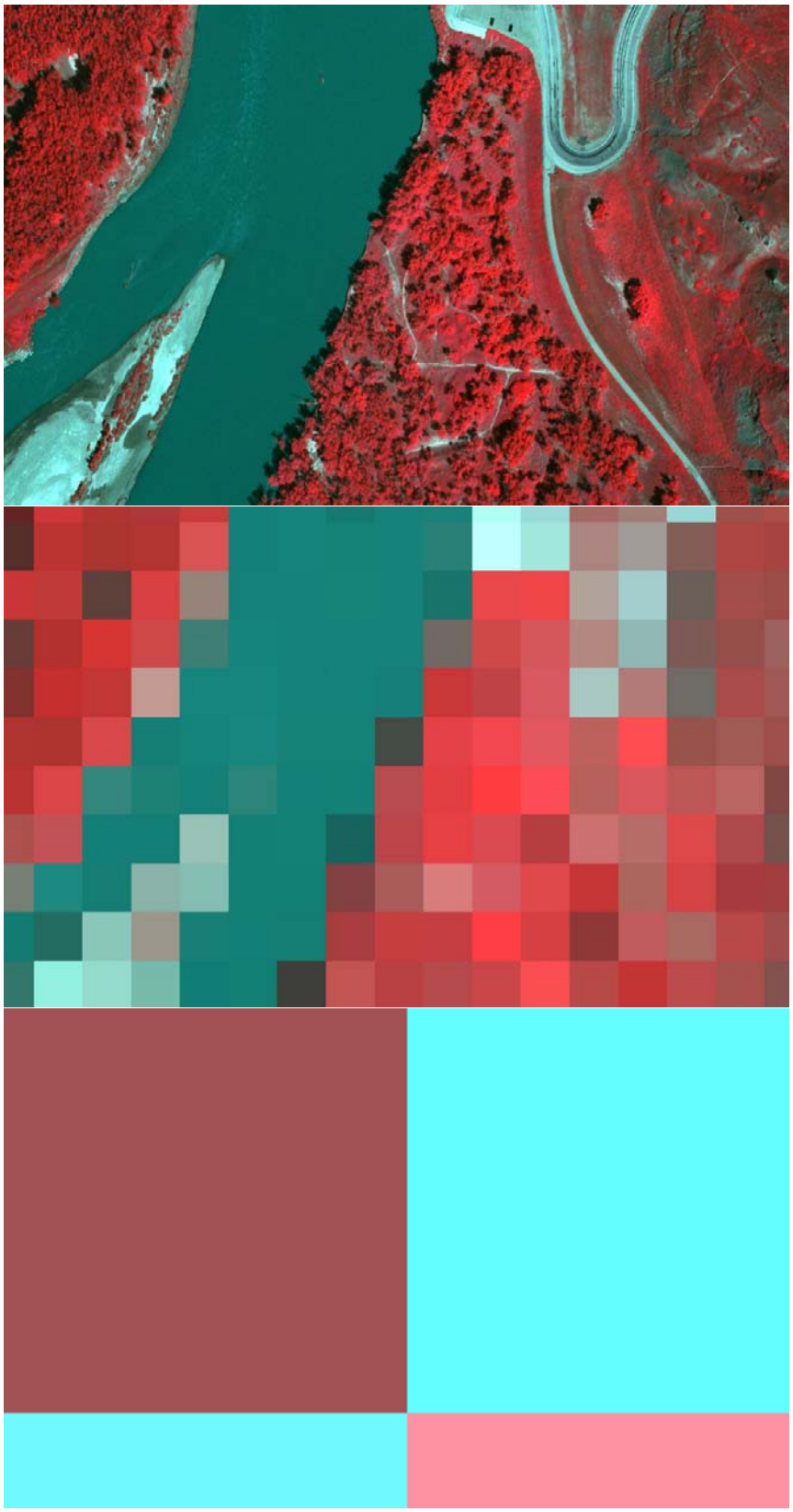

Figure 1.1 – Comparison of the same scene at three different spatial resolutions. Resolutions shown are: (a) 18 cm, (b) 30 m, and (c) 250 m.

The impact of spatial resolution is often studied by performing sensitivity analyses, examining the variations in results which occur when spatial resolution changes (Marceau & Hay, 1999). Images are acquired at multiple spatial resolutions and a quantity of interest is calculated at each spatial resolution, with changes in the estimated parameter being observed at every spatial resolution. The multi-resolution images can be acquired directly from sensors or simulated by spatially resampling high-spatial resolution image data to lower spatial resolutions.

Some spatial resolution sensitivity analyses have been carried out previously in the context of vegetation monitoring. Some studies have found that differences in spatial resolution produce differences in the products derived from a remotely sensed data, and consequently in biophysical parameter estimates (Chen, 1999; Teillet et al., 1997). Other studies have found that differences in spatial resolution do not yield significant changes in the modelled results (Sprintsin et al., 2007).

The issue of spatial scale has not been addressed in the context of riparian LAI modelling. Riparian areas are an interesting setting to examine the effects of spatial resolution due to their small spatial extent and their high-spatial heterogeneity. The author hypothesizes that these factors will result in substantial changes in LAI modelling results as the spatial resolution decreases.

In this research, a sensitivity analysis was performed on the impact of spatial resolution on riparian LAI modelling using remote sensing. The sensitivity analysis was performed to help determine an appropriate spatial resolution for operational riparian LAI monitoring.

1.5 Consumer Digital Cameras as Remote Sensing Instruments

The use of inexpensive consumer digital cameras in airborne remote sensing has been a growing trend in recent years, attributable to the ever increasing quality of

digital camera systems which allows the user to obtain high quality results that were previously only achievable using professional-grade airborne and space-borne sensors. The proliferation of UAV platforms has also led to the growing use of digital cameras. Consequently, digital cameras have been used in a wide range of applications including mapping (Laliberte et al., 2008), crop monitoring (Hunt et al., 2010), forestry (Wang et al., 2011), natural disaster assessment (Bendea et al., 2008), archaeology (Fallavollita et al., 2013) and more.

Sensor characterization and calibration is an important aspect of traditional remote sensing. Satellite-based sensors are subject to rigorous characterization both before being put into orbit as well as ongoing checks during the lifespan of the sensor (Nagaraja Rao & Chen, 1996; Slater et al., 1995; Teillet et al., 1990; Thorne et al., 1997). This characterization allows calibrations to be created and applied to convert raw sensor data into physical units of radiance or spectral reflectance.

Digital camera characterization and calibration has been extensively explored in the field of computer vision (Ebner, 2007; Grossberg & Nayar, 2004; Vora et al., 1997a, 1997b; Zhang, 2000). Unfortunately, the subject has not been treated with the same level of detail within the UAV and digital camera remote sensing fields. Often it is not addressed, or is given a cursory, incomplete treatment. Consequently much of the data being generated by digital cameras are afflicted by various aberrations which negatively impact the data quality. Furthermore, these studies often use raw digital numbers (DN) output by the camera rather than calibrating the data to some standard, such as units of radiance or spectral reflectance (Ide & Oguma, 2010; Jensen et al., 2007; Richardson et al., 2007). Uncalibrated sensor data is of limited utility, as the raw DNs are not physically meaningful and are inconsistent, making it difficult to compare images between sites or over time (Jensen, 2005).

The research conducted in this thesis used consumer digital cameras to obtain airborne image data for riparian LAI modelling. Consequently, a substantial portion of the thesis deals with the issue of camera characterization and calibration. Sensor characteristics were assessed in laboratory-based experiments, and calibrations were applied to compensate for sensor aberrations and to convert the raw camera data to spectral reflectance units. The quality of the calibrated camera data was evaluated through comparison with professional-grade terrestrial and satellite sensors.

1.6 Objectives

The main objective of this research was to study the effects of differing spatial resolutions on modelling the LAI of riparian areas using optical remote sensing data. A secondary goal of this study was to evaluate the use of calibrated digital cameras in a quantitative remote sensing application. These objectives were broken down into the following sub-objectives:

- Determine the spatial, spectral, and radiometric characteristics of consumer-grade digital cameras and develop calibrations to compensate for detrimental sensor effects.
- Obtain airborne image data over southern Alberta riparian areas and compare the calibrated airborne images with data from professional-grade sensors.
- Simulate images of varying spatial resolutions from the airborne image data.
- Create models for LAI prediction using the images at each spatial resolution and use the models to predict riparian LAI.
- Evaluate the changes in both the LAI models and in the modelled LAI predictions as the spatial resolution changes.

1.7 Thesis Organization

This thesis is divided into 5 chapters. Chapter 2 discusses background information relevant to the research performed in the subsequent chapters. Background is provided on riparian areas, LAI, and remote sensing. Chapter 3 details the camera characterization and calibration study. Chapter 4 presents the study of spatial resolution effects on modelling riparian LAI, as well as the comparison of the calibrated digital camera data with professional-grade sensors. Chapter 5 concludes the thesis, summarizing the major findings and providing potential directions for future research.

2. BACKGROUND

2.1 Introduction

This chapter presents the relevant background pertaining to the research in this thesis. Riparian areas are discussed first, as the threats facing these important ecosystems form the main motivation for the research. Leaf area index, the biophysical parameter of interest in this study, is discussed in the following section.

As this was primarily a remote sensing study, the third and largest section discusses remote sensing, including how remote sensing is used to estimate LAI over landscapes and how the factor of scale, or spatial resolution, impacts the information derived from remote sensing data. This section also defines important remote sensor characteristics and preprocessing tasks pertaining to the camera characterization and calibration work performed in this thesis.

2.2 Riparian Areas and Cottonwood Trees

Riparian ecosystems are found on the floodplain adjacent to water courses. Riparian zones are transitional, acting as the interface between the terrestrial and aquatic ecosystems (Gregory et al., 1991). These areas are important for maintaining regional biodiversity, typically possessing a much higher species richness than their surroundings (Gregory et al., 1991; Naiman et al., 1993). This difference is particularly pronounced in arid and semi-arid climates, where the riparian ecosystem hosts many plant and animal species that are not found elsewhere in the region (Patten, 1998). The unique richness of the riparian zone is primarily due to abundant and readily available moisture caused by a shallow water table and regular flooding, along with the large volume of nutrients deposited by the river (Naiman et al., 1993). Consequently, riparian areas are able to support a wide variety of plant species, which

in turn provide food, habitat, breeding grounds, and migration corridors for various animal species (Naiman et al., 1993).

Aside from their ecological importance, healthy riparian zones confer many benefits. Riparian vegetation contributes to water filtration by intercepting sediments, pollutants, and nutrients from agricultural runoff (Anbumozhi et al., 2005). Their roots help to stabilize the river bank, which, along with increased interception of sediment runoff, reduces soil erosion and channel siltation that is harmful to fish and other marine species (Patten, 1998). During floods, riparian vegetation slow the river velocity and absorb some of the water, reducing the flood severity (Brismar, 2002). With each of the above there are associated economic advantages. Less severe floods reduce the damage to residences and infrastructure, a healthy fish stock aids the commercial and recreational fishing industries, and better water filtration reduces the cost and resource use associated with water treatment, to name but a few benefits.

Deciduous trees of the genus *Populus*, commonly called cottonwoods, are the dominant vegetation in many riparian areas, where the trees form the basis for the entire ecosystem (Gom & Rood, 1999). Their roots stabilize the river channel and develop the soil, allowing for other vegetation to become established (Rood et al., 2003). The tree canopy also provides shade for understory vegetation and animals, as well as providing key animal habitat (Rood et al., 2003).

2.2.1 Cottonwood Decline

Riparian cottonwoods are in a state of decline along many North American rivers (Braatne et al., 2007; Howe & Knopf, 1991; Rood & Heinze-Milne, 1989; Scott et al., 1999). Flow regulation mechanisms including dams and other water diversions are implicated as a major contributor to this decline (Nilsson & Berggren, 2000; Rood & Mahoney, 1990; Williams & Cooper, 2005). Flow regulation has altered the natural

flow regimes by reducing annual stream discharge and reducing the occurrence of flood events, altering the timing of peak flows in the spring, and blocking the transport of sediments downstream (Rood & Mahoney, 1990; Williams & Cooper, 2005).

The reduction in discharge has led to a lowering of the floodplain water table, causing chronic moisture stress and increased mortality in the trees, with younger trees being particularly impacted due to their shallow roots (Scott et al., 1999).

The reduction in flood events has negatively impacted seedling recruitment. Cottonwoods seedlings can only become established on bare sediment that has been scoured of other vegetation during floods (Rood et al., 2003). Reduced flooding has resulted in less scoured sites being available for seedlings to germinate.

Cottonwoods seedling release occurs within a limited window corresponding with the end of the peak flows in the spring in order to capitalize on freshly scoured sites (Mahoney & Rood, 1998). Alterations in the timing of peak flows mean that cottonwood seeds are being released at sub-optimal times, further reducing their odds of survival. Finally, the blocking of sediments by dams has led to reduced deposition and increased down-cutting of the river channel downstream of the dam, reducing the amount of suitable sites for cottonwood establishment (Rood et al., 2003).

Cottonwood forests are threatened by a number of other factors besides flow regulation. Climate change has caused similar effects to those of stream regulation by altering the timing and magnitude of spring flooding and reducing summer flows (Rood et al., 2008). The negative impacts of climate changes are predicted to become more pronounced in the future (Rood et al., 2008; Stromberg et al., 2010). The grazing of livestock, natural resource extraction, and urban development are other major contributors to riparian damage (Belsky et al., 1999; Patten, 1998).

The decline of cottonwood forests on regulated rivers has led to the investigation of alternate water management practices to prevent further losses and rejuvenate the riparian zone. Some strategies are based upon maintaining minimum in-stream flows to support vegetation. These strategies are generally considered to be overly simplistic, as they ignore the patterns and dynamism of the natural flow regime (Poff et al., 1997). A better alternative involves the integration of minimum stream flows along with emulation of the natural flow patterns of the river by allowing higher peak flow during the spring followed by a more gradual decline in flow during the summer months (Poff et al., 1997; Rood et al., 2005). These so-called "ramped flow" regimes have been attempted on a number of regulated rivers, including the Oldman River and St. Mary River in Southern Alberta (Rood & Mahoney, 2000; Rood et al., 1998). Following their implementation, a large increase in cottonwood recruitment and seedling survival was observed along both rivers.

Despite the positive initial results, it is necessary to obtain more quantitative data to evaluate the effectiveness of these alternative dam management practices (Rood et al., 2005). This should include ongoing monitoring of the health status of riparian areas downstream of the dams. While monitoring the health status of a select number of riparian areas through ground measurements is possible, it is infeasible to monitor large stretches of a river in this way. Remote sensing can be used in conjunction with ground measurements to provide quantitative riparian monitoring along entire rivers. Remote sensing can estimate quantities related to cottonwood health and function including the evapotranspiration (Nagler et al., 2005), the leaf area index (Gray & Song, 2012), the fraction of absorbed photosynthetically active radiation (fAPAR) (Fensholt et al., 2004), the concentration of foliage biochemicals

such as nitrogen and chlorophyll (Yoder & Pettigrew-Crosby, 1995), and the density and percent cover of the trees (Xiao & Moody, 2005).

This thesis used remote sensing to estimate the leaf area index for riparian zones. Within this context, remote sensing data were coupled with ground measurements to create empirical models for predicting the leaf area index of riparian zones along the Oldman River.

2.3 Leaf Area Index

Foliage density is a governing factor in many important vegetation processes including gas exchange, biomass production, photosynthesis, and water interception (Asner et al., 2003; Chen & Cihlar, 1996; Running & Coughlan, 1988). The leaf area index (LAI) is a biophysical parameter that quantifies foliage density, commonly defined as half of the total green leaf area per unit ground area (Chen & Black, 1992). It is a critical variable in many vegetation, climatic, and hydrologic models (Running & Coughlan, 1988; Sellers et al., 1997). These models are used in a range of applications including vegetation monitoring (Beck et al., 2006), climate forecasting (Buermann et al., 2001), water management (Duchemin et al., 2006), and biomass yield prediction (Moran et al., 1995). LAI has been recognized as an essential climate variable for the Global Climate Observing System – an international initiative for climate monitoring – due to its key role in vegetation-atmosphere interactions (GCOS, 2010).

Of particular importance for this thesis is how LAI relates to evapotranspiration (ET). ET is the sum of water lost to the atmosphere through evaporation from the land and water bodies and transpiration through vegetation foliage (Wilson et al., 2001). Transpiration occurs through stomata, tiny pores on the surface of leaves which also allow the exchange of carbon dioxide and oxygen

(Landsberg & Sands, 2011). When water is in short supply, plants narrow their stomata to conserve water, making the rate of ET a measure for detecting moisture stress in vegetation (Landsberg & Sands, 2011). The ET rate can also be used to assess the water requirements of vegetation, and thus the minimum instream flow needs for riparian vegetation (O'Keeffe & Davies, 1991).

For these reasons, knowledge of riparian ET is important for assessing the vegetation response to alternative dam management strategies. LAI is a required input for many ET models (Glenn et al., 2007). Thus, being able to provide the LAI estimates needed for riparian ET modelling is the driving motivation for this research.

2.3.1 Ground Measurement of LAI

LAI measurements may be obtained through a variety of ground-based methods. The most direct method involves destructive sampling, where entire plants are harvested and their leaves removed, dried, and weighed. This dry weight is then multiplied by the specific leaf area (SLA), the average leaf area per unit dry weight, and then divided by the plant footprint to determine the LAI (Gower et al., 1999). While it is considered the most accurate method, destructive sampling is very labour intensive, particularly within forests, making it difficult to obtain large sample sizes (Jonckheere et al., 2004). The technique also damages the ecosystem under study, which may prevent its use in environmentally protected areas (Jonckheere et al., 2004).

Litter traps are an indirect measurement technique, using containers that collect leaves falling from the trees during senescence. As with destructive harvesting, the collected leaves are then dried and weighed, with the weight being multiplied by the SLA and divided by the trap footprint (Jonckheere et al., 2004). Litter traps have the advantage of being non-destructive and less labour intensive than destructive

harvests; however, the traps have a small measurement footprint, and the method is based on the assumption that the leaves caught in the traps are representative for the leaf-fall over the entire site (Jonckheere et al., 2004). The accuracy of litter traps also suffers in evergreen forests where the trees maintain much of their foliage year round (Jonckheere et al., 2004).

Allometric models are another indirect method for LAI estimation. Allometry is the study of proportional scaling relationships between the size of different components of an organism, or scaling between the size of an organism and physiological processes (Damuth, 2001). Allometric LAI models use relationships between canopy leaf area and other plant dimensions, such as the diameter at breast height (DBH), sapwood area, and tree height to estimate LAI (Gower et al., 1999). Allometric relationships must first be determined through destructive harvesting of a representative sample of plants (Gower et al., 1999). Once the model is calibrated, measurements of the proxy parameter can be used to estimate LAI. Often studies will use allometric models derived from other areas to avoid the use of destructive sampling. However, allometric relationships are often site-specific, and using a model outside the area it was calibrated for can result in large errors (Gower et al., 1999).

It is also possible to estimate LAI indirectly through measurements of optical light transmission through the canopy. Such techniques have become popular in recent LAI studies (Arias et al., 2007; Chen et al., 2006; Cutini et al., 1998; Garrigues et al., 2008). The popularity of optical techniques is due to the fact that they are non-destructive and much less labour intensive than other methods, allowing a greater number of samples to be collected more rapidly (Jonckheere et al., 2004). Optical methods use upward facing sensors to measure the transmission of light passing through the canopy, which is quantified using canopy gap analysis (Weiss et al.,

2004). Gaps are the areas in a canopy devoid of vegetation that allow the transmission of light. Gap analysis involves measuring either the fraction of gaps within the measured area (gap fraction analysis), or the size and distribution of gaps in the canopy (gap size distribution analysis) (Weiss et al., 2004). LAI is calculated from gap analysis using light extinction models based on the probability of a beam of radiation being able to pass unobstructed through a vegetated canopy (Gower et al., 1999).

One issue with optical measurements is that most instruments do not distinguish between leaves and other materials such as branches and stems; thus, the measured quantity includes these elements, and is often referred to as Effective LAI (eLAI) or as the Plant Area Index (PAI) to distinguish it from the true LAI (Jonckheere et al., 2004). In deciduous forests, LAI may be derived from PAI by taking measurements of the fully senesced trees, then correcting the leaf-on measurements using the woody-to-total area ratio (Chen, 1996).

The LAI-2000 Plant Canopy Analyzer (Li-Cor, Inc., Lincoln, NE, USA), shown in Figure 2.1, calculates LAI using gap fraction analysis, and has been employed in many studies (Arias et al., 2007; Cutini et al., 1998; Deblonde et al., 1994; Garrigues et al., 2008). The instrument measures light transmittance using 5 concentric detector rings below a fisheye lens with the following zenith angle ranges: 0 – 13°, 16 – 28°, 32 – 43°, 47 – 58° and 61 – 74° (Figure 2.1) (Li-Cor, 1992). Gap fraction is calculated by comparing differential measurements of above and below canopy light transmission (Welles & Norman, 1991).

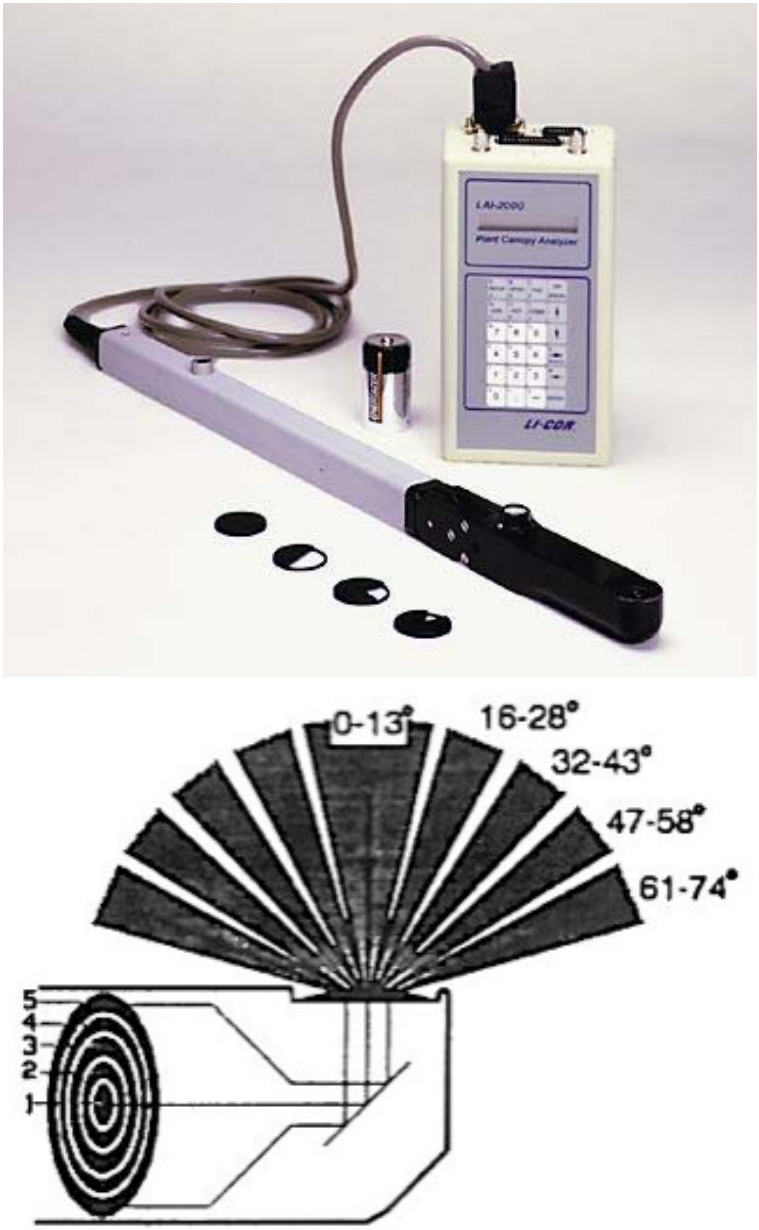

Figure 2.1 – LAI-2000 Plant Canopy Analyzer. The top shows the instrument, while the bottom depicts fisheye lens and 5 concentric detector rings (Li-Cor, 1992).

The LAI-2000 calculation of LAI assumes a random foliage distribution, while in reality, foliage tends to be non-random and clumped, leading to the LAI being often underestimated (Chen & Cihlar, 1995). The clumping index is a correction factor which may be applied to LAI-2000 measurements in order to correct them for foliage clumping effects (Chen & Cihlar, 1995). This index quantifies the amount of clumping of foliage elements within a vegetated canopy. The index ranges from 0 to

1, with 0 being a perfectly clumped canopy and 1 being perfectly random (Chen & Cihlar, 1995). The Tracing Radiation and Architecture of Canopies (TRAC, 3rd Wave Engineering, Ottawa, ON, CA) instrument may be used to calculate the clumping index from the canopy gap size distribution. The TRAC measures the size and distribution of canopy gaps in the direction of the sun at a high frequency while a user walks at a steady pace along a transect (Figure 2.2) (Chen & Cihlar, 1995).

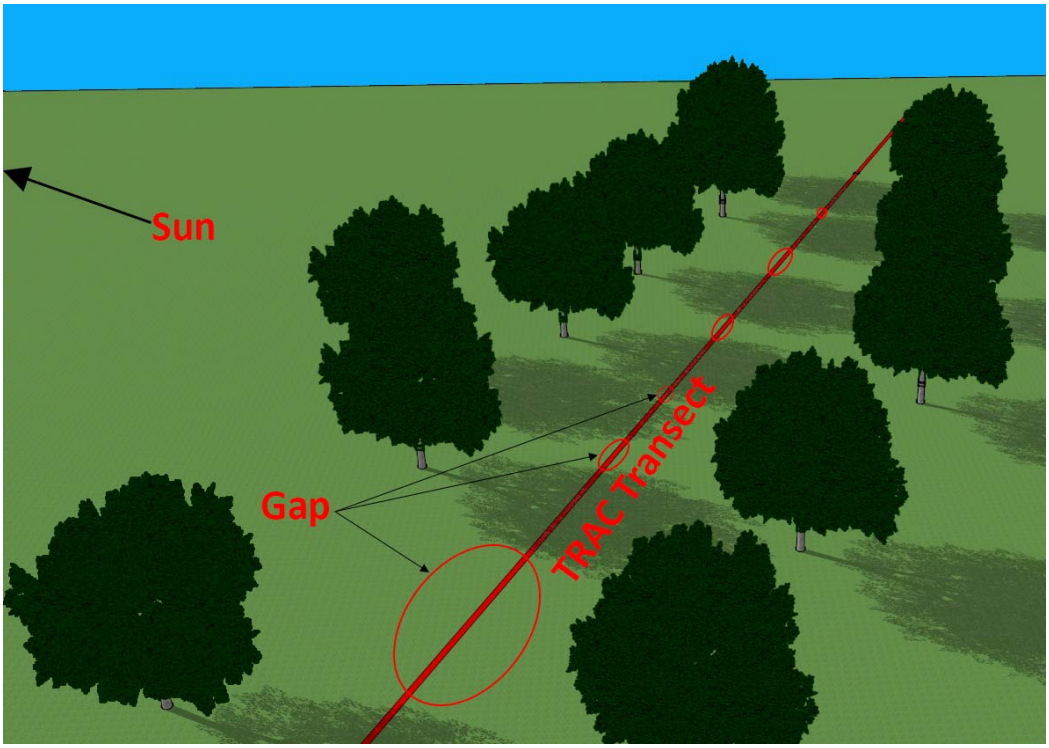

Figure 2.2 – Diagram of TRAC function. Canopy gap size and distribution is measured along a transect using the upward facing TRAC sensors. The gap-size distribution is used to calculate the clumping index.

In this research, both direct and indirect measurements of LAI were acquired on the ground. Destructive harvest methods were used to estimate the riparian understory LAI, while litter traps and optical measurements were used to estimate the tree canopy LAI. Optical LAI measurements were obtained using two LAI-2000 instruments, while a TRAC was used to derive the clumping index which was used to correct the LAI-2000 measurements.

2.4 Remote Sensing

Remote sensing, broadly defined, is the science of deriving information about an object or phenomenon without being in physical contact with it (Schott, 2007). Terrestrial remote sensing refers to the observation of the Earth's surface, typically through the use of airborne or space-borne sensors. These sensors measure electromagnetic radiation (EMR) that is reflected, emitted, or transmitted by objects on the ground. The EMR is recorded in the form of a 2-dimensional image, allowing differences in EMR to be observed and quantified across a landscape. The discussion in this section is limited to terrestrial remote sensing.

Electromagnetic radiation propagates through space as a wave in the form of photons, discrete packets of radiant energy which possess a spectrum of different wavelengths. Wavelengths are typically measured in units of micrometres (μm, 10^{-6}m), or nanometres (nm, 10^{-9}m), and broad regions of the EMR spectrum are classified by wavelength. Table 2.1 shows the boundaries for some of the EMR wavelength regions commonly used in optical remote sensing. The exact wavelengths for these regions can differ, but are typically similar to those in the table.

Table 2.1 – Optical Regions of the Electromagnetic Spectrum.

Spectral Region Name	Wavelength Range
Ultraviolet (UV)	0.01 – 0.4 μm
Visible Light (VIS)	0.4 – 0.7 μm
Near Infrared (NIR)	0.7 – 1.1 μm
Shortwave Infrared (SWIR)	1.1 – 3.0 μm
Midwave Infrared (MWIR)	3.0 – 5.0 μm
Longwave Infrared (LWIR)	5.0 – 20.0 μm
Far Infrared (FIR)	20.0 – 1000 μm

EMR is quantified as irradiance and radiance. Irradiance is the radiant flux (radiation per unit time) being received by a surface per unit area (Schott, 2007). The main source of irradiance is usually the Sun, referred to as solar irradiance. Radiance is the radiant flux that is exiting the surface and being measured by the remote sensor

(Schott, 2007). Radiance and irradiance are typically expressed per unit wavelength, quantities referred to as spectral irradiance and spectral radiance, respectively. Objects on the ground can be characterized based on their spectral reflectance, calculated by dividing spectral radiance by spectral irradiance (Schott, 2007).

Depending on the physical characteristics of objects, they will often reflect, absorb, emit, and transmit EMR differently from one other. These differences allow object characteristics to be inferred from spectral measurements. Differences in the spectral reflectance of vegetation, water, and pavement, for instance, can allow these land surface types to be spectrally distinguished and classified in a remotely sensed image (Landgrebe, 2005). Likewise, differences in the properties of the same type of object – the density or photosynthetic activity of vegetation, for example – are often correlated to differences in spectral reflectance, allowing these properties to be estimated using remotely sensed spectral data (Jensen, 2007).

The primary advantage of remote sensing over other measurement techniques is the ability to obtain a synoptic view of an area. While the information derived from remote sensing is more limited and is prone to higher uncertainty than ground measurements, remote sensing is the only feasible means to obtain data at the landscape, regional, and global scales required for many applications. Another key advantage is the ability to repetitively image an area, providing the ability to detect changes over time.

Because of these advantages, remote sensing is widely used in vegetation monitoring. It has been used to detect changes in vegetation cover (Rogan et al., 2002; Stow et al., 1996), to estimate biophysical variables including LAI (Chen, 1996; Lee et al., 2004), chlorophyll content (Datt, 1998; Gitelson & Merzlyak, 1996), and evapotranspiration (Glenn et al., 2007; Nagler et al., 2005) for yield estimation in

agriculture and forestry (Doraiswamy et al., 2003; Goetz & Prince, 1996) among many other applications.

2.4.1 Remote Sensing Estimates of Leaf Area Index

Ground measurements of LAI are labour intensive and costly to carry out, limiting their ability to be employed for estimating LAI over large areas (Zheng & Moskal, 2009). In order to provide regional or global estimates of LAI it is necessary to use remote sensing data.

LAI has been traditionally modelled using passive optical remote sensing. Optical remote sensing is not capable of directly measuring LAI; instead, measurements of EMR from the vegetation are used as a proxy to estimate it using models (Asner et al., 2003). These models are based on the fact that differences in vegetation spectral reflectance in various spectral regions are correlated with differences in LAI (Jordan, 1969).

More recently, active remote sensing methods including RADAR and LiDAR have been used to model LAI (Manninen et al., 2005; Morsdorf et al., 2006; Riaño et al., 2004; Xu et al., 1996). Active sensors send out pulses of EMR and measure the timing and characteristics of the return signal. LAI modelling with active remote sensing has several advantages over passive optical methods. Active methods can provide additional information on vegetation structure and height (Zheng & Moskal, 2009). Active remote sensing is also not reliant on clear skies or on sunlight, meaning measurements can be obtained at night and during overcast conditions (Manninen et al., 2005).

There are a number of methods for estimating LAI using passive optical remote sensing. The oldest and most common approach is through the use of empirical models. These models are based on regression between ground-based

measurements of LAI and image spectral reflectance to create LAI prediction models (Propastin & Panferov, 2013). Empirical models are appealing due to their relative simplicity and low data requirements (Propastin & Panferov, 2013). They are usually based on spectral vegetation indices (SVIs), mathematical transformations of spectral reflectance data (Huete, 1988). These indices are often based on the relationship between reflected visible and infrared EMR, and are correlated to many aspects of vegetation function (Huete, 1988). SVIs have a positive correlation with LAI, with higher SVI values being correlated with higher LAI values.

One of the main issues with the relationship between SVIs and LAI is the tendency for the SVI to saturate at moderate to high LAI values, becoming insensitive to further increases in LAI (Baret & Guyot, 1991). Another problem is that, due to the SVIs being correlated with many different vegetation properties, differing values for an SVI may not be strictly due to differences in LAI (Baret & Guyot, 1991). The relationships can also be sensitive to soil properties, sun-sensor geometry, atmospheric effects, and the spatial arrangement of the vegetation (Baret & Guyot, 1991; Broge & Leblanc, 2001). Despite the issues associated with them, SVI-based empirical models have been implemented in many remote sensing studies of LAI (Asrar et al., 1984; Colombo et al., 2003; Gonsamo & Pellikka, 2012; Myneni et al., 1997; Soudani et al., 2006; Turner et al., 1999).

Hundreds of SVIs have been developed over the years, often for very specific applications. The most commonly used SVI is the Normalized Difference Vegetation Index (NDVI), which can be calculated as follows (Rouse et al., 1974):

$$NDVI = \frac{NIR - Red}{NIR + Red} \tag{2.1}$$

where NIR stands for spectral reflectance in near infrared wavelengths and Red stands for spectral reflectance in visible red wavelengths.

While the NDVI is extensively used, it has been shown to be sensitive to soil brightness at low vegetation cover, as well as to atmospheric effects, introducing noise into its relationship with vegetation parameters (Baret & Guyot, 1991). Many different indices have been developed to improve on the deficiencies of the NDVI (Baret et al., 1989; Broge & Leblanc, 2001; Haboudane et al., 2004; Huete, 1988; Qi et al., 1994). The abundance of SVIs has led to many studies on the relative performance of different SVIs for modelling different vegetation parameters (Baret & Guyot, 1991; Broge & Leblanc, 2001; Colombo et al., 2003; Elvidge & Chen, 1995; Haboudane et al., 2004). What has been shown by these studies is that there is no overall best SVI; rather, SVI performance is variable depending on the vegetation type, the site conditions, the parameters of interest, and the range of values exhibited by the parameters (Broge & Leblanc, 2001). Therefore, it is prudent to test more than one SVI when attempting to model vegetation parameters.

More complex methods for modelling LAI have been developed aside from simple SVI-based empirical models. One method makes use of canopy reflectance (CR) models, which simulate the spectral reflectance properties of a vegetated canopy using input biophysical, biochemical, and structural parameters, including LAI (Goel & Thompson, 1984; Jacquemoud et al., 2009; Peddle et al., 2004). When inverted these CR-based models can be used to estimate the parameters of interest based on the spectral reflectance of input imagery (Jacquemoud et al., 2009). CR-based models have the advantage of being physically based, as well as being capable of providing estimates for various key vegetation parameters in addition to LAI, such as the chlorophyll content, water content, and fAPAR (Jacquemoud et al., 2009). Despite

this advantage, CR models can be complex and difficult to parameterize, requiring, for instance, accurate knowledge of the vegetation structure, sun-sensor geometry, and atmospheric conditions (Jacquemoud et al., 1995; Propastin & Panferov, 2013).

Spectral mixture analysis (SMA) is another method which has been employed in LAI estimation (Hu et al., 2004; Peddle & Johnson, 2000; Peddle et al., 1999). The theoretical basis for SMA is that the radiance measured in a given pixel is contributed by the individual "pure" surface components contained within that pixel, in amounts proportional to each component's abundance (Adams et al., 1993). The "pure" spectral signature of a single component is known as an endmember. If the endmember spectra are known, SMA can be used to spectrally unmix image pixels, deriving the fraction of each endmember represented in each pixel (Adams et al., 1993). In a forest canopy, the fundamental scene components are the sunlit canopy, the sunlit background, and shadow (Peddle et al., 1999). Through SMA, the fraction of each component can be estimated for each scene pixel, and the separate fractions can be used to estimate LAI through regression analysis (Peddle et al., 1999). SMA-based models have demonstrated an improvement in LAI prediction over SVI-based empirical models; however, implementation of these models requires accurate measurements of the spectral signature of the scene endmembers (Peddle & Johnson, 2000; Peddle et al., 1999)

In this thesis, empirical models based on SVIs calculated from optical remote sensing data were created and used to estimate riparian LAI. While more complex CR or SMA-based models could possibly provide more robust and accurate LAI estimates, the simplicity and low data requirements of empirical models make them attractive for this research.

Few studies have implemented SVI-based empirical LAI models in riparian environments. Nagler et al. (2001) studied several SVIs as predictors of LAI and vegetation cover for riparian vegetation along the Colorado River in Mexico. The indices compared in the study were the NDVI, the Soil Adjusted Vegetation Index (SAVI), and the Enhanced Vegetation Index (EVI). They found that the NDVI performed slightly better than the SAVI and EVI, but all three were similar (R^2 = 0.73, 0.65, and 0.64 respectively).

2.4.2 Sensor Characteristics

Sensors are the devices used in remote sensing to detect and record EMR. Traditionally, optical remote sensing was performed using film-based sensors; however, electro-optical sensors are much more commonly used today. An electro-optical sensor is made up of several key components, namely the optics, the detectors and their associated electronics, and the analog-to-digital converter (ADC) (Landgrebe, 2005). The optics serve to direct and focus EMR onto the focal plane of the sensor, where the detectors reside. The detectors are made from photo-sensitive materials which, when struck by photons, emit electrons, producing a current and a buildup of electric charge. This charge is amplified and then passed to the ADC where it is converted from an analog to a digital signal, a process called quantization (Landgrebe, 2005). This digital signal is recorded in the form of a digital number (DN). The greater the radiance incident on the detector, the larger the electric charge generated, and the higher the resulting DN.

The final output from the sensor is an image, a 2-dimensional array of picture elements (pixels). Pixels are discrete points (typically square) whose locations can be denoted by row and by column within the image, or by their physical location on the

ground. Each pixel contains the DNs recorded at different wavelengths over that particular area on the ground.

Multiple detectors are typically used to record EMR at different wavelengths (referred to as spectral bands). Broadband EMR entering the sensor must be divided and sorted to pass only EMR of the desired wavelengths to specific detectors. This can be accomplished using several mechanisms including prisms and diffraction gratings to split the EMR, or bandpass filters which allow only specific wavelengths of EMR to pass through, as illustrated in Figure 2.3 (Landgrebe, 2005).

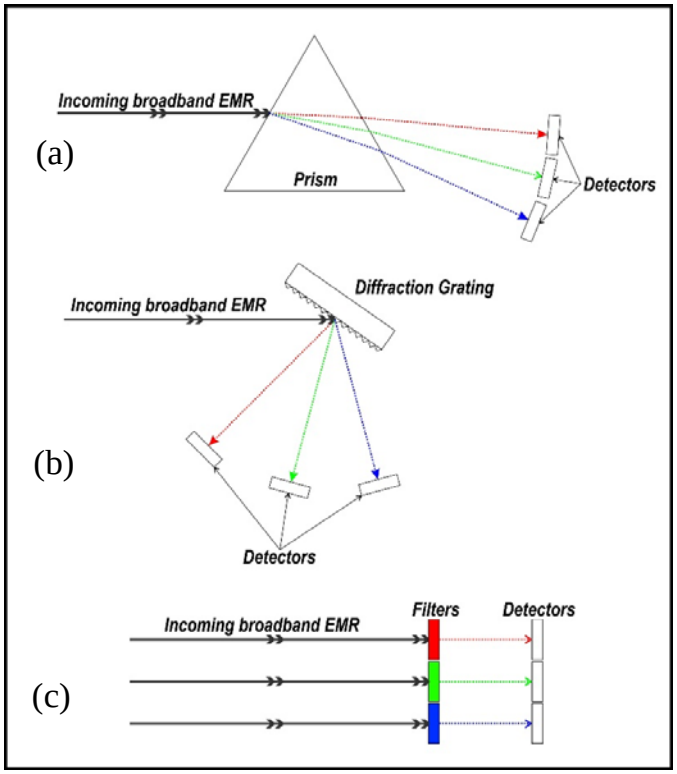

Figure 2.3 – Illustration of light sorting mechanisms. (a) prism splitting; (b) diffraction grating splitting; (c) bandpass filtering.

Sensor systems are classified by a number of metrics. One key metric is the signal-to-noise ratio (SNR) which is the ratio between the signal (the measured radiance) and the noise (random variations which cause uncertainty in the measured signal) (Landgrebe, 2005). Higher SNR sensors allow smaller differences in the signal to be more confidently measured.

Another key metric is the spatial extent, the ground area covered in a single image (Jensen, 2007). A related term is the swath width, referring to the width of an image perpendicular to the travel direction of the sensor. Space-borne sensors, being much further from the ground, almost always have a much larger spatial extent and swath width than airborne sensors.

Another important metric is the location and width of the spectral bands, which determine the portions of the EMR spectrum and range of wavelengths within each (Landgrebe, 2005). While some sensors only cover a narrow portion of the spectrum, such as only visible wavelengths, others like the Moderate-resolution Imaging Spectroradiometer (MODIS) sensor provide coverage from visible to longwave infrared wavelengths (Xiong et al., 2009).

In addition to the above metrics, sensor systems are normally classified according to four fundamental resolutions. These are the spatial resolution, the spectral resolution, the radiometric resolution, and the temporal resolution.

2.4.2.1 Spatial Resolution

Spatial resolution refers to the level of spatial detail in an image. The spatial resolution of a sensor is related to the detector instantaneous field-of-view (IFOV). The IFOV is the angular field-of-view of a detector element over which radiance is integrated (Schott, 2007). Projecting the IFOV onto the ground yields the ground-projected instantaneous field-of-view (GIFOV), the ground area over which the detector measures radiance (Schott, 2007). Thus, the GIFOV is a product of the IFOV and the height of the platform above the terrain.

Another spatial resolution metric is the ground sampling distance (GSD), the ground distance between two adjacent pixel centres in an image (Warner et al., 2009). The GSD is related to the height of the platform above the ground and the sampling

interval, the distance between spectral samples measured by the sensor (Driggers, 2003). The GSD is almost always approximately equivalent to the GIFOV (Driggers, 2003). Because the GSD is variable depending on the terrain, a nominal value may be used to describe the average GSD within an image.

The spatial resolution of a sensor depends on the distance between the sensor and the ground, the magnification of the optics, and the size of the detectors (Schott, 2007). Spatial resolution may be increased by moving the sensor closer to the ground, by increasing the magnification of the optics, or by decreasing the size of the sensor detector elements.

A higher spatial resolution allows more spatial detail to be recorded in an image. High-spatial resolution data can always be aggregated to simulate coarser spatial resolutions, while the opposite is not possible. Consequently, when the appropriate resolution for an application is unknown, it is likely better to obtain data with a high-spatial resolution and spatially resample it as needed. However, in practice, achieving a high-spatial resolution comes with some important trade-offs. If the detector element size is decreased, the ground area represented by each pixel is decreased; this decreases the irradiance being detected for each pixel, reducing the SNR (Chen et al., 2000). The amount of measured irradiance for each pixel can be increased by increasing the spectral bandwidth of the detectors; however, this lowers the spectral resolution of the sensor (Schott, 2007). Finally, increasing the optical magnification or moving the sensor closer to the ground reduces the spatial coverage of the imagery (Landgrebe, 2005).

In an ideal sensor, each pixel in an image would contain spectral data from only within the pixel footprint. In reality, the signal recorded by a detector is partially influenced by areas surrounding the pixel. The spatial sensitivity of a detector is

represented by a point spread function (PSF), the response of the detector to a point source of radiance (Warner et al., 2009). The PSF can be described by a three-dimensional function, with peak sensitivity in the centre and a gradual reduction in sensitivity with increasing distance from the centre. The full-width-at-half-maximum (FWHM) describes the distance from the centre of a detector element where sensitivity falls to 50% of maximum (Schott, 2007). The GSD of the sensor is most often set to be equivalent to the FWHM of the detector PSF; however, since some sensitivity remains beyond this threshold, some spectral bleeding occurs between adjacent pixels (Warner et al., 2009). Due to the influence of the PSF, low resolution sensor data cannot be accurately simulated by simple spatial resampling of higher resolution imagery. Accurate simulation requires modelling the sensor PSF as well. In cases where the PSF for the desired sensor is unknown, it can be approximated using a three-dimensional Gaussian function (Kavzoglu, 2004).

2.4.2.2 Spectral Resolution

The spectral resolution quantifies the wavelength region over which EMR is sampled. While EMR occurs along a continuous spectrum, sensors sample it over discrete ranges called spectral bands. The width of the band determines how many wavelengths of EMR are integrated in the measured signal (Warner et al., 2009).

Spectral bands are described by their central wavelength and their bandwidth. The central wavelength is where the relative spectral response of the band is highest. Spectral sensitivity for the band declines to either side of the central wavelength (Jensen, 2007). The nominal bandwidth for a band is equal to the FWHM of the spectral sensitivity function, the spectral distance to either side of the peak where spectral response falls to half its maximum. Accordingly, the region of spectral

sensitivity for the band is often wider than the nominal bandwidth (Warner et al., 2009).

Optical sensors are characterized by the number of spectral bands they possess. Panchromatic sensors have only one spectral band. Panchromatic bands are usually very broad spectrally, integrating a large portion of the EMR spectrum (usually visible wavelengths) in order to achieve a high-spatial resolution (Warner et al., 2009). Multispectral sensors can possess between two to several dozen bands. Multispectral bands are often broad, being tens or hundreds of nanometres wide in the spectral dimension, and are usually non-contiguous, instead being located at key areas of interest along the EMR spectrum (Jensen, 2007). Hyperspectral sensors possess many narrow, contiguous bands, allowing a more detailed, continuous sampling of the EMR signal (Hu et al., 2009).

As with spatial resolution, achieving a better spectral resolution comes with trade-offs. With narrow spectral bands, the spectral region being integrated by each is small; this means the total radiance per pixel is low, decreasing the SNR of the sensor (Landgrebe, 2005). To increase the amount of radiance per pixel, the spatial resolution must be decreased (Landgrebe, 2005). Consequently, hyperspectral sensors usually have lower spatial resolutions than multispectral sensors. They are also more complex, expensive, and tend to be more sensitive to calibration errors than multispectral sensors (Schott, 2007).

It is important to know the spectral characteristics of a sensor to understand if it may be used for a particular application, or to facilitate comparisons between different sensors. The most common method for assessing a sensor's spectral sensitivity is to image EMR passed through an EMR splitting device such as a monochromator (Vora et al., 1997b). By measuring narrow-band radiation across a

spectrum of different wavelengths, the spectral sensitivity of the sensor at those wavelengths can be assessed. Spectral response curves can be created by interpolation between the measurements (Vora et al., 1997b).

2.4.2.3 Radiometric Resolution

Radiometric resolution refers to the ability of a sensor to discriminate differences in EMR intensity. Sensors with a higher radiometric resolution can resolve smaller differences, increasing the number of separable signal levels (Jensen, 2007).

The radiometric resolution of a sensor refers to the bit-level used to digitally quantify the measured radiometric signal into digital numbers (Jensen, 2007). Higher bit-levels have a greater number of possible DN values, allowing a more precise measurement of EMR intensity. Images are often quantized in 8 bits, with 256 DN values, allowing 256 levels of radiometric difference to be distinguished. Higher bit-levels are often used by more sophisticated sensors including 12 bits (4096 DN levels) and 16 bits (65536 DN levels).

While a higher radiometric resolution is preferable for achieving more precise measurements, it comes at a cost. A higher bit-level can greatly increase the file size of images, making downloading images from a satellite sensor more challenging, and increasing the time needed for image processing tasks (Schowengerdt, 2006). Furthermore, if the SNR of the sensor detectors are not sufficiently high, quantization at a higher bit-level may not yield a tangible increase in data precision (Schowengerdt, 2006).

2.4.2.4 Temporal Resolution

The temporal resolution, or revisit period of a sensor system, describes the time interval between successive images of the same area on the ground (Warner et al., 2009). It is typically only used in reference to satellite-based sensors, which have

a fixed orbit, as airborne platform revisit periods are flexible. Satellite revisit periods can vary from weeks, to days, to even hours. A higher temporal resolution allows better monitoring of an area, as well as increasing the chances of obtaining cloud-free imagery.

For a single satellite sensor looking directly downwards (nadir), the revisit period is related to the swath width of the sensor system and its orbital period (Jensen, 2007). Sensors with a wider swath have significant overlap between images acquired on adjacent passes, allowing them to repeatedly image the same area on multiple passes. Satellites with a shorter orbital period will orbit the globe faster, allowing them to image the same area on multiple orbits as the Earth will not have rotated as much between multiple satellite orbits.

The temporal resolution of a sensor can be increased through off-nadir imaging (tilting the sensor to look at an angle rather than straight down) to view the same area on multiple passes (Jensen, 2007). The temporal resolution can also be increased by launching multiple satellites in a constellation. This allows multiple sensors to image an area sequentially, greatly increasing the temporal resolution (Warner et al., 2009).

As with the other resolutions, there are trade-offs required to increase the sensor temporal resolution. Sensors with a wider swath generally have a lower spatial resolution (Jensen, 2007). Images acquired off-nadir can also suffer from lower spatial resolutions (Huete et al., 2002), geometric distortions (Schowengerdt, 2006), and changes in target reflectance due to bi-directional reflectance (Roy et al., 2002). Using a constellation of sensors has no inherent disadvantage, but it limits the pool of selectable sensors, as many are not part of a constellation.

2.4.2.5 Sensor Errors

Sensors are often afflicted by a number of errors that can reduce the quality of the data output. These errors include both geometric and radiometric errors. Geometric errors are those which cause pixels to appear in different locations compared to their real ground locations. Radiometric errors are issues with the EMR signal measured by the sensor.

Optical lens distortion is a common geometric error that is caused by the sensor optics, making straight lines appear curved in an image. Optical lens distortion has both a radial and tangential component. Radial distortions are symmetrical, radiating out evenly from the optical centre of the camera (Brown, 1966). Radial distortion manifests as either barrel distortion or pincushion distortion (Figure 2.4). Barrel distortion is an apparent shifting of points away from the centre of the image frame, while pincushion distortion is a shifting of points toward the centre of the image frame. Tangential distortions are asymmetrical, appearing as a displacement of the radial distortion component toward one part of the image frame. Tangential distortions occur due to imperfect alignment of the lens optical elements and the detectors (Brown, 1966).

Both radial and tangential distortions can be characterized by imaging a planar calibration grid with known geometric characteristics (Zhang, 1999). The grid is imaged from multiple orientations and software is used to extract the grid intersections. Camera distortion coefficients are estimated by comparing the grid intersection locations extracted from the images to their expected locations in a distortion-free image (Zhang, 1999). Distortion coefficient estimates are optimized using iterative least-squares optimization, and a camera distortion model is created (Zhang, 1999).

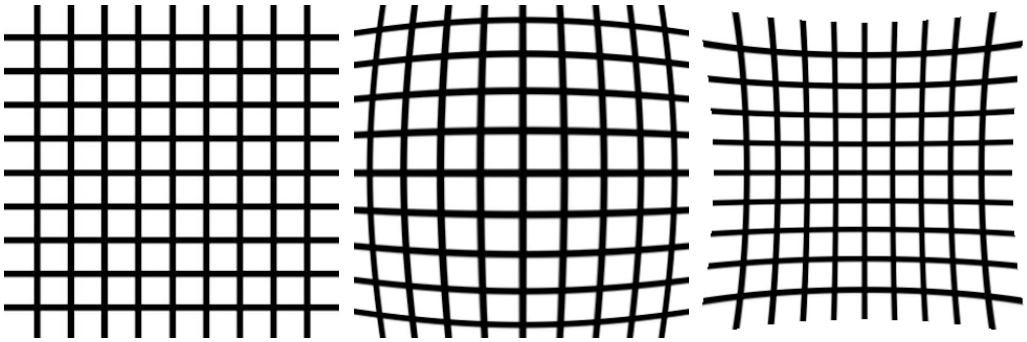

Figure 2.4 – Illustration of optical lens distortion on an evenly spaced grid. Left shows the undistorted grid; centre shows the effects of barrel distortion; right shows the effects of pincushion distortion.

Geometric errors can also be caused by variations in the exterior orientation of the sensor relative to the ground due to changes in the pitch, roll, and yaw of the imaging platform (Breuer & Albertz, 2000). These errors are less common with satellite sensors, which have a fixed orbit, but occur frequently with airborne sensors. These errors can be characterized if the sensor orientation parameters were recorded at the time of image acquisition. These data can be derived from gyroscope-based sensors like an inertial measurement unit (IMU) (Cramer et al., 2000).

The main source of radiometric error is noise, random variations in the values recorded by a sensor which are not caused by actual variations in the EMR signal being measured (Schott, 2007). Noise is undesirable as it adds uncertainty to the remotely sensed data. Many factors contribute to image noise including random fluctuations in the number of photons striking the detectors (shot noise), thermal variations in the detectors (Johnson noise), atmospheric scattering of radiation into the sensor, variations in detector electric charge (dark noise), and errors in the conversion of the electric charge to a discrete DN (quantization noise) (Fiete & Tantalo, 2001).

Sensor noise can be characterized by measuring a radiometrically uniform target such as a uniform light source. As the input signal is uniform, the standard deviation in the measured signal represents the image noise (Fiete & Tantalo, 2001).

The SNR of the sensor may then be calculated by dividing the average signal value by the standard deviation (Fiete & Tantalo, 2001).

Another common radiometric error is a gradual diminishing of pixel values toward the edges of the image frame, making the edges appear darker than the centre of the image. This effect is caused by a number of factors, including light falloff and vignetting. Light falloff is a reduction in light intensity that occurs when light enters the lens at increasingly oblique angles. The falloff is proportional to the fourth power of the cosine of the angle at which the light strikes the sensor (Wüller & Gabele, 2007). Vignetting occurs when light entering the lens is partially obstructed by lens elements (Yu, 2004). Another form of vignetting called pixel vignetting, occurs due to the fact that detectors are less efficient at converting incident radiation into freed electrons when the light strikes the detector at oblique angles (Catrysse et al., 2000).

Because both light fall off and vignetting manifest as the same effect, it is very difficult to separate them. Thus, their cumulative effects are usually characterized together. The effects of vignetting and light falloff can be characterized by imaging a spectrally uniform target (flat field imaging) (Yu, 2004). As the light entering the camera is uniform, aside from noise, differences in pixel values between the centre and the periphery of the image are due to vignetting and light falloff.

Consumer digital cameras often demonstrate another radiometric issue, namely a nonlinear response to changes in EMR intensity. While the digital sensors themselves respond linearly, the camera electronics quantize the signal in a nonlinear manner (Grossberg & Nayar, 2004). This is done for a number of reasons: firstly, both the human eye and camera film have a nonlinear response to light intensity (Grossberg & Nayar, 2004). For digital images to appear “correct” to the eye, the digital response is made nonlinear as well. Secondly, due to the often limited dynamic

range of camera sensors, introducing a nonlinear response can increase the range of scene brightness which can be recorded in an image (Kim & Pollefeys, 2008). As digital cameras are designed to create attractive pictures, both of these properties are more important to camera manufacturers than providing radiometrically accurate data. Sensor linearity can be evaluated by imaging light sources at various light intensities, and plotting the changes in sensor response against the changes in light intensity (Vora et al., 1997a). Radiometric response models can then be created by interpolation between the measured responses.

2.4.3 Data Pre-processing

In order to be properly used in information extraction, images acquired from a sensor must first be pre-processed. Common pre-processing tasks include correction of geometric and radiometric errors, geo-registration, and the conversion of raw DNs into physical units. For satellite sensors, many geometric and radiometric errors are often corrected prior to an end-user receiving the imagery. For airborne data gathered directly by the user, however, some or all of these errors should be addressed.

To correct lens distortions, the distortion must first be characterized and a distortion model created. The model is then used to geometrically warp the imagery, adjusting the location of pixels to compensate for the distortion (Zhang, 1999).

Geometric errors due to the exterior sensor orientation can be corrected if orientation parameters were recorded using an IMU (Cramer et al., 2000). The orientation data is used to warp the imagery to match a nadir perspective. If the orientation parameters were not recorded, the distortion can also be corrected or minimized during geo-registration (Jensen, 2005)

While totally removing image noise is difficult due to its unpredictability, methods have been developed to reduce its impact. Spatial filters (Church et al., 2008)

and spectral filters (Tsai & Philpot, 1998) can be used to reduce the variability in the imagery. Another method involves transformation of the data using techniques like the minimum noise fraction (MNF) to de-correlate the dataset and isolate the image variability caused by noise (Lee et al., 1990). Noise is reduced by discarding the noise component, and the data is then transformed back to spectral space. Unfortunately, any method for reducing noise can also reduce the information content of the imagery by suppressing not only the variability due to noise but also variability caused by actual spatial and spectral features (Schott, 2007).

The cumulative effects of light falloff and vignetting may also be corrected during pre-processing. If the effects have been characterized through flat-field imaging, digital filters can be constructed to apply a gain factor to each pixel, which increases the pixel value proportionally to the amount it is affected by light falloff and vignetting (Yu, 2004).

Geo-registration is used to convert the coordinates within an image to a known geographical coordinate system, allowing objects in the imagery to be spatially located on the Earth surface. Geo-registration is usually performed using ground control points (GCPs), areas with known coordinates which can be identified in the image (Jensen, 2005). GCPs are derived from surveys, maps, or other geo-registered images. They are located within the image and the relationship between image coordinates and GCP coordinates is computed. The image is then rotated, resized, and warped to align with the GCP locations (Jensen, 2005).

If the sensor has a nonlinear radiometric response, it is possible to mitigate this issue through pre-processing. The camera radiometric response must first have been measured and radiometric response models created. Lookup tables (LUTs) can then be created from the response models and used to convert the DNs for every pixel in

the image into a corresponding linear value (Vora et al., 1997a). This method linearizes the images, although it cannot address the fact that the sensor will have different levels of radiometric sensitivity throughout its dynamic range.

Preprocessing is also necessary to convert the DNs output from a sensor into units of radiance or reflectance. Assuming a sensor is radiometrically linear, DNs are computed from the radiation signal through applying a gain (signal amplification) and offset (fixed addition of DN) (Peddle et al., 2003). If the gain and offset values are known, it is possible to convert from a DN value to an at-sensor radiance value (Peddle et al., 2003). Division of the at-sensor radiance by the exo-atmospheric irradiance from the Sun allows the at-sensor spectral reflectance to be derived (Jensen, 2005).

Unfortunately, at-sensor radiance and spectral reflectance are not the same quantities as the irradiance and spectral reflectance are from targets on the ground. This is because gas molecules and aerosols in the atmosphere attenuate both incoming radiation from the Sun and outgoing radiation from the Earth's surface (Jensen, 2005). Atmospheric attenuation includes both scattering and absorption of radiation. Due to atmospheric attenuation, some target irradiance is scattered or absorbed before reaching the sensor (Jensen, 2005). Scattering can also cause irradiance from adjacent areas or from the atmosphere itself to be scattered into the sensor optics, contributing to signal noise (Jensen, 2005). Atmospheric effects are variable both spatially and temporally, and also depend on the wavelength of the EMR. These effects can thus introduce significant uncertainty to remotely sensed data when comparing between spectral bands and between images acquired on different dates or in different areas (Peddle et al., 2003).

Atmospheric correction allows removal or mitigation of atmospheric attenuation. A number of atmospheric correction methods exist, which can be characterized as relative and absolute corrections (Jensen, 2005). Relative corrections seek to radiometrically normalize the DNs between images acquired on different dates to facilitate comparisons between them (Jensen, 2005). Relative techniques use one image as a reference, with all other images being normalized to match the reference image (Peddle et al., 2003). One relative approach uses targets within the reference scene to develop an empirical relationship, which is then used to transform the DNs for all other images with the same targets present (Peddle et al., 2003). The targets should ideally be fairly large, cover a large amount of the scene dynamic range, and be spectrally invariant (Jensen, 2005). Unfortunately, while relative techniques can facilitate change detection between sets of images acquired from the same sensor, they do not allow proper comparison between images acquired from different sensors (Peddle et al., 2003).

Unlike relative corrections, absolute corrections seek not only to remove atmospheric effects, but also to convert sensor DNs into physical units of surface radiance or reflectance (Peddle et al., 2003). A number of absolute corrections methods may be used. Most commonly, absolute corrections make use of radiative transfer models, which model the interactions between radiation and atmospheric particles (Peddle et al., 2003). Radiative transfer models are a robust and accurate method for retrieving surface parameters; however, the drawback of these models is they require information on atmospheric variables such as the aerosol optical depth and the water vapour content, which are not always available (Peddle et al., 2003). In the absence of measurements for these parameters they may be estimated; however, this can introduce error.

Another absolute correction method is the empirical line calibration (ELC). This method is similar to the relative empirical correction, making use of targets within the scene to create an empirical model to normalize all pixel values within an image (Smith & Milton, 1999). Unlike the relative correction, the ELC method uses targets with known reflectance characteristics, allowing the images to be converted to true ground reflectance (Smith & Milton, 1999). Consequently, it is possible to compare data corrected with the ELC method to data acquired from other sensors. As with the relative correction, the ELC method requires spectrally invariant targets which cover a large portion of the sensor dynamic range (Smith & Milton, 1999). Targets can be natural providing they are spectrally invariant, or man-made targets such as calibration tarps can be used (Smith & Milton, 1999). The advantage of the ELC method over radiative transfer methods is that additional information on atmospheric parameters are not required, making the method simpler to employ. The major disadvantage over using radiative transfer models is that it necessitates the placement of targets within the scene or the presence of natural targets. The ELC method can also result in substantial errors, if the targets do not adequately cover the sensor dynamic range or are not spectrally invariant (Smith & Milton, 1999).

2.4.4 Spatial Scale in Remote Sensing

Spatial scale is a fundamental property of key importance for geographical studies. The definition of “spatial scale” differs, but typically refers to either (or both) the level of spatial detail in a study, measurement, or map, or its geographic coverage (Quattrochi & Goodchild, 1997). These two properties are also referred to as “grain” and “extent”, respectively.

The impact of spatial scale has been recognized for many years and has been extensively discussed in both the social and natural sciences (Clark, 1990; Gehlke &

Biehl, 1934; Greig-Smith, 1961; Marceau, 1999; Sheppard & McMaster, 2008). Far from a minor issue, spatial scale plays a fundamental role in the entities, processes, and patterns that are observed within a landscape (Marceau, 1999). Furthermore, because complex processes operate at multiple scales, to understand and model them it is necessary not only to study how they operate at each scale, but also to understand the linkages between them (Marceau, 1999).

With the wide-spread use of remote sensing and geographic information systems (GIS) in modern spatial analysis, the scale issue has received newfound attention (Chen et al., 2004; Chen, 1999; Marceau & Hay, 1999; Quattrochi & Goodchild, 1997; Teillet et al., 1997). In remote sensing, the spatial resolution of an image is equivalent to the grain size of the data, while the image size is equivalent to the extent (Woodcock & Strahler, 1987). Depending on the spatial resolution, the fundamental entities of a study can change. At a very high-spatial resolution, individual trees may be observable, while at a very low spatial resolution, an entire forest stand may be represented by only a handful of pixels. With a plethora of different sensors now available with a wide variety of different spatial resolutions, the selection of a sensor or sensors for a study must be informed by the desired scale of analysis. This is especially true given the trade-offs in sensor design between spatial resolution and other characteristics, such as temporal or spectral resolution.

A classic problem in spatial analysis is the modifiable areal unit problem (MAUP). The MAUP refers to the sensitivity of measurements to how a phenomenon of interest is partitioned into non-overlapping spatial units (Openshaw & Taylor, 1979). It is characterized by two interrelated issues: the scale problem and the aggregation problem.

The scale problem refers to the variance in results when small spatial units are aggregated into larger, coarser units (Openshaw & Taylor, 1979). For instance, analysis of the same census data can yield different results depending if it is aggregated into census districts or standard regions (Openshaw & Taylor, 1979). The scale problem often manifests as a decline in the variance of the data as it is progressively aggregated, even if the mean value remains the same (Dark & Bram, 2007)

The aggregation problem refers to the variance in results when units of a similar size are used, but the size and/or placement of the units is varied (Openshaw & Taylor, 1979). A classic example of the aggregation problem is the fact that the outcome of voting systems based on majority rule can change depending on the boundaries of voting districts. This had led to the adjustment of voting district boundaries to yield more favourable outcomes for a political party, a practice known as Gerrymandering (Sauer, 1918).

The MAUP has been widely studied, primarily in the social sciences, and has demonstrable effects in a variety of areas including multivariate statistical analysis (Fotheringham & Wong, 1991), location-allocation modelling (Goodchild, 1979), urban neighbourhood analysis (Mitra & Buliung, 2012), and spatial interaction modelling (Putman & Chung, 1989).

Remote sensing is also impacted by the MAUP (Marceau & Hay, 1999). The pixels in a remotely sensed image arbitrarily divide the continuous surface of the Earth into discrete non-overlapping units. The larger the pixel size, the larger the area over which surface reflectance is aggregated. Depending on the placement of the pixels, different areas are aggregated within each pixel. Variance in results due to different pixels sizes or different pixel placements are thus analogous to the scale and

aggregation problems, respectively. The MAUP has been shown to cause variable results in image classification (Arbia & Espa, 1996; Marceau et al., 1994) and landscape structure analysis (Jelinski & Wu, 1996). Despite the demonstrated impacts, the MAUP has not often been directly studied in the context of remote sensing.

The relationship between spatial resolution, SVIs, and LAI has been investigated in a number of studies. In Teillet et al. (1997), the effects of spatial resolution on NDVI were examined within forested settings. Images were simulated at a range of spatial resolutions between 20 m and 1100 m and NDVI was calculated. They found that the spatial resolution could have a large impact on NDVI; however, this was dependent on the land-cover type. In a mixed aspen and spruce forest stand, NDVI remained stable at 0.75 until a spatial resolution of 260 m, after which it steadily decreased to below 0.6 at an 1100 m spatial resolution. In a clear cut area, NDVI was found to remain essentially stable around 0.78 at every spatial resolution. In a mixed clear cut and forested stand, NDVI increased from 0.5 to 0.7 as spatial resolution decreased from 20 m to 260 m, after which it remained unchanged with further decreases in spatial resolution.

In Chen (1999), the effects of spatial resolution on LAI prediction using SVIs were examined within a boreal forest ecosystem in Canada. A Landsat Thematic Mapper image was resampled to resolutions up to 1000 m, with LAI being calculated from both NDVI and the Simple Ratio (SR) using models developed at the native 30 m resolution. The study found that predicted LAI decreased as resolution coarsened. By measuring the sub-pixel fractional land cover, they found that the change in predicted LAI depended on the heterogeneity of the land surface being aggregated within the coarse resolution pixels. The largest changes in predicted LAI occurred

when pixels contained contrasting surfaces, such as interfaces between vegetation and water.

Spatial resolution was not found to have a large impact on LAI modelling in Sprintsin et al. (2007). In their study, LAI was modelled for a plantation forest in Israel located in a desert transition zone. LAI was modelled using NDVI calculated from a 4-m spatial resolution IKONOS image and a 250-m spatial resolution MODIS image. The study found that the average LAI declined with spatial resolution by 11% (2.53 m^2/m^2 for IKONOS compared to 2.25 m^2/m^2 for MODIS), and the coefficient of variation decreased marginally as well (0.57 for IKONOS compared to 0.52 for MODIS). However, the authors deemed that the MODIS spatial resolution was sufficient for retrieval of LAI within this context.

2.5 Summary

Riparian vegetation faces a number of challenges due to regulation mechanisms, which have altered the natural flow regime. Alternative dam management strategies are being attempted to simulate the natural flow patterns, but there is a need for quantitative monitoring to evaluate the impact of these strategies on riparian vegetation. The LAI is an important variable to monitor due to its functional linkages with vegetation health processes, particularly evapotranspiration.

Ground measurements of LAI, while possible, are labour intensive and costly. To provide economical monitoring of riparian vegetation along entire rivers, remote sensing can be used to estimate LAI. The simplest method to provide operational LAI monitoring is to create empirical prediction models based on regression between ground measurements of LAI and spectral vegetation indices calculated from optical remote sensing data.

In order to select a sensor for riparian LAI monitoring, it is necessary to determine an appropriate spatial resolution. The information derived from remote sensors has been previously shown to be sensitive to differences in spatial resolution. Accordingly, the selection of a sensor with an inappropriate spatial resolution may lead to poor quality data being generated. The spatial resolution required for riparian LAI monitoring must be high enough to provide reasonable LAI estimates for riparian areas along the river, but too high a spatial resolution will add no valuable information. Thus, the impact of spatial resolution should be investigated in order to help determine an appropriate sensor for use in operational riparian LAI monitoring.

Sensor systems require pre-processing to correct spatial, spectral, and radiometric errors, as well as calibration to some standard scale such as spectral radiance or spectral reflectance. Many pre-processing tasks are often carried out prior to a user receiving the image data. In cases where the data is gathered from the sensor directly by the user, these pre-processing tasks must be addressed. Sensor calibration methods require the spectral, spatial, and radiometric characteristics of the sensor to first be determined. These characteristics can be measured through laboratory experiments prior to field use of the sensor.

3. CHARACTERIZATION AND CALIBRATION OF DIGITAL CAMERAS FOR QUANTITATIVE REMOTE SENSING

3.1 Introduction

This chapter presents a study of the spatial, spectral, and radiometric characteristics of two consumer-grade digital cameras. Calibration procedures were also developed to compensate for some well-known spatial and radiometric effects. This work was carried out to prepare the cameras for use in the quantitative remote sensing research performed in the subsequent chapter.

This research was also motivated by the proliferation of uncalibrated consumer-grade digital cameras being used in quantitative remote sensing applications. The explosion of unmanned aerial vehicle (UAV) technology in recent years has led to the widespread use of digital cameras for remote sensing in a variety of fields (Fallavollita et al., 2013; Hunt et al., 2010; Laliberte et al., 2010; Wang et al., 2011; Zhang & Kovacs, 2012). Digital cameras and UAV remote sensing have proven especially attractive for users outside the traditional remote sensing community. Many users are not familiar with the importance of sensor characterization and calibration, and companies selling digital camera systems often make dubious claims about the nature and quality of the data produced by these systems. Consequently, calibration issues are often ignored to the detriment of the data that is being acquired. The current research can contribute to ameliorating this issue by highlighting methods for measuring key camera characteristics as well as calibration of the data to provide accurate, consistent measurements.

Five major characteristics were investigated though laboratory-based experiments: geometric lens distortion, vignetting, noise, spectral response functions, and radiometric response functions. Based on the characterization experiments,

calibration procedures were created and implemented to correct camera images for geometric distortions and radiometric response nonlinearities.

3.1.1 Term Definitions

This section defines terms relating to digital cameras, which are important for the discussion in the remainder of this chapter.

- Aperture: The size of the opening in a lens which light can pass through. Wide apertures allow in more light while narrower apertures allow in less light. Most modern lenses have a diaphragm that allows the size of the aperture to be adjusted. Aperture settings are denoted by F-numbers, which refer to the ratio of the lens focal length to the diameter of the aperture. Smaller F-numbers (e.g., F/1.8) correspond to a larger aperture opening, while larger F-numbers (e.g., F/11) correspond to a smaller aperture opening.
- Bayer colour filter array: A mosaic of colour filters which is placed over digital sensors to allow colour imaging. The Bayer filter consists of a checkerboard pattern of filters for red, green, and blue light, respectively. Each filter corresponds to a single detector element on the sensor, allowing only light of the specified wavelengths to pass through and excite the detector. The Bayer pattern consists of 25 % red, 50 % green, and 25 % blue filters, in order to mimick the light sensitivity of the human eye, which has a greater sensitivity to green light than to red and blue light. Due to the filter, each pixel in raw camera images only record measurements for a single spectral band. The camera processes the raw sensor data and interpolates the other two spectral band values to create the final image in a process called demosaicing. Bayer colour filter arrays are ubiquitously used in consumer digital cameras to produce colour using a single inexpensive sensor.

- CCD: Stands for charge-coupled device. A type of sensor used in consumer digital cameras, although in recent years complementary metal-oxide-semiconductor (CMOS) sensors have become more widely used due to lower production costs and higher pixel densities, although at the expense of sensor quality. CCD sensors contain an array of photoactive silicon detectors which, when struck by photons, emit electrons at a rate proportional to the light intensity and/or exposure duration. This electric charge is amplified and converted to a digital number (DN) by an analog-to-digital converter. Each photodetector element corresponds to a single pixel in the resulting image.
- Exposure: The amount of light which strikes the camera sensor to create an image. Exposure is the product of the amount of light passing through the lens per unit time (controlled by the aperture) and the duration of the light exposure (controlled by the shutter speed). A greater exposure level results in a greater amount of light striking the sensor and, thus, higher values being recorded in an image.
- Focal length: The distance between the lens node (optical centre) and the focal plane of a camera. In digital cameras, the sensor resides at the focal plane, and the lens focuses incident light upon it. Focal length affects the magnification and the field-of-view of an image. Shorter focal lengths have low magnification and a wide field-of-view. Increasing the focal length increases the image magnification and decreases the field-of-view. As differences in focal length can alter the pathway of light entering the sensor, focal length also impacts the lens geometric distortion. On lenses with variable focal length settings, the greatest amount of geometric distortion tends to occur at both the shortest and longest focal length settings.
- ISO: Stands for International Standards Organization, and refers to the sensitivity of the camera sensor to light. The term was originally used to refer to the

sensitivity of different types of film, but is also used for digital sensors. Higher ISO values correspond to higher sensitivity, allowing images to be created from less gathered light (narrower apertures and faster shutter speeds). For digital sensors, the ISO controls the magnitude of the amplification applied to the analog signal prior to it being converted to a digital value. While higher ISO settings increase the sensor's sensitivity to light, they also increase its sensitivity to noise. Therefore, to avoid high noise levels in the camera images, the lowest ISO setting should be used whenever possible.

- Shutter speed: Refers to the duration of light exposure on the camera sensor. The camera shutter can be physical or electronic. Physical shutters allow light to pass through the lens and impact the sensor for a set duration before closing. Electronic shutters control the amount of time that the sensor is actively gathering light. The shutter speed is the amount of time that the shutter is held open (for physical shutters) or that the sensor is on and recording light (electronic shutter). Shutter speed is quantified in units of seconds. Shorter shutter speeds reduce the chances of image blurring, which is important when either the camera or the photographed subject is in motion.
- White balance: Setting which controls how image colours are rendered in an image. Depending on the type of scene illumination, the apparent colour of objects can change, for example by making white objects appear slightly green (referred to as "colour casts"). This variation is based on the "colour temperature" of the scene illumination, which refers to the dominant colour of the light source, which varies from "cool" colours (those closer to blue) to "warm" colours (those closer to red). The white balance setting applies a scaling factor on the red, green, and blue camera bands in order to render white objects "correctly" (digitally represented by

balanced red, green, and blue DN values). Therefore, the white balance setting can significantly alter the apparent response of the camera bands to light. Most digital cameras have numerous preset white balance settings corresponding with common types of illumination (e.g. daylight, cloudy, tungsten, etc). The ability to create a custom white balance setting is also often available, as well as an auto white balance setting, which calculates an appropriate white balance based on the detected scene illumination. Due to the alteration of camera responses by white balance, a consistent setting should be used for quantitative remote sensing. Therefore, the automatic white balance setting should be avoided.

3.2 Methods

3.2.1 Camera Description

This study was performed on two Canon Powershot S50 cameras (Canon Inc., Tokyo, Japan). These digital "point-and-shoot" cameras feature a 5 megapixel (2592 x 1944 pixel) CCD sensor. The sensor dimensions are 7.2 mm x 5.3 mm. Each camera has a zoom lens allowing the focal length to be varied between 7 mm and 21 mm, with the selectable lens apertures varying between F/2.8 and F/8. The cameras have automatic, semi-automatic, and manual control modes. Images output from the camera are quantized in 8-bits with 256 DN levels (0 – 255).

One of the cameras tested was modified for imaging near-infrared EMR. This modification was performed by removal of the infrared blocking filter fitted over the camera sensor, and its replacement with a filter to block visible light and transmit only near-infrared wavelengths. The second camera was left unmodified to image visible red, green, and blue light. The modified camera is hereafter referred to as the NIR camera, while the unmodified camera is referred to as the RGB camera.

Manual camera settings were used throughout these experiments. Unless otherwise stated, the following settings were used: camera white balance was set to "daylight"; ISO was set to its lowest setting (50); aperture was set to F/4; focal length was set to 10 mm; and shutter speed was variable depending on the experiment being performed and the desired exposure level. All images were acquired in the jpeg format.

All image processing tasks were performed using either Matlab (Version R2012a, MathWorks Inc., Natick, MA), ENVI (Version 5.1, Exelis VIS, Boulder, CO, USA), or Adobe Photoshop (Version CS3, Adobe Systems Inc., San Jose, CA, USA). Calculations and statistics were performed using either Microsoft Excel 2013 (Microsoft, Redmond, WA, USA) or SPSS Statistics (Version 22, IBM Corporation, Armonk, NY, USA).

3.2.2 Distortion Characterization and Calibration

Camera distortion was both characterized and corrected using the open source Camera Calibration Toolbox for Matlab from the Computational Vision lab at Caltech (available from http://www.vision.caltech.edu/). By imaging a planar checkerboard calibration grid taken from multiple angles, the program estimates the geometric and optical characteristics of the camera, creating a camera model which is used to correct both radial and tangential distortions (Zhang, 2000). Thirty images from each camera were taken of a checkerboard calibration grid at a variety of camera and grid orientations (Figure 3.1). All images were acquired at a fixed 10-mm focal length, as each change in focal length would require its own characterization.

Once the images were downloaded from the cameras, the four corners of the grid were manually selected for each image (Figure 3.1 top). With the corners selected, the program predicted the remaining grid intersections (Figure 3.1 bottom).

The extracted grid intersections were then manually inspected. In cases where the automatic extraction performed poorly – such as when the selected point was several pixels away from the correct location – a manual estimate for the distortion coefficient was input to aid in corner extraction. If corner extraction remained poor for an image, the image was removed and another image was substituted.

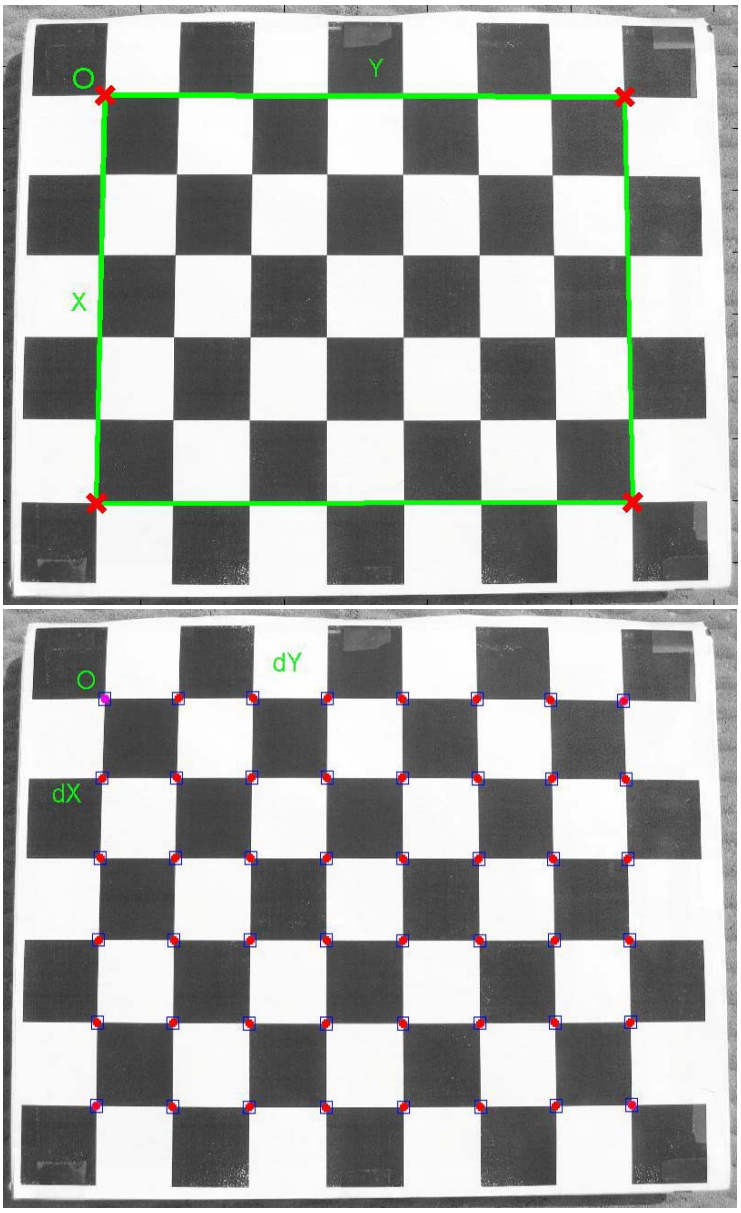

Figure 3.1 – Calibration grid corner extraction. Top shows the 4 manually selected grid intersections, while bottom shows the remaining grid intersections predicted by the program. "X", "Y", "dX" and "dY" denote the x and y axes of the grid. "O" denotes the origin point, which is the first selected grid corner.

Following the automatic grid extraction, distortion parameters were estimated by the program and camera distortion models were created. These distortion models were applied to three images of the calibration grid from each camera, and the uncalibrated and calibrated images were compared. The comparison was performed in Photoshop, with lines being drawn from corner to corner along the edges of the grid in each pair of images (Figure 3.2). The distortion in the uncalibrated images was measured by measuring the perpendicular displacement of the edge of the grid from the drawn lines at the point where the distortion appeared to be the greatest (Figure 3.3 top). This resulted in four measurements from each image, one for each grid edge. The displacement between the drawn lines and the grid was then measured at the same points in the calibrated images, and the values were compared between the two sets of images (Figure 3.3 bottom).

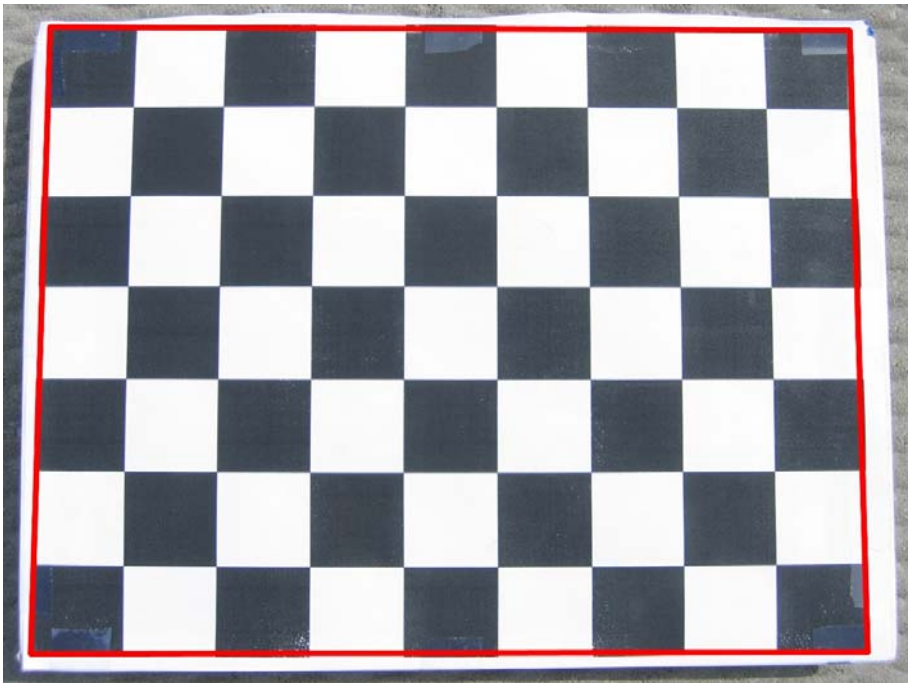

Figure 3.2 – Illustration of distortion correction validation. Lines shown in red were drawn along the edges of the calibration grid in both the uncalibrated and calibrated images.

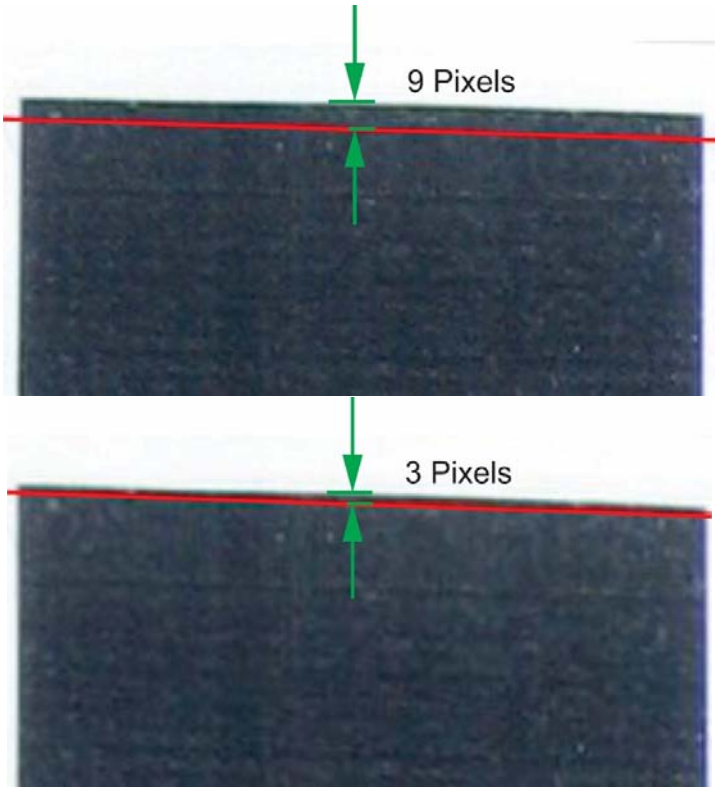

Figure 3.3 – Close-up of distortion correction validation. At the point of maximum apparent distortion in the uncalibrated image, pixel displacement between the red line and the edge of the calibration grid was measured (top). This measurement was repeated at the same location in the calibrated image (bottom).

3.2.3 Vignetting Characterization

The gradual reduction in pixel values with increasing distance from the optical centre of the camera can be caused by either light falloff or vignetting. Light falloff is the reduction in intensity when light strikes a sensor at progressively oblique angles (Wüller & Gabele, 2007). Vignetting is caused either by obstruction of light by the camera lens elements or by decreasing detector quantum efficiency (Catrysse et al., 2000; Yu, 2004). As both light falloff and vignetting manifest as the same effect, it was not possible to decouple them and measure the contribution of each for this camera system. Consequently, only the cumulative impact of light falloff and vignetting were measured in this research, which is referred to as vignetting in the remainder of this chapter for simplicity.

Vignetting was measured by directly imaging a uniform light source. The light source used in this research was a USS-1200 Integrating Sphere (Labsphere Inc., North Sutton, NH, USA). The inside of the sphere is coated in Spectralon, a material made from a compressed polytetrafluoroethylene (PTFE) polymer resin, which demonstrates the highest diffuse reflectance of any known material (Bruegge et al., 1993). The integrating sphere features four input lamps, with one lamp fitted with a variable attenuation aperture that allows light intensity to be precisely varied. Radiation from the lamps reflect through the interior of the sphere before leaving through an exit port, ensuring a uniform, diffuse output of light.

To measure vignetting each camera was mounted on a calibration table facing the integrating sphere exit port (Figure 3.4). The integrating sphere was left at a constant light intensity setting throughout the experiment. Camera aperture and focal length settings were varied in order to measure the vignetting effects at each. Settings tested spanned the range from the widest to narrowest aperture (F/2.8 to F/8) and shortest to longest focal length (7 mm to 21 mm). At each combination of aperture and focal length an image was taken with the cameras. It should be noted that due to limitations of the camera lens, at longer focal lengths not every aperture setting was selectable. The camera shutter speed was varied at each aperture setting to ensure a balanced exposure, while the ISO was left at its lowest setting (ISO50).

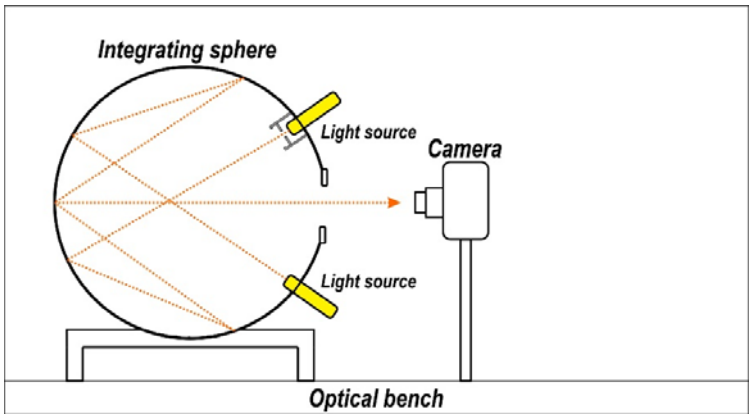

Figure 3.4 – Experimental setup for the vignetting tests.

Following the laboratory experiments the images were downloaded and processed. A 50 pixel x 50 pixel region was extracted from the centre of each image and the average DN was calculated from this subset. Next each pixel in the image was divided by the average central value (computed from the 50 pixel x 50 pixel subset) to determine the relative intensity of each pixel value compared to the image centre, creating a new set of relative intensity images. A 9 pixel x 9 pixel low-pass filter was applied to the relative intensity images to reduce noise and more clearly show the vignetting effects. Transects were then measured vertically, horizontally, and from corner to corner across each relative intensity image to observe the level of vignetting in the images (Figure 3.5).

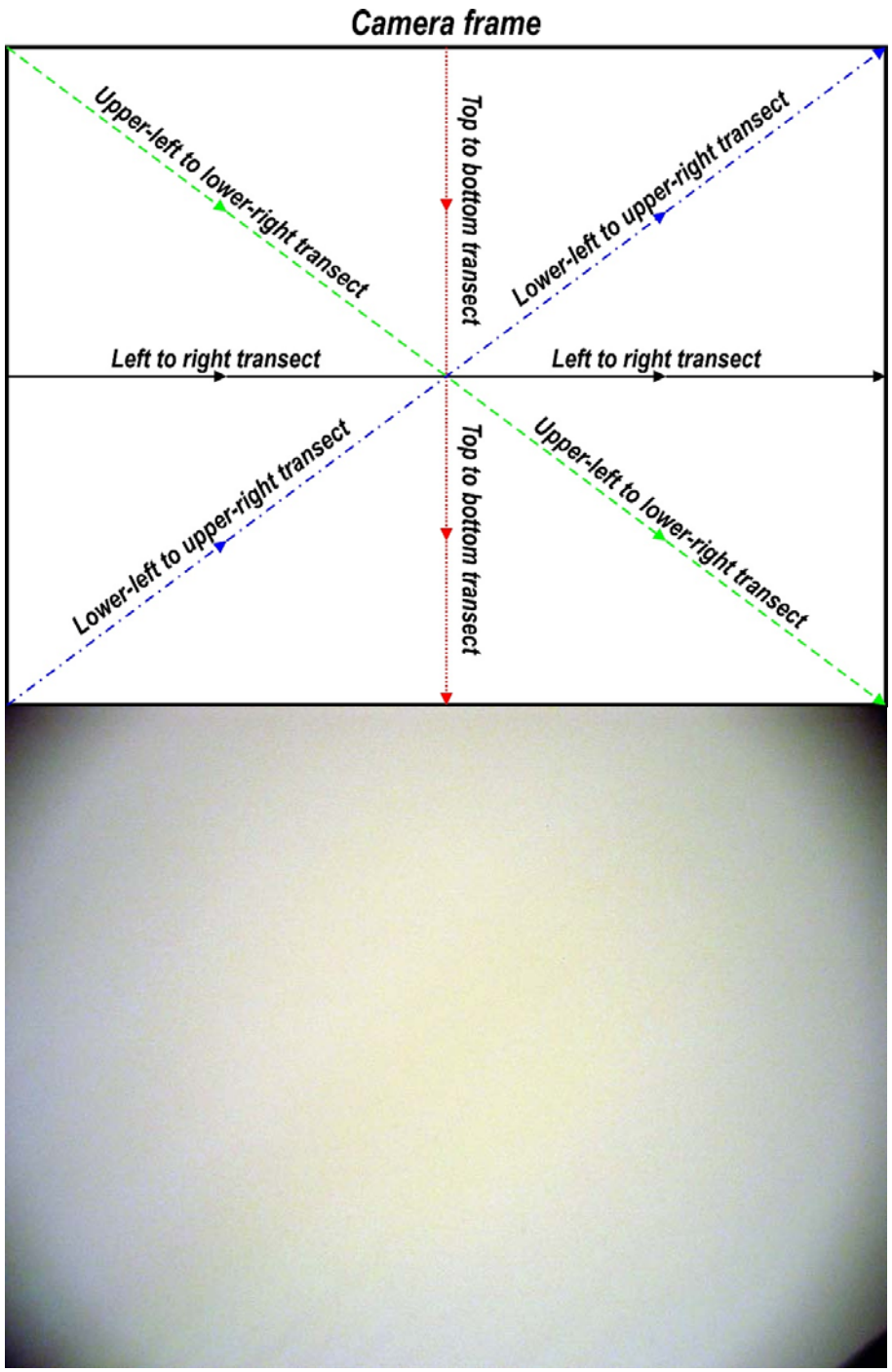

Figure 3.5 – Illustration of vignetting characterization. The top presents the transects taken across the relative intensity camera images. The bottom shows an example of a relative intensity image, where white denotes high relative intensity and black denotes low relative intensity.

3.2.4 Noise Characterization

To measure sensor noise, images were acquired with the cameras pointed directly into the integrating sphere in the same manner as the vignetting experiment (Figure 3.6 top). 10 images were acquired at each of the four different camera ISO settings (50, 100, 200, and 400) to characterize how image noise changed with increasing ISO. To measure the dark noise, 10 images at each ISO setting were captured under a total lack of illumination with the camera lens covered (Figure 3.6 bottom).

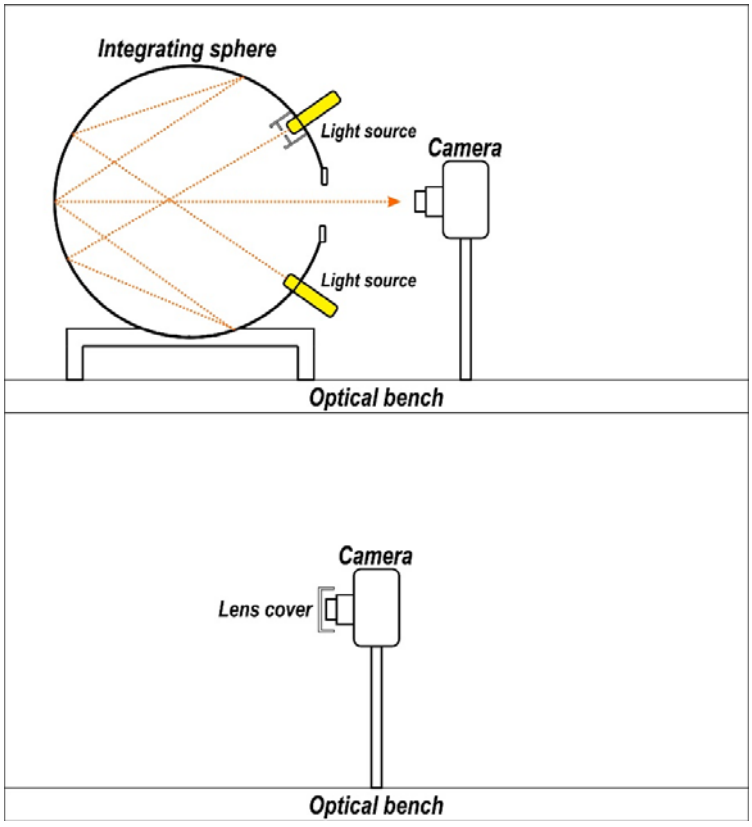

Figure 3.6 – Experimental setup for camera noise tests. The top shows the illumination noise measurements, while the bottom shows the dark noise measurements.

Images were downloaded following the laboratory experiment and each image was cropped by 40 % in the vertical and horizontal directions in order to mitigate vignetting issues. The standard deviation of the images was calculated and this was

taken to represent the image noise. Both the illumination noise and dark noise for each camera band were added together to get the total noise. From this the signal-to-noise ratio (SNR) was calculated as follows:

$$SNR(j) = \frac{Signal(j)}{Noise(j)} \tag{3.1}$$

where SNR(j) is the signal-to-noise ratio for camera band j, Signal(j) is the average image signal (average DN response) for band j, and Noise(j) is the total image noise (illumination noise plus dark noise) in DN for band j.

The image noise and SNR computed for each image were then averaged for the 10 images acquired at each ISO setting to obtain the average noise and SNR for each camera band at each ISO setting.

3.2.5 Spectral Response Characterization

The procedures used in this section are adapted from those in Vora et al. (1997b). Equipment used to characterize the spectral response functions of the cameras included the integrating sphere light source, a monochromator, and a spectroradiometer. A monochromator uses a diffraction grating to split incident broadband EMR into narrowband EMR. The wavelength of EMR passed through is tunable by rotating the diffraction grating, with the bandwidth of the EMR being dependent on the quality of the diffraction grating and the size of the entry and exit ports. The monochromator used in this experiment was a SPEX 1681B (Horiba Ltd., Kyoto, Japan) fitted with a 1200 groove/mm diffraction grating, allowing wavelengths to be selected between 300 nm and 1300 nm.

A spectroradiometer is a portable hyperspectral instrument which is used to measure radiation across a range of wavelengths using many narrow contiguous bands. The spectroradiometer used in this research was an ASD FieldSpec-3

(Analytical Spectral Devices Inc, Boulder, CO, USA). The ASD measures EMR between 350 nm and 2500 nm at 1 nm intervals. Note that this value is interpolated; the actual spectral resolution varies between 3 nm in the visible/near infrared to 10 nm in the short-wave infrared) (ASD Inc., 2010).

The integrating sphere and monochromator were placed in series, with the ASD facing into the monochromator exit port (Figure 3.7 top). The integrating sphere was set to full intensity and the monochromator entry and exit ports were adjusted to yield a spectral bandpass of approximately 3 nm. EMR was passed from the integrating sphere through the monochromator and measured by the ASD, which was set to measure in units of radiance ($W \cdot m^{-2} \cdot s^{-1}$). Measurements were taken at 10 nm intervals between 350 and 1250 nm. Following the ASD measurements the procedure was repeated, this time with the cameras instead of the ASD. Each of the two cameras imaged the light passing through the monochromator at every wavelength (Figure 3.7 bottom).

To process the results, a 100 pixel x 100 pixel area was cropped from the centre of each image, and the average DN for each camera band was calculated from the cropped images. This subset was used as only the central portion of the image frame received light from the monochromator (Figure 3.8). To determine the absolute spectral responses for the cameras, the average DN from each image was plotted at the corresponding wavelength of light at which the image was acquired.

A problem with examining only the absolute response of the cameras at every wavelength is that the amount of light output from the integrating sphere was not the same at every wavelength. To account for differences in light intensity between measurements, the camera responses were adjusted as follows:

$$Cam\sigma(j,\lambda) = \frac{Cam(j,\lambda)}{ASD(\lambda)} \tag{3.2}$$

where Camσ(j, λ) is the intensity-adjusted camera response for camera band j at wavelength λ, Cam(j, λ) is the camera DN for camera band j at wavelength λ, and ASD(λ) is the ASD radiance measurement at wavelength λ.

The adjusted camera responses were then normalized to a relative scale between 0 and 1 by dividing each adjusted response by the overall highest adjusted response for that camera. These values were plotted at the corresponding wavelengths at which the images were acquired to derive the normalized spectral responses for each camera band.

Spectral response curves were created for both the absolute and normalized camera responses using linear interpolation between the sampled camera responses.

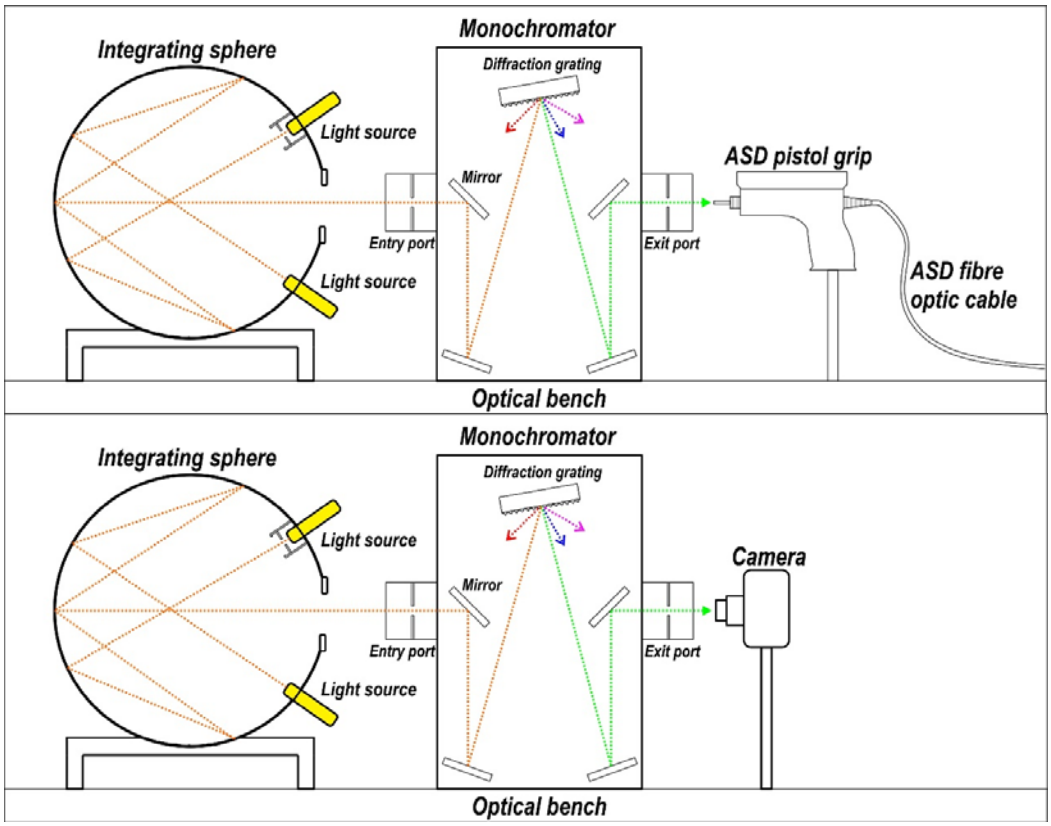

Figure 3.7 – Experimental setup for the spectral sensitivity tests. The top shows the ASD measurements, while the bottom shows the camera measurements.

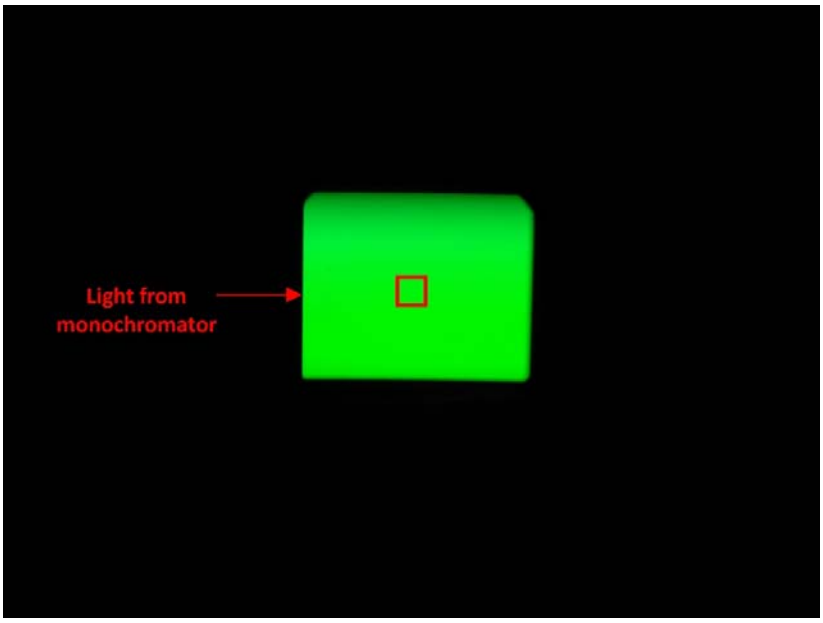

Figure 3.8 – Camera image acquired during spectral response test. The green patch is light passed through the monochromator exit port, while the red square shows the 100 pixel x 100 pixel area from which the average response was calculated.

3.2.6 Radiometric Response Characterization and Linearization

3.2.6.1 Radiometric Response Measurements

The procedures in this section were adapted from Vora et al. (1997a). The same experimental setup was used to characterize the camera radiometric responses as for the spectral responses; however, for this experiment instead of using the integrating sphere at full intensity with all four lamps on, only the lamp fitted with the variable attenuator was used in order to allow the light intensity to be varied (Figure 3.9).

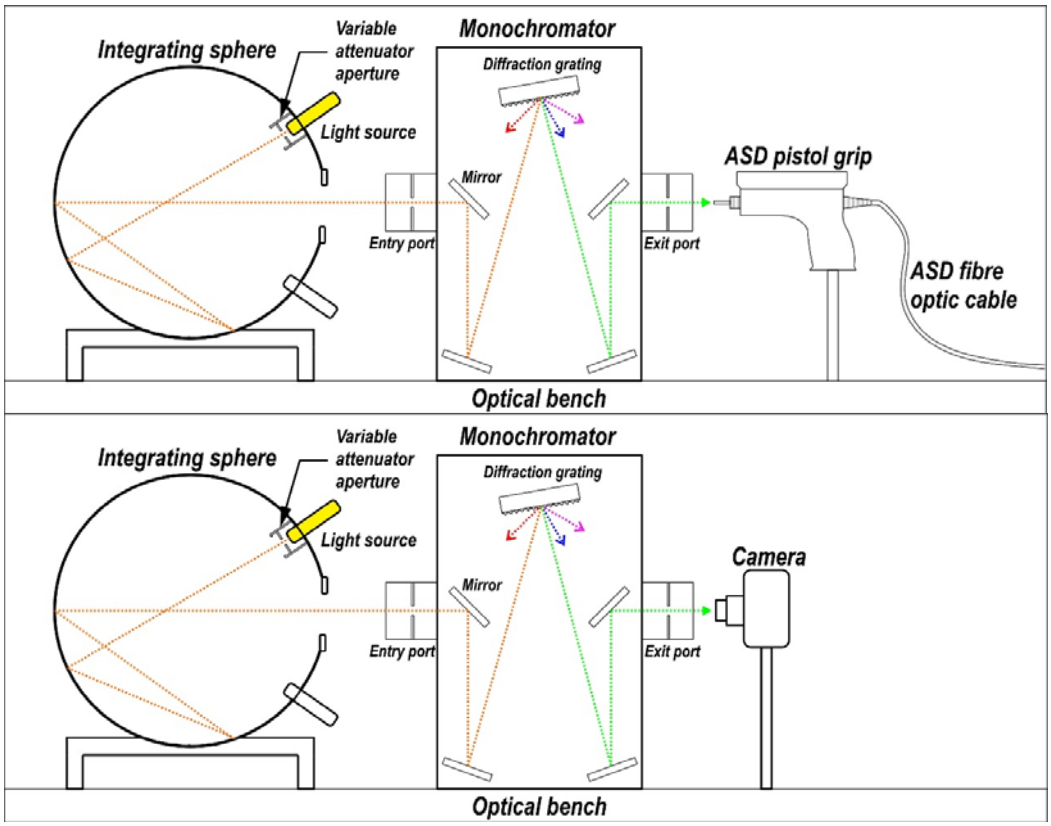

Figure 3.9 – Experimental setup for the radiometric sensitivity tests. Top shows the ASD measurements. Bottom shows the camera measurements. The variable attenuator aperture was used to vary the sphere light throughput from low to high intensity.

Based on the results of the spectral response experiment, wavelengths corresponding to the peak absolute response for each camera band were selected, resulting in four different wavelengths (3 for the RGB camera, 1 for the NIR). For each wavelength the light output from the integrating sphere was varied from low to high intensity. For each intensity setting the light was measured using the ASD. Once the full range of stops from low to high intensity were measured with the ASD the procedure was repeated with the cameras. Camera exposure was set to have the images as close as possible to saturation (without actually saturating the sensor) at the maximum light intensity, providing adequate coverage of the camera dynamic range.

To process the data, first the differences in light intensity between each intensity setting were assessed using the ASD data. Because the ASD radiometric

response is linear (ASD Inc., 2010), a change between ASD measurements was taken to indicate a change of the same magnitude in the sphere light intensity. Differences in light intensity were measured on a relative scale. While it was possible to measure absolute light intensity in units of radiance, this was deemed unnecessary for the current research, as the camera response at a given radiance level will vary depending on the camera settings used. The relative light intensity was computed from the ASD data at each intensity setting as follows:

$$Int(\lambda) = \frac{ASD(\lambda)}{ASDmax(\lambda)} \tag{3.3}$$

where Int(λ) is the relative intensity value at wavelength λ, ASD(λ) is the ASD response at wavelength λ (in radiance), and ASDMax(λ) is the ASD response (in radiance) for the maximum light intensity setting at wavelength λ. The maximum light intensity setting was assigned a value of 1.

To process the data a 100 pixel x 100 pixel area was extracted from the centre of each camera image from which the average DN was calculated. Average camera DNs were plotted against relative light intensity, and radiometric response models were created for each band by fitting a curve to the sampled image-intensity pairs using a 3rd order polynomial function.

As the radiometric response models did not include a relative intensity value associated with the maximum camera response of 255, the relative intensity value corresponding to this maximum camera DN was extrapolated from the models. All relative intensity values were then divided by the extrapolated maximum intensity value and the response curves were recreated using the adjusted intensity values, yielding radiometric response curves for the full camera dynamic range.

3.2.6.2 Radiometric Response Linearization

To compensate for non-linear sensor responses to changes in EMR intensity, a method was used to convert non-linear image DNs to linearized values. Lookup tables were created for each camera band using the radiometric response models created in the previous section, which gave a corresponding linear intensity value between 0 and 1 for each camera spectral band for every DN value between 0 and 255. A program was created which iterated through every pixel in an image, converting the DNs for each camera band to a corresponding linearized value derived from the lookup tables. The program then output the final linearized image.

3.2.6.3 Radiometric Linearization Model Validation

An experiment was performed to evaluate the radiometric linearization models. The evaluation was done by comparison of linearized camera responses with ASD measurements. The change in the linearized camera values were compared to the changes in the ASD-measured values with changing light intensity. For this experiment, EMR from the integrating sphere was imaged by the cameras and measured with the ASD through the same range of intensities as before; however, this time the broad spectrum EMR from the integrating sphere was measured directly without using the monochromator to split it (Figure 3.10).

Following the laboratory measurements, the camera images were linearized using the models developed for this procedure. A 100 pixel x 100 pixel area was then extracted from each linearized image and the average linear value was calculated corresponding to each sphere intensity setting. This subset was used in order to avoid vignetting and to be consistent with the method used to create the models, which were based on a 100 pixel x 100 pixel subset as well.

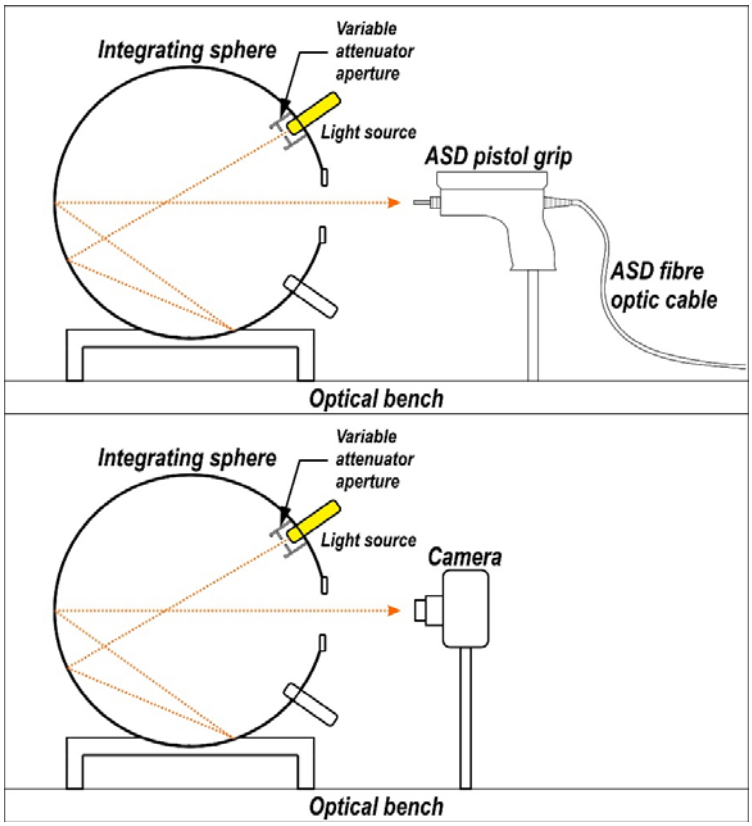

Figure 3.10 – Experimental setup for the linearization validation tests. The top shows the ASD measurements, while the bottom shows the camera measurements. The variable attenuator aperture was used to vary the sphere light throughput from low to high intensity.

To compare with the linear camera responses, The ASD measurements were normalized to the same intensity scale as the linearized camera responses. This was done separately for each camera band as follows:

$$ASD\sigma(i,j) = ASD(i) * \left(\frac{CamMax(j)}{ASDMax(j)}\right) \tag{3.4}$$

where ASDσ(i, j) is the ASD measurement normalized to the camera intensity scale of camera band j at light intensity i, ASD(i) is the ASD measurement (in radiance) at light intensity i, CamMax(j) is the maximum linearized camera response for camera band j, and ASDMax(j) is the ASD measurement corresponding to the maximum camera response for band j.

The normalized ASD measurements were compared with the linearized camera values for each band to assess how well the models were able to linearize the camera responses. To compare the measurements, the Root-Mean-Square-Error (RMSE) was calculated for each band as follows:

$$RMSE = \sqrt{\frac{1}{N}\sum_{i=1}^{N}(Cam(i) - ASD\sigma(i))^2} \tag{3.5}$$

where N is the number of corresponding camera and ASD responses, Cam(i) is the i^{th} linear camera response, and ASDσ(i) is the i^{th} normalized ASD response.

The difference between each corresponding set of measurements was also calculated according to Equation 3.6, and these differences were plotted and examined:

$$Error = Cam - ASD\sigma \tag{3.6}$$

Finally, the camera responses and corresponding normalized ASD responses were plotted against each other and linear regression lines were fitted. The regression line coefficients were compared with a perfect one-to-one relationship with slope of 1 and intercept of 0 by examining the 95 % confidence interval calculated for each coefficient.

3.3 Results

3.3.1 Distortion Characterization and Calibration

Figure 3.11 shows the distortion models created for both the RGB and NIR cameras. The models show total distortion, with both the radial and tangential distortion components combined. The figure shows the spatial displacement of image pixels from where they should be in a distortion-free image.

The two cameras were found to be very similar in terms of the level of distortion and the shape of the distortion. For both cameras distortion increased with distance from the centre of the image frame, getting as high as a 30-pixel displacement toward the corners. The distortion for both cameras was asymmetrical, with more pixel displacement being evident toward the bottom and left of the frame than the top and right. The displacement of the calculated principal point from the centre of the frame reinforces this observation, as shown in the figure by the difference in location between the “x” symbols (camera frame centre) and the “o” symbols (calculated principal point). Because radial distortion is symmetrical around the principal point, the calculated principal point should be in the centre of the image frame if the distortion were symmetrical (Zhang, 1999).

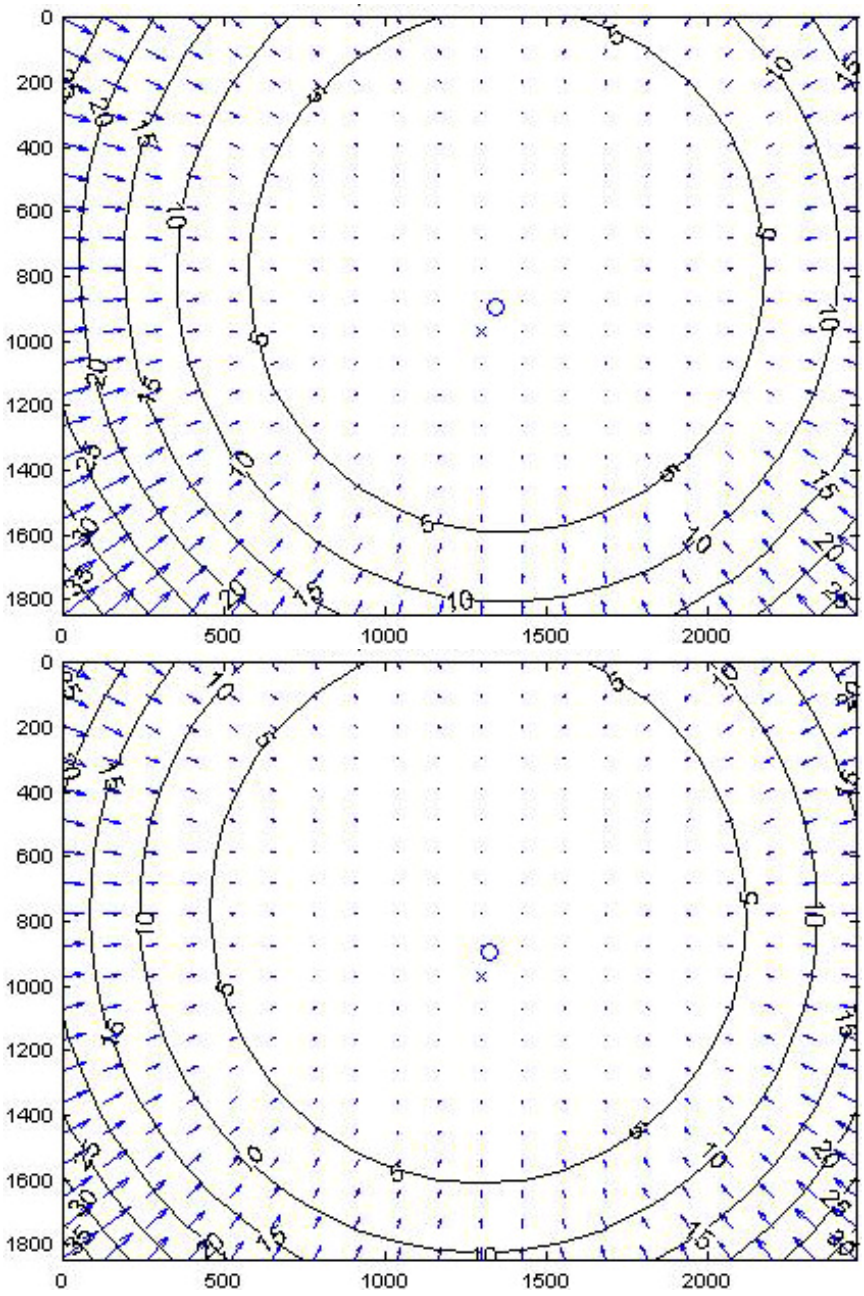

Figure 3.11 – Distortion models for the RGB and NIR cameras. Both radial and tangential distortion components are included. The top graph shows the RGB model while bottom one shows the NIR model. Arrows indicate the direction and magnitude of displacement correction by the model. Concentric rings are isolines of equal pixel displacement. The camera frame centre is indicated by an "x" marker, while the calculated camera principal point is shown with an "o" marker.

The distortion asymmetry was less pronounced with the NIR camera than the RGB camera. This was particularly notable in the horizontal direction. This is evident by the computed principal point for the RGB camera being displaced further to the

right of the image frame centre compared to the principal point computed for the NIR camera. The magnitude of this difference in displacement was approximately 16 pixels.

Using the distortion models to calibrate the camera imagery greatly reduced image distortion in most cases, but did not remove it entirely. Table 3.1 shows the results of the comparison of the distortion between the calibrated and uncalibrated images for the RGB camera, while Table 3.2 shows the results for the NIR camera.

In most cases applying the distortion models to the camera images removed most or all of the observed pixel displacement. Some figures were less impressive, such as only 57 - 67 % removal with several of the measurements in the RGB images, and 0 % and 50 % with the NIR. Nonetheless, in most cases the use of the distortion correction improved the geometric quality of the images, and was never found to negatively impact the quality.

Based on the comparisons performed, the NIR model appears to have done a better job overall of removing image distortion. The NIR model was able to completely remove image distortion more often than the RGB model; however, as noted before, in two cases distortion did not improve much or at all. Nonetheless, in both cases the initial pixel displacement in the uncalibrated images was low, representing only a few pixels each.

Table 3.1 – Comparison of pixel displacement between geometrically uncorrected and corrected images for the RGB camera.

Uncalibrated Displacement (pixels)	Calibrated Pixel Displacement (pixels)	Displacement Reduction (pixels)	Displacement Reduction (percent)
7	3	4	57
7	2	5	72
6	1	5	83
12	1	11	92
3	0	3	100
7	2	5	71
2	0	2	100
9	1	8	89
9	3	6	67
3	1	2	67
3	0	3	100
4	0	4	100

Table 3.2 – Comparison of pixel displacement between geometrically uncorrected and corrected images for the NIR camera.

Uncalibrated Displacement (pixels)	Calibrated Pixel Displacement (pixels)	Displacement Reduction (pixels)	Displacement Reduction (percent)
6	0	6	100
7	0	7	100
8	2	6	75
10	0	10	100
4	0	4	100
5	0	5	100
4	1	3	75
16	3	13	81
4	2	2	50
2	2	2	0
6	0	6	100
3	0	3	100

3.3.2 Vignetting Characterization

3.3.2.1 RGB Camera

Vignetting effects were evident in images obtained from the RGB camera at all focal length and aperture combinations. Figures 3.12 and 3.13 show some of the results from the transects measured across the relative intensity images. Not all results are presented in the figures; rather, they highlight the major trends in the data resulting from changes in the aperture and focal length. Furthermore, as it was

observed that the amount of vignetting did not differ between the red and green camera bands, the figures only present the results for the red band. The results for the blue band did differ markedly from the other two bands, and these results are presented subsequently. Figure 3.12 shows the results using a fixed focal length (7 mm) and 4 different aperture settings. Figure 3.13 shows the results from using a fixed aperture (F/5.6) and 4 different focal length settings.

The greatest amount of vignetting was found at the widest aperture (F/2.8) and shortest focal length (7 mm). This was most evident in the corners of the image, where DNs fell below 70 % of the mean central value, getting as low as 60 % in the far corners (Figure 3.12 c and d). Vignetting was consistently more pronounced along the diagonal transects than the horizontal and vertical transects. The vignetting was always lowest along the vertical transects. The pattern of the vignetting was found to be somewhat asymmetrical along the upper-left to lower-right diagonal transect, though largely symmetrical in the other transects.

Both increasing the focal length and narrowing the aperture reduced vignetting. The greatest improvement occurred when stopping down from an aperture of F/2.8 to F/4 at the 7 mm focal length (Figure 3.12). Further narrowing the aperture at this focal length only marginally reduced the vignetting, mainly in the corners of the frame. The next greatest decrease in vignetting occurred by increasing the focal length from 7 mm to 10 mm (Figure 3.13). Once again, increasing the focal length beyond this only marginally reduced vignetting. The least amount of vignetting was evident at a focal length of 21 mm and aperture of F/8, although focal lengths between 15 mm and 21 mm as well as apertures between F/5.6 and F/8 were all very similar.

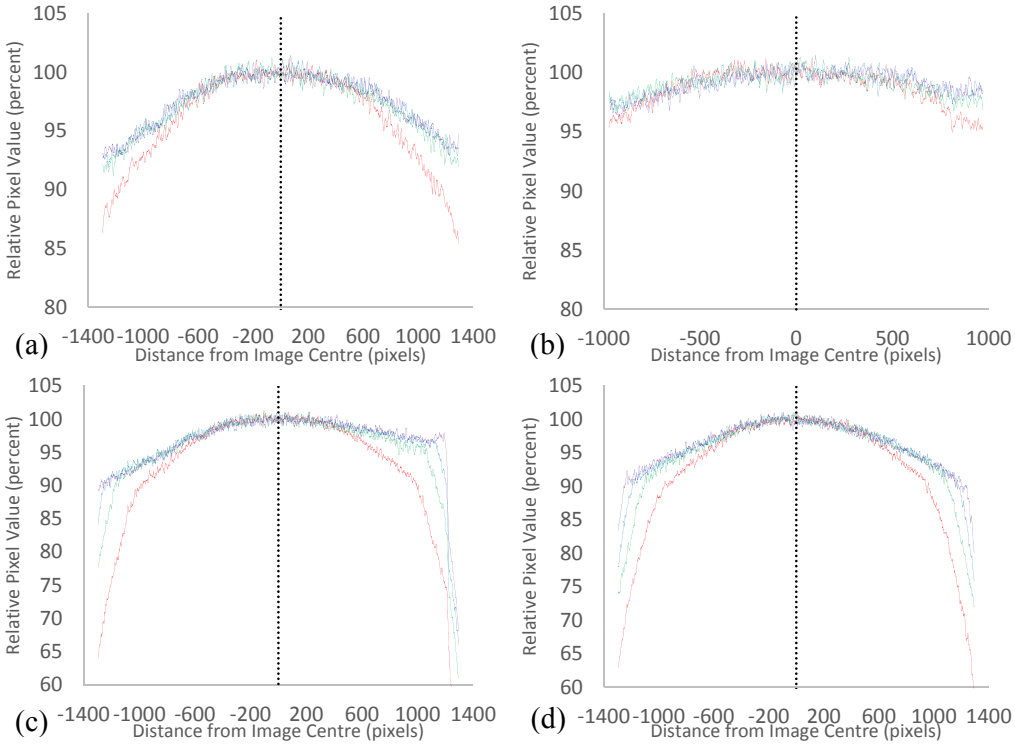

Figure 3.12 – Relative difference in pixel values for the RGB camera red band at a focal length of 7 mm and 4 different aperture settings. Apertures shown are: F/2.8 (red), F/4 (green), F/5.6 (blue), and F/8 (violet). Transects shown are: (a) left to right, (b) top to bottom, (c) upper-left to lower-right, and (d) lower-left to upper-right.

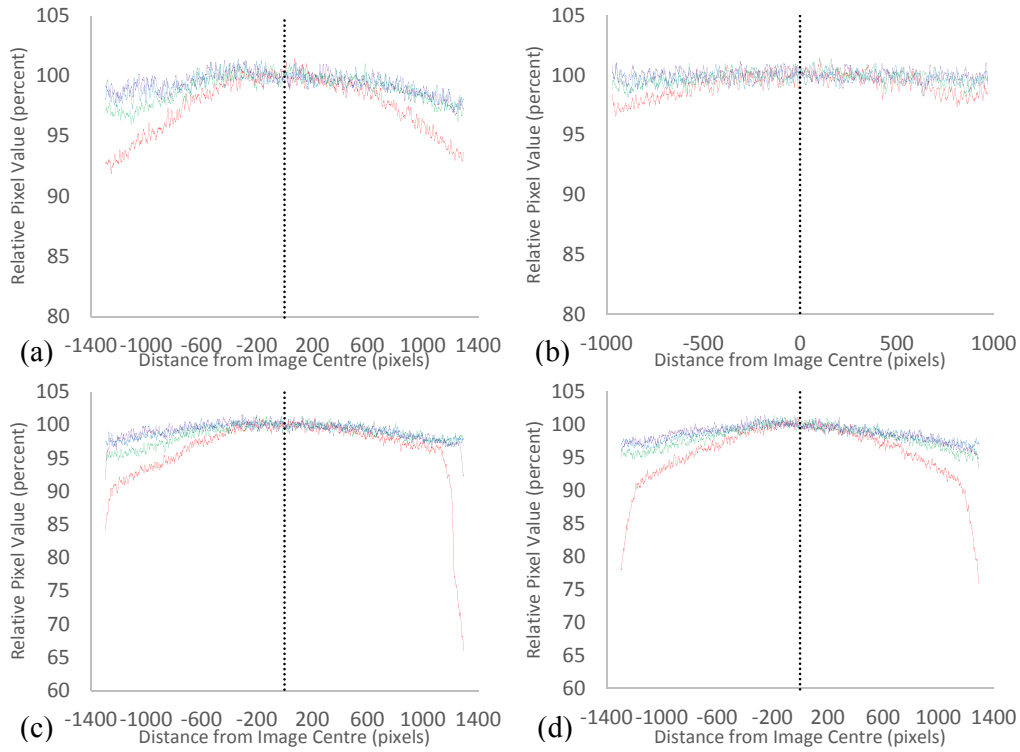

Figure 3.13 – Relative difference in pixel values for the RGB camera red band at an aperture setting of F/5.6 and 4 different focal length settings. Focal lengths shown are: 7 mm (red), 10 mm (green), 15 mm (blue), and 21 mm (violet). Transects shown are: (a) left to right, (b) top to bottom, (c) upper-left to lower-right, and (d) lower-left to upper-right.

As previously mentioned, vignetting results for the blue camera band differed unexpectedly from those of the red and green bands. Figure 3.14 shows the results for the blue band using a fixed focal length and variable aperture, while Figure 3.15 presents the results using a fixed aperture and variable focal length. At an aperture of F/2.8 the pattern was similar to the other two bands; pixel values gradually reduced as distance from the image centre increased (except in the case of the top-to-bottom transect, which did not change much across the image). As aperture was decreased the DNs for the blue band stayed the same or increased toward the edges of the images. This pattern differed from the other two bands, where pixel values decreased with increasing distance from the frame centre. The increase in pixel values became more pronounced as aperture was narrowed, with the greatest increases occurring at the

narrowest F/8 aperture, becoming as high as 120 % of the mean central value in the lower-right corner of the frame (Figure 3.14 c).

There was also a pronounced asymmetry evident in the responses across the frame, most noticeable along the diagonal transects, although also present in the vertical transect. This asymmetry showed that the pixel values were higher in the bottom portion of the frame than the top (Figure 3.14 b, c and d). Finally, there were also much larger differences between adjacent pixel values (increased noise) across the image in comparison to the red and green bands.

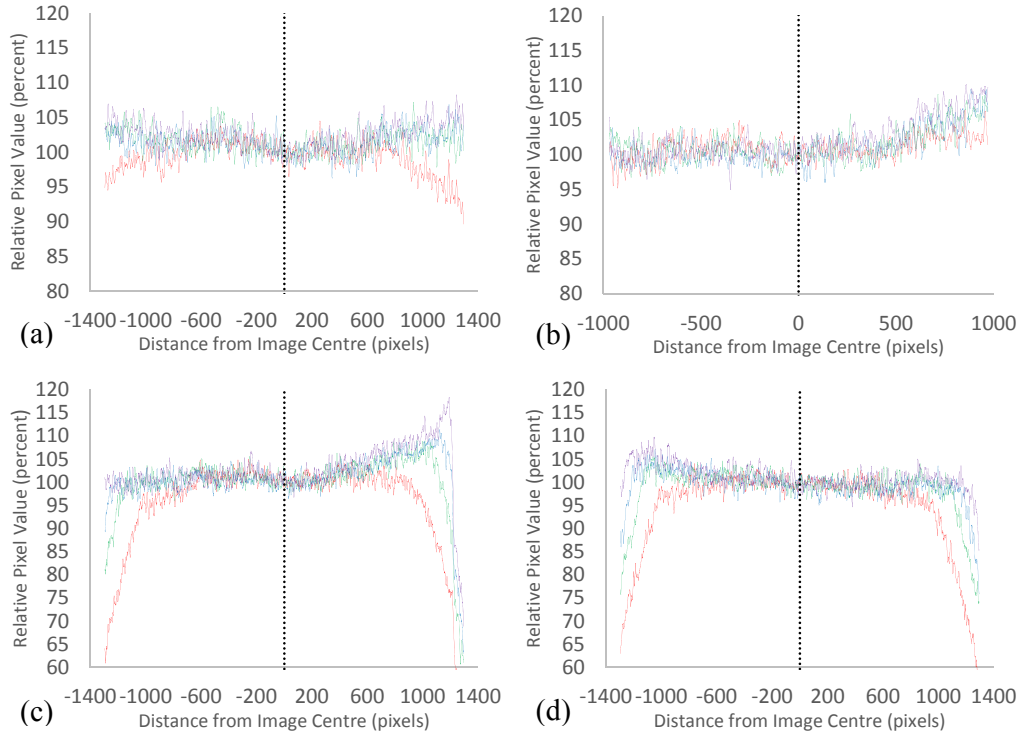

Figure 3.14 – Relative difference in pixel values for the RGB camera blue band at a focal length of 7 mm and 4 different aperture settings. Apertures shown are: F/2.8 (red), F/4 (green), F/5.6 (blue), and F/8 (violet). Transects shown are: (a) left to right, (b) top to bottom, (c) upper-left to lower-right, and (d) lower-left to upper-right.

Changes in focal length at a constant aperture did not lead to substantial changes in the relative pixel values across the images (Figure 3.15). In the upper-left to bottom-right transect, however, as focal length increased, the increase in pixel values observed in the bottom-right of the frame vanished and became a reduction in

pixel values at the 15 mm and 21 mm focal lengths (Figure 3.15 c). A marginal decrease in pixel values was also observed in the bottom-left of the frame (Figure 3.15 d).

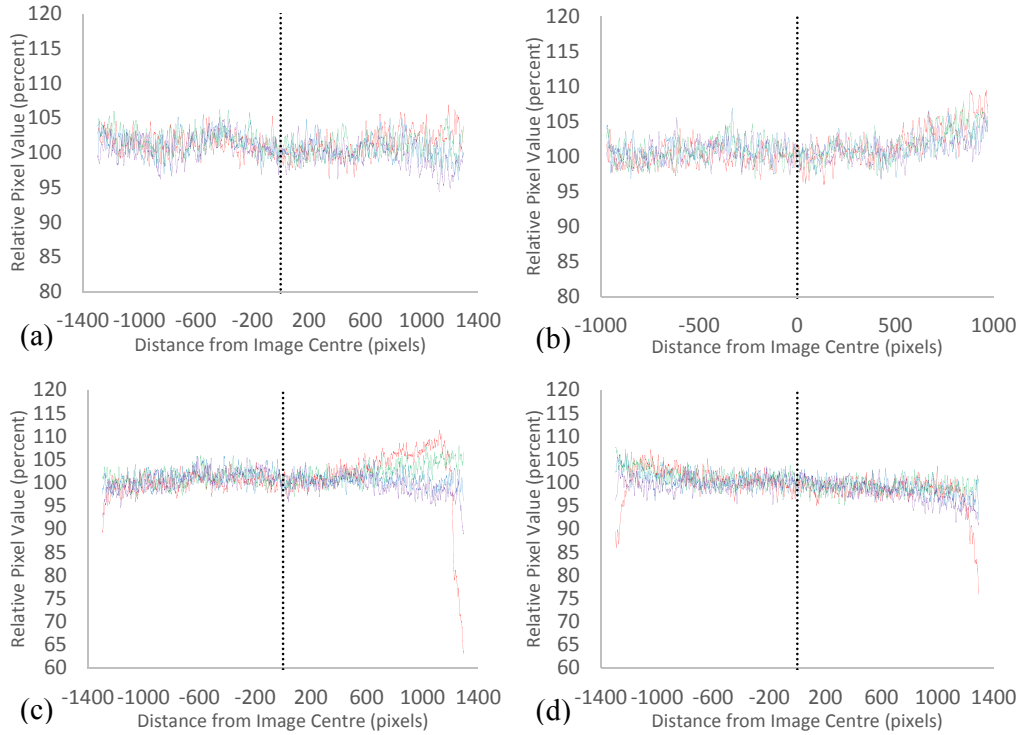

Figure 3.15 – Relative difference in pixel values for the RGB camera blue band at an aperture of F/5.6 and 4 different focal length settings. Focal lengths shown are: 7 mm (red), 10 mm (green), 15 mm (blue), and 21 mm (violet). Transects shown are: (a) left to right, (b) top to bottom, (c) upper-left to lower-right, and (d) lower-left to upper-right.

3.3.2.2 NIR Camera

As with the RGB camera, vignetting was evident for the NIR camera at all aperture and focal length combinations. Figure 3.16 shows results from the NIR camera at a fixed focal length with variable aperture settings, while Figure 3.17 shows the results using a fixed aperture and variable focal length. Results were substantially similar between the spectral bands; consequently, only the results for the red band are presented.

Vignetting was more pronounced than for the RGB camera, demonstrating a steeper falling off of pixel values to either side of the image centre. As with the RGB camera, a large amount of vignetting was seen in the far corners at 7 mm, especially at the widest F/2.8 aperture where values in the corners fell as low as 70 % of the mean central value (Figure 3.16 c and d). As with the RGB, the vignetting was somewhat asymmetrical, with values toward the left and top of the frame being lower than the bottom and right. Reducing the aperture size decreased vignetting in the far corners; however, unlike the RGB camera, narrowing the aperture also caused an increase in vignetting closer to the center. Thus, at the 7 mm focal length, aside from the far corners, the least vignetting occurred using an aperture of F/2.8. The most vignetting occurred with an aperture of F/8.

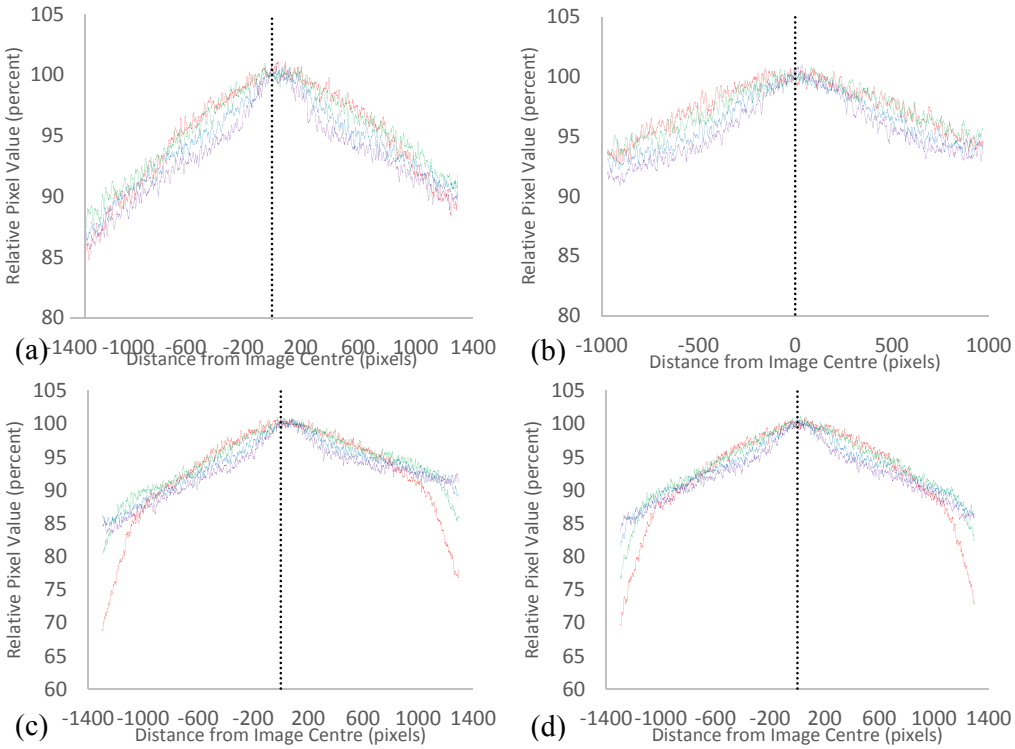

Figure 3.16 – Relative difference in pixel values for the NIR camera red band at a focal length of 7 mm and 4 different aperture settings. Apertures shown are: F/2.8 (red), F/4 (green), F/5.6 (blue), and F/8 (violet). Transects shown are: (a) left to right, (b) top to bottom, (c) upper-left to lower-right, and (d) lower-left to upper-right.

There was a distinctive peak in the data, where a sharp drop in pixel values occurred within a short distance of the centre of the frame, with the slope of the pixel value fall-off becoming shallower as distance further increased. This effect was noticed at the F/5.6 aperture and became more pronounced at the F/8 aperture.

Increasing the focal length from 7 mm to 10 mm reduced the amount of vignetting, especially in the left portion of the image frame (Figure 3.17). Increasing to 15 mm slightly reduced vignetting further; however, increasing further to 21 mm actually increased vignetting. The peak effect was observed at all focal lengths, but became more pronounced at 21 mm, with pixel values falling more precipitously in the areas immediately adjacent to the image centre.

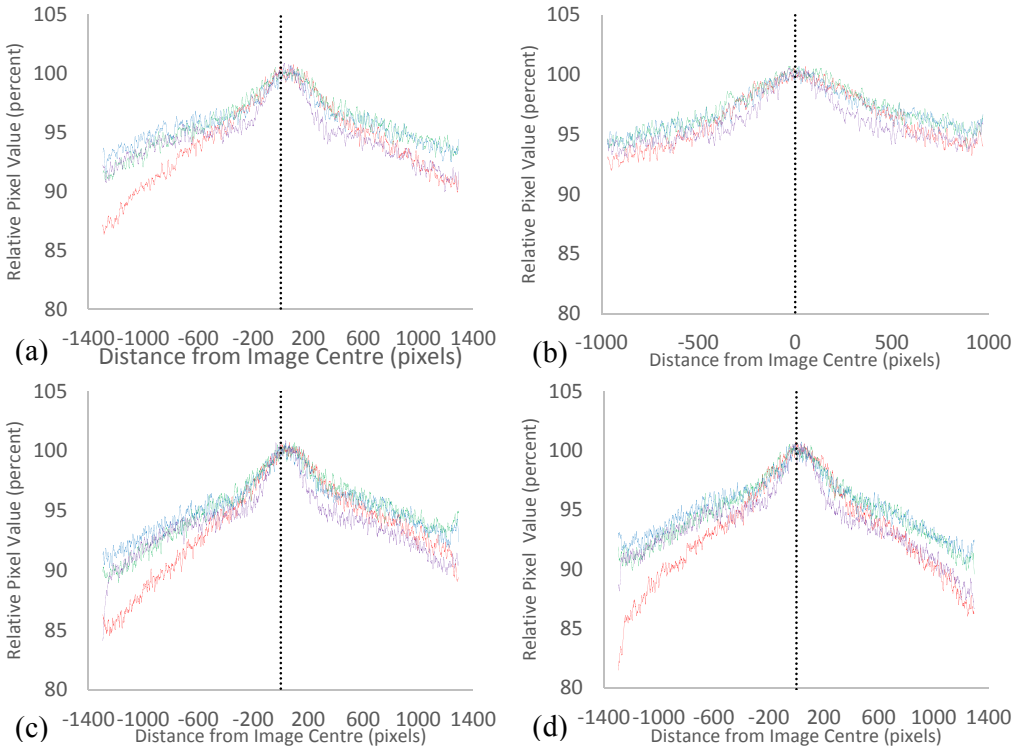

Figure 3.17 – Relative difference in pixel values for the NIR camera red band at an aperture setting of F/5.6 and 4 different focal length settings. Focal lengths shown are: 7 mm (red), 10 mm (green), 15 mm (blue), and 21 mm (violet). Transects shown are: (a) left to right, (b) top to bottom, (c) upper-left to lower-right, and (d) lower-left to upper-right.

3.3.3 Noise Characterization

3.3.3.1 RGB Camera

Tables 3.3 and 3.4 show the results of the noise characterization experiment for the RGB camera red band. Tables 3.5 and 3.6 present the results for the green band, and Tables 3.7 and 3.8 present the results for the blue band.

Noise under both illumination and dark conditions was lowest at the ISO 50 setting for all 3 bands, with both forms of noise gradually increasing as ISO was increased. Illumination noise greatly exceeded dark noise in all cases. The amount of noise was similar between the red and green bands, although the green band had consistently lower amounts of noise (Tables 3.3 and 3.5). The blue band had the highest amount of noise at all ISO settings under illuminated conditions, although the dark noise for the blue band was marginally lower than for the red band (Tables 3.3 and 3.7).

The SNR for the red band was higher than for the green and blue bands at all ISO settings, despite the green band demonstrating a lower amount of noise on average (Tables 3.3 and 3.5). This was owed to the higher signal of the red band under illumination conditions. Despite the difference, the SNR was similar between the two bands. The SNR of the blue band was much lower than those of the red and green bands, often less than half as high (Tables 3.3, 3.5, and 3.7). This was a result of the blue band having a somewhat higher amount of noise and a lower signal value than the other two bands.

At each ISO setting above the lowest (ISO 50), the noise for the red band increased by 40 % to 50 % over the previous ISO, and by 40 % to 98 % over the ISO 50 value, resulting in noise at ISO 400 that exceeded the ISO 50 value by almost 200 % (Table 3.4). The SNR of the red band decreased by approximately 30 % between

each ISO setting, or from 15 % to 30 % relative to the value at ISO 50, leading to an SNR that was 65 % lower at ISO 400 compared to ISO 50.

Noise increased at a greater rate for the green band (Table 3.6). The increase in noise was between 46 % and 56 % higher than the previous ISO, and from 46 % to 122 % higher than at ISO 50, resulting in noise at ISO 400 being 240% higher than the ISO 50 value. SNR decreased by 32 % to 34 % at each ISO setting, or by 15 % to 32 % relative to ISO 50, with the SNR at ISO 400 being 70 % lower than at ISO 50.

The noise increase for the blue band was between 44% and 52% between ISO settings, and from 43 % to 107 % relative to the ISO 50 value (Table 3.8). The amount of noise at ISO 400 was 213 % greater than the value at ISO 50. SNR decreased by approximately 30 % between each ISO setting, or from 15 % to 30 % relative to the ISO 50 value. The SNR at ISO 400 was 65% reduced compared to the ISO 50 value.

For all bands, the smallest increase in noise occurred between ISO 50 and ISO 100, while the largest increase was between ISO 200 and 400; however, the reduction in SNR was greatest between ISO 50 and 100, and lowest between ISO 200 and 400.

Table 3.3 – Noise and SNR for the RGB camera red band at every ISO setting.

ISO Setting	Illuminated Signal (DN)	Illuminated Noise (DN)	Dark Noise (DN)	Total Noise (DN)	Signal-to-Noise Ratio
ISO 50	168.30	2.32	0.24	2.56	65.93
ISO 100	167.56	3.23	0.33	3.56	47.10
ISO 200	167.63	4.52	0.57	5.09	32.91
ISO 400	172.54	6.41	1.18	7.59	22.73

Table 3.4 – Changes in noise and SNR at each ISO for the RGB camera red band.

ISO Setting	Noise Increase over Previous ISO (%)	Noise Increase over ISO 50 (%)	SNR Decrease over Previous ISO (%)	SNR Decrease over ISO 50 (%)
ISO 100	39.4	39.4	28.6	28.6
ISO 200	43.2	99.5	30.1	50.0
ISO 400	49.0	197.3	30.9	65.5

Table 3.5 – Noise and SNR for the RGB camera green band at every ISO setting.

ISO Setting	Illuminated Signal (DN)	Illuminated Noise (DN)	Dark Noise (DN)	Total Noise (DN)	Signal-to-Noise Ratio
ISO 50	131.72	1.87	0.19	2.06	63.86
ISO 100	131.42	2.80	0.21	3.01	43.64
ISO 200	130.86	4.04	0.45	4.49	29.12
ISO 400	135.51	5.90	1.11	7.01	19.32

Table 3.6 – Changes in noise and SNR at each ISO for the RGB camera green band.

ISO Setting	Noise Increase over Previous ISO (%)	Noise Increase over ISO 50 (%)	SNR Decrease over Previous ISO (%)	SNR Decrease over ISO 50 (%)
ISO 100	46.0	46.0	31.7	31.7
ISO 200	49.2	117.9	33.3	54.4
ISO 400	56.0	239.9	33.6	69.7

Table 3.7 – Noise and SNR for the RGB camera blue band at every ISO setting.

ISO Setting	Illuminated Signal (DN)	Illuminated Noise (DN)	Dark Noise (DN)	Total Noise (DN)	Signal-to-Noise Ratio
ISO 50	78.71	2.74	0.19	2.93	26.89
ISO 100	79.36	4.00	0.22	4.22	18.82
ISO 200	80.83	5.59	0.46	6.05	13.37
ISO 400	86.72	8.05	1.12	9.16	9.46

Table 3.8 – Changes in noise and SNR at each ISO for the RGB camera blue band.

ISO Setting	Noise Increase over Previous ISO (%)	Noise Increase over ISO 50 (%)	SNR Decrease over Previous ISO (%)	SNR Decrease over ISO 50 (%)
ISO 100	44.1	44.1	30.0	30.0
ISO 200	43.4	106.6	29.0	50.3
ISO 400	51.7	213.4	29.3	64.8

3.3.3.2 NIR Camera

Tables 3.9 and 3.10 show the results of the noise characterization experiment for the NIR camera red band. Tables 3.11 and 3.12 present the results for the green band, while Tables 3.13 and 3.14 list the results for the blue band.

Noise results for the NIR camera were similar to the RGB camera, although overall the amount of noise was slightly higher. As with the RGB camera, noise was lowest at ISO 50, with both illuminated and dark noise increasing as ISO was increased. As with the RGB camera, illumination noise greatly exceeded dark noise at

every ISO setting. The amount of noise was similar between the three bands at all ISO settings. The red band demonstrated the highest amount of noise, closely followed by the blue band (Tables 3.9 and 3.13), while the green band had the lowest amount of noise at every ISO setting (Table 3.11).

The SNR values for the red and blue bands were essentially identical, although the blue had a marginally higher SNR at every ISO setting besides ISO 50. The green SNR was much lower than the other two bands. This was because this band demonstrated a similar amount of noise to the other two bands, but had a much lower average signal level. Thus when the signal was divided by the noise using Equation 3.1, the resulting SNR was lower than for the NIR camera red and blue bands.

Noise in the red band increased at each ISO setting above ISO 50 by 28 % to 44% over the previous setting, or from 28 % up to 78 % relative to the ISO 50 value (Table 3.10). Noise at ISO 400 was 156 % higher than the ISO 50 value. The SNR decreased by 2 4% to 31 % over the previous ISO, or by 17 % to 24 % relative to the SNR at ISO 50. The SNR at ISO 400 was 61 % lower than at ISO 50.

For the green band, the noise increase at each ISO was from 33 % to 50 % relative to the previous ISO setting, or from 33 % to 99 % relative to the ISO 50 value, resulting in noise at ISO 400 being almost 200 % greater than at ISO 50 (Table 3.12). The SNR decrease at each ISO was between 26 % and 33 % relative to the previous ISO, or 17 % to 26 % relative to the ISO 50 value, with an SNR at ISO 400 that was 66 % lower than at the ISO 50 setting.

Noise in the blue band increased by 24 % to 44 % over each ISO setting, or by 24 % to 76 % relative to ISO 50, leading to noise at ISO 400 being 151 % higher than at ISO 50 (Table 3.14). The SNR decreased between 20% and 30% over the previous

ISO, or by 18 % to 22 % compared to ISO 50, with the SNR at ISO 400 being 60 % lower than at ISO 50.

As with the RGB camera, the smallest increase in noise for all bands occurred between ISO 50 and ISO 100, while the largest increase was between ISO 200 and ISO 400. Changes in SNR were smallest between ISO 200 and ISO 400 for all bands, and largest between ISO 50 and ISO 100 for the red and green bands; however, for the blue band, the reduction in SNR between ISO 100 and ISO 200 was marginally higher.

Table 3.9 – Noise and SNR for the NIR camera red band at every ISO setting.

ISO Setting	Illuminated Signal (DN)	Illuminated Noise (DN)	Dark Noise (DN)	Total Noise (DN)	Signal-to-Noise Ratio
ISO 50	180.78	3.26	0.24	3.50	51.65
ISO 100	177.49	4.03	0.47	4.5	39.50
ISO 200	181.18	5.38	0.84	6.22	29.11
ISO 400	180.95	7.33	1.65	8.98	20.16

Table 3.10 – Changes in noise and SNR at each ISO for the NIR camera red band.

ISO Setting	Noise Increase over Previous ISO (%)	Noise Increase over ISO 50 (%)	SNR Decrease over Previous ISO (%)	SNR Decrease over ISO 50 (%)
ISO 100	28.4	28.4	23.5	23.5
ISO 200	38.5	77.8	26.3	43.6
ISO 400	44.2	156.4	30.7	61.0

Table 3.11 – Noise and SNR for the NIR camera green band at every ISO setting.

ISO Setting	Illuminated Signal (DN)	Illuminated Noise (DN)	Dark Noise (DN)	Total Noise (DN)	Signal-to-Noise Ratio
ISO 50	113.54	2.76	0.10	2.86	39.71
ISO 100	111.09	3.57	0.22	3.79	29.29
ISO 200	114.61	5.01	0.63	5.64	20.35
ISO 400	115.20	7.00	1.46	8.46	13.61

Table 3.12 – Changes in noise and SNR at each ISO for the NIR camera green band.

ISO Setting	Noise Increase over Previous ISO (%)	Noise Increase over ISO 50 (%)	SNR Decrease over Previous ISO (%)	SNR Decrease over ISO 50 (%)
ISO 100	32.7	32.7	26.2	26.2
ISO 200	48.5	97.0	30.5	48.8
ISO 400	50.3	196.2	33.1	65.7

Table 3.13 – Noise and SNR for the NIR camera blue band at every ISO setting.

ISO Setting	Illuminated Signal (DN)	Illuminated Noise (DN)	Dark Noise (DN)	Total Noise (DN)	Signal-to-Noise Ratio
ISO 50	176.92	3.10	0.35	3.45	51.38
ISO 100	173.90	3.80	0.46	4.26	40.84
ISO 200	177.66	5.19	0.81	6.00	29.63
ISO 400	177.75	7.07	1.58	8.65	20.56

Table 3.14 – Changes in noise and SNR at each ISO for the NIR camera blue band.

ISO Setting	Noise Increase over Previous ISO (%)	Noise Increase over ISO 50 (%)	SNR Decrease over Previous ISO (%)	SNR Decrease over ISO 50 (%)
ISO 100	23.6	23.6	20.5	20.5
ISO 200	40.8	74.1	27.5	42.3
ISO 400	44.2	151.0	30.6	60.0

3.3.4 Spectral Response Characterization

3.3.4.1 RGB Camera

Figure 3.18 shows the absolute spectral responses for the RGB camera bands. The red band demonstrated the highest response compared to the blue and green bands. Peak responses occurred at approximately 480 nm, 535 nm, and 600 nm for the blue, green, and red bands, respectively.

The bands of the RGB camera were quite broad, with significant overlap between them. Full-width-at-half-maximum (FWHM) values were 85 nm for the blue, 95 nm for the green, and 90 nm for the red band. The total range for sensitivity was approximately 150 nm for the blue (380 to 530 nm), 190 nm for the green (460 to 650 nm), and 140 nm for the red (560 to 700 nm). A slight amount of blue and green sensitivity continued until 700 nm, and a slight amount of sensitivity was found for the green and red bands between 375 nm and 405 nm.

The region of overlap between the blue and green bands was 65 nm wide, extending between 465 and 530 nm. Overlap between the green and red bands was 70 nm wide (560 to 630 nm), although as mentioned before, slight green sensitivity continued until 700 nm.

The sensitivity curves for the blue and red channels were somewhat asymmetrical. For the blue band, sensitivity to the left of the peak (shorter wavelengths) declined quicker than sensitivity to the right of the peak (longer wavelengths). The opposite occurred with the red, with sensitivity tapering off more gradually on the left side of the peak. The green band response was mostly symmetrical.

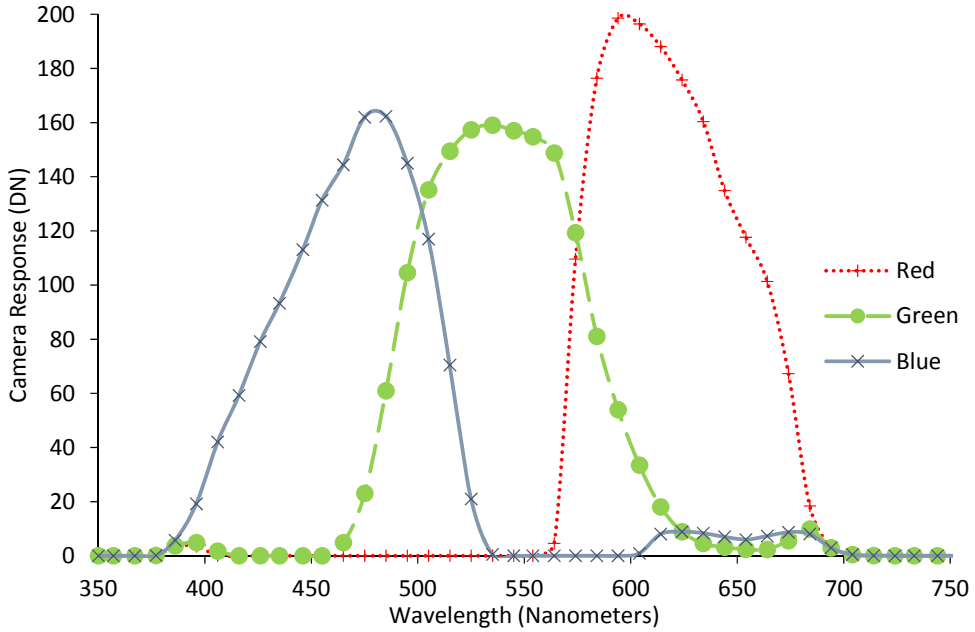

Figure 3.18 – Absolute spectral responses for the RGB camera. Markers indicate measurements while lines show the interpolated curves.

Normalizing the camera responses to account for variations in EMR intensity changed the response curves somewhat, especially for the blue band (Figure 3.19). The blue band was found to have the highest peak sensitivity, with both the red and green bands around 65 % of the blue sensitivity at their respective peaks. The peak response for the blue band shifted to 455 nm, while the green peak became 515 nm. The red peak remained at 600 nm. The FWHM for the blue band widened slightly to approximately 105 nm, while the green and red bands remained the same (95 nm and 90 nm respectively).

The shape of the sensitivity curves changed as well. The blue band became more symmetrical, although now the sensitivity to the left of the peak initially fell off more gradually than to the right of the peak. The green band, which was mostly symmetrical in the absolute response curves, now had an asymmetry as well, with a more gradual decline seen to the right of the peak. The shape of the red curve remained substantially unchanged.

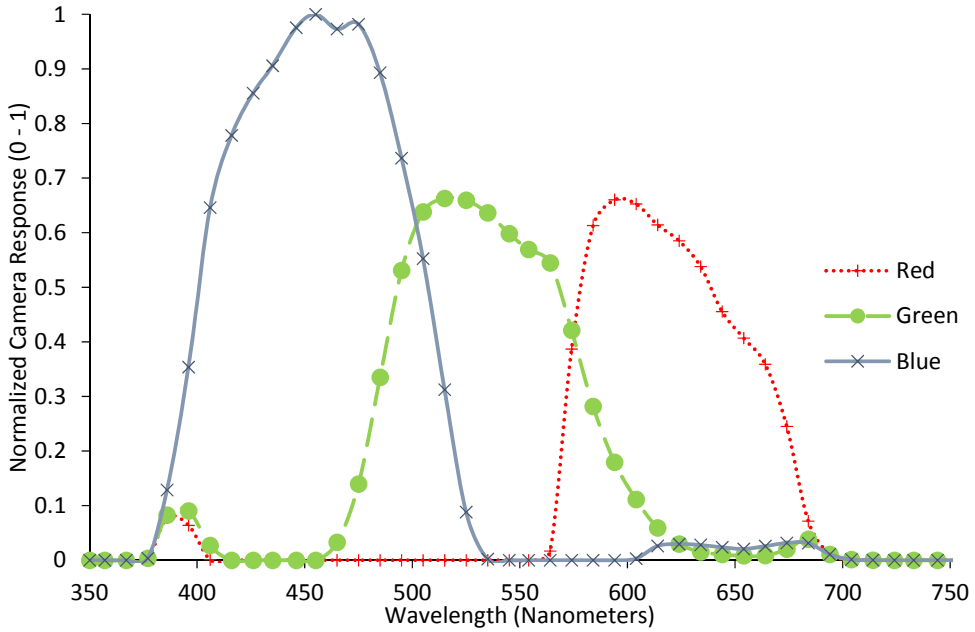

Figure 3.19 – Normalized spectral responses for the RGB camera. Markers indicate measurements, while lines show the interpolated curves.

3.3.4.2 NIR Camera

The absolute spectral responses for the NIR camera bands are presented in Figure 3.20. The shape, peak sensitivity, and band width for all three camera bands were found to be essentially identical. Peak sensitivity occurred at 865 nm, with a FWHM of 140 nm and total sensitivity range of 300 nm (800 nm to 1100 nm). The only notable difference was a difference in magnitude for the green band response compared to the red and blue bands. While the red and blue were virtually identical, the green channel response at peak was only 65 % as high.

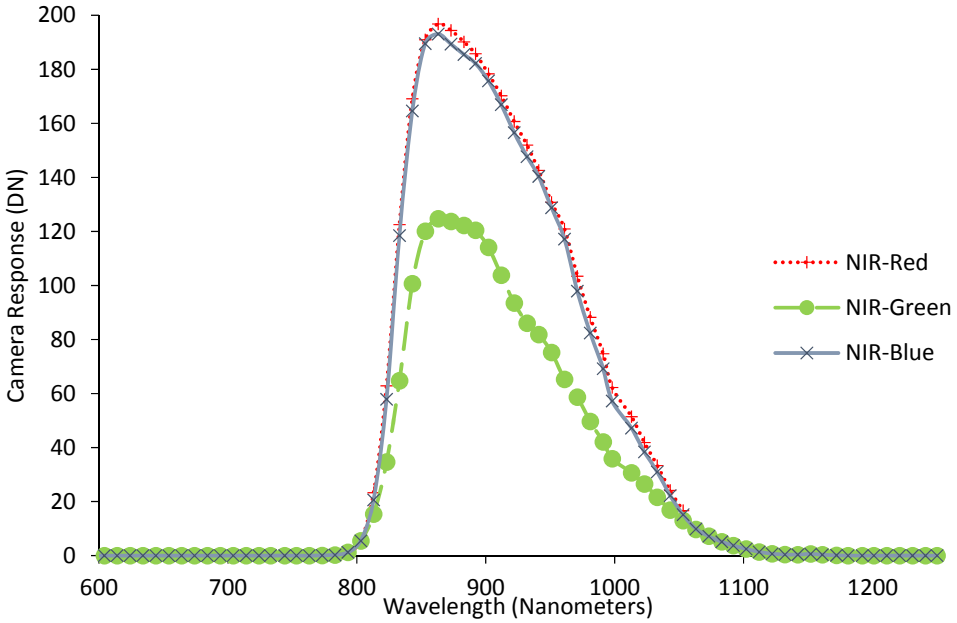

Figure 3.20 – Absolute spectral responses for the NIR camera. Markers indicate measurements, while lines show the interpolated curves.

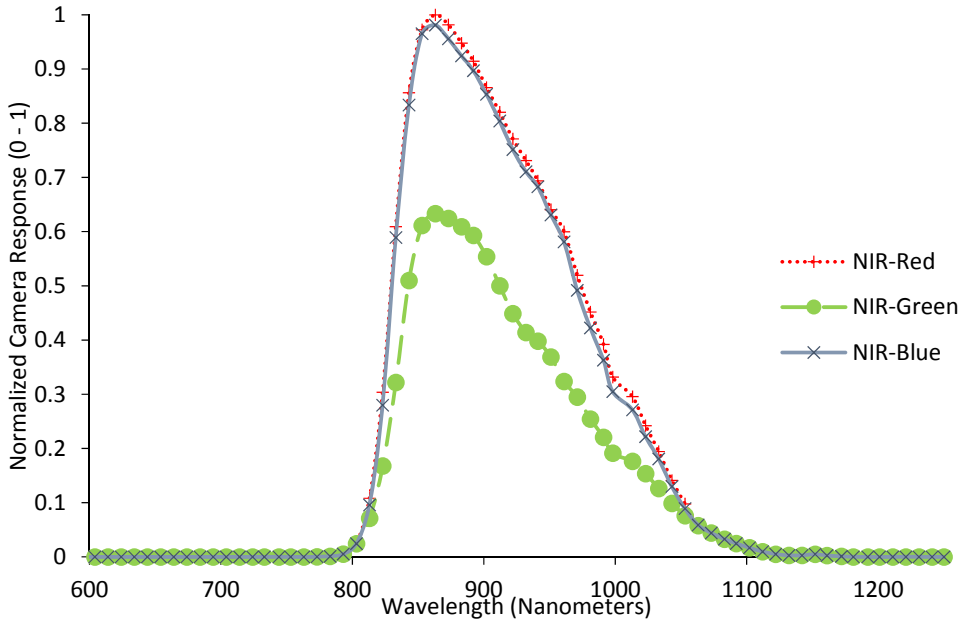

Figure 3.21 – Normalized spectral responses for the NIR camera. Markers indicate measurements, while lines show the interpolated curves.

The shape of the sensitivity curves were asymmetrical about the peak, with sensitivity reducing much more gradually on the right side of the peak (toward longer wavelengths) compared to the left side of the peak. Normalizing for EMR intensity left the spectral response curves for this camera unchanged (Figure 3.21).

3.3.5 Radiometric Response Characterization and Linearization

3.3.5.1 Radiometric Response Characterization

Figures 3.22, 3.23, and 3.24 show the radiometric response curves for the RGB camera red, green, and blue bands, respectively. Figure 3.25 presents the radiometric response curve for the NIR camera red band. Because all three NIR bands were found to be identical in spectral sensitivity and similar in performance in terms of vignetting and noise, it was decided to only analyze the radiometric response of the red band. This was done because in any potential application, using a single band would provide the same information content as the other two bands. Thus, there was no reason to further analyze all three bands.

Each of the figures show the camera response along the y-axis and light intensity in the x-axis. Light intensity is relative, with an intensity value of 1 corresponding to a peak camera response of 255. As shown in the figures, each camera band demonstrated a notably non-linear response to increasing light intensity, with a rapid response at lower intensities followed by a gradual flattening of the response at higher intensities. The response curves of each band were similar in shape to one another.

With the RGB camera red band, there was a slight non-linear feature at very low DNs from 0 to approximately 15 (Figure 3.22). DNs between 15 and 100 had a linear response to changes in light intensity. This was followed by a nonlinear region extending approximately from 100 to 220 DN, where camera response increased at a progressively lower rate with increasing light intensity. From 220 DN onward, the red band response appeared to become mostly linear again. A similar pattern was seen with the RGB green and blue bands and the NIR red band (Figures 3.23, 3.24, and 3.25), although the non-linearity at low DNs was not as pronounced with those bands.

In all cases the major region of non-linear response occurred with DNs from approximately 120 to 200.

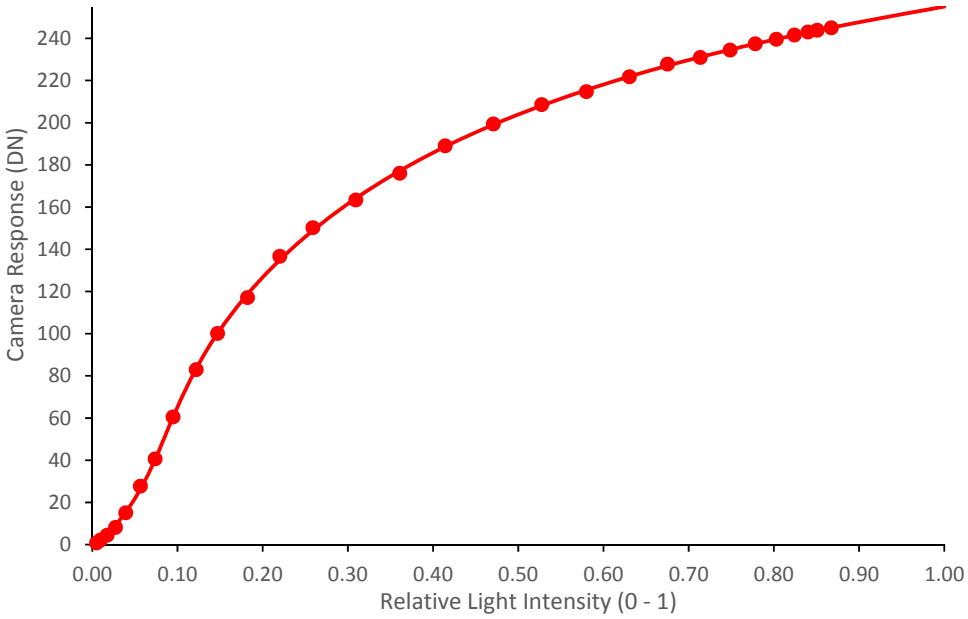

Figure 3.22 – Radiometric response of the RGB camera red band. Markers indicate measured responses, while the line shows the interpolated response curve.

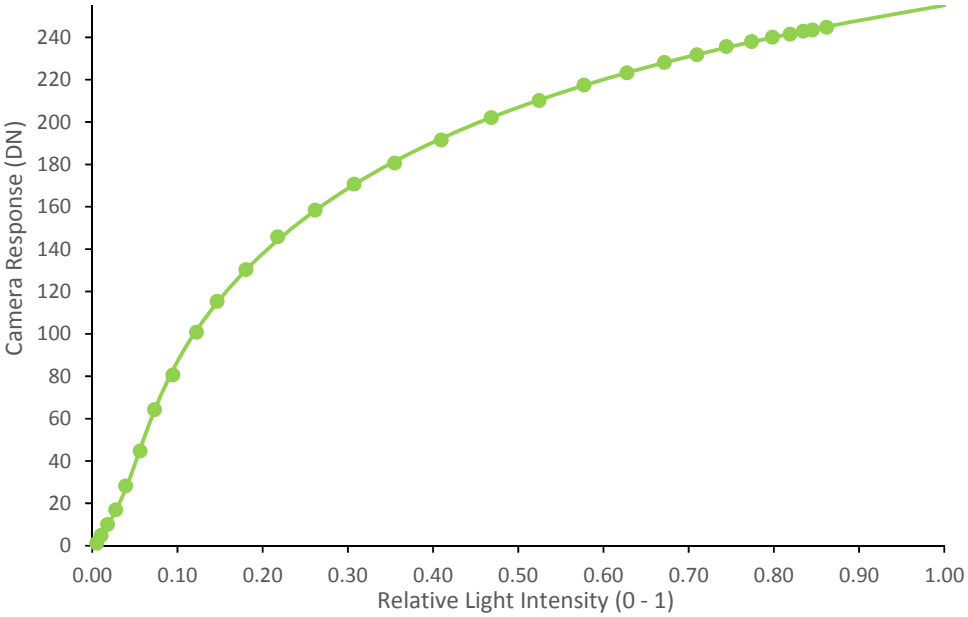

Figure 3.23 – Radiometric response of the RGB camera green band. Markers indicate measured responses, while the line shows the interpolated response curve.

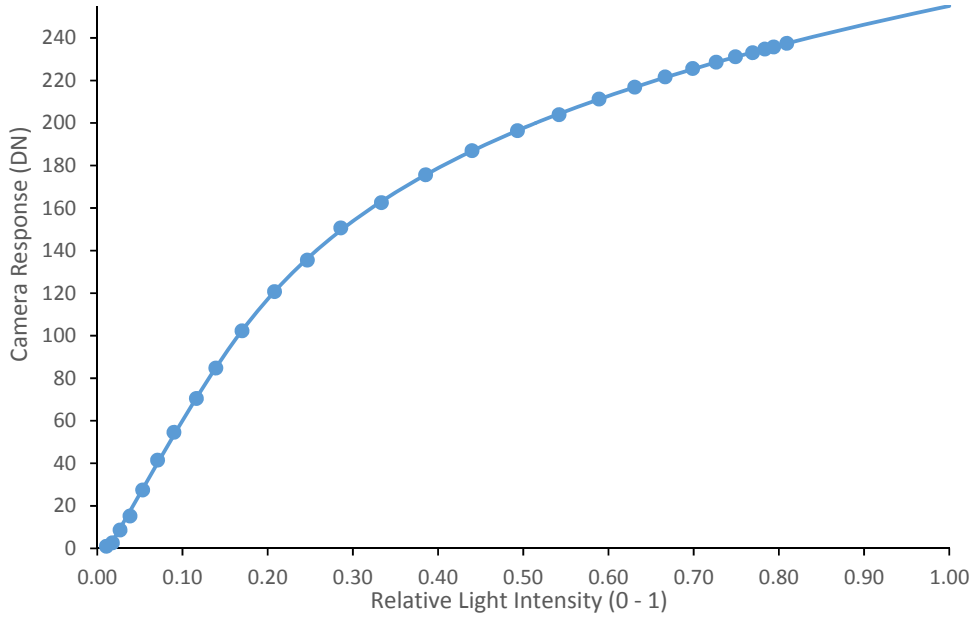

Figure 3.24 – Radiometric response of the RGB camera blue band. Markers indicate measured responses, while the line shows the interpolated response curve.

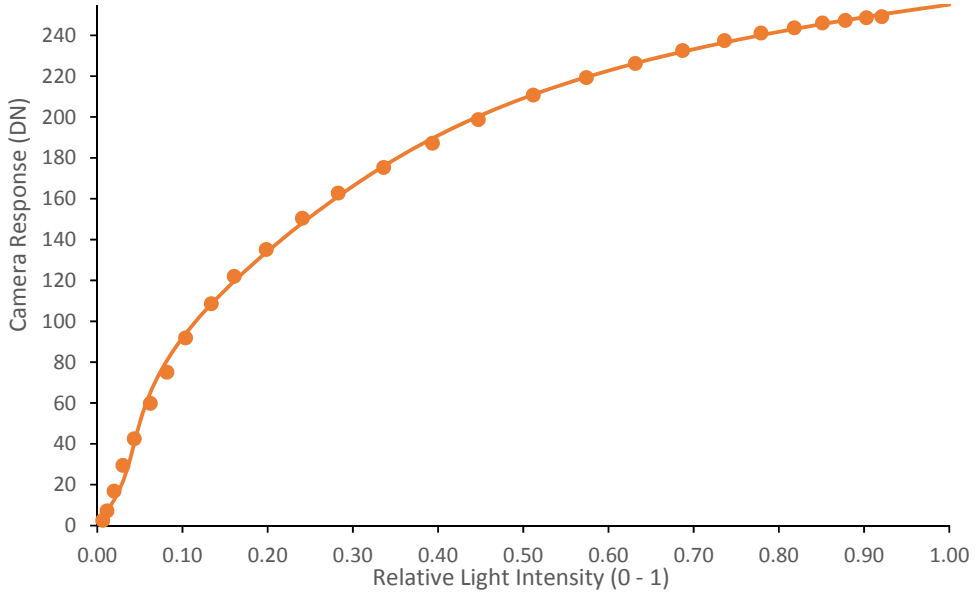

Figure 3.25 – Radiometric response of the NIR camera "red" band. Markers indicate measured responses, while the line shows the interpolated response curve.

3.3.5.2 Radiometric Linearization Model Validation

Table 3.15 lists the RMSE values for the comparison between linearized camera responses and the normalized ASD responses. The NIR camera red band compared the best with the ASD measurements, with an RMSE of just under 0.01, or

1 % relative intensity. This was followed by the RGB camera red band, with an RMSE of just over 0.02 (2 %), while the RGB camera green band RMSE was higher still at 0.027 (2.7 %). The RGB camera blue band had the highest RMSE figure at 0.042 (4.2 %).

Table 3.15 – Root Mean Square Error of the difference between linearized camera responses and normalized ASD responses.

Camera Band	Root Mean Squared Error (RMSE)
RGB-Red	0.0207
RGB-Green	0.0272
RGB-Blue	0.0422
NIR-Red	0.0092

Figures 3.26 to 3.29 show the camera and ASD responses plotted against each other for each of the camera bands. The dotted line shows the regression line plotted through the data, while the solid line shows a one-to-one relationship for comparison. The R^2, slope, and intercept of the regression lines are listed, along with the 95 % confidence bounds for the slope and intercept. Figure 3.30 shows the difference between the ASD and camera responses for all camera bands. The x-axis shows the normalized ASD value, while the y-axis shows the difference between the measurements at a given ASD value.

In general the camera responses for the RGB camera red and green bands and the NIR camera red band matched closely to the ASD responses and followed a linear progression. R^2 values were very high for all 3 bands. The slope for each regression line was very close to 1, although the NIR red regression slope differed significantly from 1 ($p < 0.05$) (Figure 3.29). The slope for the RGB red and green bands did not differ significantly from 1 (Figures 3.26 and 3.27).

The intercept for each of the 3 bands was also close to 0; however, the intercept was significantly above 0 ($p < 0.05$) for the RGB red and green bands.

Examining the data points for the two bands it can be seen that in most cases, the camera responses exceeded the ASD responses, indicating a positive bias in the linearizing for these two bands. The intercept for the NIR red band was not significantly different from 0.

The linearization of the RGB blue band did not compare as favourably with the ASD responses. While the R^2 value was high for the regression line and the intercept close to 0, the slope was significantly lower than 1 ($p < 0.05$) (Figure 3.28). The graph shows a clear departure from linearity, with camera responses progressively falling below the ASD responses before gradually recovering.

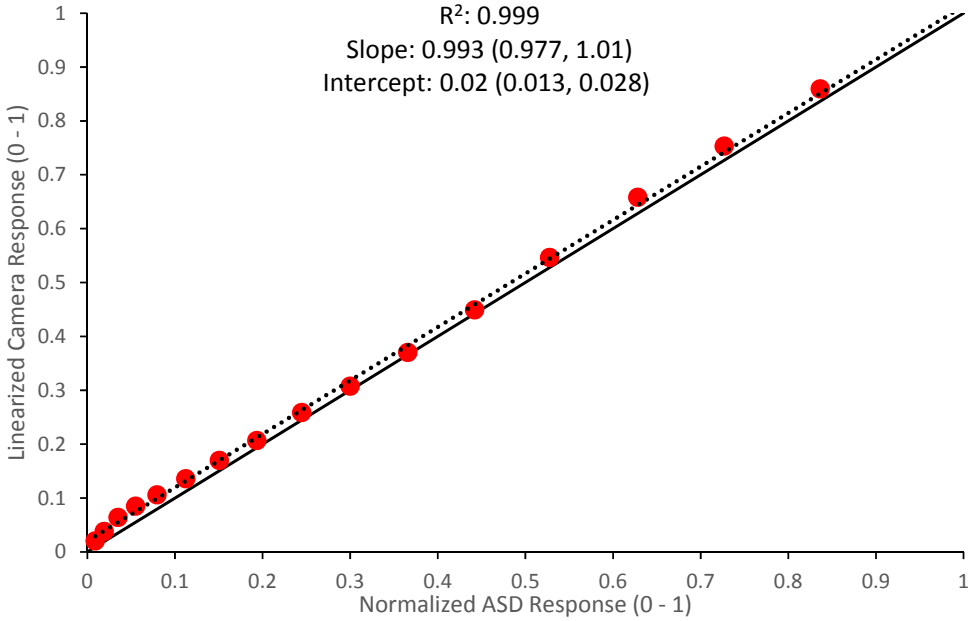

Figure 3.26 – Regression of linearized camera responses for the RGB camera red band against normalized ASD responses. The dotted line shows the regression line through the data, while the solid line shows a one-to-one relationship for comparison. R^2, slope, and intercept for the regression line are listed, along with the 95 % confidence intervals for the slope and intercept in brackets.

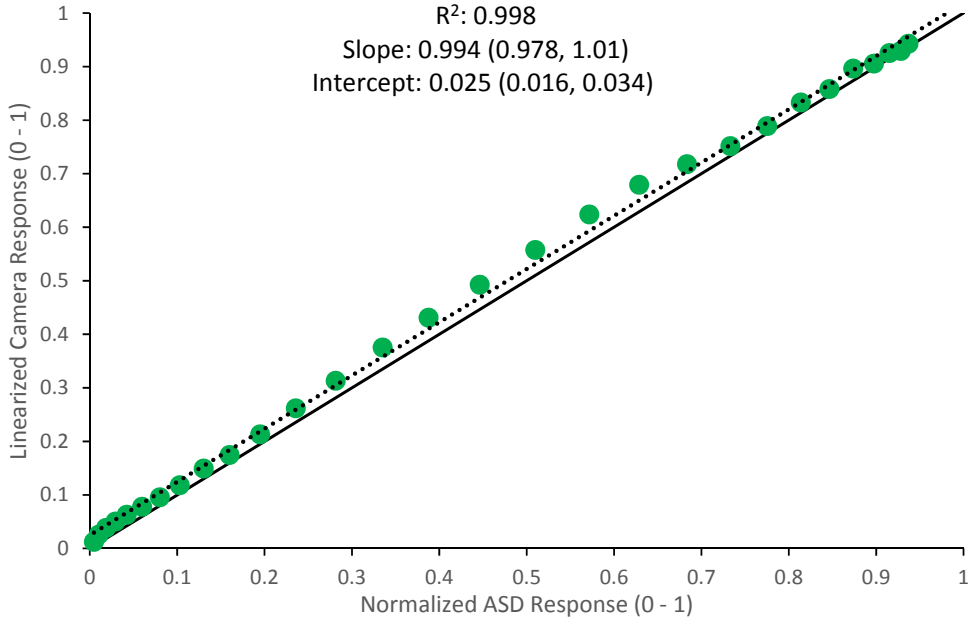

Figure 3.27 – Linearized camera responses for the RGB camera green band plotted against normalized ASD responses. The dotted line shows the regression line through the data, while the solid line shows a one-to-one relationship for comparison. R^2, slope, and intercept for the regression line are listed, along with the 95 % confidence intervals for the slope and intercept in brackets.

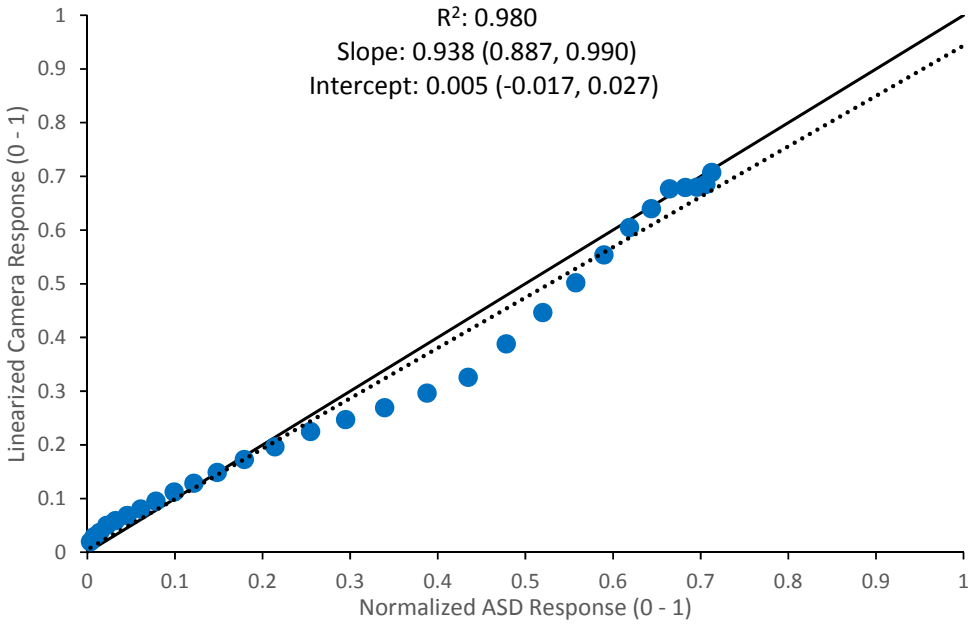

Figure 3.28 – Linearized camera responses for the RGB camera blue band plotted against normalized ASD responses. The dotted line shows the regression line through the data, while the solid line shows a one-to-one relationship for comparison. R^2, slope, and intercept for the regression line are listed, along with the 95 % confidence intervals for the slope and intercept in brackets.

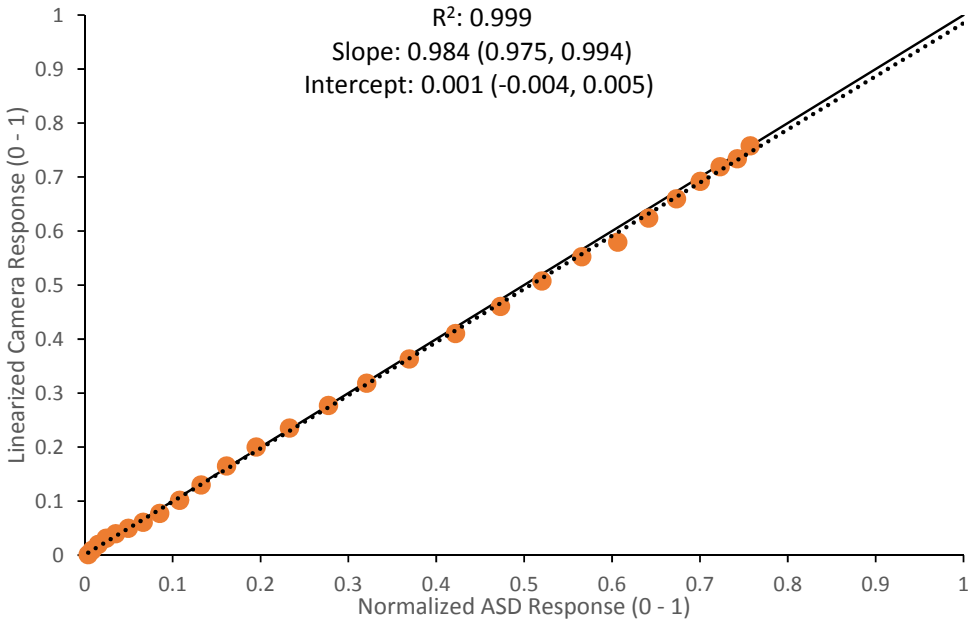

Figure 3.29 – Linearized camera responses for the NIR camera red band plotted against normalized ASD responses. The dotted line shows the regression line through the data, while the solid line shows a one-to-one relationship for comparison. R^2, slope, and intercept for the regression line are listed, along with the 95 % confidence intervals for the slope and intercept in brackets.

Figure 3.30 shows the differences between the camera and ASD response values more clearly. It is shown that the RGB camera red band values were moderately higher than the ASD at low light intensities. The difference gradually decreased as light intensity increased until an ASD-measured value of around 0.35, hitting a minimum difference of 0.005 before gradually increasing again, reaching a difference of 0.03 around an ASD value of 0.62. Following this, the difference declined as light intensity further increased. In every comparison the RGB red band values were higher than the normalized ASD values.

The RGB green values also exceeded the ASD values at every light intensity. Between an ASD-measured intensity of 0.2 and 0.57 this overestimation for the green band gradually increased, reaching a maximum overestimation of 0.052. Following this, the overestimation gradually decreased, reaching a minimum difference of 0.001

at an ASD response of 0.93. As with the red band, the green camera values were higher than the ASD values in every comparison.

The RGB camera blue band had the largest differences between camera and ASD responses. The differences at very low light intensities were similar to the red and green bands; however, as light intensity increased, the blue band values were progressively lower than the ASD, reaching a maximum underestimation of 0.11 at an ASD-value of 0.44. Following this trend, the blue band underestimation became progressively smaller until an ASD-value of 0.64, where the blue value was lower than the ASD by only 0.004. At higher light intensities the blue band values remained similar to the normalized ASD values.

Compared to the RGB camera, the differences between the NIR camera red band and the ASD were smaller. Small differences of no more than 0.01 characterized the NIR response from ASD values of 0 to 0.32, with the differences alternating between being positive and negative. Beyond this point, the NIR response became progressively lower than the ASD, with a maximum negative difference of 0.027 occurring at an ASD value of 0.6. Further increases in light intensity reduced the negative difference until the final data point, where the camera response was essentially equal to the ASD response at an ASD value of 0.76.

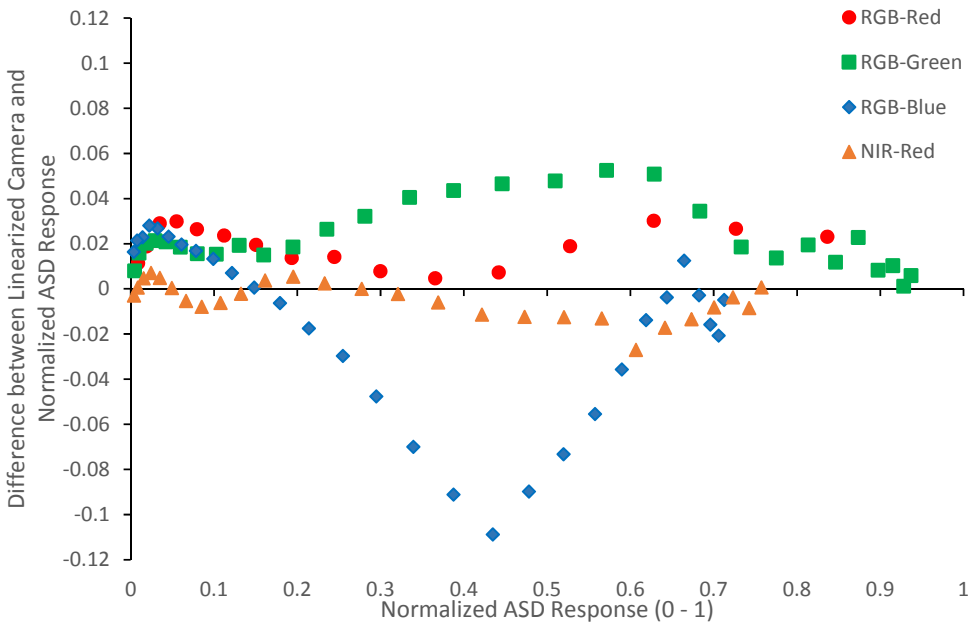

Figure 3.30 – Difference between linearized camera responses and normalized ASD responses across a range of EMR intensities.

3.4 Discussion

3.4.1 Geometric Distortion Characterization and Calibration

Geometric distortions for both cameras were successfully characterized and calibrated in this research. Distortions for the cameras were found to be moderate, with high levels of distortion in the edges of the camera frame. The distortion was also found to be asymmetrical for both cameras, with a greater amount of distortion occurring in the bottom and left portion of the camera images. The likely cause of this asymmetry is a misalignment between the sensor and the camera optics caused during the manufacturing of the cameras. Since radial distortion occurs symmetrically about the centre of the camera optics, a misalignment with the sensor would cause the distortion to be offset in the images, resulting in the observed asymmetry (Brown, 1966). This is a common defect among mass produced consumer digital cameras (Sanz-Ablanedo et al., 2010).

Using the distortion models from each camera to correct distortion resulted in pixel displacement being reduced by 50 % to 100 %. However, the fact that 100 %

was not always corrected (and in one case none of the distortion was corrected) shows that the distortion correction was not perfect. The correction for the NIR camera generally performed better than the RGB correction. It is possible that the NIR camera distortion was characterized more accurately, resulting in a better distortion model. While care was taken to acquire photos of the calibration grid from the same positions and angles for both cameras, the images obtained from the NIR camera may have been better suited for characterizing distortion. Another possibility is that the calibration grid corners were poorly selected in some images from the RGB camera, leading to a poor result during the automatic extraction of the grid intersections.

While the validation demonstrated the effectiveness of the distortion corrections, the validation itself could be improved. Validation should be performed using more images for each camera and more points distributed throughout the image frame. A validation should also be performed on images outside the dataset used to create the distortion models. Another limitation was that it was not possible to measure distortion in the furthest corners of the frame, where it was predicted to be highest. This was because the edges of the calibration grid were not present in the far corners of any of the images. Validation of the models in the edges of the frame would be advisable, although potential issues can be mitigated either by cropping the edges out of images or by creating mosaics using multiple images with high overlap.

Another important caveat is that the distortion characterization is only valid for the camera settings used. Changes in the focal length, and potentially changes in aperture will impact the image distortion. If other settings are desired, the experiment will need to be repeated using those settings.

Finally, the corrections only compensate for internal camera distortion. Distortion can also be caused by the external orientation of the camera relative to the

ground. To compensate for this distortion it is necessary to know the position and orientation parameters at the time of image acquisition, which can be provided by an IMU (Cramer et al., 2000).

3.4.2 Vignetting Characterization

The results from the vignetting characterization experiment showed a notable falloff in pixel values outside the image centre for both cameras, with values falling by 5 % to almost 30 % at wide apertures and short focal lengths. Vignetting had a larger impact on the NIR camera than the RGB camera.

Reductions in aperture and increases in focal length yielded decreases in vignetting for the RGB camera. This result was not surprising, as vignetting tends to be highest at wide apertures and short focal lengths (Yu, 2004). The best combination of settings for reducing vignetting was using the narrowest aperture (F/8) and longest focal length (21 mm). However, decreases in aperture beyond F/4 and increases in focal length beyond 10 mm yielded only marginal improvements. There are trade-offs associated with narrower apertures (necessitates slower shutter speeds) and longer focal lengths (lower areal coverage per image). Therefore, the best practical combination for reducing image vignetting is an aperture of F/4 and focal length of 10 mm.

For the NIR camera, narrowing the aperture from F/2.8 to F/4 yielded a decrease in vignetting, but further narrowing increased overall vignetting near the centre of the images. Likewise, increasing the focal length from 7 mm to 10 mm reduced vignetting, but further increases either yielded no improvement or increased vignetting near the image centre. As with the RGB camera, the best combination of settings to reduce vignetting was an aperture of F/4 and focal length of 10 mm.

The vignetting pattern was asymmetrical for both cameras, with a greater amount of falloff evident toward to left side of the image frame. This difference was more apparent at shorter focal lengths and wider apertures. This asymmetry reinforces the findings of the distortion characterization, suggesting the optics are not centred over the sensor. As vignetting generally occurs radially from the lens centre, a poor alignment of the lens over the sensor could lead to the asymmetrical patterns that were observed.

A relatively typical vignetting pattern was demonstrated by all bands of the NIR camera, and the red and green bands of the RGB camera; however, vignetting for the RGB camera blue band followed a quite different and unusual pattern. For this band, pixel values remained the same or increased with increasing distance from the image centre. It was also characterized by a large asymmetry, with pixel values increasing toward the bottom portion of the frame, but remaining the same or decreasing toward the top of the frame. There was also a larger amount of noise evident in the pixel values compared to other bands tested.

It is not clear why the blue band behaved in this way. The asymmetrical increase in pixel values could be a result of differential sensitivity or signal amplification for pixels toward the bottom of the frame compared to the centre and top. This could be a flaw with the camera, and an absence of these effects with the NIR camera blue band suggests the problem resides with the RGB camera specifically. The increase in noise is likely simply a result of the fact that less blue light was emitted from the integrating sphere, meaning blue pixel values were lower. Accordingly, the same amount of noise would yield a greater percentage difference from the mean pixel value. Returning to the original images confirmed that the mean

blue value in each image was indeed lower, while the standard deviations were comparable to those of the other 2 bands.

While vignetting was characterized, no attempt was made to correct the issue. If desired, a digital anti-vignetting filter could be created to boost the values of image pixels proportionally based on the amount they are afflicted by light fall-off (Yu, 2004). For the purposes of the subsequent research in this thesis, it was deemed unnecessary to correct the vignetting. Use of the recommended aperture and focal length settings along with high overlap between images to create mosaics should remove or minimize any issues due to vignetting.

3.4.3 Noise Characterization

Noise levels for all bands of the RGB and NIR cameras were similar. Overall noise was slightly higher with the NIR camera than the RGB camera. Noise under illumination conditions was always found to greatly exceed noise under dark conditions.

The least amount of overall noise was found with the green band for each camera (Tables 3.5 and 3.11). For the RGB camera, the most noise occurred in the blue band, while for the NIR camera, the red band had the most noise (Tables 3.7 and 3.9). The red band had the best SNR for the RGB camera, while the blue band had the best SNR for the NIR camera (Tables 3.3 and 3.13). The blue and green bands had the poorest SNR for the RGB and NIR cameras, respectively (Tables 3.7 and 3.11). The low SNR value of these bands, despite a similar or lower amount of noise compared to the other bands, is due to the lower signal recorded by each.

Noise increased and SNR decreased for both cameras as the ISO was increased. This was expected, as the greater amplification applied at higher ISO settings, amplifies both the measured signal as well as the noise (Rabie, 2004). The

increase in noise and decrease in SNR was similar between the bands of each camera, although the changes were smaller for the NIR camera. At each ISO the RGB camera suffered an increase in noise of 40 % to almost 60 %, and an SNR decrease of around 30 % compared to the previous ISO setting (Tables 3.4, 3.6, and 3.8). The noise level at the highest ISO setting was around 200 % to 240 % higher, while the SNR was 65 % to 70 % lower than at the lowest ISO setting.

For the NIR camera, noise increased by 30 % to 50 % and SNR decreased by 20 % to 30 % at each ISO setting (Tables 3.10, 3.12, and 3.14). This resulted in noise being 150 % to 200 % higher and SNR being 60 % to 65 % lower at the highest ISO setting compared to the lowest setting. These findings suggest that the lowest ISO setting should always be used unless it is absolutely necessary to have higher sensor sensitivity, for instance in order to allow the use of a faster shutter speed to avoid image blurring. At the very least, the higher ISO settings (ISO 200 and ISO 400) should be avoided.

Even at the lowest ISO settings, the SNR values obtained from the cameras were fairly poor compared to high quality satellite and airborne sensors. At the lowest ISO setting, SNR values were from 27:1 to 66:1 for the RGB camera, and from 40:1 to 52:1 for the NIR camera. For comparison, the SNR for Landsat-8 bands range from 150:1 to 350:1 under typical illumination conditions (Irons et al., 2012). The airborne Hymap hyperspectral sensor has a nominal SNR of 500:1 (Cocks et al., 1998). This disparity in performance is not surprising, as inexpensive digital cameras cannot be expected to match the performance of high quality sensors. Nonetheless, it is important to keep the noise performance of the cameras in mind as it impacts the level of confidence that can be placed in their data.

While this study provided a measure of noise levels under moderate and no EMR intensity, more work should be done to provide a better idea of how noise and SNR change as a function of EMR intensity and camera exposure. Noise levels were found to remain similar between the bands despite differing signal levels, leading to some bands having greatly reduced SNR values. This may imply a relatively constant level of noise, which could greatly impact the SNR at lower light intensities. On the other hand, the very low dark noise results suggest that noise is greatly reduced at lower light levels. To better characterize noise it should be measured throughout the dynamic range for each camera. This could be performed by imaging the integrating sphere over a range of different light intensity settings.

While noise was characterized in this study, no attempt was made to reduce it. Future improvements to the study could involve investigation of noise reduction methods such as spectral filtering (Tsai & Philpot, 1998), spatial filtering (Church et al., 2008), or data transformations (Lee et al., 1990). For the purposes of this research, using area-averaged spectral signals instead of individual pixel values should reduce the impact of image noise.

3.4.4 Spectral Response Characterization

The spectral response functions for both cameras were able to be measured using the monochromator method. The bands for both cameras were found to be quite broad, with spectral FWHM values between 90 nm and 105 nm for the RGB camera and 140 nm for the NIR camera (Figures 3.18 to 3.21). A large amount of overlap was found between the bands of the RGB camera, while the bands of the NIR camera perfectly overlapped.

The findings of broad bands and high band overlap for the RGB camera agrees to what has been found in other research on the spectral characteristics of digital

cameras (Barnard & Funt, 2002; Jun et al., 2013; Lauziere et al., 1999; Vora et al., 1997b). The shape, bandwidth, central wavelengths, and relative sensitivity for the RGB camera bands were also similar to those found in a number of other studies (Barnard & Funt, 2002; Jun et al., 2013; Lauziere et al., 1999; Martinez-Verdu et al., 2002). However, these results also differed somewhat from other studies. For instance, in Vora et al. (1997b) the relative response of the blue band was much lower than the red and green bands, unlike the results of the current study, which indicated the relative blue band response was higher than for the other two bands. The green and red band peak responses also occurred at longer wavelengths (550 nm and 630 nm, respectively). Ebner (2007) found their camera bands were more symmetrical, while the blue band peaked at shorter wavelengths (430 nm) and the red band peaked at longer wavelengths (675 nm).

Assessment of the NIR characterization using the literature was more difficult, as there were fewer studies available on infrared imaging digital cameras. Other studies have found NIR sensitivity extending further into shorter wavelengths and the peak sensitivity occurring at shorter wavelengths as well (Hunt et al., 2008; Verhoeven et al., 2009). However, this could be the result of the type of visible EMR blocking filter fitted to the camera. The lack of camera response at wavelengths shorter than 800 nm found in this research does not mean the sensor is not sensitive to these wavelengths, but simply that the filter fitted to the sensor is blocking all shorter wavelengths.

Differences from other studies do not invalidate the results of this research, but emphasize the fact that cameras can and do differ in their spectral response. Consequently, if the spectral response of a camera is important for a particular application, it is important to characterize it. Knowledge of the spectral response of a

sensor is important when using or comparing data from multiple sensors, as differences in spectral response functions can lead to significant differences in the measurements from each (Trishchenko et al., 2002). Knowing the spectral sensitivity of a sensor can also allow assessment of its suitability for an application. For example, if the sensor is not sensitive within the desired spectral range, or if the bands are too broad to detect a narrow spectral feature of interest, then the sensor is not useful.

The spectral sensitivity characterization performed in this research could be improved in a number of ways. Firstly, the issue of radiometric nonlinearity was not factored in to the response models. As seen in the radiometric response characterization, both cameras demonstrated nonlinear responses to light intensity changes. Consequently, the exact shape of the spectral response curves for each band would likely change, primarily by the shoulders to either side of the spectral peak becoming steeper. Linearization was not included in this experiment to avoid potential complication due to errors in the linearization models. Despite its omission, the width and wavelength of peak sensitivity for each band is not likely to be any different, and it is these features that were of primary interest.

Another improvement would be to validate the spectral response curves. The use of a monochromator for assessing sensor spectral sensitivity is a common practice in spectral response studies and has been shown to be accurate (Farrell et al., 2008; Lauziere et al., 1999; Verhoeven et al., 2009; Vora et al., 1997b). Nonetheless, validation would increase confidence in the measured spectral response functions. Validation could involve using the measured spectral response functions from the cameras to create simulated images of targets with known reflectance properties (e.g., a Macbeth ColorChecker chart). The targets would also be imaged with the cameras,

and the values in the simulated and real images would be compared (Farrell et al., 2008; Vora et al., 1997b).

3.4.5 Radiometric Response Characterization and Linearization

The radiometric responses for both cameras were found to be nonlinear. This was expected, as consumer digital cameras are commonly designed to be nonlinear (Grossberg & Nayar, 2004).

The lookup table linearization method was able to correct the nonlinearities for both cameras reasonably well. Linearized responses for the RGB camera red and green bands and the NIR camera red band compared well to ASD responses. The linearized responses for the RGB red and green bands were higher than the ASD responses; however, increases and decreases in light intensity yielded a mostly linear change in camera values. The difference between camera and ASD responses did vary somewhat with light intensity, suggesting that the correction was not perfect and that some nonlinearity remains.

The NIR camera red band compared more favorably to the ASD, with the difference between camera and ASD responses being smaller than for the RGB red and green bands. As with the RGB camera, the difference between the linearized NIR red band values and ASD values did vary with light intensity, but the variations were smaller. However, the slope of the regression line fitted to the data was slightly under 1, indicating that the corrected responses may remain somewhat nonlinear.

The linearization of the RGB camera blue band did not perform well compared to the other camera bands. Blue band responses remained strongly nonlinear relative to the ASD measurements. Large differences between the blue band response and ASD response were evident, with the blue band values being much lower than the ASD for much of its dynamic range. The poor quality of the

linearization model for the RGB camera blue band indicates that it should not be used for quantitative spectral measurements, as the assumption of a linear sensor response is not valid for this band.

The methods used in this study could be improved upon. The fact that light from the integrating sphere was used to both create and validate the linearization models is a potential issue, although the use of an integrating sphere is common and accepted practice (European Machine Vision Association, 2010). In future work the validation could be performed using other targets, including both natural and synthetic objects with varying reflectance properties under daylight illumination (Mitsunaga & Nayar, 1999; Shafique & Shah, 2004).

Another issue is that a differing number of data points were used to validate the linearization models for each band. Specifically, there were fewer data points used for the RGB camera red band than for the other bands. This was because a single set of images were used to validate the response models for all 3 bands. Red band saturation occurred at higher integrating sphere light intensities and, consequently, those images could not be used in the comparison. The green and blue channels did not saturate. Thus, all measurements for those bands could be used in the comparison.

Another problem related to the above is that the dynamic range was not covered fully for every band. While the RGB camera green band highest response was 94 % of the maximum, the highest red band response was only 86 % of the maximum, while for the blue band it was only 72 %. For the NIR camera red band, the highest response was only 76 % of the maximum. In order to better validate the response models, the experiment could be repeated for each camera band separately, taking care to ensure that most of the dynamic range is covered for each band.

It is important to note that while the linearization models were able to compensate for the nonlinear response of the cameras, the cameras are not equally sensitive to changes in light intensity throughout their dynamic range. Due to the flattening of the camera response near the top of its dynamic range, a larger change in light intensity is necessary to yield a corresponding change in DNs compared to the lower portion of the dynamic range; thus, the radiometric resolution at high DNs is worse than at low DNs. Linearization of the camera responses does not correct this issue, it merely allows the camera values to properly indicate the linear differences in light intensity between one DN value and the next.

3.4.6 General Discussion

Knowledge of the spectral, spatial, and radiometric characteristics of a sensor system is important when using it to derive quantitative data. For digital cameras, it is often difficult or impossible to obtain detailed information on these characteristics from the camera manufacturer. Furthermore, even if such data are available, the characteristics of cameras of the same make and model can differ from one another. Therefore, it is advantageous to independently validate the characteristics of each camera to be used in remote sensing applications.

For several of the experiments performed here, the results may only be valid for the camera settings used. This is particularly true of the distortion characterization, where the created distortion models are only valid for the focal length settings that were used.

An important factor that warrants mentioning is the impact of the white balance setting selected for the camera. The white balance differentially amplifies the responses for each camera band in order to render colours in a manner which appears correct to the eye. Consequently, varying the white balance could have a pronounced

effect upon some of the results achieved in this study, particularly for the spectral and radiometric responses for each band. Therefore, it is important to characterize the cameras using a consistent white balance, and to use the same white balance setting during any subsequent application of the cameras. Use of automatic white balance settings must be avoided to prevent undermining the quality of the data.

It is also important to mention the impact of the Bayer colour filter array on data derived from the digital cameras. As a result of the filter, a given pixel only detects one wavelength range of EMR, with values for the other two bands being interpolated through demosaicing (Li et al., 2008). Consequently, it cannot be certain if the value for a band in a given pixel is due to an actual EMR stimulus if it has been computed. To minimize potential issues due to demosaicing, averaged camera responses were used in most of the characterization experiments performed in this research. However, this issue means that quantitative measurements based on individual pixel values should be treated with caution. It is likely better to calculate the average camera signal over a target of interest than to use individual pixel values. The use of averaged signals is also recommended on account of the relatively high-noise characteristics of the cameras.

3.5 Conclusions

In this chapter some of the key spectral, spatial, and radiometric characteristics of two digital cameras were assessed using laboratory-based experiments. The characterization experiments found the cameras were afflicted by moderate amounts of geometric distortion, vignetting, and noise, and the radiometric response for each camera was found to be nonlinear. The spectral response functions for the cameras were also successfully measured, which will aid in comparisons of the camera data with data from other sensors.

Calibrations were implemented to compensate for geometric distortion effects and nonlinear radiometric responses. The calibrations were able to minimize geometric distortion and compensate for most of the radiometric nonlinearity encountered. These calibrations will help to improve the quality of the camera data for the quantitative remote sensing measurements acquired in the next chapter.

Some unusual results were found for the RGB camera blue band. Vignetting results for this band did not adhere to the expected pattern, and, critically, the radiometric response calibration was unable to satisfactorily correct the band's nonlinear response. Consequently the RGB camera blue band will be omitted from the research in the next chapter.

Future research should examine compensating for other sensor effects such as vignetting and image noise. For the purposes of the subsequent research in this thesis, the use of high image overlap and appropriate camera settings should minimize vignetting, while aggregation of image pixels over larger areas should minimize the potential impacts from image noise.

4. THE IMPACT OF SPATIAL RESOLUTION ON RIPARIAN LAI MODELLING USING REMOTE SENSING

4.1 Introduction

This chapter examines the effects of differing sensor spatial resolutions on leaf area index (LAI) modelling within riparian zones using optical remote sensing. Throughout this chapter "spatial resolution" refers to the ground sampling distance (GSD), the ground distance between adjacent pixel centres in an image. The research was conducted to provide information on the appropriate sensor spatial resolutions for monitoring riparian LAI. This information will facilitate the selection of a sensor for operational riparian LAI monitoring, providing data for dam managers to assess the response of riparian vegetation to alternative water management regimes.

As part of this research, digital cameras were evaluated for their ability to provide quantitative remote sensing data comparable to more costly professional-grade sensors. This comparison was performed due to the prolific use of digital cameras in quantitative remote sensing applications in recent years (Hunt et al., 2010; Jensen et al., 2007; Sakamoto et al., 2011; Zhang & Kovacs, 2012). Therefore, it is appropriate to assess the quality of the data obtained from these inexpensive sensors.

Using a digital camera imaging system mounted on a light aircraft, airborne imagery was acquired over riparian areas along the Oldman River in southern Alberta. Ground measurements of LAI for both the tree canopy and understory vegetation were acquired on dates contemporary with airborne image acquisition. Two methods were used to assess canopy LAI: measurements of optical light transmission, and litter fall traps. The litter trap data were used to evaluate the optical measurement accuracy. The understory LAI was measured using a destructive harvest method.

The airborne image data were calibrated into units of spectral reflectance, and the data was then assessed through comparison with other sensors. The first

comparison was performed using an ASD spectroradiometer, a terrestrial hyperspectral sensor. The second comparison was performed using satellite image data from the Landsat-8 OLI sensor. Both the ASD and Landsat data were acquired on the same dates or within a few days of the airborne image acquisition dates.

Spectral vegetation indices (SVIs) calculated from remote sensing data are highly correlated with vegetation biophysical parameters; consequently, SVIs are often used to empirically model LAI (Colombo et al., 2003; Gonsamo & Pellikka, 2012; Soudani et al., 2006; Turner et al., 1999). In this research, SVIs were calculated from the airborne reflectance data, and these were used along with the ground LAI data to create regression models for predicting LAI.

The ability of a given SVI to model biophysical parameters is variable depending on the vegetation type, site conditions, and parameter of interest (Broge & Leblanc, 2001). Due to this fact, it is common to test a variety of SVIs for their modelling performance (Baret & Guyot, 1991; Colombo et al., 2003; Elvidge & Chen, 1995; Haboudane et al., 2004). In this research, eight different SVIs were calculated and evaluated for their ability to predict LAI. The SVI that demonstrated the highest model fit was selected for the subsequent analysis of spatial resolution effects on the estimation of riparian LAI.

A common method for evaluating the effects of spatial resolution in remote sensing applications is to perform a sensitivity analysis, observing the changes in the quantity of interest as resolution changes (Chen, 1999; Friedl et al., 1995; Marceau & Hay, 1999; Teillet et al., 1997). In this study, airborne images were spatially resampled to a range of progressively coarser resolutions between 0.18 cm and 500 m. At each resampled resolution, the selected SVI was calculated and regressed against the ground-measured LAI data, and the differences between the regression models at

each resolution were compared. Using the regression models, LAI was calculated at every resolution using two methods: firstly, by using the different regression models derived at each resolution, and secondly, by using a single regression model to predict LAI at every resolution. For both methods, the changes in LAI prediction error as resolution coarsened were examined.

4.2 Methods

4.2.1 Study Area Description

This research was conducted on riparian cottonwood forests located along a stretch of the Oldman River in Southern Alberta (Figure 4.1). The Oldman River is a snowpack-fed river originating in the Rocky Mountains. The river flows east through the communities of Fort Macleod, Lethbridge, and Taber before joining with the Bow River near the hamlet of Grassy Lake to form the South Saskatchewan River, whose waters eventually discharge into the Hudson's Bay. The river is regulated via the Oldman Dam, built in 1992, whose reservoir provides a reliable source of water for municipalities as well as for agricultural irrigation.

The regional climate is classified as "cold semi-arid" (type BSk) according to the Köppen climate classification system. Cold semi-arid climates are characterized by cold dry winters and hot dry summers, with potential evapotranspiration exceeding precipitation for most of the year (Peel et al., 2007). From 1981 to 2010, the average temperatures within the city of Lethbridge ranged between 18.2 °C in July to -6.0 °C in January, with a mean annual temperature of 5.9°C (Environment Canada, 2013). For the same years, the average annual precipitation in Lethbridge was 380 millimeters, with more than half (212 mm) falling as rain during the spring and summer months between May and August (Environment Canada, 2013). June had by far the largest amount of precipitation on average with 82 mm, with the next highest

month being May at 49.9 mm. February had the lowest average precipitation (12 mm); however, both December and January have similarly low amounts (12.9 mm and 13.5 mm respectively) (Environment Canada, 2013).

Strong chinook winds occur frequently in the area. These winds originate from the Pacific Ocean and pass through the Rocky Mountains, losing their moisture along the way in the form of orographic precipitation (Alberta Agriculture and Forestry, 2003). As the winds descend from the mountains they warm rapidly due to the greater adiabatic lapse rate of dry air compared to moist air. The warm chinook winds helps to moderate winter temperatures, frequently causing temperature increases of 20°C or more (Alberta Agriculture and Forestry, 2003). Consequently, the Lethbridge area enjoys warmer winters on average than many other parts of the prairies. The dry winds rapidly absorb moisture from the air and soil, contributing to the aridity of the region.

Soils in the region are dominated by Dark Brown Chernozems, developed from well drained lacustrine and fluvial deposits as well as glacial till parent material (Agriculture and Agrifood Canada, 1980). The high organic content in these soils make them excellent for agricultural use (Clayton et al., 1977). Regosolic soils are also commonly found on the river floodplain, developed from fluvial sediments deposited by the river and by glacial meltwater (Agriculture and Agrifood Canada, 1980). These soils are poorly developed due to the instability of the floodplain (Clayton et al., 1977).

The average height of terrain between the Oldman Dam and Lethbridge is 960 m above sea level. Along this section of the river, the floodplain is entrenched in a deep valley which was carved by glacial floods during the Wisconsinan glaciation (Beaty, 1975). Consequently, the floodplain elevation is between 20 and 100 meters

lower than the surrounding terrain. The width of the riparian zone varies from 100 meters to more than 1 kilometer on either side of the river, with most riparian areas being between 200 and 500 meters wide.

While much of the land in the Lethbridge area has been converted for agricultural purposes, mixed grassland prairies formerly dominated the region (AMEC, 2009). Due to the regional aridity, native forests are only found on the river floodplain where there is sufficient moisture to support them (Gom & Rood, 1999). Cottonwood trees form the dominant vegetation type in the riparian zone, with three main species present, along with various hybrids between them. These species are plains cottonwood (*Populus deltoids*), narrowleaf cottonwood (*Populus augustifolia*), and balsam poplar (*Populus balsamafera*) (Gom & Rood, 1999). The stretch of the Oldman River from Fort Macleod to Taber is of unique ecological significance as it is considered to be the only area in the world where the ranges of these three cottonwood species naturally overlap to produce a trispecific hybrid swarm (Floate, 2004; Rood et al., 1986).

Data for this study were collected in the Helen Schuler Nature Centre park located within the city of Lethbridge (49°42'4"N, 112°51'47"W; Figure 4.2). This site was selected as it is a representative riparian area in terms of its vegetation composition and size. Both airborne imagery and ground data were acquired at the Helen Schuler site (hereafter referred to as the HSNC site) on multiple dates from May to October, 2014, providing data from the green-up to the senescence of the trees.

Data were also acquired along an extended section of the river from the Oldman Dam (49°33'14"N, 113°51'18"W) to a location called Pearce Corner located north-west of Lethbridge (49°51'6.5"N, 113°15'9"W), covering approximately 100

kilometers of the river's course (Figure 4.3). Airborne imagery was acquired once along this stretch of the river (hereafter referred to as the River Transect site) in July, 2014 under peak LAI conditions. Note that no ground data were acquired within the River Transect site.

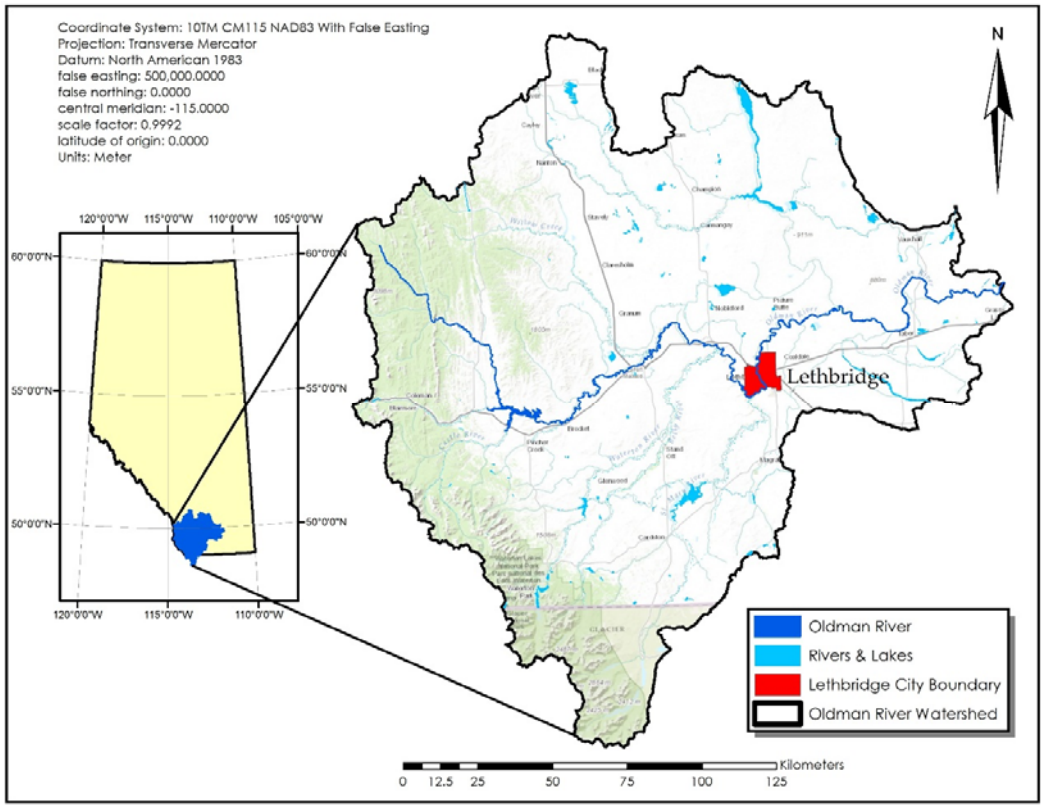

Figure 4.1 – Map of the Oldman River watershed.

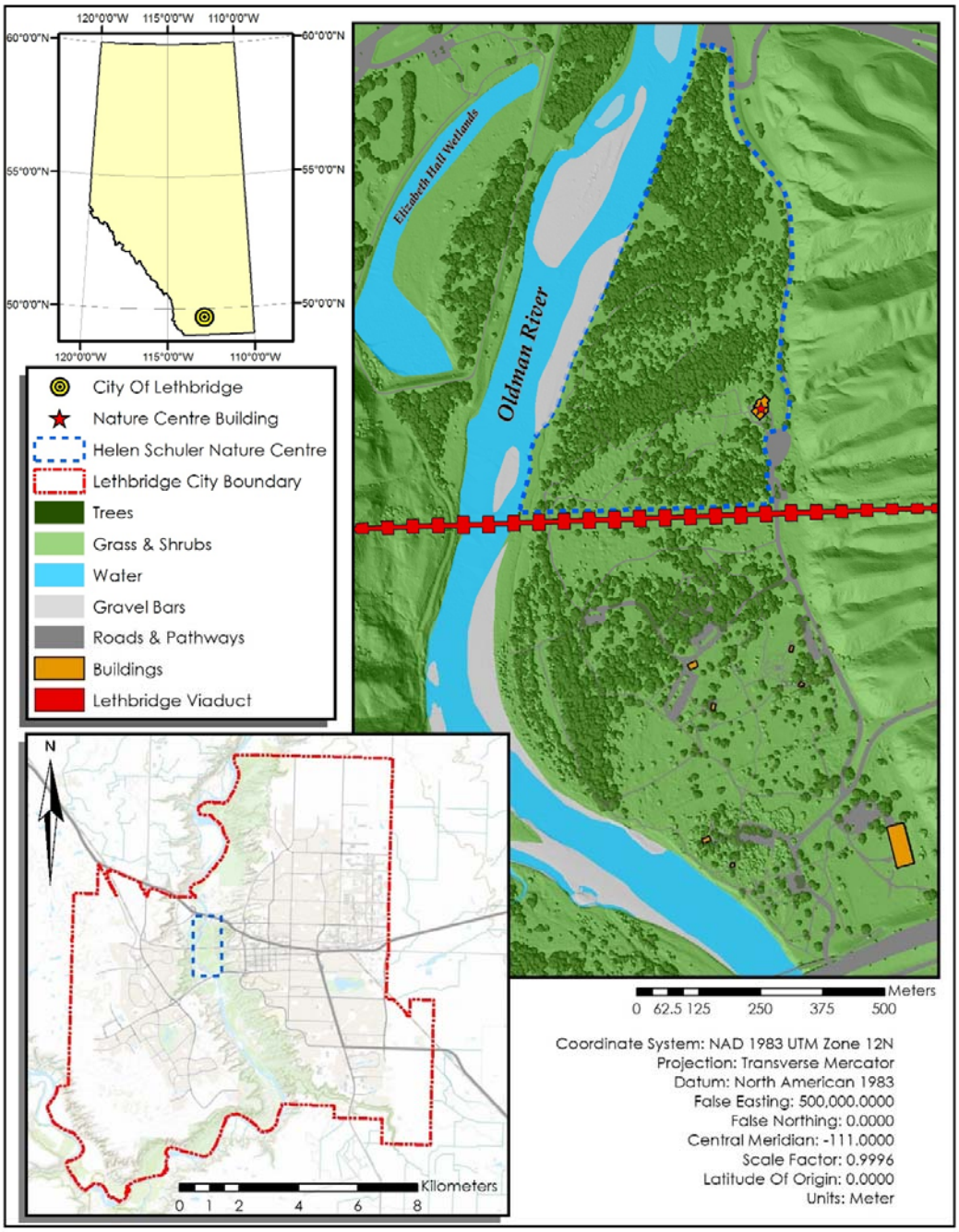

Figure 4.2 - Study area map of the Helen Schuler Nature Centre (HSNC) site within the city of Lethbridge, Alberta.

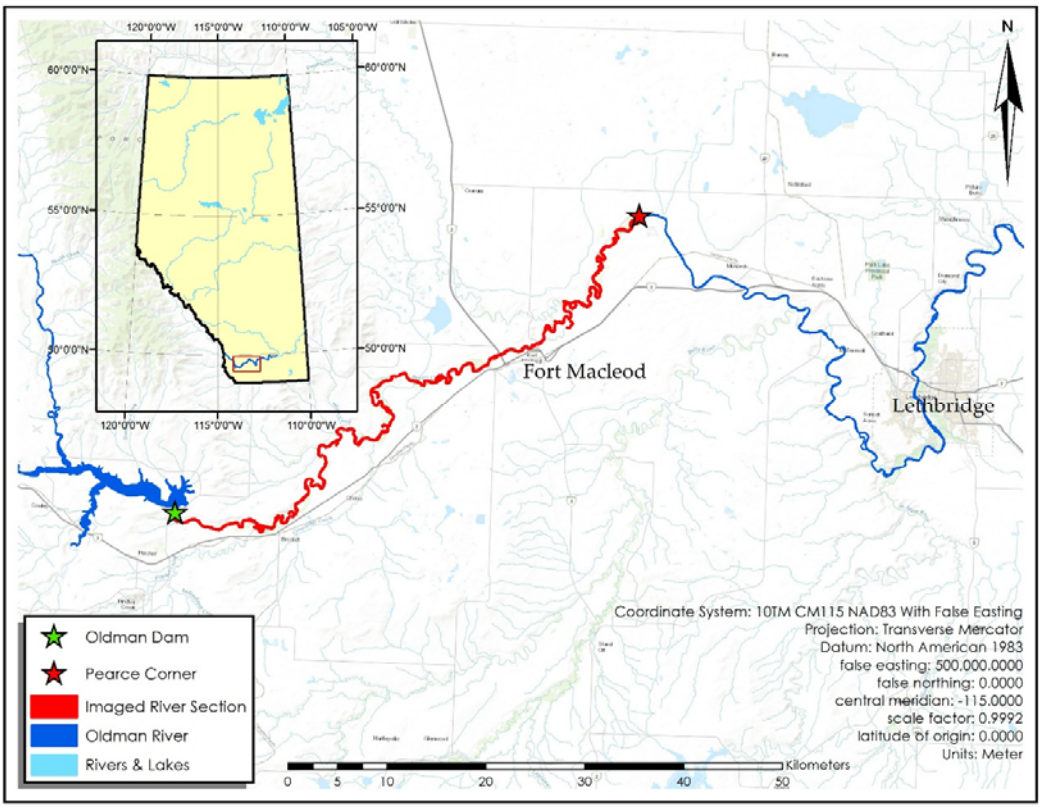

Figure 4.3 – Study area map of the River Transect site.The imaged section of the river is shown in red between the Oldman Dam and Pearce Corner.

4.2.2 Data Acquisition

Ground data collected at the HSNC site included optical measurements of canopy LAI, destructive sampling of understory LAI, and spectral reflectance measurements of natural and man-made objects. Litter traps were also deployed to provide a second measure of the tree canopy LAI. Airborne imagery was acquired over both the HSNC and the River Transect sites using a digital camera system mounted onboard a small single-engine aircraft. Landsat-8 satellite images were also obtained over both sites from the United States Geological Survey (USGS). Table 4.1 summarizes the types of data collected, the number of acquisitions, and the dates on which they were collected.

Table 4.1 – Summary table of data acquired and acquisition dates.

Data Type	Number of Acquisitions	Acquisition Date(s)
LAI-2000 measurements	7	May 22, Jun 07, Jul 11, Jul 31, Aug 26, Oct 05, Nov 03
TRAC measurements	3	Jul 31, Aug 26, Sept 17
Understory LAI harvests	6	May 20, Jun 06, Jul 10, Jul 21, Aug 25, Oct 07
Litter trap collections	3	Sept 26, Oct 07, Oct 21
ASD spectral measurements	6	May 21, June 04, July 09, Aug 04, Aug 26, Oct 05
Airborne imagery (HSNC site)	6	May 22, Jun 07, Jul 09, Aug 01, Aug 27, Oct 05
Airborne imagery (River Transect site)	1	Jul 29
Landsat-8 imagery (HSNC site)	3	Jul 12, Aug 04, Oct 05
Landsat-8 imagery (River Transect site)	1	Jul 26

4.2.2.1 Ground Data Collection

4.2.2.1.1 Optical LAI Measurements

Optical measurements of tree canopy LAI were acquired using two intercalibrated LAI-2000 Plant Canopy Analyzers (Li-COR, Inc., Lincoln, NE, USA). One LAI-2000 was placed in a large forest clearing and programmed to measure "above canopy" radiation at 30 second intervals, while the second instrument was used to sample below canopy radiation (Figure 4.4). Below canopy measurements were taken along 5 transects running from south-east to north-west, with 62 individual sample locations in total (Figure 4.5). All measurements were taken while facing north-west, and a 90° view cap was attached to each instrument to limit the field-of-view to this direction as well as to remove the possibility of shading of the instrument

by the operator. Measurements were taken at sunrise or sunset in order to provide the diffuse, indirect illumination conditions required for optimal measurement accuracy (Li-Cor, 1992).

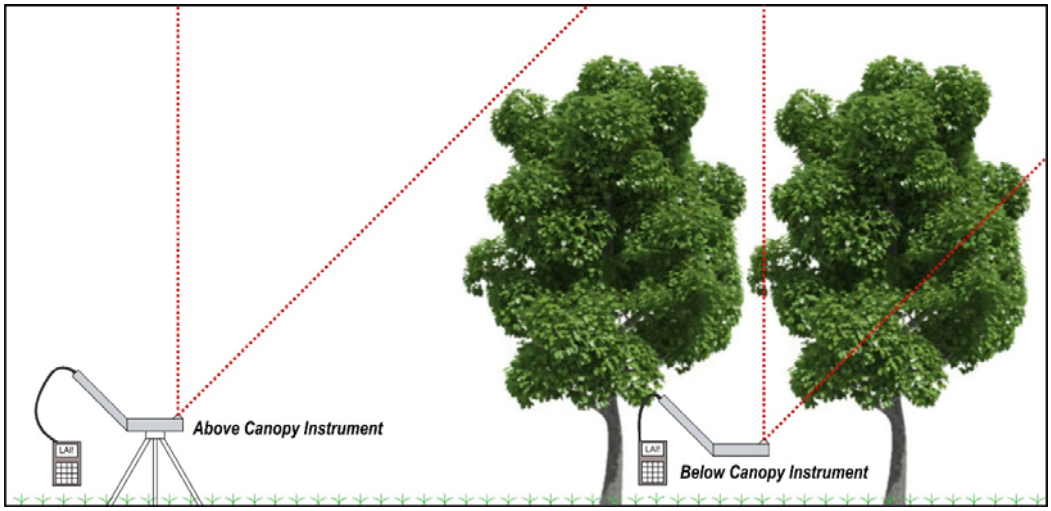

Figure 4.4 – Illustration of LAI-2000 field deployment.

LAI-2000 measurements were acquired on 6 dates from late May to early October, 2014 (Table 4.1). As the LAI-2000 does not distinguish between leaves and other canopy elements (branches and stems), the measured quantity is often referred to as "Plant Area Index" (PAI) to distinguish it from LAI (Jonckheere et al., 2004). To remove the contribution of non-leaf canopy elements, a final set of measurements were acquired in late October when the trees were fully defoliated. These measurements were used to determine the woody-to-total area ratio, which is used to calculate LAI from the PAI measurements taken during the growing season.

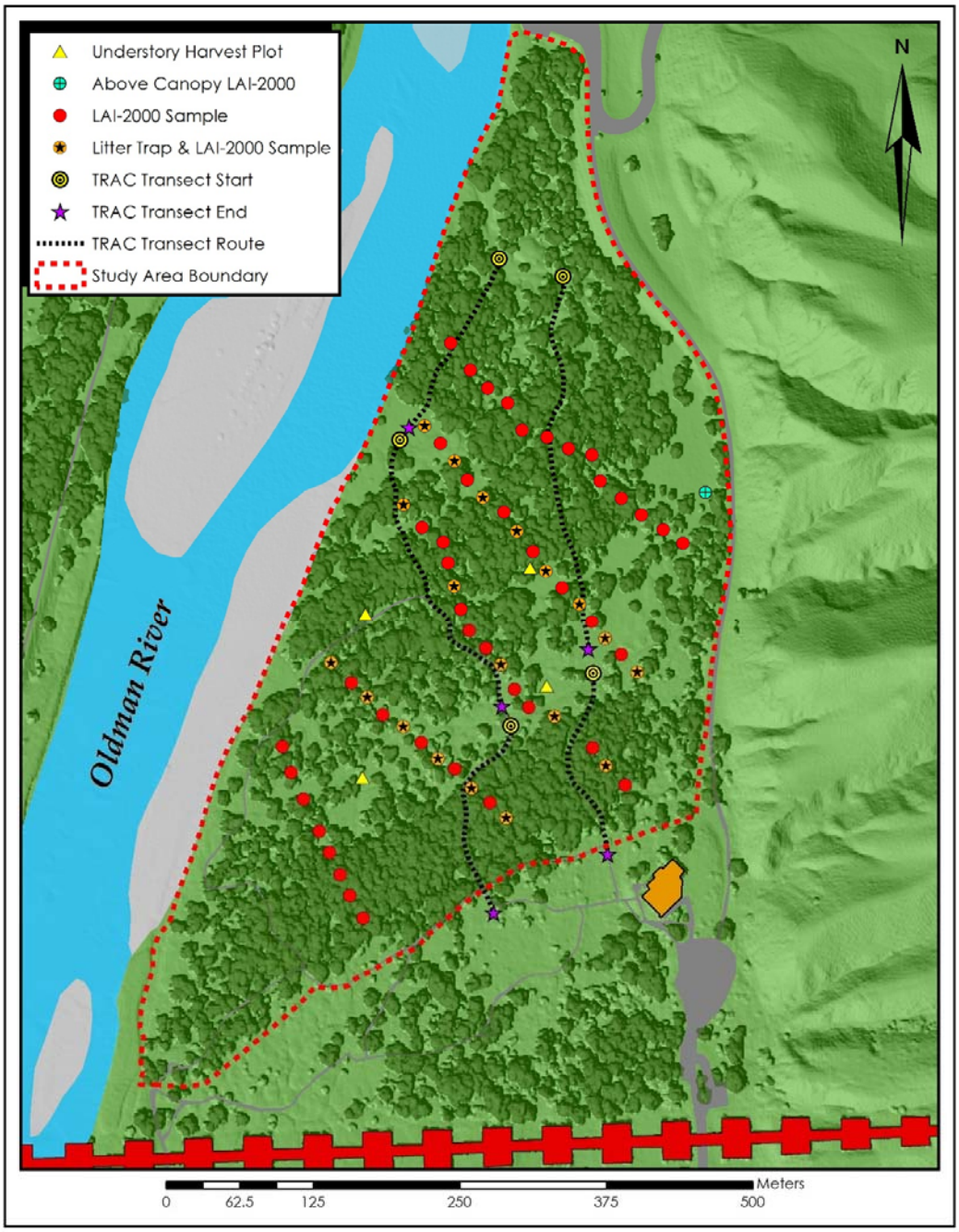

Figure 4.5 – Ground data acquisition map for the HSNC site.

The LAI-2000 calculation of LAI is based on the assumption of a random distribution for leaves in the canopy. As no vegetated canopy is truly random, the LAI-2000 has been found to often underestimate LAI (Cutini et al., 1998; Deblonde et al., 1994; Smith et al., 1993). To correct the LAI-2000 estimates, a correction factor called the clumping index was used. This index quantifies foliage clumping within the

canopy. A Tracing Radiation and Architecture of Canopies (TRAC, 3rd Wave Engineering, Ottawa, ON, CA) instrument was used to obtain the clumping index.

It was originally planned to acquire TRAC measurements along the 5 transects used for LAI-2000 measurements; however, this plan proved impractical as dense understory vegetation made maintaining the steady walking pace necessary for TRAC operation impossible. Consequently, TRAC measurements were conducted by walking the instrument at a slow, steady pace along a set of five different transects oriented approximately north to south through the HSNC site (Figure 4.5). The transects varied in length from 150 m to 300 m, and made use of walking paths and trails within the site.

TRAC measurements were taken on clear sunny days either in the late morning or early evening within the recommended solar zenith angle range of 30° to 60° (Leblanc et al., 2002). Data were acquired on the same date as LAI-2000 measurements. Unfortunately, only three dates of TRAC data were acquired, and one measurement (in September) did not correspond with a set of LAI-2000 measurements (Table 4.1).

4.2.2.1.2 Understory Harvest LAI

The understory LAI characterization in this thesis was carried out in Orchard (2015). A destructive harvest method was used to characterize the understory LAI. Four 1m² sample plots were selected within the HSNC site (Figure 4.5). At each sample plot all vegetation was clipped down to the soil and collected within a 20 cm x 50 cm frame. Vegetation was harvested on dates as close as possible to those of the LAI-2000 measurements (Table 4.1), with a new 20 cm x 50 cm portion within the 1m² plots being selected each time to avoid repeated sampling of the same areas. Note

that one harvest date was separated from its corresponding LAI-2000 capture date by 10 days (July 21 for understory harvest vs July 31 for the LAI-2000).

4.2.2.1.3 Litter Trap LAI

Litter traps were deployed throughout the HSNC site at the beginning of fall in order to characterize the peak canopy LAI and to validate the optical LAI data. These traps were made from two different kinds of laundry basket with ground footprints of 0.195 m^2 and 0.213 m^2, respectively. Holes were drilled in the bottom of the traps to allow drainage and a brick was placed inside each to prevent wind movement. A total of 19 litter traps were placed at regular intervals throughout the site (Figure 4.5). The selected locations corresponded with optical LAI sampling points. Leaf litter fall was collected from the traps every two weeks from mid-September until late October when the trees were completely senesced (Table 4.1).

4.2.2.1.4 Spectral Reflectance

Measurements of spectral reflectance were acquired using an ASD Fieldspec-3 spectroradiometer (ASD Inc., Boulder, CO, USA). These measurements were taken within the HSNC site concurrently or within a few days of airborne imaging (Table 4.1). A Spectralon reflectance panel was used as a white reflectance standard for calculating target reflectance. The instrument was set to average 20 spectral samples for each measurement in order to reduce noise, with 10 measurements in total being acquired from each target. Targets measured included asphalt, soil, grass, cottonwood trees, and two felt-topped tables placed within the site for airborne image reflectance calibration (Figure 4.6).

As it was infeasible to measure the cottonwood canopy from above, branches were clipped from the trees and placed on top of the black felt table, being arranged in an optically thick stack ensuring that only plant materials were measured by the ASD.

This method is considered reasonable for assessing the spectral characteristics of a vegetated canopy; however, it does cause significant changes to the orientation and arrangement of the plants compared to measuring them in situ, which can result in alterations to their spectral responses (Goward et al., 1994; Peddle & Smith, 2005).

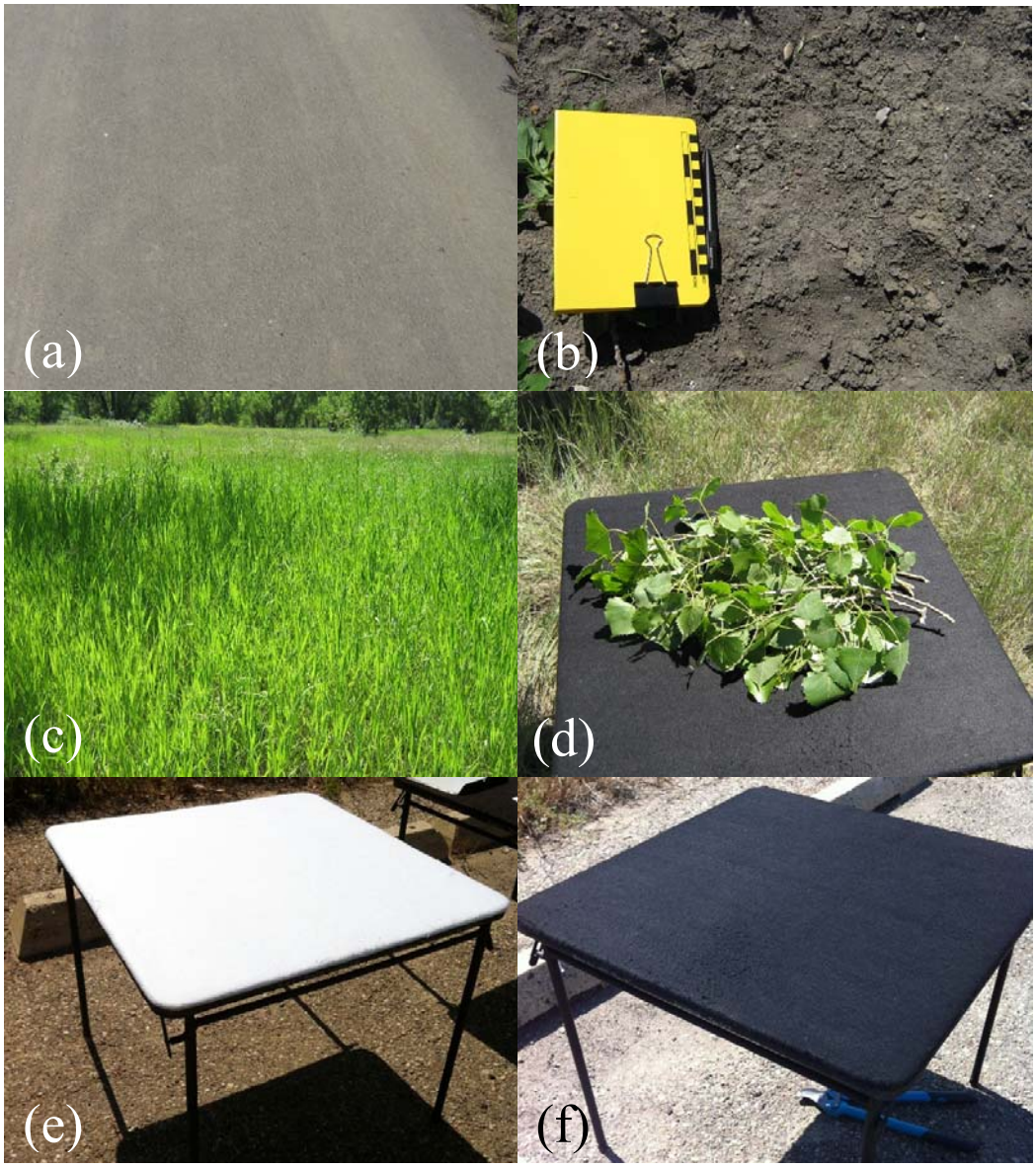

Figure 4.6 – Images of spectral reflectance targets measured with the ASD. Targets shown are: (a) asphalt, (b) soil, (c) grass, (d) cottonwood leaves (in optically thick stack), (e) white felt calibration table, and (f) black felt calibration table.

4.2.2.2 Remote Sensing Data Collection

The airborne imagery used in this research was obtained using two Canon Powershot S50 digital cameras (Canon, Inc., Tokyo, Japan). One camera was used to image in the visible red, green, and blue portions of the spectrum (hereafter called the RGB camera), while the second was modified to image in the near infrared portion of the spectrum (hereafter called the NIR camera).

Both cameras were attached in sequence to a custom camera mount (Figure 4.7) which was mounted out the window of a Cessna 172 aircraft. Both cameras were triggered simultaneously to capture a matching RGB and NIR image at each imaging location. All images were acquired using fixed camera settings to ensure data consistency.

Imagery was acquired over the HSNC site at 600 m above ground, resulting in a GSD of 18 cm. Two passes were used to cover the site, with approximately 50 % end-lap and side-lap between images. Two 1 m x 1 m felt-topped tables (one black, one white) were positioned in a clearing during the imaging overflights for use as reflectance calibration targets (Figure 4.6 e & f). Six dates of imagery were obtained over the HSNC site (Table 4.1).

Imagery of the River Transect site was captured once at mid-summer (Table 4.1). The images were taken at a constant altitude of 2750 m above sea level, or an average of 1800 m above the terrain. Due to differences in the terrain height, the GSD of the images varied between 80 cm and 1.2 m. 50 % end-lap between images was used with no side-lap as a single pass was used to cover the entire floodplain.

Satellite images were obtained from the Landsat-8 Operational Land Imager (OLI) sensor through the USGS data portal (http://earthexplorer.usgs.gov/). Images were selected on dates as close as possible to those of airborne image acquisition

(within 3 days). This resulted in a total of three images over the HSNC site and 1 image of the River Transect site (Table 4.1).

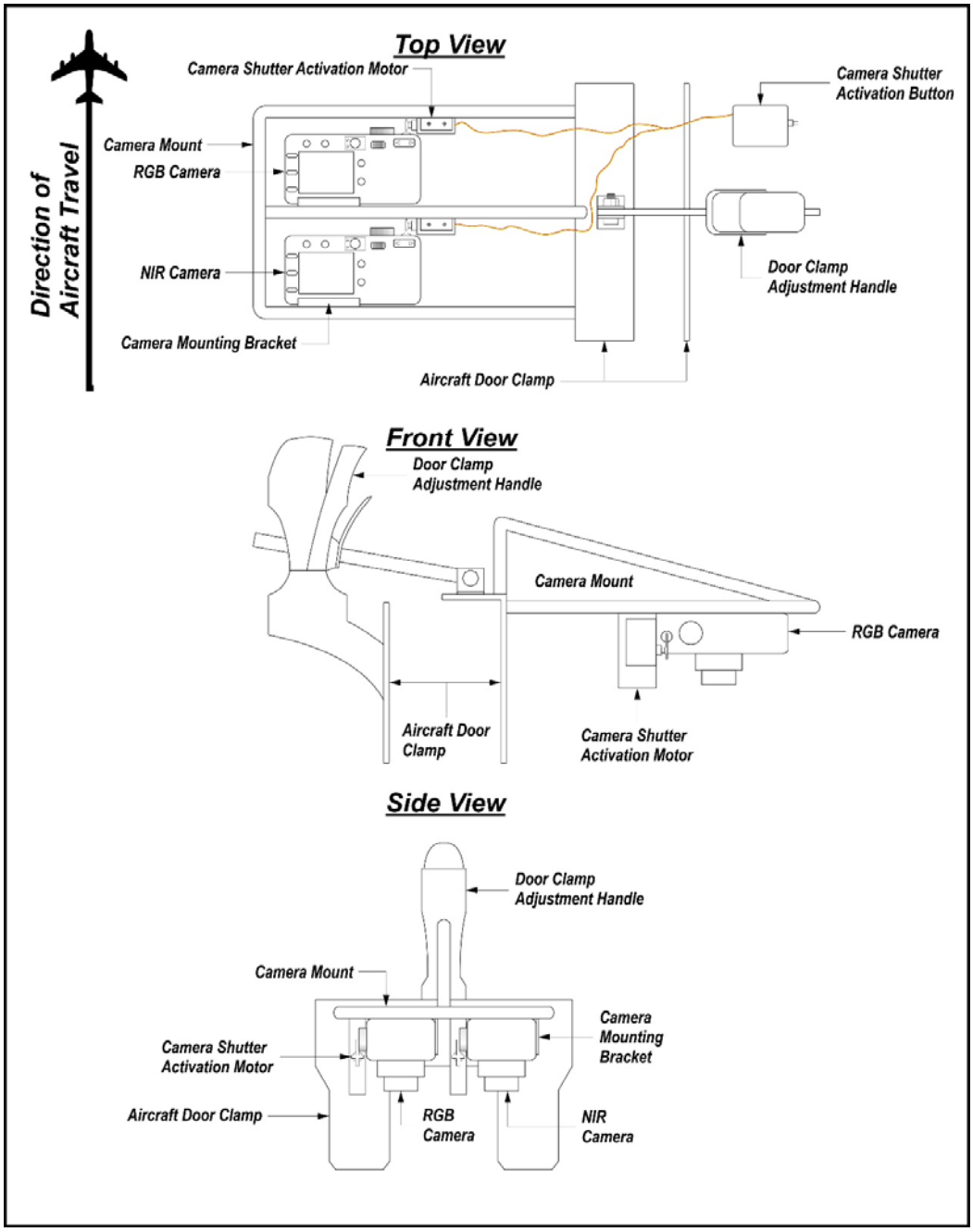

Figure 4.7 – Camera mount diagram.

4.2.3 Data Processing

4.2.3.1 Ground Data

4.2.3.1.1 Optical LAI Measurements

Each measurement from the below-canopy LAI-2000 was combined with the closest temporal measurement from the above-canopy instrument. The combined files were then used to calculate the average site PAI using the FV2000 (Li-COR, Inc., Lincoln, NE, USA) processing software. Only data from the first four sensor rings were used to calculate PAI, as the 5th sensor ring has been found to contribute to errors in the calculation (Cutini et al., 1998; Leblanc & Chen, 2001). The clumping index was calculated from the TRAC data using the TRACWin (3rd Wave Engineering, Ottawa, ON, CA) processing software. The clumping indices calculated from the three acquisition dates were averaged to obtain a seasonal-averaged clumping index. LAI was calculated from PAI as follows (Chen et al., 2006):

$$LAI = [(1 - \alpha) * PAI * \gamma]/\Omega \quad (4.1)$$

where Ω is the seasonal-average clumping index, γ is the needle-to-shoot-area ratio (equal to 1 in deciduous forests), and α is the woody-to-total area ratio, which is calculated as follows (Serbin et al., 2013):

$$\alpha = PAI_0/[PAI_1 * (\gamma/\Omega)] \quad (4.2)$$

where PAI_0 is the PAI value for the tree branches and stems measured under fully senesced conditions in late October, and PAI_1 is the PAI from the date for which the LAI is being calculated.

4.2.3.1.2 Understory Harvest LAI

Understory harvest data were processed in Orchard (2015). The collections from each quadrat were sorted to remove dead material, with the remaining green biomass being weighed. The LAI of the green biomass was then measured using an

LI-3100C Leaf Area Meter (Li-Cor Inc., Lincoln, NE, USA). This procedure was repeated with each harvest sample for half the growing season until the peak biomass was observed. Based on the data from the first half of the season, a regression equation was created to relate green biomass to measured LAI. The regression model was derived from 16 samples, with a coefficient of determination (R^2) of 0.96. The regression model was as follows:

$$LAI = 0.004 * biomass + 0.14 \quad (4.3)$$

This equation was then used to calculate understory LAI for the remaining harvests for the second half of the growing season. The calculated LAI was averaged for the entire site for each measurement date.

4.2.3.1.3 Calculation of Total Site LAI

The total LAI for the site on each measurement date was estimated by adding together the average tree canopy LAI determined through optical measurements with the average understory LAI determined through destructive harvest.

4.2.3.1.4 Litter Trap LAI

The leaf fall collected from the litter traps was sorted into three categories: plains cottonwood, narrowleaf cottonwood, and understory shrub leaves. Balsam poplar leaves, where present, were grouped with the plains cottonwood leaves, as their similar leaf shapes made them difficult to separate. Cottonwood hybrid leaves were grouped with either the plains or narrowleaf categories based on the similarity of leaf shape. The sorted leaves were then dried and weighed.

In order to calculate LAI from the dried leaf mass, the specific leaf area (SLA) – the average leaf area per unit mass – had to be determined for each leaf type. To determine the SLA, a separate collection of leaves of each type were gathered in

September, with the average leaf area being measured for each. The leaves were then dried and weighed, and the average leaf area per unit mass was calculated.

The total cottonwood leaf area for each litter trap was calculated first by multiplying the dry biomass weight of the plains and narrowleaf cottonwood groups by their respective SLA values, then by adding the resultant leaf areas together. The LAI for each trap was calculated by dividing the total leaf area by the area of the traps. The LAI for all the litter traps was then averaged to estimate LAI for the entire HSNC site.

4.2.3.1.5 Spectral Reflectance

The 10 spectral reflectance measurements for each target were averaged to create a representative spectral signature for each. The averaged spectral signatures were then converted to spectral library files in the image processing software ENVI (Version 5.1, Exelis VIS, Boulder, CO, USA). To allow comparison with the airborne image data, the hyperspectral spectral libraries were spectrally resampled to match the multispectral band profiles of the airborne digital cameras, measured in Chapter 3.

4.2.3.2 Remote Sensing Data

The Landsat-8 OLI images were already geo-registered, atmospherically corrected and calibrated to reflectance. Thus, no further processing of the satellite imagery was undertaken. For the airborne imagery, a number of pre-processing steps were necessary, which are summarized in Figure 4.8:

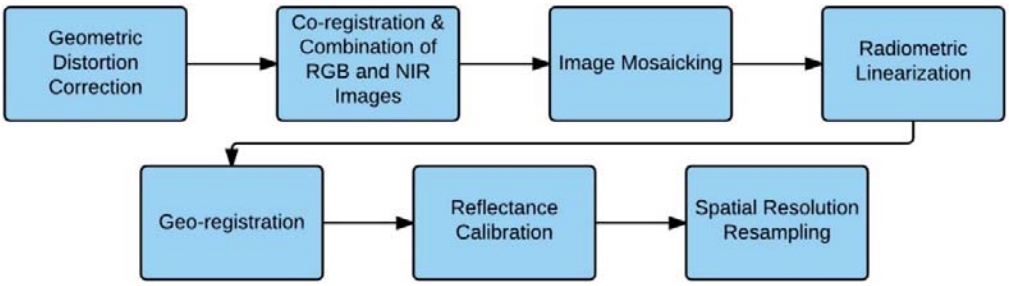

Figure 4.8 – Airborne image pre-processing workflow.

Geometric distortions were corrected for each camera image using the distortion models developed in Chapter 3. To combine each matching set of NIR and RGB images to each other, a semi-automated method was implemented based on the Scale Invariant Feature Transform (SIFT) algorithm (Lowe, 2004). A modified version of the SIFT code (available from http://www.cs.ubc.ca/~lowe/keypoints/) was used in Matlab (Version R2012a, MathWorks Inc., Natick, MA) to automatically match key points between the sets of images. These points were recorded in text files and used as ground control points (GCPs) in ENVI, where an image-to-image registration was performed to warp the NIR image to match the RGB image.

Next, the warped NIR and the RGB image were overlaid, aligned, and cropped to their common area in Adobe Photoshop (Version CS3, Adobe Systems Inc., San Jose, CA, USA). Finally, in Photoshop the red band from the NIR image was combined with the red and green bands from the RGB image to create a false-colour infrared composite image. When all the images from a given date had been combined, they were then mosaicked together using the Microsoft Image Compositing Editor (Microsoft, Redmond, WA, USA) program to create an image mosaic of the entire study site. For the River Transect site, the site was split into several mosaics due to variations in spatial resolution.

In Chapter 3 it was determined that the digital cameras used in this research had a non-linear response to changes in light intensity. Consequently, it was necessary to convert the DNs of the image mosaics to linearized values. This was done using the lookup table approach developed in Chapter 3, converting the DNs for each pixel to a corresponding linear value between 0 and 1.

In the next step the image mosaics were geo-registered. Geo-registration was performed in ENVI by manual selection of identifiable GCPs between the photo-

mosaics and geo-registered orthophotos taken over the HSNC and River Transect sites. Following geo-registration the River Transect image mosaics were combined and resampled to a nominal GSD of 1 m.

In the next step the geo-registered images were calibrated to units of spectral reflectance. The empirical line calibration method was performed using two reference targets. For the HSNC images, the two felt-topped tables were used as high and low reflectance targets. The average value for the pixels in the centre of each table was matched to the corresponding table reflectance value measured by the ASD, and the calibration was then performed in ENVI. For the River Transect site there were no calibration targets present, necessitating the use of objects occurring within the image. A portion of deep river water and a large gravel bar were selected as the low and high reflectance calibration targets, respectively (Figure 4.9). The reflectances of these targets were determined from the contemporary Landsat image over the site.

In the last processing step, the image mosaics were spatially resampled to simulate a range of spatial resolutions from 1 m to 500 m. This process was performed in two steps: point spread function (PSF) simulation and spatial resampling. The PSF was simulated in order to more accurately model the optical performance of lower resolution sensors. Without this step, all the high-resolution pixels contained within a low resolution pixel would equally contribute to the low-resolution pixel value. This is not physically valid, because with real sensors the EMR from the centre of the pixel contributes more greatly than the EMR from the periphery, and EMR from outside the pixel also contributes to the measured spectral signal (Pryor, 2012).

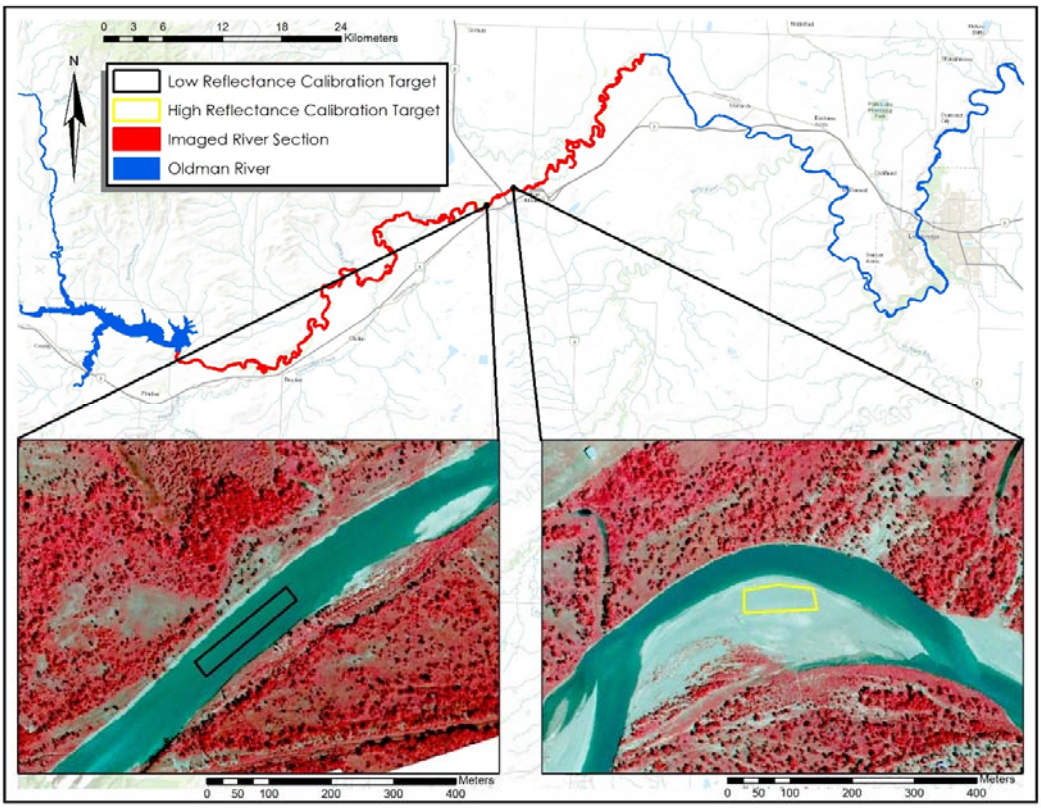

Figure 4.9 – Map of the River Transect site showing locations of bright and dark reflectance calibration targets.

To simulate the PSF, a Gaussian low-pass filter was applied to the original high resolution images in ENVI. The filter uses a moving window to pass over the image, changing each pixel value to a weighted average of its surrounding pixel values. This filter places a lower weight on pixels further from the centre of the filter. For example, if a 21 pixel x 21 pixel filter were used, a pixel located 11 pixels away from the central pixel would contribute only 50 % as much to the weighted average value as a pixel that was located immediately adjacent to the central pixel. The size of the filter was set to be approximately twice the size of the desired spatial resolution, making the spatial full-width-at-half-maximum (FWHM) of the filter roughly equal to the spatial resolution.

For the second step of the spatial convolution, the filtered image was resampled to the desired resolution using nearest-neighbour resampling. This assigned

each resampled low resolution pixel the value of the high resolution pixel closest to its centre, whose value was an area-weighed composite of the surrounding high resolution pixels. This method simulates an image derived from a sensor with a Gaussian spatial sensitivity function, which is considered a good approximation of a typical sensor PSF (Kavzoglu, 2004; Pryor, 2012).

Figure 4.10 illustrates the process. Table 4.2 lists the different resampled resolutions used in this study, along with the filter sizes used during image resampling. Note that due to the very large size of the filters it was too computationally intensive to create filtered images from the 18-cm HSNC data for each resolution. Instead, the 18-cm images were filtered and resampled to a 1-m resolution, and the 1 m images were used to simulate all other spatial resolutions.

Table 4.2 – Table of resampled image spatial resolutions along with the filter sizes used for image resampling.Note that for the HSNC site, the original 18-cm imagery was only used to resample to the 1-m spatial resolution.

Image Spatial Resolution (metres)	Gaussian Low-pass Filter Size (pixels)
1	7 x 7
2	5 x 5
5	11 x 11
10	21 x 21
15	31 x 31
20	41 x 41
30	61 x 61
40	81 x 81
50	101 x 101
60	121 x 121
70	141 x 141
80	161 x 161
90	181 x 181
100	201 x 201
125	251 x 251
150	301 x 301
175	351 x 351
200	401 x 401
350	701 x 701
400	801 x 801
450	901 x 901
500	1001 x 1001

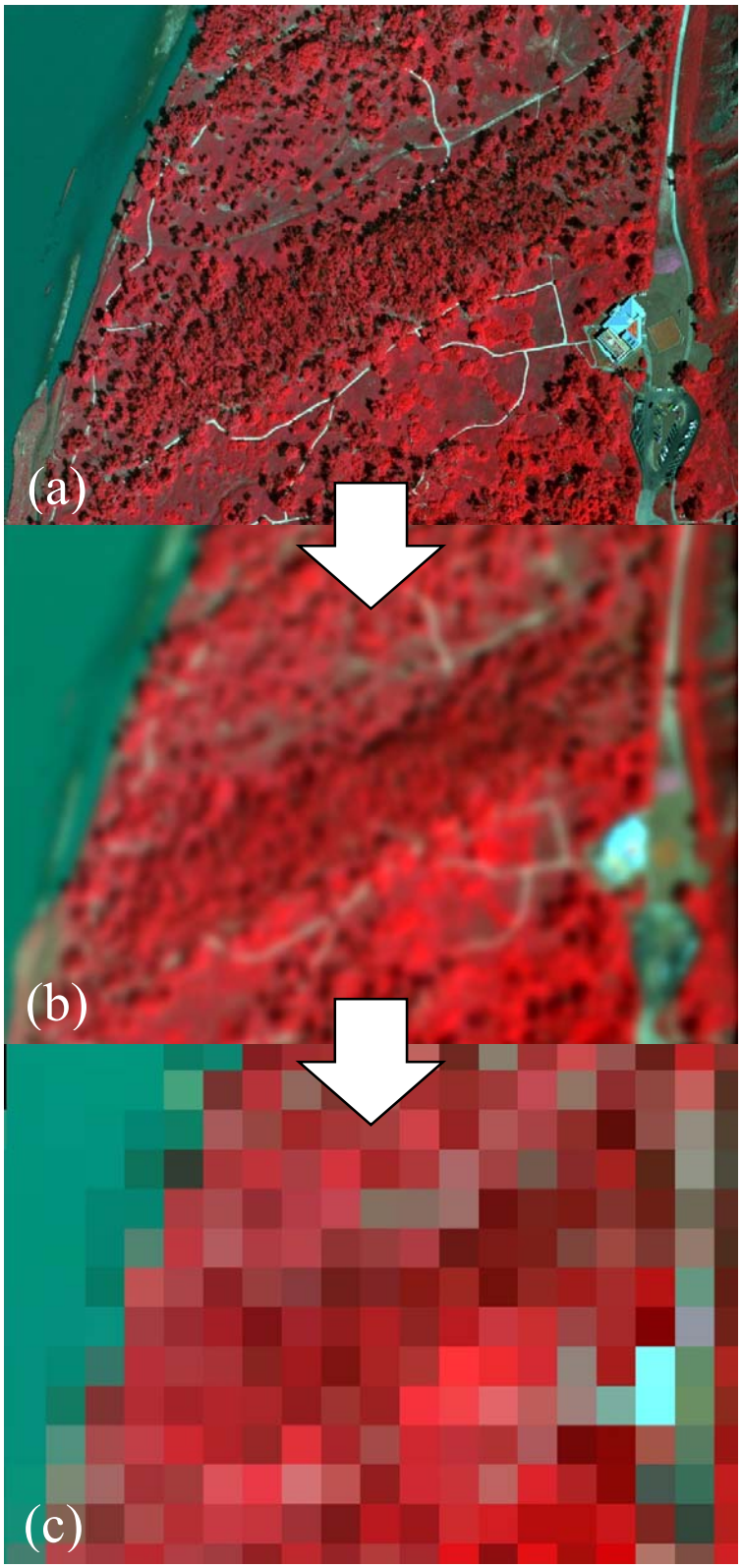

Figure 4.10 – Example of spatial resolution resampling. (a) shows a 1 m resolution image, (b) shows the original image with a 61 pixel x 61 pixel low-pass Gaussian filter applied, and (c) shows the filtered image resampled to a 30 m resolution.

4.2.4 Data Validation

4.2.4.1 Optical LAI

The optical LAI estimate for the peak canopy LAI calculated from Equation 4.1 was checked for accuracy through comparison with the LAI estimated from the litter fall traps. Only the peak optical LAI value could be compared with the litter traps, as the traps are only able to estimate the maximum canopy LAI.

The two mean LAI values were tested for a statistically significant difference using a two-sample Student's T-test as follows:

$$T = \frac{\overline{LAI}_1 - \overline{LAI}_2}{\sqrt{\frac{S_p^2}{N_1} + \frac{S_p^2}{N_2}}} \tag{4.4}$$

where $\overline{LAI}_1$ and $\overline{LAI}_2$ are the two mean LAI values, N_1 and N_2 are the sample sizes for each, and S_p is the pooled standard deviation, calculated as follows:

$$S_p = \sqrt{\frac{(N_1 - 1)S_1^2 + (N_2 - 1)S_2^2}{N_1 + N_2 - 2}} \tag{4.5}$$

where S_1 and S_2 are the respective sample standard deviations. The degrees of freedom used for the T-test were equal to $N_1 + N_2 - 2$. Significant difference was tested at both 90 % and 95 % confidence intervals.

The Student's T-test assumes equal variance for the populations the samples are taken from. This assumption was tested using an F-test as follows:

$$F = \frac{S_1^2}{S_2^2} \tag{4.6}$$

The F-test resulted in a value of 0.908 (p = 0.62). Based on this test, the variances were not significantly different, and the assumption of equal variances was accepted.

4.2.4.2 Airborne Image Reflectance

The accuracy of the airborne image reflectance calibration over the HSNC site was assessed through comparisons with both the ASD and Landsat-8 OLI data. For the ASD comparison, areas in the image corresponding to the ASD-measured targets were outlined, and pixels within each target type were randomly selected. The reflectances of the pixels for each target were then averaged, and these values were compared with the ASD-derived reflectances for each target type. To quantify the difference between ASD and airborne reflectance, the root-mean-square error (RMSE) was calculated as follows:

$$RMSE = \sqrt{\frac{1}{N}\sum_{i=1}^{N}(ASD(i) - IMG(i))^2} \tag{4.7}$$

where N is the number of reflectance values being compared, ASD(i) is the i^{th} ASD reflectance value, and IMG(i) is the i^{th} airborne image reflectance value.

RMSE was calculated for each band separately as well as for all bands together. Per-band and overall RMSE was calculated for each target separately, for each image date, and for all dates and targets. The two sets of reflectances were also regressed against each other in SPSS Statistics (Version 22, IBM Corporation, Armonk, NY, USA). In SPSS the R^2 was calculated, and the slope and intercept of the relationship was examined for statistical difference from a linear one-to-one relationship (slope = 1, intercept = 0) using the 95 % confidence intervals calculated for each parameter.

To facilitate the comparison with the Landsat-8 OLI imagery, the airborne images were spatially resampled to match the 30-m spatial resolution of the OLI sensor using the procedure outlined in Section 4.2.3.2. During the spatial resampling

procedure the 30-m pixels between the two sensors were properly aligned by manually adjusting the location of the airborne images to match the OLI images.

Unlike the ASD data, it was not possible to spectrally resample the OLI data, because it is a multispectral sensor with broad, non-contiguous bands. Thus, there were differences between the spectral characteristics of the two sensors which were unavoidable. Figure 4.11 shows the spectral band profiles for the digital camera bands and the Landsat-8 OLI bands used in the comparison. Table 4.3 lists the peak wavelengths and FWHM for the bands of the two sensors. As seen in the figure and table, the OLI red and green bands were not aligned with the camera bands, with their peaks shifted toward longer wavelengths. Both the red and green bands for the OLI sensor were also narrower than the camera bands. The peak for the OLI NIR band aligned almost perfectly with the camera NIR peak, but its bandwidth was much narrower.

To perform the comparison, areas were outlined over different targets which included vegetation, water, man-made features (roads, parking lots, buildings), and gravel bars. A random sample of pixels was selected from each area and the reflectance for each corresponding Landsat and airborne pixel was recorded. As with the ASD comparison, the RMSE of the difference in reflectance was calculated. RMSE was calculated for each band and overall. These RMSE values were separated by target type and image date, as well as being calculated for all image dates and targets overall. As before, the reflectances were also regressed against each other and the R^2 was examined, along with the slope and intercept being tested for statistical difference from a perfect one-to-one relationship.

Because there were no ASD measurements available for the River Transect site, the airborne reflectance was validated using Landsat-8 imagery only. The procedure used was identical to that used for the HSNC site.

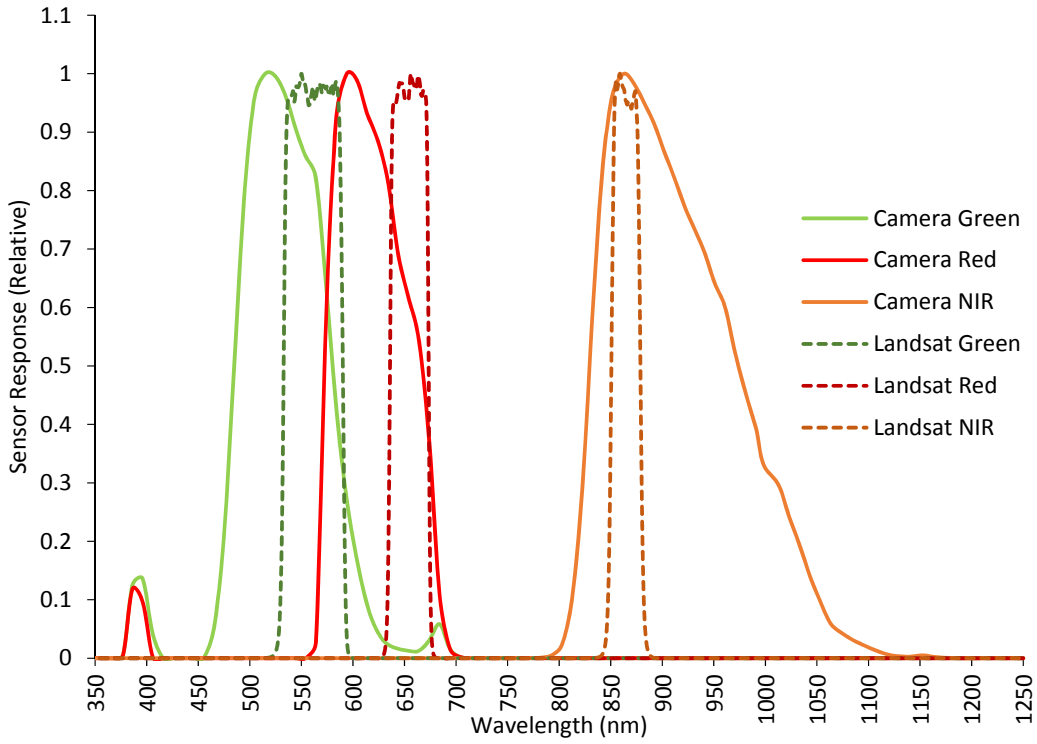

Figure 4.11 – Spectral band profiles of the digital cameras used in this research and the equivalent Landsat-8 OLI bands.

Table 4.3 – Peak wavelengths and FWHM for the digital cameras and Landsat-8 OLI spectral bands.

Band Characteristic	Digital Camera	Landsat-8 OLI
Green band peak wavelength (nm)	515	561
Green band FWHM (nm)	95	57
Red band peak wavelength (nm)	600	655
Red band FWHM (nm)	90	37
NIR band peak wavelength (nm)	865	865
NIR band FWHM (nm)	130	28

4.2.4.3 LAI-SVI Regression Modelling

To assess the ability to predict riparian LAI using airborne reflectance data, regression models were created between image reflectance and total study site LAI (understory plus canopy). The average reflectance within the HSNC site was calculated within the study area boundary for each image date using the original, highest spatial resolution imagery. These averaged reflectance values were then used to calculate a variety of SVIs.

SVIs were selected which have been previously used in the LAI modelling literature (e.g., Chen, 1996; Colombo et al., 2003; Gonsamo & Pellikka, 2012; Haboudane et al., 2004). SVIs were also selected based on the feasibility of their calculation, and if they were not functionally equivalent to each other. An SVI was feasible if it only required data from the red, green, and/or near-infrared portions of the spectrum and did not require any additional data. SVIs were considered to be functionally equivalent if they provided the same information content, and it was possible to easily convert from one to another using a linear transformation (Perry & Lautenschlager, 1984). Table 4.4 provides a list of the vegetation indices used in the regression analysis, along with their mathematical formulas.

Each of the SVIs was calculated for each image and regressed against the total study site LAI, and the resulting models were observed. The SVI that demonstrated the highest R^2 value was selected for the subsequent analysis of spatial resolution impacts on riparian LAI modelling.

Table 4.4 – List of spectral vegetation indices tested for regression modelling of HSNC site LAI. NIR stands for reflectance in the near infrared spectral band, R for the red band, and G for the green band. L is a soil adjustment factor used in the SAVI formula which is assigned a value of 0.5 for moderate vegetation cover.

Vegetation Index	Mathematical Formula	Reference
Normalized Difference Vegetation Index (NDVI)	$\frac{(NIR - R)}{(NIR + R)}$	Rouse et al. (1974)
Green Normalized Difference Vegetation Index (GNDVI)	$\frac{(NIR - G)}{(NIR + G)}$	Gitelson et al. (1996)
Modified Simple Ratio (MSR)	$\left(\frac{NIR}{R} - 1\right) \Big/ \sqrt{\left(\frac{NIR}{R} + 1\right)}$	Chen (1996)
Renormalized Difference Vegetation Index (RDVI)	$\frac{(NIR - R)}{\sqrt{(NIR + R)}}$	Roujean and Breon (1995)
Soil Adjusted Vegetation Index (SAVI)	$\frac{(1 + L)(NIR - R)}{(NIR + R + L)}$	Huete (1988)
Modified Soil Adjusted Vegetation Index (MSAVI)	$\frac{1}{2}\left[2NIR + 1 - \sqrt{(2NIR + 1)^2 - 8(NIR - R)}\right]$	Qi et al. (1994)
Modified Chlorophyll Absorption Ratio Index 2 (MCARI2)	$\frac{1.5[2.5(NIR - R) - 1.3(NIR - G)]}{\sqrt{(2NIR + 1)^2 - \left(6NIR - 5\sqrt{R}\right) - 0.5}}$	Haboudane et al. (2004)
Modified Transformed Vegetation Index 2 (MTVI2)	$\frac{1.5[1.2(NIR - G) - 2.5(R - G)]}{\sqrt{(2NIR + 1)^2 - \left(6NIR - 5\sqrt{R}\right) - 0.5}}$	Haboudane et al. (2004)

4.2.5 Spatial Resolution Impact on LAI Prediction

The SVI selected from the previous section was calculated for each of the simulated spatial resolution images for the HSNC site. Regression analysis between the SVI data and LAI was performed at every spatial resolution and the changes in the R^2, slope, and intercept of the relationship as resolution decreased were observed.

Next, the regression models for each resolution were used to estimate LAI from the images at their respective spatial resolutions and the LAI prediction error for each was examined. This method for LAI estimation is hereafter referred to as "Method A". The overall RMSE for all images combined was calculated at each resolution as follows:

$$RMSE = \sqrt{\frac{1}{N}\sum_{i=1}^{N}(LAIpred(i) - LAIactual(i))^2} \tag{4.8}$$

where N is the number of airborne images, LAIpred(i) is the predicted LAI for the i^{th} image, and LAIactual(i) is the ground-measured LAI corresponding to the i^{th} image.

In addition to the RMSE, the prediction error for each image was calculated separately as follows:

$$LAIerror(i,j) = LAIpred(i,j) - LAIactual(\mathrm{i}) \tag{4.9}$$

where LAIpred(i, j) is the LAI predicted for image date i at spatial resolution j, and LAIactual(i) is the ground-measured LAI values corresponding to that image.

Another method (referred to as "Method B") was also used to calculate LAI. In Method B, a single model was used to predict LAI at every spatial resolution. The selected model was created from the original 18 cm resolution images. Once again changes in LAI prediction at every spatial resolution were examined through the overall RMSE as well as the prediction error for each individual image.

For the River Transect site, riparian areas along the river were outlined, and the spectral reflectance was averaged within each riparian site at every spatial resolution. The selected SVI was then calculated from the average spectra for each riparian site, and both Methods A and B were applied to estimate the LAI for each site

at each spatial resolution (using the LAI models created from the HSNC images). An area-weighted average LAI value was then calculated for the entire site as follows:

$$\overline{LAI} = \frac{\sum_{i=1}^{N} LAI(i) * Area(i)}{\sum_{i=1}^{N} Area(i)} \quad (4.10)$$

where N is the number of riparian areas in the River Transect site, LAI(*i*) is the calculated LAI for the *i*th riparian area, Area(*i*) is the area of the *i*th riparian area.

Because no ground reference data were acquired within this site, the LAI calculated using the original 1-m spatial resolution images was treated as the "true" LAI. Differences from this value were examined at every resolution and treated as LAI prediction error. The average absolute difference in predicted LAI caused by coarsening spatial resolution was calculated for each riparian site as follows:

$$LAIerror_{site} = \frac{\sum_{i=1}^{N} |LAIpred(i) - LAIactual|}{N} \quad (4.11)$$

where N is the number of different spatial resolutions, LAIpred(*i*) is the predicted LAI for the riparian site at resolution *i*, and LAIactual is the "true" LAI for that site modelled from the original, highest resolution (1-m) imagery.

The average absolute prediction error for each site was examined for a relationship with two variables of interest: the area of the riparian site, and the initial SVI value calculated for that site using the original 1-m resolution imagery. The relationships were examined through regression of the average prediction errors against each of the two variables, then observing the fit of the resulting regression models.

4.3 Results

4.3.1 HSNC Site LAI

Figure 4.12 presents the ground measured LAI data for the HSNC site. The figure shows the canopy LAI calculated from optical measurements, the understory LAI measured through destructive harvesting, and the total site LAI from adding the two together.

Canopy LAI was found to follow a pattern typical of vegetation, with low LAI in May, increasing through June into July, before stabilizing in July and August as LAI peaked. This was followed by a reduction in LAI in early October as senescence occurred. The lowest LAI was 0.33 m^2/m^2, measured on May 22, while the peak LAI was 1.03 m^2/m^2 on July 31.

Understory LAI followed a similar pattern, increasing from 0.24 m^2/m^2 on May 20 up to a peak value of 1.12 m^2/m^2 on July 21. While understory LAI increased at a similar rate as the canopy before reaching its peak, it had a more gradual senescence, decreasing only to 0.77 m^2/m^2 on October 7 compared to 0.43 m^2/m^2 for the canopy on October 5.

When added together, the total LAI for the site ranged from a minimum of 0.84 m^2/m^2 to a peak value of 2.11 m^2/m^2. Note that due to the July 21 understory LAI measurement being separated by 10 days from the July 31 canopy LAI, a linear interpolation was performed between the July 21 and August 05 understory LAI data points, resulting in a value of 1.08 m^2/m^2 which was added to the July 31 canopy LAI.

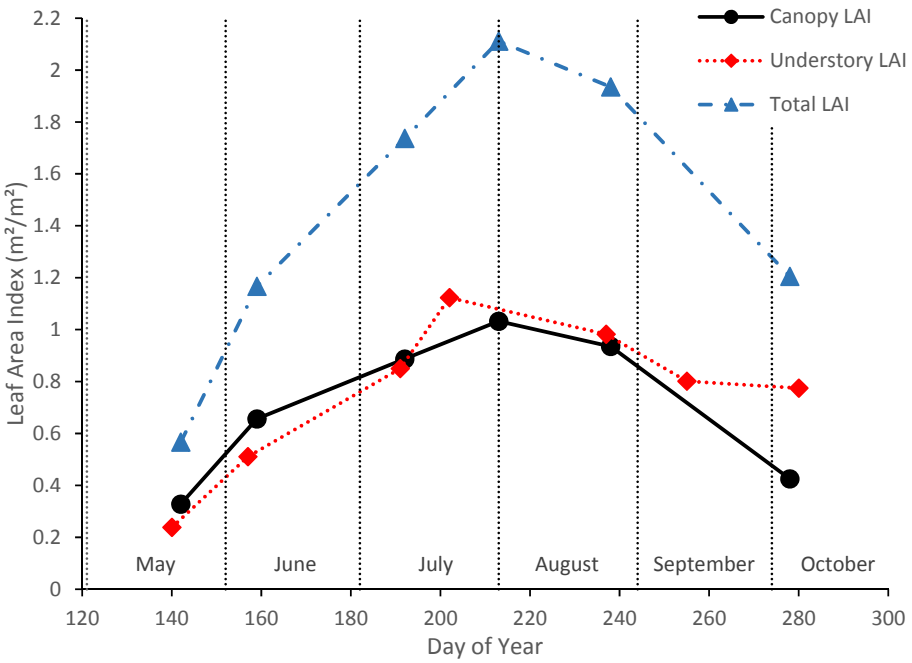

Figure 4.12 – Ground measured LAI for the HSNC site. Canopy LAI, understory LAI, and the total LAI (canopy and understory LAI added together) are shown.

4.3.2 Data Validation

4.3.2.1 Optical LAI Measurements

Table 4.5 lists summary statistics for the peak tree canopy LAI derived from the LAI-2000 optical measurements and the litter traps. The optical LAI estimated a value of 1.03 m²/m² for peak canopy LAI, while the litter traps estimated a value of 1.31 m²/m², a difference of 0.28 m²/m².

Table 4.5 – Statistics for peak canopy LAI estimates derived from optical and litter trap measurements.

Statistic	Optical Data	Litter Traps
Average LAI (m²/m²)	1.03	1.31
Standard deviation (m²/m²)	0.914	0.959
Number of samples	58	19
T-value	1.14	
Critical T-value (90 %)	1.684	
Critical T-value (95 %)	2.021	

The T-test between the two means resulted in a value of 1.14. This value was lower than the critical value for both the 90 % and 95 % confidence intervals,

showing that despite their apparent difference, the estimates of peak LAI from the two methods were not significantly different.

4.3.2.2 Airborne Reflectance

4.3.2.2.1 HSNC Site: ASD Comparison

Figure 4.13 shows ASD reflectance plotted against airborne reflectance for all image dates. All reflectance values are reported as decimals between 0 and 1, with 0 corresponding to 0 % reflectance and 1 corresponding to 100 % reflectance. A strong positive relationship was found between the airborne and ASD data, with an R^2 of 0.91 (Figure 4.13). Based on a 95 % confidence interval, the slope and intercept of the regression line between the two datasets did not differ significantly from a perfect linear relationship with slope of 1 and intercept of 0. The maximum differences in reflectance were 0.148 for the NIR, 0.114 for red, and 0.112 for the green band.

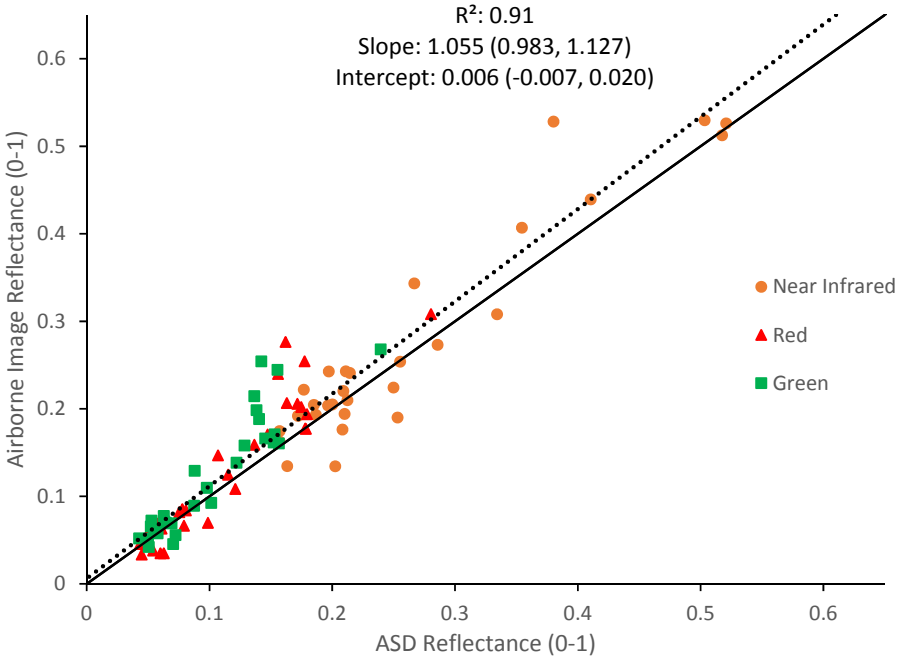

Figure 4.13 – Airborne image reflectance plotted against ASD reflectance for all image dates and targets. A one-to-one relationship is shown by the solid line, while the dotted line shows the regression line through the data. The coefficient of determination, slope, and intercept for the regression line are listed, along with the 95 % confidence intervals in brackets.

Figures 4.14 and 4.15 show the RMSE between ASD and airborne reflectance. Figure 4.14 shows the RMSE overall, as well as separated by image date, while Figure 4.15 shows the RMSE separated by target type.

The May 22 image had the highest overall RMSE (0.062), while the October 05 image had the lowest overall RMSE (0.011) (Figure 4.14). The NIR band had the highest RMSE (0.042), while the red band had the lowest (0.036). The NIR RMSE was highest in the July 09 image (0.076), with the highest RMSE for the red and green bands occurring in the May 22 image.

Separated by target, asphalt demonstrated the highest overall RMSE, followed by cottonwoods, soil, and grass with the lowest RMSE (Figure 4.15). The NIR RMSE was highest for cottonwoods (0.068), with the highest RMSE for the red and green bands occurring for asphalt targets (0.058 and 0.06).

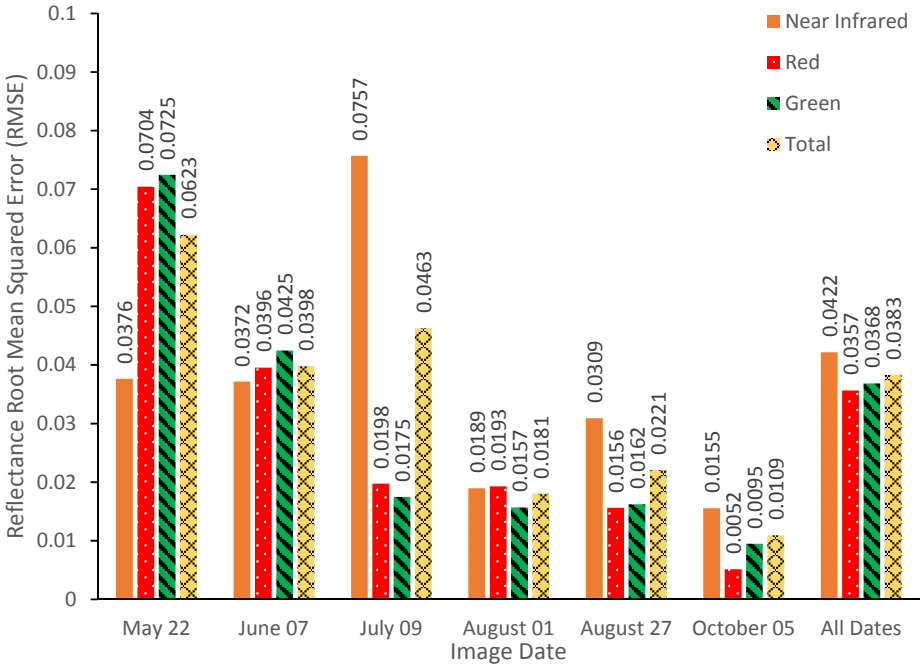

Figure 4.14 – RMSE for the difference between the ASD and airborne image reflectance separated for each spectral band and image date.

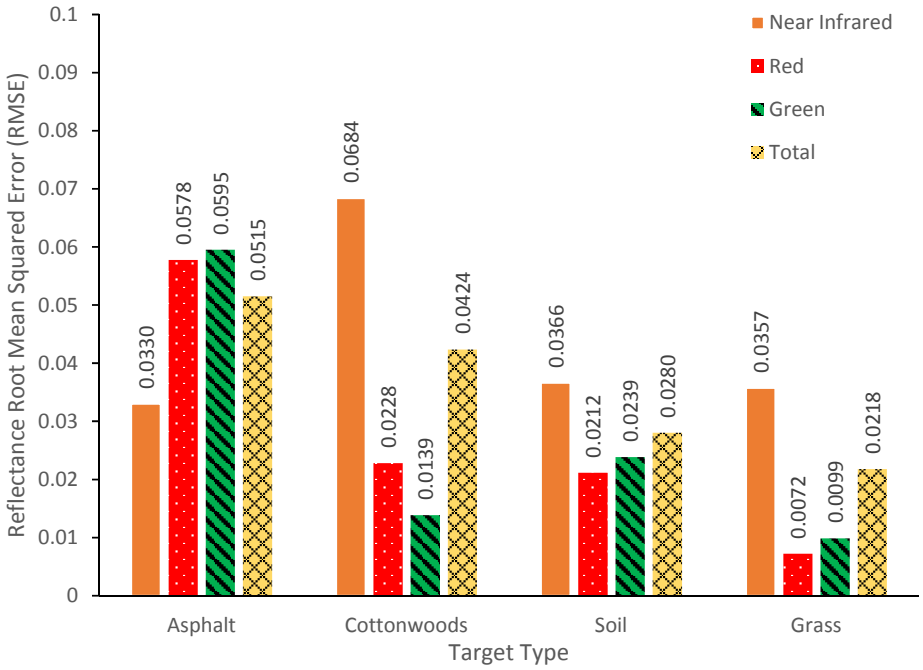

Figure 4.15 – RMSE for the difference between ASD and airborne image reflectance separated for each spectral band and target type.

4.3.2.2.2 HSNC Site: Landsat Comparison

Figure 4.16 shows airborne image reflectance plotted against Landsat-8 OLI reflectance for the HSNC site. There was a strong linear relationship between airborne and Landsat reflectance; however, there was considerable scatter in the data. The maximum reflectance differences were 0.142 for the NIR, 0.165 for the red, and 0.135 for the green band. It is also notable that the airborne images had negative reflectance values occurring in the NIR channel. These negative values occurred exclusively over water bodies.

The regression line through the data differed significantly from a one-to-one linear relationship ($p < 0.05$). The slope of the line was greater than 1, while the intercept was slightly below zero.

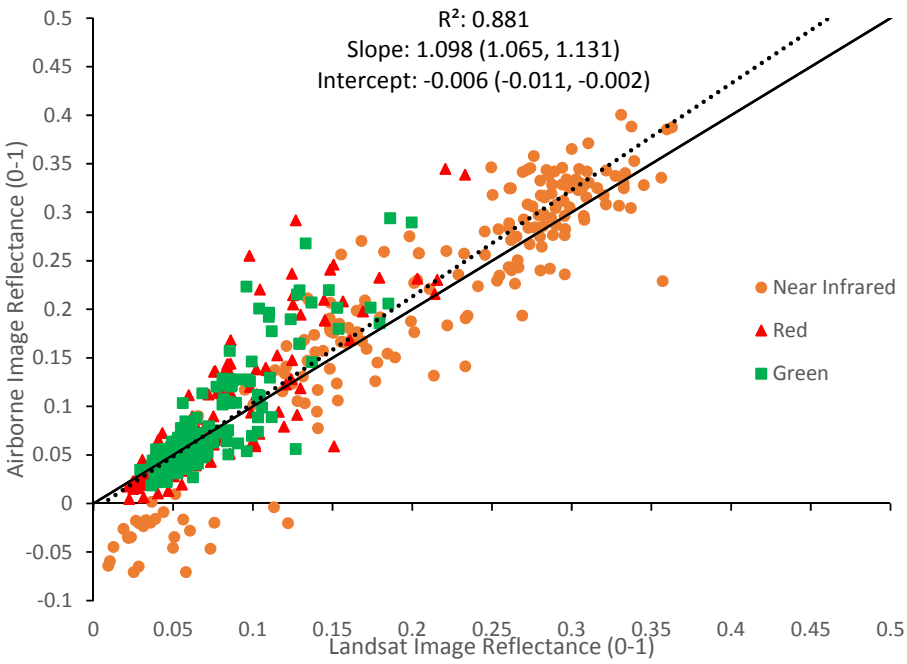

Figure 4.16 – Airborne reflectance plotted against Landsat reflectance for individual pixels over the HSNC site. A one-to-one relationship is shown by the solid line, while the dotted line shows the regression line through the data. The coefficient of determination, slope, and intercept for the regression line are listed, along with the 95 % confidence intervals in brackets.

Figures 4.17 and 4.18show the RMSE between airborne and Landsat reflectance separated by date and by target type, respectively. The July 09 image demonstrated the highest RMSE (0.0478), while the August 01 image had the lowest RMSE (0.0294). The NIR band had the highest overall RMSE (0.0471), with the green band being the lowest (0.0307). Separated by target, the man-made class had the highest overall RMSE (0.0560), although the gravel bar class was almost as high (0.055) (Figure 4.18). The vegetation class had the lowest RMSE (0.0230). The highest RMSE for the NIR band occurred over water (0.0749), while the highest RMSE in the red band occurred for man-made targets (0.0622). The highest RMSE for the green band occurred in the gravel bar class, although the man-made class was almost as high (0.0547 compared to 0.0537 for man-made).

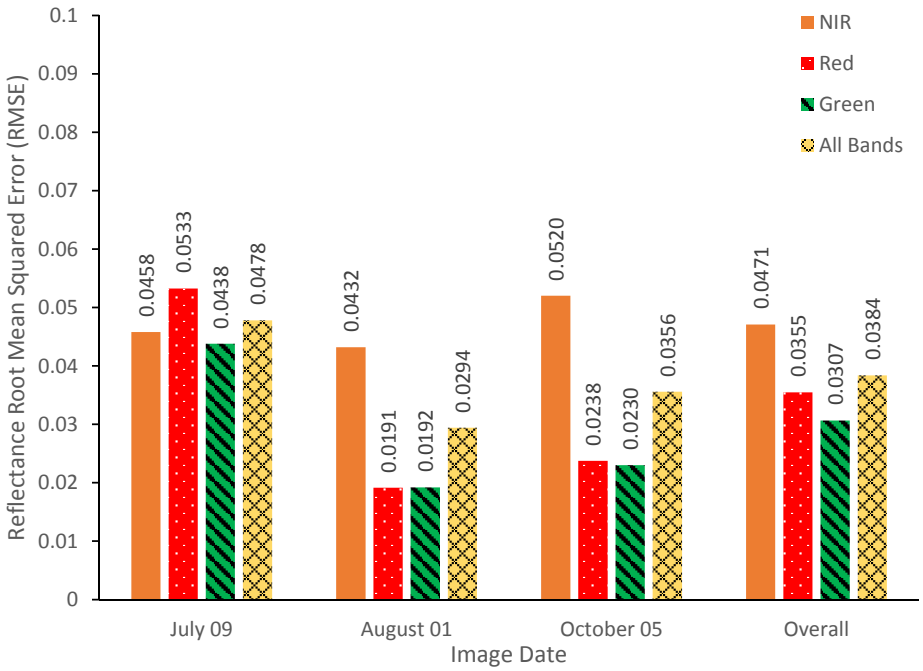

Figure 4.17 - RMSE for the difference between airborne and Landsat pixel reflectance over the HSNC site, separated for each spectral band and image date.

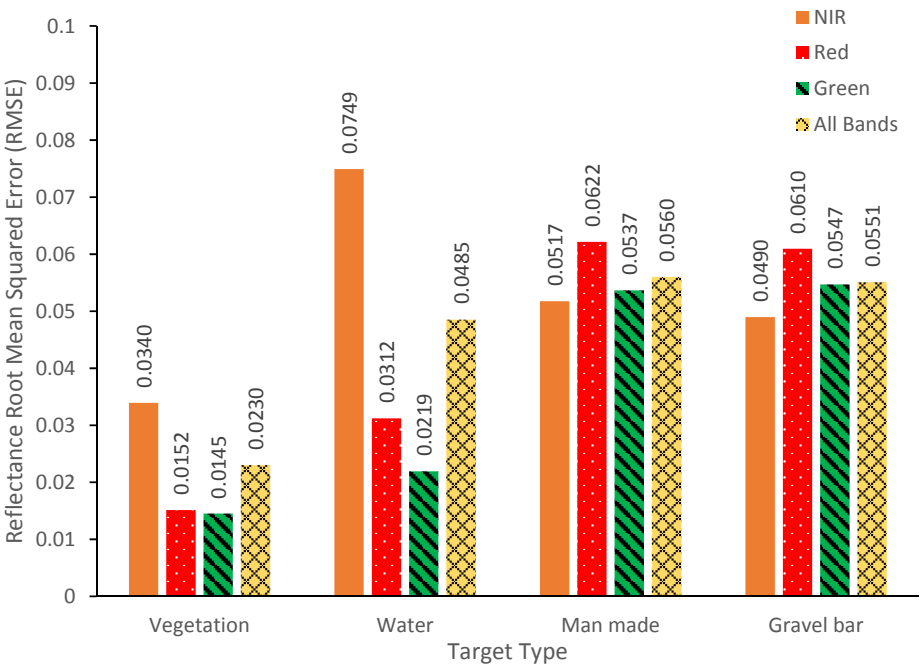

Figure 4.18 – RMSE for the difference between airborne and Landsat pixel reflectance over the HSNC site, separated for each spectral band and target type.

4.3.2.2.3 River Transect Site: Landsat Comparison

Figure 4.19 presents airborne image reflectance plotted against Landsat reflectance for pixels in the River Transect site. A strong linear relationship was found between the two sensors with an R^2 of 0.941. However, There were some large reflectance differences of 0.2 and higher. The maximum reflectance differences were 0.29 for the NIR, 0.22 for the red, and 0.21 for the green band. The regression line through the data was found to be significantly different from a perfect one-to-one relationship ($p < 0.05$); however, when major outliers were removed, the regression line was found to no longer significantly differ from the 1:1 model.

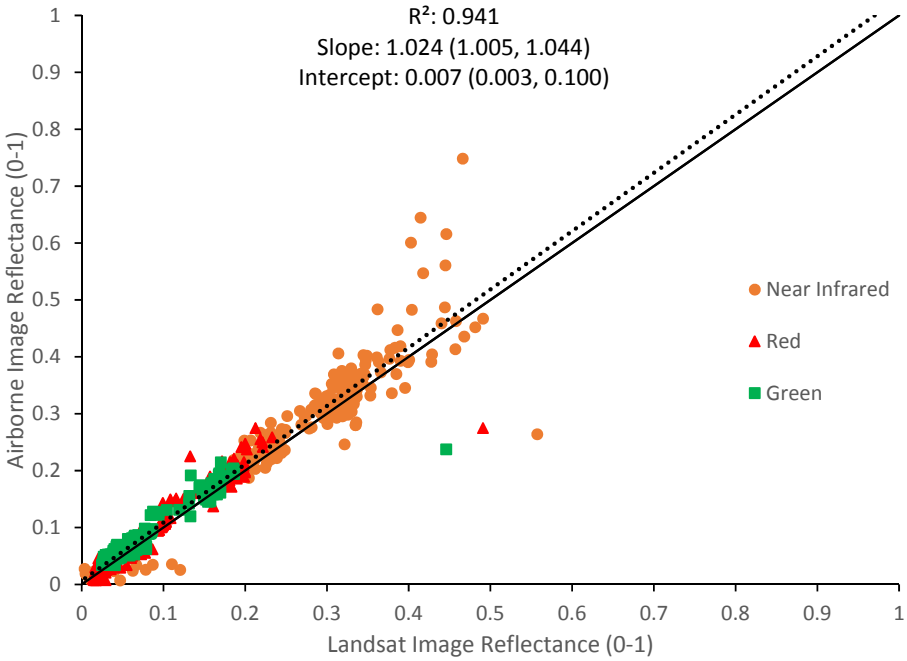

Figure 4.19 - Airborne reflectance plotted against Landsat reflectance for individual pixels over the River Transect site. A one-to-one relationship is shown by the solid line, while the dotted line shows the regression line through the data. The coefficient of determination, slope, and intercept for the regression line are listed, along with the 95 % confidence intervals in brackets.

Figure 4.20 lists the RMSE for the difference between airborne and Landsat data broken down by target type. The overall RMSE for all targets was 0.0327. The

NIR band had the highest overall RMSE (0.0483), followed by red (0.0213), then green (0.0204). Of the different targets, the man-made class had the highest overall RMSE (0.0655), as well as the highest RMSE for each of the individual image bands. The fallow class had the lowest overall RMSE, followed closely by water (0.0162 compared to 0.0195 for water).

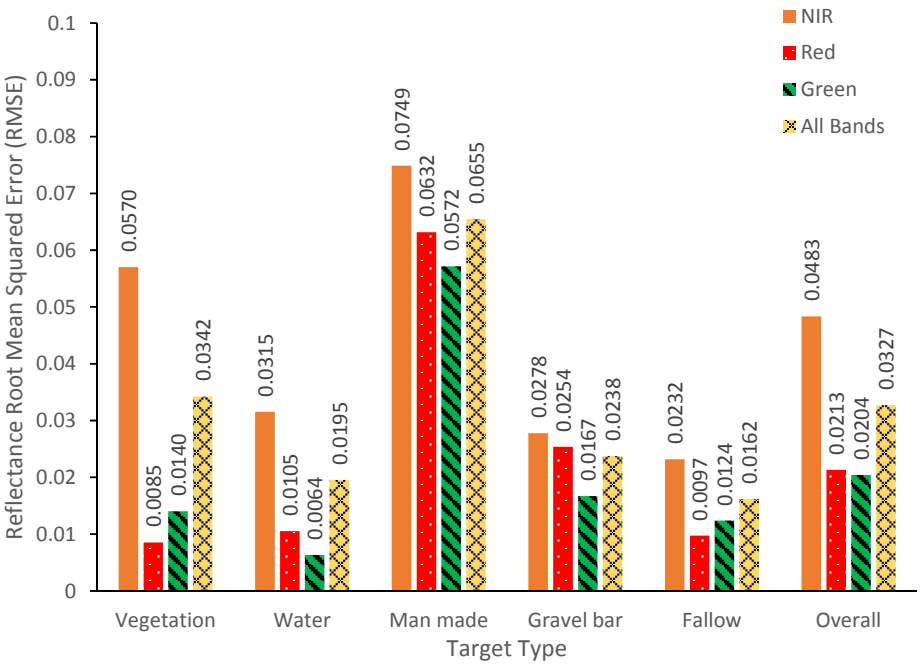

Figure 4.20 - RMSE of the difference between airborne and Landsat pixel reflectance over the River Transect site, separated for each spectral band and target type.

4.3.3 LAI-SVI Regression Modelling

Table 4.6 lists the R^2, slope, intercept, and standard error of the estimate for the 8 SVI models used to estimate LAI in the HSNC site. All SVI models were similar in their prediction power. The MSR model was the best predictor of LAI, with the highest R^2 (0.826) and lowest standard error (0.27). The MSAVI model had the lowest R^2 (0.74) and highest standard error (0.33).

The MSR model was selected for use in the subsequent spatial resolution sensitivity analysis. MSR was selected because it had the highest fit compared to the other models. The relationship between the MSR and LAI is shown in Figure 4.21.

Table 4.6 – R^2, standard error of the estimate, slope, and intercept for regression models between SVIs and LAI for the HSNC site.

SVI Model	R^2	Standard Error of the Estimate (m^2/m^2)	Slope	Intercept
NDVI	0.792	0.2953	2.568	-0.24
GNDVI	0.792	0.2953	2.953	-0.432
MSR	0.826	0.2700	0.605	0.303
RDVI	0.755	0.3201	3.618	0.105
SAVI	0.742	0.3290	3.306	0.182
MSAVI	0.740	0.3301	3.032	0.331
MCARI2	0.754	0.3211	2.240	0.409
MTVI2	0.754	0.3210	3.072	0.405

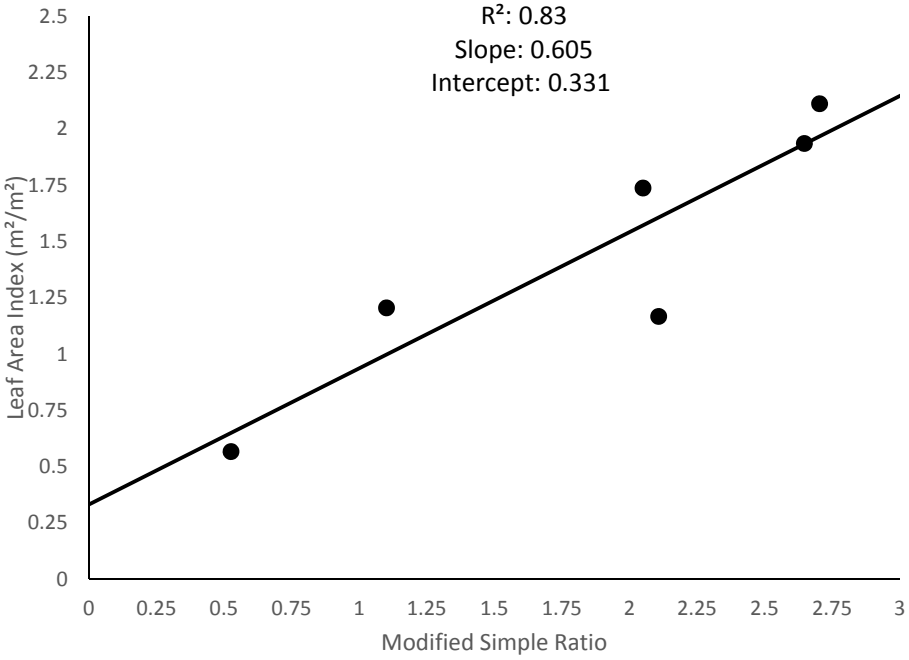

Figure 4.21 – Regression model for predicting LAI using the Modified Simple Ratio.

4.3.4 Spatial Resolution Impact on LAI Modelling and Prediction

The results from the analysis of the spatial resolution impact on LAI modelling are discussed in this section. In the first subsection, the effects of differing spatial resolutions on regression models between LAI and MSR are discussed. In the second subsection the effects of spatial resolution on the prediction accuracy of LAI using MSR regression models are discussed for both the HSNC and River Transect sites.

MSR values were not able to be calculated for each image in the HSNC site at some very coarse spatial resolutions. This is because negative red reflectance values resulted in an error in the denominator term of the MSR formula. The affected images were the August 27 image at the 450-m resolution, as well as the May 22 and June 07 images at the 500-m resolution.

The negative reflectance values occurred because of spectral mixture with regions outside the image mosaic boundaries, which contained no spectral data. Despite the lack of spectral data, these areas outside the border were counted as part of the image mosaics and their spectral signal was aggregated within some of the coarse spatial resolution image pixels. The areas outside the image borders had been assigned a negative reflectance value for all bands as a result of the empirical line calibration and, thus, reduced the reflectance values of pixels within which they were aggregated, making the aggregate pixel reflectance negative in some cases.

4.3.4.1 Spatial Resolution Impact on LAI Regression Models

Figure 4.22 shows the changes in R^2 and standard error for the regression models created at every spatial resolution, while Figure 4.23 shows the changes in the slope and intercept of the models. As resolution coarsened, R^2 was found to slowly increase while standard error decreased. This trend continued until the 175 m resolution. At the 200-m resolution, R^2 declined sharply while standard error increased. However, following this at 250 m and 300 m, R^2 and standard error recovered. At the 300 m resolution the model R^2 was highest (0.896) and standard error lowest (0.209) compared to every other resolution. Immediately following the 300-m resolution, the model performance plummeted, falling to a minimum R^2 of 0.049 at 500 m. Standard error peaked at 0.62 at a resolution of 450 m, dropping to 0.47 at 500 m.

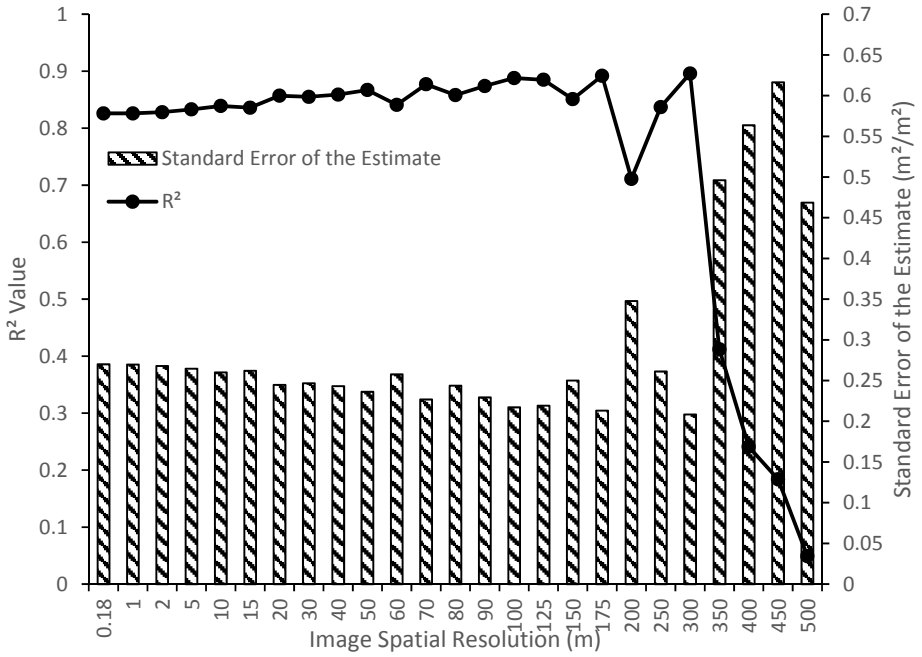

Figure 4.22 – R^2 and standard error of regression models for predicting LAI from MSR at every simulated spatial resolution.

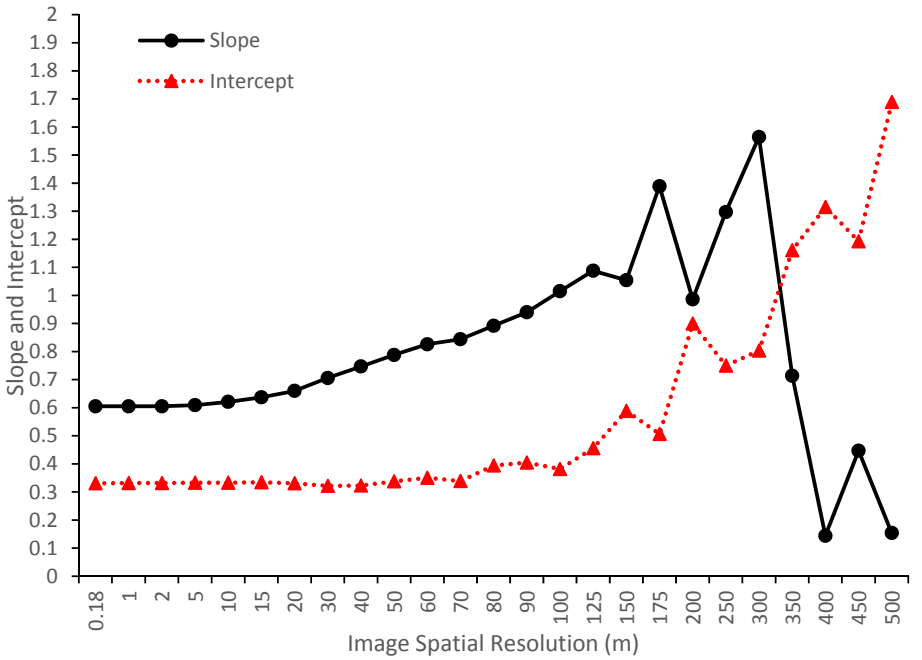

Figure 4.23 – Slope and intercept of regression models for predicting LAI from MSR at every simulated spatial resolution.

As shown in Figure 4.23, beyond the 5-m resolution, the slope began gradually increasing. The increase between 5 m and 20 m was very slight. As resolution decreased from 20 m to 60 m, the model slope increased more rapidly.

Between 70 m and 125 m the slope increased at an even greater rate. A slight decrease occurred at 150 m, followed by erratic changes where slope greatly increased and decreased as resolution coarsened, hitting a maximum of 1.56 at 300 m before falling to 0.14 at 400 m, increasing slightly to 0.45 at 450 m, then dropping again to 0.15 at 500 m.

The intercept of the models remained fairly stable from 0.18 m to 70 m, increasing then levelling off between 80 m and 100 m. Beyond the 100-m resolution, the intercept began increasing rapidly, along with some moderate decreases at certain resolutions (175 m, 250 m, and 450 m). The model intercept reached a maximum value of 1.69 at the 500-m resolution.

4.3.4.2 Spatial Resolution Impact on LAI Prediction

4.3.4.2.1 HSNC Site

Figure 4.24 shows the RMSE for LAI prediction using the different regression models created for every spatial resolution (Method A). Figure 4.25 breaks this error down by showing the LAI prediction error for each image separately. The results in Figure 4.24 follow essentially the same pattern (though inverted) as the R^2 shown in Figure 4.22. RMSE slowly decreased as resolution coarsened – with exceptions at 60 m and 150 m – until 175 m, followed by a large increase at 200 m. It then began decreasing again, hitting a minimum of 0.17 at 300 m, 23% lower than the initial RMSE at 18 cm (0.22). Beyond 300 m, the RMSE greatly increased, hitting a maximum of 0.48 at 450 m, 117% higher than the initial value, before falling to 0.33 at 500 m.

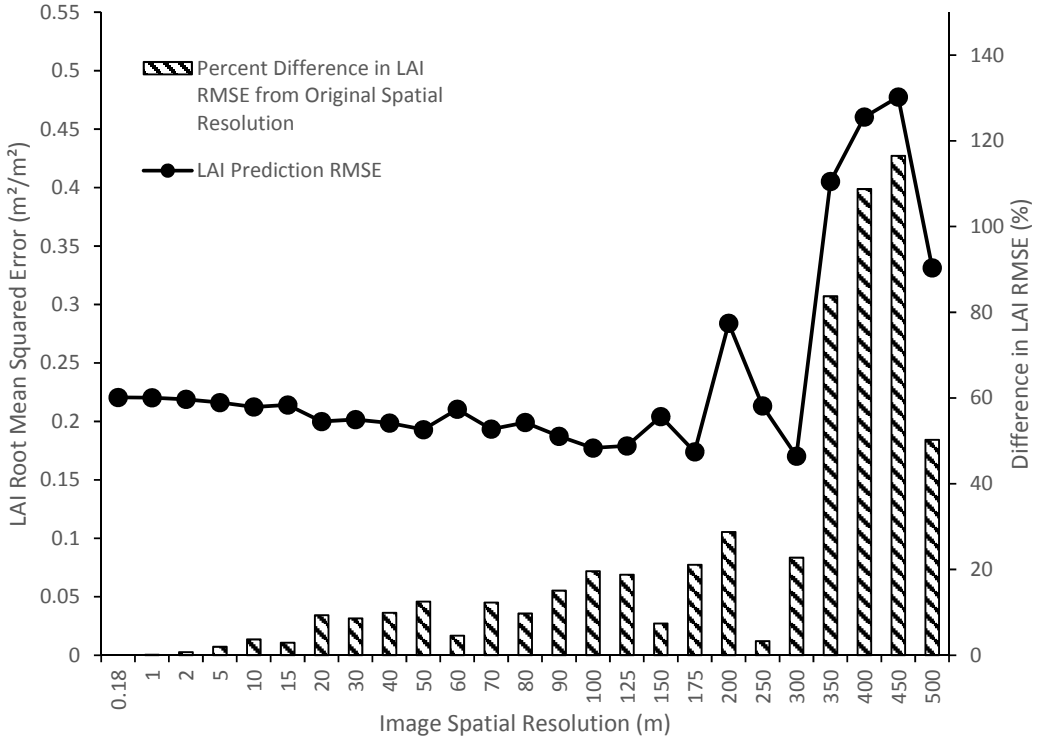

Figure 4.24 – RMSE of LAI prediction for every spatial resolution using Method A.

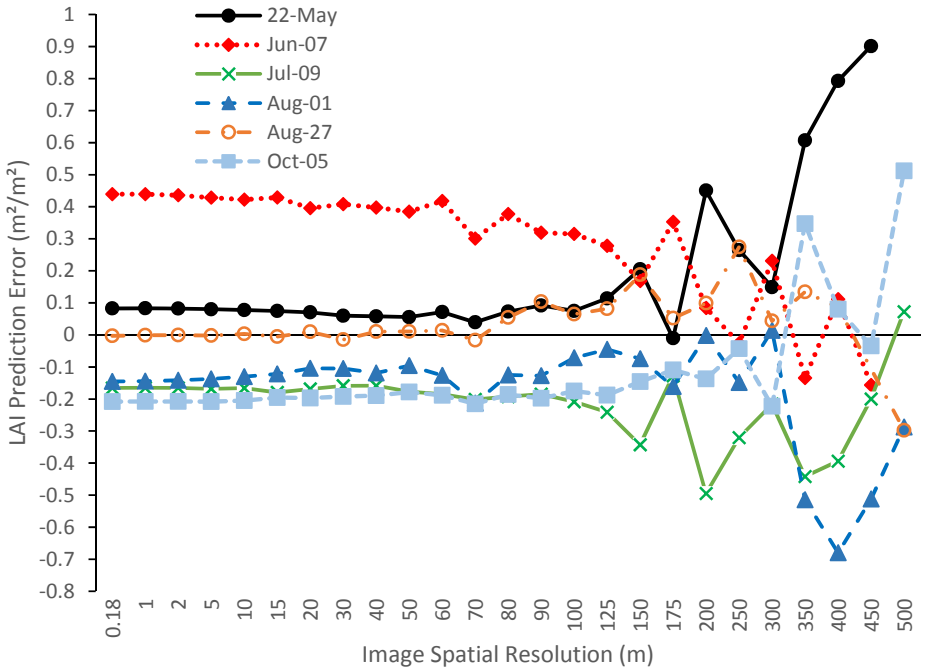

Figure 4.25 – LAI prediction error for each image date at every spatial resolution using the Method A.

Figure 4.25 shows that prediction error held fairly constant or decreased for most images up until 125 m. At 150 m, moderate increases in prediction error

occurred for the May 22, July 09, and August 27 images. At 175 m, large decreases in prediction error occurred in the May 22, July 09, and October 05 images resulting in the low RMSE at this resolution. The large RMSE increase at the 200-m resolution is primarily attributable to the increases in prediction errors for May 22 and July 09, even though others decreased (June 07, August 01) or held constant (October 05, August 27).

At 300 m, large decreases in prediction error for May 22 and July 09 along with more modest reductions for August 01 and August 27 resulted in the lowest RMSE for any resolution, despite marginal error increases for the June 07 and October 05 images. At 350 m and 400 m large increases in prediction error occurred for the May 22 and August 01 images, with error also increasing for the October 05 and July 09 images at 350 m, leading to the large RMSE increases at these resolutions. At 450 m, despite the marginally higher RMSE, error appears to have decreased for every resolution, aside from May 22 and June 07. Note that no LAI value was present for August 27 at this resolution. At 500 m, the error greatly increased for the October 05 image but decreased for July 09 and August 01, while no data was present for June 07 and May 22, contributing to the decrease in RMSE seen at this resolution.

The results from applying the same model at every spatial resolution (Method B) differed from those of Method A. Figure 4.26 shows the overall prediction RMSE at each spatial resolution, while Figure 4.27 shows the LAI prediction error for each image separately. RMSE remained stable until 20 m, after which it steady increased as resolution decreased. Between 30 m to 100 m the rate of increase was fairly constant. From 125 m to 200 m the RMSE increased at a greater rate. From 250 to 400 m the RMSE continued to increase at a more variable rate.

The RMSE at 400 m was 1.09, almost 400% higher than the initial RMSE at the 18 cm resolution (0.22). At 450 m the RMSE fell to 0.94 before a large increase at 500 m to a maximum RMSE of 1.25, 470% higher than the initial RMSE.

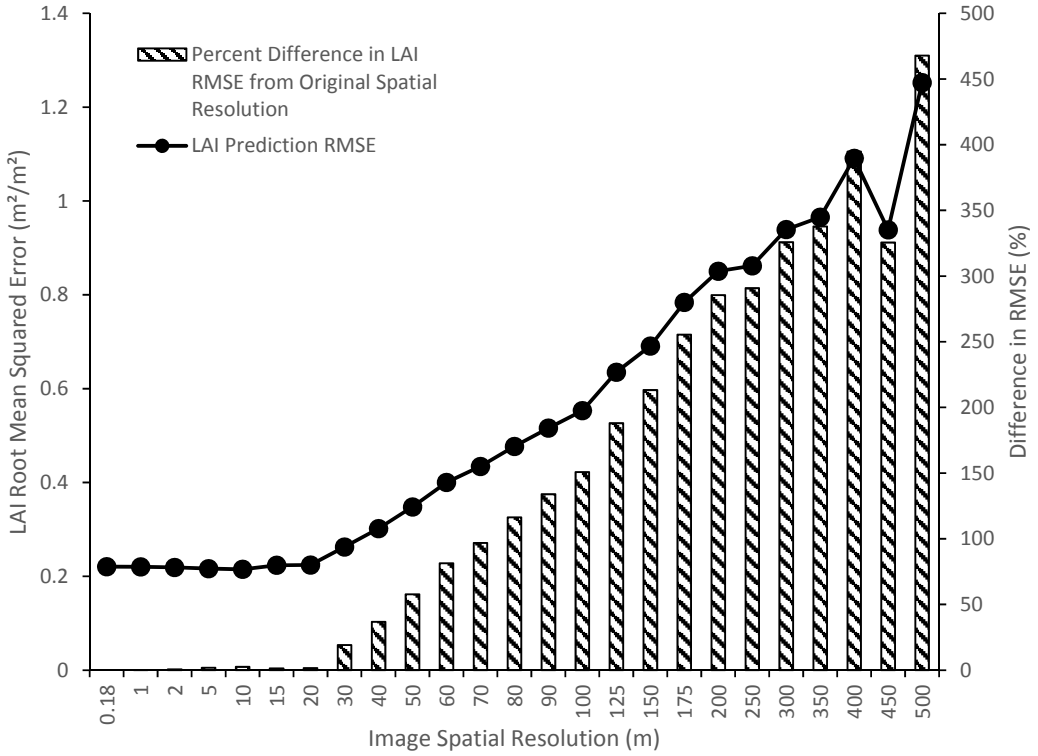

Figure 4.26 – RMSE of LAI prediction for every spatial resolution using Method B.

Examining Figure 4.27, prediction error held constant for all images up until the 10-m spatial resolution. Beyond 10 m, the predicted LAI began decreasing for all images. This decrease resulted in the LAI being under-predicted for every image at 70 m and coarser resolutions.

The rate of decrease was not the same for all image dates. While June 07, July 09, August 01, and August 27 followed a similar rate of decrease in predicted LAI, both May 22 and October 05 were less affected, showing a shallower rate of decline as resolution decreased. This was especially notable for May 22, which only had a

slow decrease in LAI prediction up to a resolution of 300 m, after which the predicted LAI actually began increasing as resolution decreased.

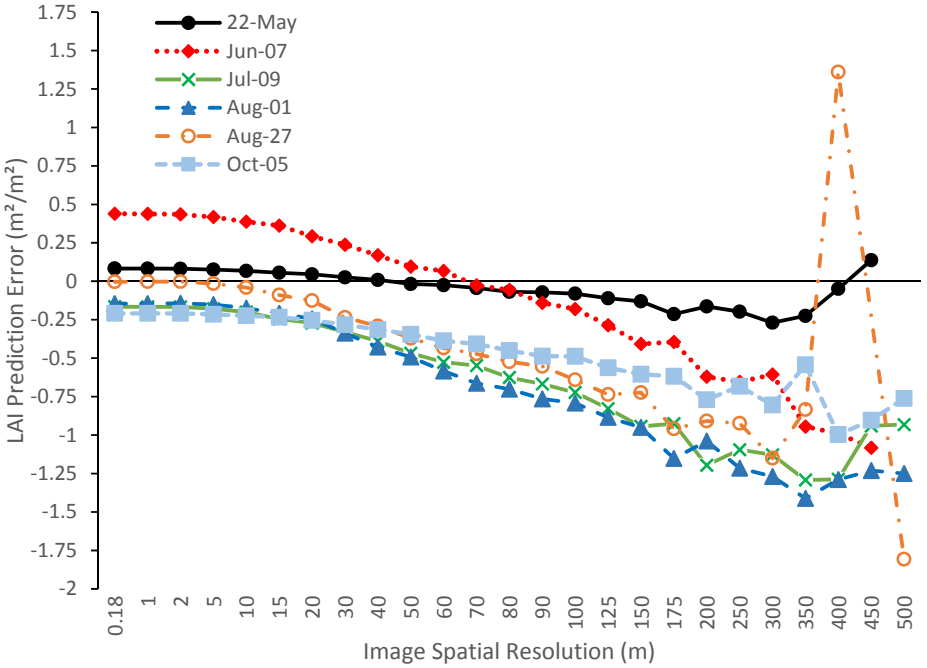

Figure 4.27 – LAI prediction error for each image at every spatial resolution using Method B.

For most images the predicted LAI steadily decreased until the 125-m resolution. Beyond 125 m the general trend continued but became more variable, with prediction errors decreasing for certain images even as it increased for others. For instance, predicted LAI increased for the August 01 and June 07 images between 150 m and 175 m even as it decreased for other image dates. Beyond 300 m, the pattern changed further, with large increases and decreases in predicted LAI occurring for several image dates as the spatial resolution continued to decrease.

A major outlier occurred with the August 27 image between 350 m and 400 m, which went from an LAI under prediction of 0.84 m²/m² to an over-prediction of 1.36 m²/m², a difference of 2.2 m²/m². Due to negative red reflectance, no MSR value was

calculated for the August 27 image at 450 m; however, at 500 m predicted LAI fell to an LAI under-prediction of 1.81 m²/m².

4.3.4.2.2 River Transect Site

The results of the LAI spatial resolution analysis for the River Transect site are presented. Figure 4.28 shows the area-weighted average LAI calculated using Method A. The figure shows the area weighed LAI, as well as the percent difference between the LAI calculated at each resolution and the value calculated from the original 1-m resolution imagery.

At the original 1-m spatial resolution, the modelled LAI was 1.79 m²/m². Predicted LAI remained relatively stable up to 10 m. Beyond 10 m, the predicted LAI began steadily increasing. Predicted LAI increased at a greater rate from 20 m to 90 m, with a slight decrease at 70 m. From 80 m to 100 m LAI prediction increased at an even greater rate. Predicted LAI increased at 125 m, but then held steady until 150 m, with a predicted LAI of 2.41 m²/m², 0.63 (35%) higher than the value at 1 m.

Beyond 150 m, the predicted LAI increased and decreased greatly and erratically. Predicted LAI increased up to 2.79 m²/m² at 175 m (1.01, or 56% higher than at 1 m), decreasing at 200 m, and then increasing again from 250 to 300 m, where it peaked at 3.13 m²/m², 1.35 (75%) higher than the LAI value at the 1-m resolution. Between 300 m and 400 m the predicted LAI massively decreased, falling to a minimum of 1.51 m²/m², 0.27 (15%) lower than the 1-m resolution LAI. Modelled LAI increased at 450 m and 500 m to 1.89 m²/m² and 1.92 m²/m², 0.10 and 0.13 (5.6% and 7.3%) higher, respectively, than the LAI at 1 m.

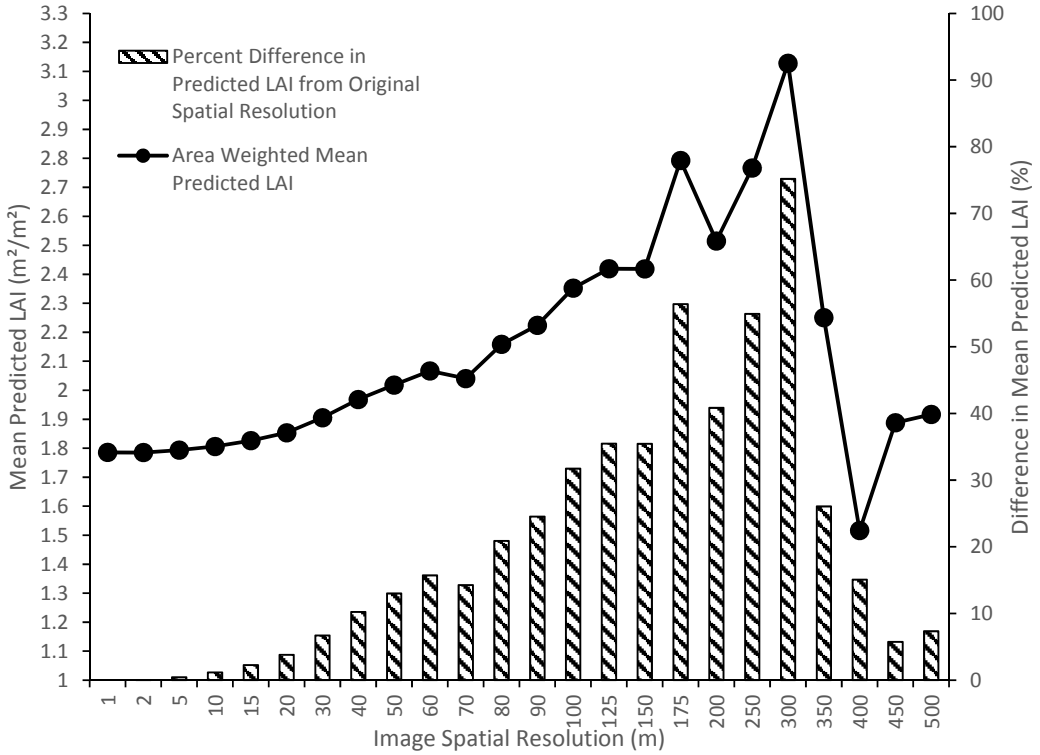

Figure 4.28 – Area-weighted average LAI for the River Transect site at each spatial resolution using Method A.

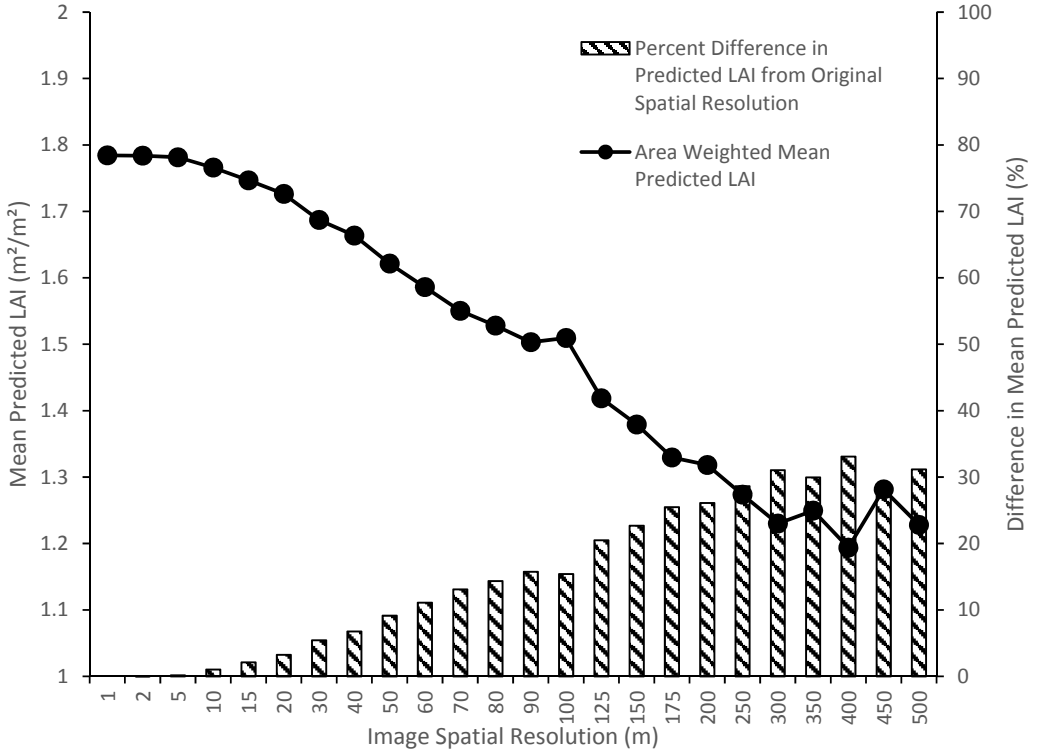

Figure 4.29 – Area-weighted average LAI for the River Transect site at each spatial resolution using Method B.

Figure 4.29 shows the results for the River Transect site using Method B. Using this method, predicted LAI remained stable until a resolution of 10 m. Beyond this value, the predicted LAI consistently decreased as resolution decreased. Predicted LAI began decreasing at a greater rate from 20 m to 300 m. Two minor increases broke up the downward trend, occurring at 100 m and 350 m. At 400 m the lowest LAI prediction of 1.19 m^2/m^2 occurred, 0.59 (33%) lower than the LAI predicted from the 1-m spatial resolution data. Predicted LAI then increased at 450 m to 1.28 m^2/m^2 before falling again at 500 m to 1.23 m^2/m^2.

Figure 4.30 shows the average absolute LAI prediction error due to decreasing spatial resolution plotted against the areas for all riparian zones along the river. There was no discernable relationship between the area of a riparian zone and the amount of resolution-induced LAI prediction error it experienced for Method A. Likewise for Method B, while the fit was marginally better and a slight downward trend appears possible, there was no notable relationship.

Figure 4.31 shows the average absolute LAI prediction error plotted against the initial MSR value calculated from the original 1-m spatial resolution imagery. Here again there was no relationship evident for Method A. For Method B, on the other hand, there appeared to be a relationship between the two variables. There was an upward trend between higher LAI prediction errors and higher initial MSR values. Although there was considerable scatter, the model explained almost 44% of the variance in the LAI prediction error. When examined in closer detail it was found that the vast majority of LAI prediction errors were negative (not shown in Figure 4.31), indicating that for riparian areas with high initial MSR values, LAI predictions progressively decreased as resolution decreased.

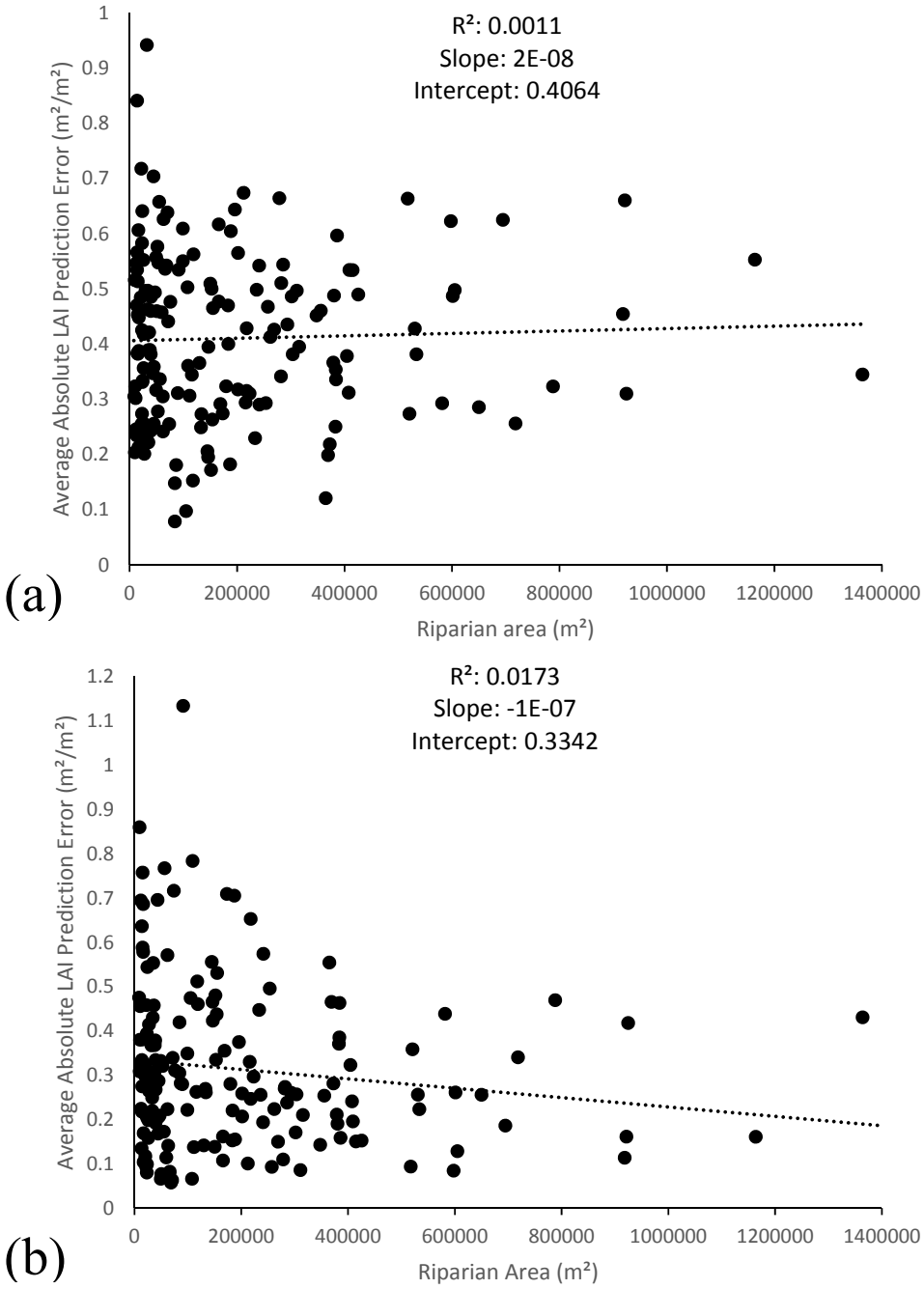

Figure 4.30 – Relationship between the average absolute LAI prediction error and riparian zone area for the River Transect site. (a) shows results for Method A and (b) shows results for Method B.

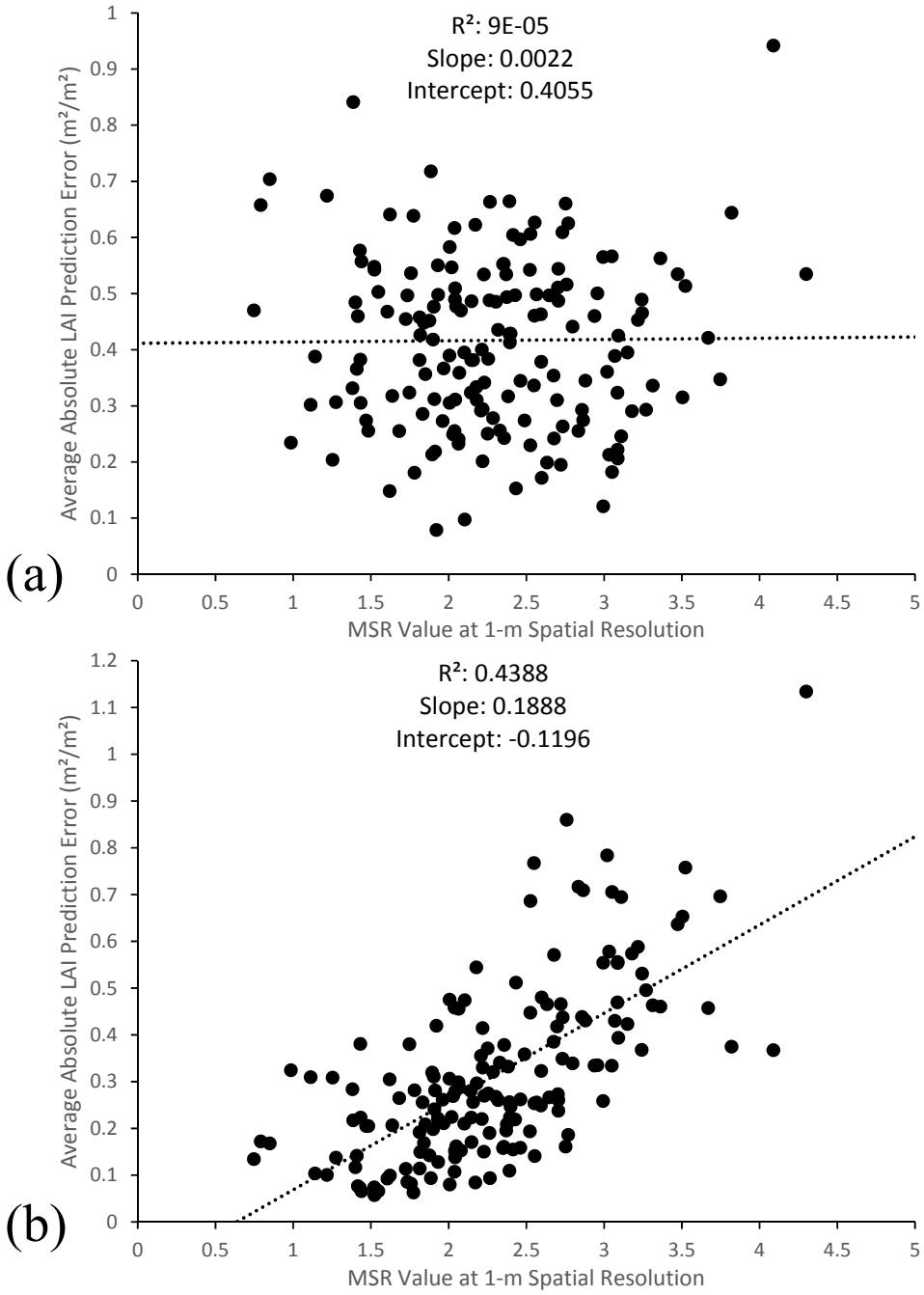

Figure 4.31 – Relationship between the average absolute LAI prediction error and the initial MSR value calculated from the 1 metre spatial resolution for the River Transect site. (a) shows results for Method A and (b) shows results for Method B.

4.4 Discussion

The main objectives of this study were to assess the effects of spatial resolution on riparian LAI modelling, and to evaluate the quality of calibrated digital camera imagery. In this section the study results are discussed in the context of these two objectives.

The first subsection discusses the characterization of the HSNC site LAI using ground measurements. This section discusses how reasonable the LAI estimates were and the level of confidence in the measurements.

The second subsection describes the comparison of the airborne image data with the ASD and Landsat-8 OLI data. The discussion focusses on how well the instruments compared, and attempts to explain some of the differences that were observed between them.

The third subsection discusses the sensitivity analysis of the eight different SVIs used for predicting riparian LAI. The relative performance of the SVIs in LAI prediction is considered, along with the sources of error and uncertainty in the modelling performed in this study.

The last subsection examines the results from the spatial resolution sensitivity analysis on LAI modelling. This section is further subdivided to discuss the results for HSNC site and River Transect site separately, with a final section providing an overall discussion of the findings.

4.4.1 Riparian LAI Ground Measurements

The peak LAI for the HSNC site was 2.11 m^2/m^2. This value was split almost evenly between overstory and understory LAI. A lack of studies on riparian LAI makes it difficult to assess this estimate using the literature. Direct comparisons of LAI between studies are also complicated due to the use of differing methods,

differing definitions of LAI, differing climate regimes, and different species measured in each study, which can lead to greatly varying results (Asner et al., 2003).

In a synthesis of more than 1000 published LAI estimates, Asner et al. (2003) calculated a global mean LAI of 4.5 m^2/m^2. Unfortunately, riparian ecosystems were not included as a separate biome and are not mentioned in the paper. All forest biomes had mean LAI values higher than 2.1 m^2/m^2, ranging from 2.6 m^2/m^2 for boreal deciduous forests to 6.7 m^2/m^2 for temperate evergreen broadleaf forests (Asner et al., 2003). The mean LAI for Shrublands (2.1 m^2/m^2), Tundra (1.9 m^2/m^2), and Grasslands (1.7 m^2/m^2) were closer to the riparian LAI found in this research (Asner et al., 2003).

In Nagler et al. (2004), LAI was estimated for a number of riparian vegetation species along the Colorado River using both biomass sampling and optical measurements. Among the species measured were cottonwoods, which themselves had an average LAI of 3.5 m^2/m^2, notably higher than the estimate in the current study, despite not including the understory LAI (Nagler et al., 2004). A difference in methods could explain this difference. In their study, LAI was measured for individual trees, without measuring the open spaces between trees, while these gaps in the canopy were included in the measurements conducted in this study. Acquiring measurements in these open areas typically results in lower LAI values than when LAI is measured only under the tree canopy (Carlson & Ripley, 1997). Calculating LAI by measuring only under the vegetation canopy LAI has been termed “Local LAI”, while inclusion of the gaps in the canopy is referred to as “Global LAI” (Carlson & Ripley, 1997). In another study both Local and Global LAI were measured for riparian vegetation along the Colorado River. Most species were found to have a Local LAI of between 2.0 m^2/m^2 and 3.0 m^2/m^2, with cottonwoods around 2.2 m^2/m^2 (Nagler et al., 2001). Global LAI values were more comparable to the value

of 2.11 m²/m² measured in this thesis, ranging from just under 0.2 m²/m² to just over 2.0 m²/m² over 63 different sites (Nagler et al., 2001).

The agreement between the litter trap measurements and the optical LAI measurements increased the confidence in the optical data. While the peak optical LAI was lower than that calculated from the traps, it was not a statistically significant difference. The difference between the two methods was not altogether surprising. Optical measurements of LAI – particularly when using the LAI-2000 – have been found to underestimate LAI compared to direct methods such as litter traps (Jonckheere et al., 2004; White et al., 2000). Furthermore, considering the difference in the measurement footprint of the two techniques and the different number of sample points, differences between the two could be anticipated. Unfortunately the litter trap data could only be used to assess peak canopy LAI, leaving the possibility of errors in the optical LAI measured on other dates.

It is unfortunate that there was not a separate method used to compare with the understory LAI measurements; however, direct harvest methods are generally considered more accurate and reliable than indirect methods (Jonckheere et al., 2004). What is potentially concerning is that only four sampling quadrats were used, and the locations were not varied for the different measurement dates. It is not clear if this limited sampling provided adequate characterization of the understory LAI. In studies on grasslands, differing numbers of harvest quadrats have been used to characterize LAI, from five (Fan et al., 2009), to twelve (Asrar et al., 1986), to upwards of twenty quadrats (Turner et al., 1999). Examples of the technique being applied in riparian areas were not forthcoming; nonetheless, given the variability of riparian areas, future studies would likely benefit from more extensive sampling of the understory LAI.

4.4.2 Airborne Image Reflectance Calibration

The calibrated digital camera images from the HSNC site compared well with the ASD data, with a high R^2 and low overall RMSE. The performance did, however, vary between images, between spectral bands, and between targets (Figures 4.13, 4.14, and 4.15). Differences between ASD and camera data were as high as 0.15 (15% reflectance). Unfortunately, in this comparison it was not possible to ensure the exact same targets were measured with both the ASD and the cameras. While it was attempted to find areas in the images which corresponded to the ASD measurement locations, the ASD measurement spatially locations were not recorded at the time they were acquired, and so it was impossible to ensure accurate registration. Consequently, some uncertainty exists for this comparison.

In the comparison of the HSNC airborne images with Landsat-8 OLI images, a good overall agreement was evident, albeit with a high level of scatter and in some cases large differences in reflectance as high as 0.17 between individual pixels (Figure 4.16). Performance was more uniform across the different image dates compared to the ASD comparison, although only 3 images were used in this comparison, while all 6 were compared with the ASD (Figure 4.17). Here again differences in performance were evident over different target types (Figure 4.18).

Based on the HSNC site comparisons, the felt topped tables functioned well as calibration targets using the empirical line method. However, it appears that the tables did not lead to the most consistent reflectance calibration. This is evidenced by the differing amount of error between image dates, although it is possible this is an issue with the raw imagery rather than the calibration. The negative NIR reflectances over water also suggests an issue with the calibration (Figure 4.16).

The small size of the tables resulted in them appearing as only a handful of pixels in the images. Consequently only a small number of pixels could be aggregated for each table, increasing the impact of image noise. Additionally, the few selected pixels were possibly affected by the reflectance of their surroundings, a phenomenon known as the adjacency effect (Richter et al., 2006). This adjacency effect could have increased the dark table DN values and decreased the bright table values. The ASD-measured reflectance for the dark table was very low (around 2% reflectance); therefore, an inflation of the dark table DN values in the images could have resulted in an empirical calibration which reduced low reflectance values and assigned negative reflectances to pixels with DNs lower than the dark table value. The presence of negative reflectance values is a common issue with this calibration technique (Smith & Milton, 1999). The calibration targets could be improved by making them larger, although this would reduce their ease of field deployment. Using additional calibration targets has also been shown to increase the accuracy of empirical calibrations substantially over using just two targets (Smith & Milton, 1999).

The River Transect imagery compared very well with the Landsat-8 OLI imagery, with the highest R^2 of all the comparisons. This is not entirely surprising, as the targets used in the empirical line calibration were derived from the Landsat image used in the comparison. The targets were also very large, decreasing the issue of spectral mixing that may have affected the calibration tables used in the HSNC site. The drawback of using targets derived from Landsat scenes is that it requires a Landsat scene which is contemporary with the airborne imagery, as well as large, spectrally stable features being present in both images.

Despite the strong relationship, this comparison had the greatest differences in reflectance for individual pixels (over 0.2 for the red and green, and up to 0.29 for the

NIR band) (Figure 4.19). It was found that most of these high error pixels were over man-made targets. This also explains the high RMSE in the man-made class that was double the overall RMSE for all classes (0.0655 for man-made compared to 0.0327 overall) (Figure 4.20).

Aside from the calibration targets, there are a number of factors that may have contributed to some of the differences observed between the OLI and airborne images for both the HSNC and River Transect sites. Firstly, the spectral sensitivity for the bands of each sensor are not the same (Figure 4.11 & Table 4.3). The Landsat bands are narrower than the airborne bands and, with the exception of the NIR band, they are centred at different wavelengths. Therefore, some differences between the data from the two sensors should be expected (Trishchenko et al., 2002).

Different data capture geometry between the sensors could also account for some of the differences. While it was attempted to ensure alignment between the airborne and Landsat pixels, it is unlikely that the spectral information aggregated within each pixel was gathered from the exact same area on the ground. Depending on the scene heterogeneity, differences in the pixel spectral mixture may have produced different reflectance values. This issue relates to the modifiable areal unit problem (MAUP) in remote sensing, specifically the aggregation problem, where the reflectance recorded in an image is affected by the placement of the pixels within the scene (Marceau & Hay, 1999). This may explain the large differences found in the man-made class in the River Transect site. Most man-made objects used in the comparison were small and contrasted highly with the surrounding vegetation. As with the calibration tables, the small size of these areas relative to the pixel size means they likely suffered from the adjacency effect, especially given their high contrast with their surroundings (Richter et al., 2006).

Another issue is related to the difference between images simulated at a particular spatial resolution compared to images natively acquired by a sensor at that resolution. Simulation of low-resolution images through aggregating high-resolution pixels leads to noise being artificially low compared to images natively acquired at a low resolution (Börner et al., 2001). Thus, the impact of noise may have been greater in the Landsat images than the resampled airborne images, contributing to the differences in reflectance between them.

Overall, the calibrated digital camera images were able to produce data that compared well to both terrestrial and satellite measurements of reflectance. While the reflectance accuracy of the ASD and the Landsat-8 OLI data was not assessed in this study, this research supports the notion that inexpensive cameras with proper radiometric and spectral calibration can produce data that is comparable to data from high-quality sensors.

It should be noted the reflectance values derived from this study did not cover the full spectrum of reflectance values from 0 to 1. In the ASD comparison the maximum reflectance was just over 0.50 for the camera NIR band and around 0.3 for the red and green bands. In the HSNC Landsat comparison, the highest camera reflectance was 0.40 for the NIR, 0.33 for the red, and 0.29 for the green. For the Landsat River Transect comparison the maximum camera reflectance was 0.75 for the NIR band (a large outlier), 0.28 for the red band, and 0.24 for the green band.

Unfortunately the sites being imaged did not contain many high reflectance targets. Consequently, the accuracy of the cameras at high reflectances could not be assessed in this study. In the future, imaging a scene with targets covering a wide range of reflectances from high to low would help to better assess the data quality of the cameras throughout their dynamic ranges.

Finally, while this research was able to show that calibrated camera imagery compared well to data from other sensors, it is not known how much the calibration improved the data over its raw, uncalibrated form. Future comparisons should include the raw images as well in order to show the differences between calibrated and uncalibrated data.

4.4.3 LAI-SVI Regression Modelling

The SVIs used in this research worked well for modelling LAI, with all eight SVIs resulting in strong, positive, linear relationships. This correlation between SVIs and LAI has been well established in many other studies (Broge & Leblanc, 2001; Chen, 1996; Colombo et al., 2003; Gonsamo & Pellikka, 2012; Haboudane et al., 2004; Jordan, 1969; Turner et al., 1999). While some SVIs fit the LAI data better than others, each SVI performed similarly well. The lowest R^2 was 0.740 for MSAVI, while the highest was 0.826 for MSR, a difference of only 0.086 (Table 4.4). Thus despite the MSR model fitting the LAI data marginally better, any one of them would have performed almost equally well for LAI prediction. This differs from some other studies, which have found large differences in the prediction power of different SVIs (Broge & Leblanc, 2001; Colombo et al., 2003; Turner et al., 1999).

A common issue with SVI-LAI empirical models is a tendency for the relationship to become nonlinear and saturate, with the SVI becoming insensitive to LAI differences (Baret & Guyot, 1991). The issue was not encountered in this research. All models demonstrated a linear relationship and maintained sensitivity throughout their range. This was not surprising, as the maximum LAI encountered was just over 2 m^2/m^2. Non-linearity and saturation only typically become issues at moderate to high LAIs between 2 and 6 m^2/m^2, depending on the vegetation type, the SVI being used, and experimental conditions (Baret & Guyot, 1991; Chen & Cihlar,

1996; Turner et al., 1999). Unfortunately this introduces the possibility of substantial underestimation of LAI if applying the SVI models in riparian areas with LAIs much higher than the values that were measured in the HSNC site.

An important limitation of the regression models created in this research is a lack of data. With only 6 LAI measurements and corresponding images, it is difficult to have a high level of confidence in any of the models, despite their reasonably good fit. It is possible that the good fit can be at least partially attributed to the low number of data points, causing the models to over-fit the training data. Due to the limited dataset, it was also impossible to independently validate the models. The difficulty in obtaining sufficient data to both train and validate remote sensing vegetation models has led to the widespread use of canopy reflectance models to create simulated data for empirical model training (Carlson & Ripley, 1997; Gonsamo & Pellikka, 2012; Haboudane et al., 2004). An improvement for future research would be using simulated data to train the models, reserving the field collected data for model validation. Collecting data from more field plots and/or collecting data over several years would also allow for a better assessment of the SVI-LAI relationship.

There are other confounding factors, which cause uncertainty in the SVI models. It is well known that SVIs are correlated not just with LAI, but with other vegetation properties including fractional vegetation cover and photosynthetic activity (Baret & Guyot, 1991; Glenn et al., 2008). In this research, the largest outlier in the models was for the data collected on June 07, with the LAI measured on this date being much lower than would be suggested based on the SVI values from the imagery. A difference in photosynthetic activity could possibly account for the disparity between the ground-measured LAI and the SVI value on this date.

Other confounding factors include differences in soil background effects, sun-sensor geometry, atmospheric conditions, and leaf inclination angle. SVIs have been shown to be sensitive to variations in all of these properties, further contributing to uncertainty in the models created in this research (Baret & Guyot, 1991; Broge & Leblanc, 2001).

A final issue is the fact that a single regression model was developed to predict total riparian vegetation LAI. This could impact the accuracy of the models, as the relationship between SVIs and LAI can vary depending on the vegetation type (Chen et al., 2002; Colombo et al., 2003). A potential improvement for future efforts would be to stratify the site by vegetation type, developing separate LAI models for each. However, such an approach would complicate the implementation of the model, and is not as practical for coarse-spatial resolution imagery where it is more difficult to separate out different vegetation types.

4.4.4 Spatial Resolution Impact on LAI Modelling and Prediction

4.4.4.1 HSNC Site

The results of the regression of LAI and MSR over the HSNC site demonstrated that it was possible to obtain models with good fit from spatial resolutions as coarse as 300 metres (Figure 4.22). However, the models were found to change along with the resolution. The slope of the regression models remained fairly constant until a resolution of 20 m where it began steadily increasing up to 150 m, followed by large increases and decreases with further changes in spatial resolution (Figure 4.23). The intercept remained stable until 70 m, followed by a gradual increase until 150 m. After 150 m the intercept experienced large increases and decreases. Thus, while the models created at 18 cm and 300 m had a similarly good fit to the data, the models themselves were very different, suggesting that caution should

be used when applying a model developed at one resolution to imagery at another resolution. Beyond the 300 m spatial resolution the model fit collapsed, with no discernable relationship between MSR and LAI being evident.

When the models created from each resolution were used to predict LAI (Method A), the LAI prediction RMSE followed the inverse pattern as the R^2 for the models (Figure 4.24). This was not surprising given the models were used to predict the training data. Thus, when the model fit the LAI data well, the LAI prediction RMSE was low, and when the model fit was poor, RMSE was high.

Examining the prediction error of the individual images, it was shown that beyond a spatial resolution of 125 m the changes in LAI prediction error with decreasing resolution became large and unpredictable, increasing and decreasing seemingly at random (Figure 4.25). This indicates that large changes in the models and/or the MSR data were occurring as resolution decreased beyond this point. Beyond the 300-m spatial resolution predicted LAI changed greatly and erratically, corresponding with the large increase in model RMSE for these spatial resolutions.

The results using a single SVI model to predict LAI at every spatial resolution (Method B) gave more insight into what is occurring with the underlying MSR data. Since the model was held constant, changed in predicted LAI with decreasing resolution are exclusively due changes in the MSR values. With Method B, LAI prediction RMSE remained stable until the 20 m resolution, beyond which it increased more or less consistently (Figure 4.26). The prediction error trend was negative for all images, showing that as spatial resolution decreased, MSR also decreased (Figure 4.27). The decrease in predicted LAI occurred at different rates for the different images, with the rate of decrease being lower for both the May 22 and October 05 images. As both these dates had the lowest LAI and MSR values, this

result shows that the coarsening of spatial resolution seems to have had a greater impact when LAI/MSR was high. This difference in the rate of MSR decrease also explains why the slope of the models increased as resolution decreased. As the higher MSR values decreased, they became closer in value to the lower MSR values, which had not decreased by the same amount. This compressed the MSR dynamic range, and consequently increased the slope of the models.

Beyond the 125-m resolution, the pattern changed somewhat, with predicted LAI increasing for certain images while still decreasing for others (Figure 4.27). For example, when resolution decreased from 175 m to 200 m, predicted LAI decreased for the July 09 image, but increased for the August 01 image. Beyond 300 m, the pattern destabilized further, with large increases in predicted LAI for certain images (August 27, October 05). The large changes in MSR for certain dates at these coarse resolutions resulted in very different regression models being created, thus, accounting for the large differences in predicted LAI when Method A was used.

The reduction in MSR as resolution decreased was likely due to increased mixing of the riparian spectral signal with those of adjacent areas. At coarse resolutions, pixels on the border of the HSNC study area became progressively more mixed with spectra from the river, the north and south parking lots, and at very coarse resolutions, with the area outside the image borders. Because these areas had lower MSR values than the riparian vegetation, the aggregate MSR value for the site would be lowered as mixing increased. Figure 4.32 demonstrates this effect. It shows MSR calculated from the July 09 image, with the HSNC study site boundary, and the pixel grids from four different spatial resolutions. Note that as resolution coarsened the pixels along the border of the study site became increasingly mixed with neighbouring areas.

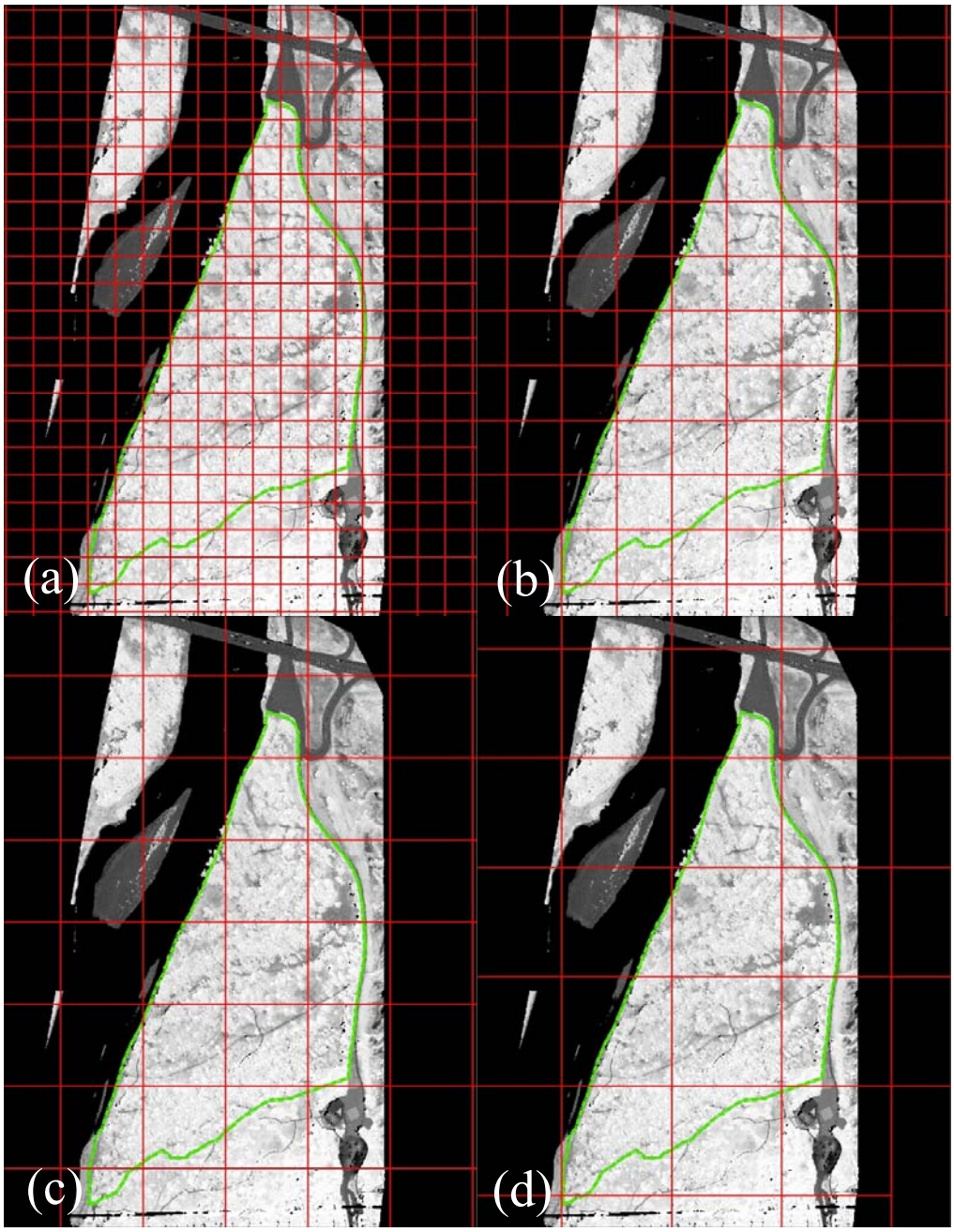

Figure 4.32 – MSR image from July 09 over the HSNC site with resampled image pixel grids of varying spatial resolutions overlaid. The HSNC study area boundary is shown in green. White indicates a high MSR value, while black indicates low MSR. Pixel grids (shown in red) are for the following resolutions: (a) 50-m pixels, (b) 100-m pixels, (c) 150 m pixels, and (d) 200 m pixels.

Spectral mixtures can also explain why the changes in LAI prediction tended to be greater for images with higher MSR values. When the MSR value for the riparian area was low, the spectral mixing impact was lower, because the MSR of the

adjacent areas was similar to that of the riparian area itself. When MSR for the site was high, the mixing had a more pronounced impact, because the MSR of the surrounding areas was lower than that of the study site.

The changing patterns in LAI prediction for each image at resolutions beyond 125 m does suggest that something else besides increasing spectral mixing is occurring at these low-spatial resolutions. A possible cause involves the placement of the image pixels. The image mosaics from the different dates were all different sizes, leading to varying locations for the pixels when the images were resampled. At coarse resolutions beyond 100 m, the HSNC site was composed of very few pixels, and the influence of the border pixels on the aggregate spectra for the site was large. Depending on where the border pixels were located, they would have mixed with the spectra of adjacent areas to differing degrees, leading to the unpredictable patterns observed at these coarse resolutions.

Figure 4.33 shows this effect. The figure shows MSR calculated from the July 09 and August 01 HSNC images. Overlaid is the HSNC study area outline and the pixel grids for the 175 m and 200 m resolutions. As the resolution decreased from 175 m to 200 m, the predicted LAI for the July 09 image decreased (Figures 4.25 and 4.27). On the other hand, for the August 01 image, predicted LAI increased between these two resolutions. Examining the July 09 images, it can be seen that between 175 m and 200 m, there was an increase in the number of pixels partially mixed with the water and the area outside the image border that were aggregated within the study area. Conversely, because of the placement of the pixels, the opposite is true of the August 01 image; the number of pixels mixed with the water and outside the image border that were being aggregated within the study area polygon decreased as the

resolution decreased. Thus, while the average MSR value decreased between the resolutions for July 09, it increased for August 01.

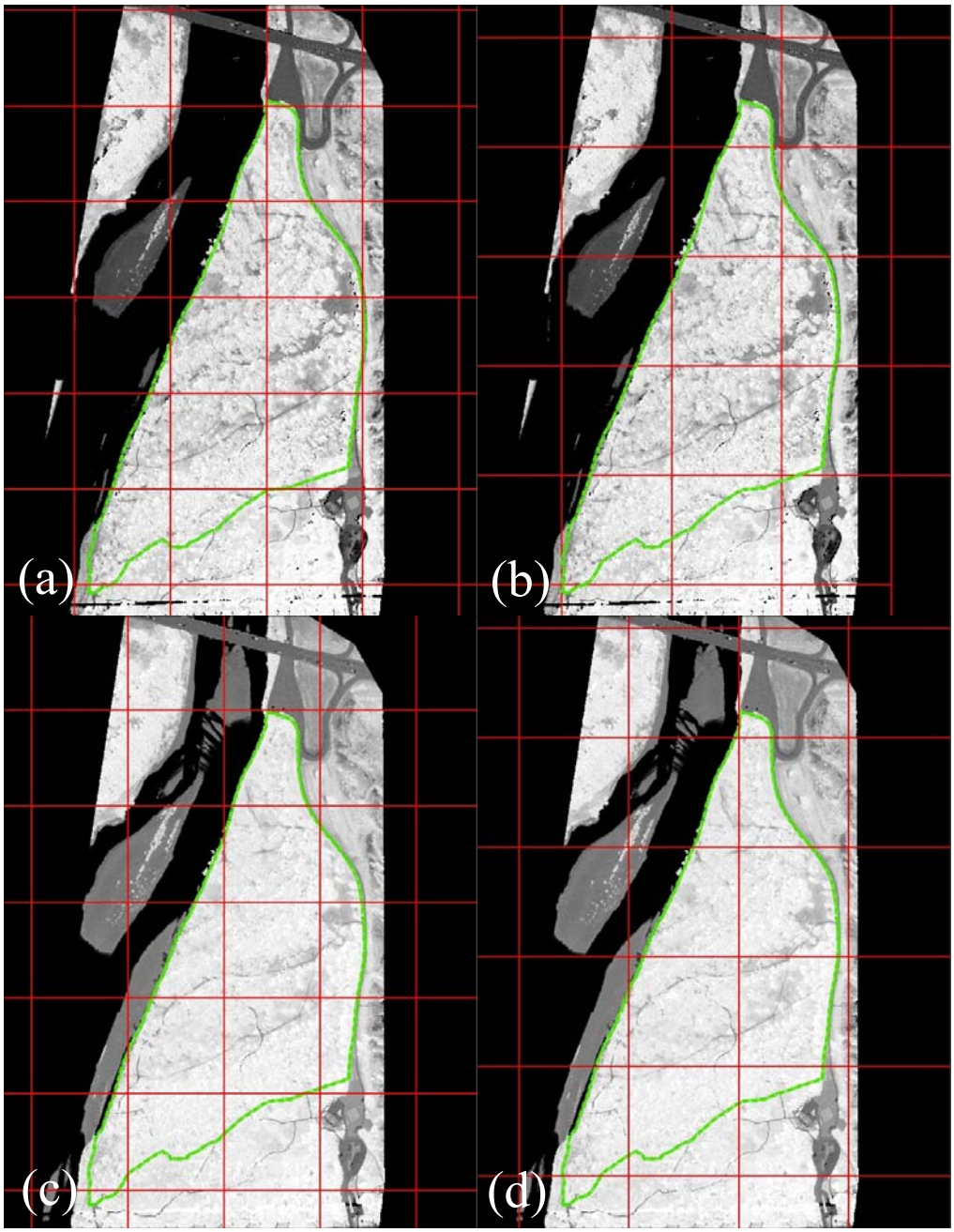

Figure 4.33 – MSR images from July 09 and August 01 over the HSNC site with resampled image pixel grids overlaid. The HSNC study area boundary is shown in green. White indicates a high MSR value, while black indicates low MSR. Images and pixel grids (shown in red) are: (a) July 09 (175-m pixels), (b) July 09 (200-m pixels), (c) August 01 (175-m pixels), and (d) August 01 (200 m pixels).

The large outlier for the August 27 image at the 400-m resolution should be addressed (Figure 4.27). Between 350 m and 400 m, the MSR, and thus predicted LAI massively increased. Figure 4.34 shows the August 27 MSR image with the 350-m and 400-m pixel grids overlaid.

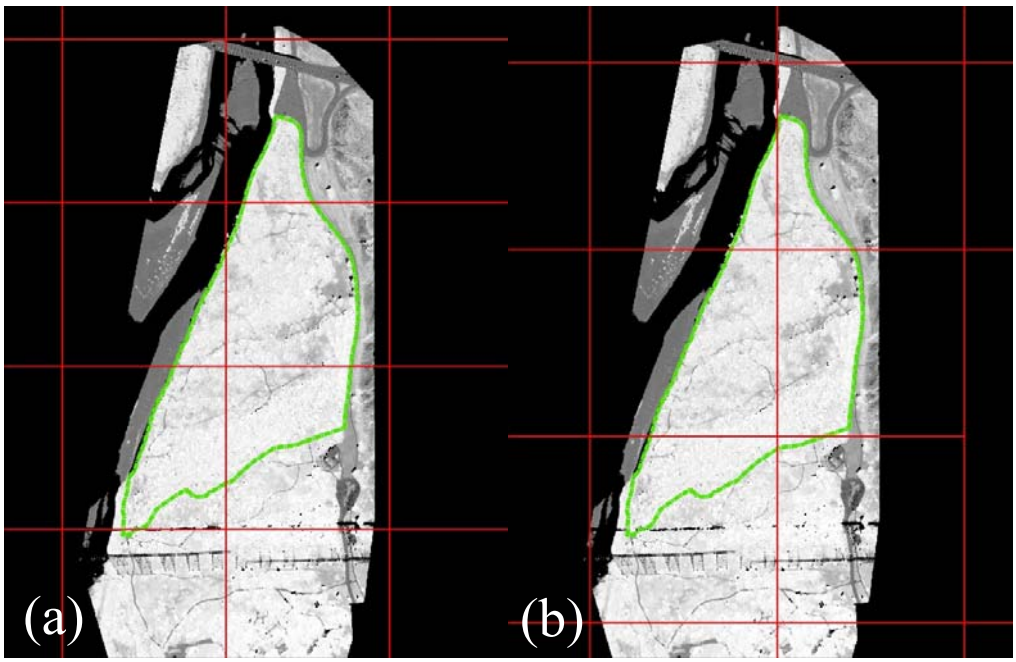

Figure 4.34 – MSR image from August 27 over the HSNC site with pixel grids from two different spatial resolutions overlaid. The HSNC study boundary is shown in green. White indicates a high MSR value, while black indicates low MSR. Pixel grids (shown in red) are: (a) 350-m pixels, and (b) 400-m pixels.

Based on the figure it does not seem that differences in the pixel spectral mixture would have led to the observed changes in predicted LAI. It appears that a greater amount of mixing with the water and outside the image border is occurring within the 400-m pixels. Thus, it should be expected that the resulting MSR value would be lower. Examination of the reflectance data used to calculate MSR shows that between 350 m and 400 m, both NIR and red reflectance aggregated within the study area decreased due to the increased mixture with the water and area outside the image border. Both NIR and red reflectance decreased by a similar amount (2% reflectance for the NIR and 2.4% for red). For the NIR band this resulted in a decrease

from 10.3% reflectance to 8.3%. For the red band, which was much lower than the NIR reflectance at 2.7%, reflectance decreased to 0.003%. These values resulted in an MSR of 1.27 at 350 m, and 4.90 at 400 m. One issue with SVIs like MSR is that the range of possible values is not normalized to a maximum possible value like the NDVI, which can reach a maximum of 1. Thus, as the red band reflectance approaches 0, the MSR value will exponentially increase. Figure 4.35 demonstrates this effect. In the figure, NIR reflectance is held constant at 10%, with red reflectance starting at 3% and decreasing steadily, approaching 0%. Because of this issue, the MSR index should not be used for estimating LAI when red reflectance is very low.

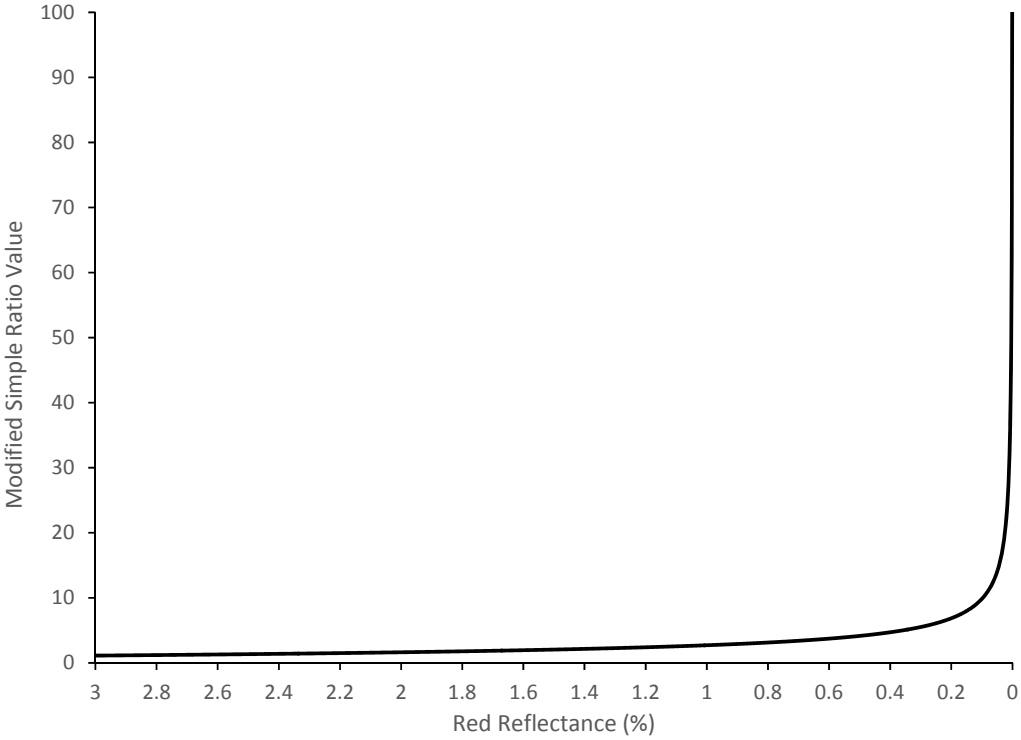

Figure 4.35 – Modified Simple Ratio values with decreasing red band reflectance. In this example NIR reflectance is held constant at 10%.

4.4.4.2 River Transect Site

The use of Method A for the River Transect site delivered different results compared to when it was used for the HSNC site. Rather than the average LAI remaining essentially unchanged until resolutions beyond 100 m, LAI began steadily

increasing when resolution decreased beyond 10 m (Figure 4.28). The largest over-prediction of LAI occurred at 300 m, the same resolution that had the lowest prediction error for all images at the HSNC site. While these results differed from the LAI prediction error in HSNC, the pattern is similar to the increase in the regression model slope as spatial resolution decreased (Figure 4.23). The largest departure from the pattern occurred at 500 m, where modelled LAI increased even as the model slope decreased; however, this difference may be accounted for by the increase in the intercept of the model. Based on these results, it appears that the changes in the predicted LAI from using Method A in the River Transect site were mostly due to the changing slope and intercept of the models, rather than changes in the underlying MSR data. The difference of these results from those of the HSNC site also shows that the models created in the HSNC site, while capable of fitting to the training LAI data, may not be valid and transferable to other riparian areas.

Using Method B in this site shows that the underlying MSR data did indeed change as spatial resolution decreased (Figure 4.29). Once again the average predicted LAI remained stable until 10 m, followed by a steady decrease, with this trend bottoming out around 300 m. These findings were similar to when Method B was applied at the HSNC site. Once again, the major factor behind the changes in MSR and thus changes in LAI prediction appears to have been spectral mixing of the riparian signal with adjacent areas, including water, gravel bars, roads and buildings, prairie grass, agricultural fields, and the areas outside the border of the image mosaics. Figure 4.36 shows an MSR image of a section of the River Transect site with the riparian area boundaries and pixel grids from four different resolutions overlaid. As with the HSNC site, as spatial resolution decreased, the pixels being aggregated

within the riparian polygons were increasingly mixed with the river, the prairie, and to a lesser degree, the area outside the image boundary.

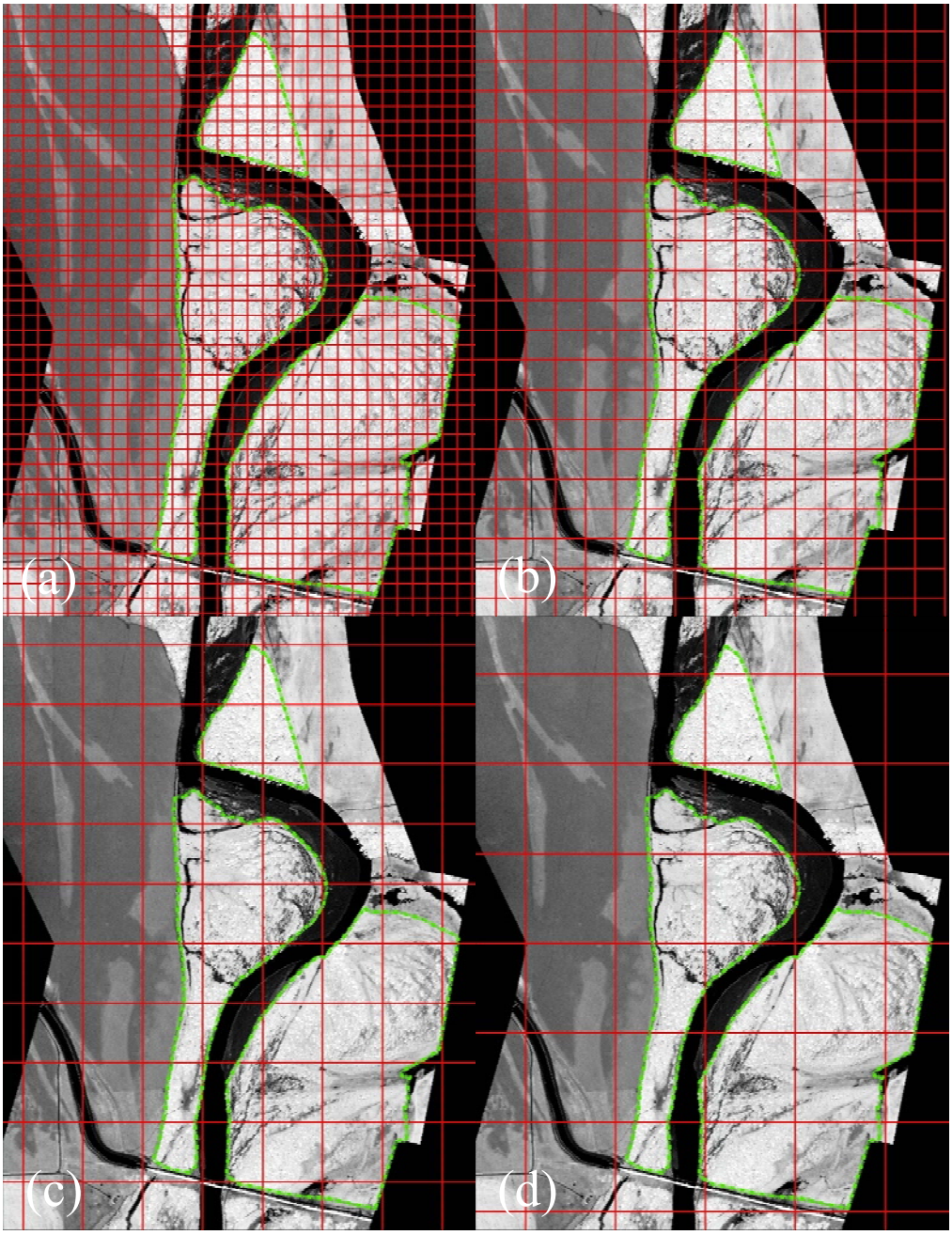

Figure 4.36 – MSR image from a portion of the River Transect site with resampled image pixel grids overlaid. White indicates a high MSR value, while black indicates low MSR. The green borders show 3 riparian areas within which spectra were averaged to calculate LAI. Pixel grids (shown in red) are: (a) 50-m pixels, (b) 100-m pixels, (c) 200-m pixels, and (d) 300-m pixels.

For individual riparian areas along the river, there was no relationship noted between the area of a riparian zone and the sensitivity of predicted LAI to spatial resolution (Figure 4.30). Therefore, it appears that the size of a riparian area has little impact on how greatly LAI prediction is affected by changes in spatial resolution.

The relationship between the initial MSR value calculated for a riparian area and the average change in LAI due to changing spatial resolution was also insignificant when Method A was used; however, there was a moderate correlation evident between the two variables when Method B was used (Figure 4.31). As with the HSNC site, this relationship shows that the impact of decreasing spatial resolution on modelled LAI was typically greater when the initial MSR value is high. As noted with the HSNC site, this effect could be due to the large spectral difference between high MSR riparian areas and their surroundings, with spectral mixing having a more pronounced impact if the reflectance of the riparian area contrasts greatly with the surrounding targets. It is important to note that the correlation was not very strong, with an R^2 of only 0.44, showing that other factors are contributing to the changes in MSR with decreasing spatial resolution.

4.4.4.3 General Discussion of Spatial Resolution

The findings from both the HSNC and River Transect sites demonstrated that the relationship between MSR and riparian LAI was not scale invariant. As spatial resolution decreased, MSR values were progressively reduced, leading to lower LAI predictions as resolution coarsened. This reduction in MSR tended to be larger when the initial MSR value was high. Consequently, LAI regression models developed using coarser spatial resolution data had steeper slopes as the MSR dynamic range was compressed. The reduction in MSR also meant that using a model developed at a higher spatial resolution resulted in lower LAI predictions when applied at a lower

resolution. Minor differences were evident at spatial resolutions as high as 10 m or 15 m, although moderate differences did not generally manifest until spatial resolution coarsened beyond 30 m.

By using models which were developed at each resolution, the effect of MSR reduction could be compensated for, and reasonable LAI predictions were possible at fairly coarse spatial resolutions in the HSNC site. However, when applied to the River Transect images, the models developed at each resolution overcompensated for the reduction in MSR and led to LAI being over-predicted at lower spatial resolutions. Thus, while it may be possible to accurately model LAI at coarse spatial resolutions by using a resolution-appropriate LAI model, the evidence provided from this research is inconclusive.

The results of this study suggest that low-spatial resolution sensors such as MODIS (250-m spatial resolution), MERIS (300-m spatial resolution), AVHRR (1.1-km spatial resolution), and SPOT Vegetation (1.15-km spatial resolution) should be avoided when modelling riparian LAI. However, it appears that sensors with spatial resolutions of 30 m or better can be used for riparian LAI modelling with minimal negative scale issues. There are many satellite sensors offering spatial resolutions of 30 m or better, including Landsat-8 OLI (30-m spatial resolution), Rapideye (5-m spatial resolution), IKONOS (4-m spatial resolution), and SPOT 6 and 7 (6-m spatial resolution). Therefore, satellite imagery is well suited for operational riparian LAI monitoring, and the very high sub-metre spatial resolutions offered by airborne or UAV imaging are not needed. Higher resolution data may be needed if it is desired to map the spatial distribution of LAI within a given riparian area; however, for the landscape scale estimates used in this study, lower spatial resolution data are sufficient.

Future research should examine the impact of other sensor attributes on riparian LAI modelling. Other characteristics of interest include the spectral resolution, number of spectral bands, band placement, and more. Research on spectral bands could be performed using a hyperspectral sensor, which would allow a variety of different spectral band characteristics to be simulated. Studying other sensor characteristics will allow an optimal sensor to be selected for riparian LAI monitoring.

The results of this thesis were similar to the findings of some other studies, which have found that decreasing spatial resolution can have significant impacts on both SVIs (Teillet et al., 1997) and biophysical parameter modelling (Chen, 1999). In Teillet et al. (1997) large changes in NDVI were found to occur with decreasing spatial resolution, depending on the land-cover type. However, unlike the current study, NDVI did not always decrease along with resolution, and was often found to increase instead (Teillet et al., 1997). Similar to the results of the current study, Chen (1999) found that LAI estimates were progressively lower when an SVI model derived at a fine spatial resolution was used to predict LAI at coarser resolutions.

Differences in SVIs and LAI prediction seem to be influenced by the heterogeneity of the scene, especially when there is a large contrast between different land-cover types. In Teillet et al. (1997) large changes in NDVI of more than 0.2 were observed at relatively high-spatial resolutions in an image with a mixture of clear cuts and forested areas, two contrasting surfaces. Other more homogeneous areas either experienced no changes, or only changed at very coarse resolutions. In Chen (1999), large changes in predicted LAI of greater than 40% were observed when the coarse resolution pixels contained mixtures of high contrast features, such as the interfaces between forests and water. Given that the riparian areas in our study were almost

always adjacent to contrasting surfaces including water and gravel bars, this may explain the large differences in predicted LAI that occurred when resolution decreased. Future research could attempt to quantify the effects of spatial heterogeneity. This could be done by using geostatistical measures of image texture (Coburn & Roberts, 2004; Hu & Islam, 1997), or by measuring the sub-pixel fractional land cover within low-resolution images pixels (Chen, 1999).

The results of this thesis differed from Sprintsin et al. (2007), which used both high-spatial resolution IKONOS data (4-m spatial resolution) and low resolution MODIS data (250-m spatial resolution) to model LAI for a forest plantation in a desert transition zone. The average LAI and distribution of LAI values within the study area were compared between the two sensors, finding only a moderate decrease in the mean LAI (11%) and the coefficient of determination (9.6%) when MODIS imagery was used. The authors, however, mention that further decreases in spatial resolution is not desirable due to too much spectral mixture causing a loss of land-surface information. The forest plantation site they used, while somewhat heterogeneous, covered a large area (~3000 hectares) and was not narrow like the riparian areas measured in the current study. Furthermore, they compared only the mean LAI and the shape of the distribution of LAI values for all pixels within the study area rather than comparing the LAI predictions for specific areas within the site. Thus, the issue of spectral mixing may not have been as much of an issue due to the scale of comparison used in their study. These differences in methods and results reinforce the importance of selecting an appropriate spatial resolution for the size of the landscape being studied.

This research demonstrated how remotely sensed data are impacted by the MAUP, as has been observed in other studies (Arbia & Espa, 1996; Jelinski & Wu,

1996; Marceau et al., 1994). The changes in MSR and, thus, predicted LAI as spatial resolution coarsened provide evidence of the scale problem, one of the two aspects of the MAUP. At low-spatial resolutions, the placement of the image pixels and how they were aggregated within the borders of the riparian area polygons also appears to have led to differences in LAI prediction between different images at the same spatial resolution. This effect demonstrated the aggregation problem, the other aspect of the MAUP. Unfortunately, both these effects occurred simultaneously, and it is not possible to separate them based on the current research. In future work the effect of the scale problem could be better isolated by examining the differences in modelled LAI at different resolutions while holding the area constant over which high-spatial resolution pixels are aggregated into low-spatial resolution pixels. The effects of the aggregation problem could be better analyzed through controlled experiments where a variety of alternative pixel placements are tested at the same resolution.

It is important to note that the changes in riparian MSR and, consequently, the changes in modelled LAI are related to the method that was used for aggregating the data within each riparian area. In this study, a polygon was drawn around each riparian area using the highest resolution imagery. These polygons were used to average the spectral data from the images at every resolution, and these averaged spectra were used for modelling LAI.

The riparian polygons themselves are in fact another manifestation of the MAUP. If a different method was used to average the image spectra, different results could be expected. For instance, by selecting rectangular subsets located within the centre of each riparian polygon and averaging the spectra within each subset, it is possible that the impact of spectral mixture with adjacent areas would be mitigated, at least until the image spatial resolution came close to equalling or exceeding the size of

the riparian area itself. Training the SVI-LAI models using such rectangular subsets may also result in better models being created at low-spatial resolutions, allowing LAI to be modelled accurately even at these low spatial resolutions.

Using subsets for estimating LAI would not give a full assessment of riparian LAI along the river, because significant portions of the total riparian area would be excluded from the analysis. Such omissions may result in substantial errors if LAI was not spatially uniform within each riparian zone. Therefore, the method used in this study is appropriate when it is desired to characterize riparian LAI for the entire river as opposed to sampling it. Nonetheless, future research could examine the potential for this alternative approach, as it may allow riparian LAI to be reasonably estimated using lower spatial resolutions than the findings from this study suggest.

The results of this research should be interpreted with caution for a number of reasons. As previously mentioned, the confidence in the LAI regression models is low due to the small training dataset and limited dynamic range of the ground LAI measurements. The lack of data was particularly pronounced at the 450 m and 500 m resolutions, as some images were not able to be used. The lack of data also meant that there was no independent dataset to validate the models. For the River Transect site there were no ground data at all; therefore, only the differences in LAI prediction could be compared, while the accuracy of the predictions could not be assessed.

Another issue is the impact that the borders of the image mosaics had on the results. The raw pixel values for the areas beyond the border were necessarily zero, as no data was recorded there. Due to the empirical reflectance calibration, these areas were assigned a negative reflectance value. The pixels outside the borders were in many cases aggregated within the riparian area polygons, contributing to the spectral mixing occurring at low-spatial resolutions. Therefore, the changes of the riparian

MSR values were greater than if data were present in these areas. Thus, the changes observed in this study are likely more pronounced than they would be if, for instance, a satellite image of the area were used without the problem of image borders being adjacent to the riparian zone. At the same time, the presence of these borders emphasize the impact of the spectral mixing that is occurring with adjacent areas, which is valuable even if it limits the real world applicability of the results. In future research, satellite imagery could be used to avoid the impact of image borders.

A final point of caution is the fact that images of differing resolutions were simulated rather than acquired from real sensors. The aggregation of high-spatial resolution image pixels to create a lower-spatial resolution image suppresses the effects of noise, leading to unrealistic signal-to-noise ratios in the simulated images (Börner et al., 2001). To mitigate this issue, simulated noise can be added back into the resampled images (Guanter et al., 2009).

4.5 Conclusions

In this chapter the impact of image spatial resolution on estimating riparian LAI using remote sensing was investigated. Both airborne and ground data were acquired within riparian areas along the Oldman River in Southern Alberta and LAI was empirically modelled using eight different SVIs calculated from the remotely sensed data. Of the SVIs tested, the MSR resulted in the most accurate LAI model, and it was selected for further analysis.

Different spatial resolutions were simulated through spatial resampling of the airborne images. The spatial resolutions examined in this study ranged from 0.18 m to 500 m. LAI was modelled at every simulated resolution using the MSR index using two methods: firstly, separate regression models were created and applied at each

spatial resolution separately. Secondly, LAI was modelled at each resolution using the same model, which was derived from the original high-spatial resolution imagery.

The results of this study indicate that the empirical relationship between MSR and LAI is not scale invariant. Decreasing image spatial resolution was found to result in a progressive reduction of MSR values within the riparian areas examined. The reduction in MSR values with decreasing spatial resolution is likely the result of increased mixing of the riparian spectral signal with adjacent areas, most of which have a lower MSR value than the riparian areas. The reduction in MSR was more pronounced in areas with a high initial MSR value, because there was a greater contrast between the riparian area and that of the surrounding areas, exacerbating the impact of spectral mixing.

Despite the changing relationship, differences in modelled LAI were only evident beyond resolutions of approximately 10 m, while moderate changes only manifested beyond 30 m. Consequently, it does not appear necessary to use very high-spatial resolution data for operational monitoring of riparian LAI. Many modern satellite sensors have spatial resolutions of 30 m or higher, providing plenty of choices. Furthermore, by using subsets within each riparian area for training LAI models and for LAI prediction, it may be possible to avoid some spectral mixture effects, allowing LAI to be predicted at coarser spatial resolutions than suggested by the results in this thesis.

While the findings in this study suggest that low-spatial resolution sensors should be avoided in riparian LAI monitoring, for larger more homogeneous areas it is likely acceptable to select a sensor with a lower spatial resolution. Thus, it is important to select a spatial resolution which is suitable for the size of the landscape being studied.

Several improvements are suggested for future research on this topic. First of all, more sets of LAI measurements and corresponding images should be used to create the LAI models, and the models should be validated using a separate set of LAI measurements. Secondly, the influence of the image borders on the results should be removed. Potential causal factors for the observed changed in the LAI modelling results, such as spatial heterogeneity, should be quantitatively investigated. Finally, the spatial resolution simulation should be made more robust and realistic.

The secondary objective of this research was to assess the ability of consumer digital cameras to provide data which are comparable to professional-grade sensors. To assess the camera data quality, camera images were calibrated reflectance units and compared to data from an ASD spectroradiometer as well as the Landsat-8 OLI satellite sensor. The camera data compared reasonably well to both sensors. There were, however, some large discrepancies in reflectance values, suggesting that direct comparison between them may lead to errors in some cases.

Future research should investigate whether these errors are a result of the camera data, differences between the sensors, or due to the methods used to calibrate the image data. Future comparisons should also ensure that the full dynamic range of the cameras from low to high spectral reflectance is validated. A final improvement would be to include uncalibrated sensor data in the comparison in order to assess to what extent the calibrations improved the camera images.

5. CONCLUSIONS

This thesis was motivated by the need for the monitoring of riparian areas on dam-regulated rivers to assess the health response of riparian vegetation to alternative water management strategies. The leaf area index (LAI) was targeted as the variable of interest due to its key role in vegetation biophysical processes. Remote sensing is capable of estimating LAI for an entire river basin; however, in order to record the spatial variation in LAI along the river, it is important to select a sensor system with an appropriate spatial resolution. Thus, the research in this thesis examined the sensitivity of modelled riparian LAI results to differences in the sensor spatial resolution.

In order to accomplish this goal, high-spatial resolution image data were obtained using inexpensive digital cameras. The cameras were first spatially, radiometrically, and spectrally characterized and calibrated. This was done to compensate for common aberrations associated with digital camera imagery, allowing them to be properly used in the same way as quantitative sensors. In addition to facilitating the main objective of the thesis, this work was motivated by a lack of detailed methods outlined in the remote sensing literature for performing digital camera characterization and calibration. The need for such methods are made more important given the proliferation of digital cameras being used now for remote sensing, especially by non-experts who may not be aware of the issues, let alone how to correct them.

What follows is a discussion of the major findings from this thesis. Directions for possible future research are also suggested.

5.1 Key Research Findings and Future Research

5.1.1 Digital Camera Use in Quantitative Remote Sensing

Following spectral and radiometric calibration, the data from the Canon Powershot S50 digital cameras used in this research compared quite well to terrestrial and satellite measurements of spectral reflectance. Some large differences in spectral reflectance were found in some cases (as high as 20% differences in reflectance), indicating potential issues remain even after calibration; however, these discrepancies may also be the result of differences in the ground areas being compared or differences in the spectral characteristics of the sensors.

Despite the favourable comparison, the digital cameras were not of the same quality as professional-grade remote sensors. Signal-to-noise ratios were mediocre, and the cameras were afflicted by a number of other issues, including optical lens distortion, vignetting, and nonlinear radiometric responses to changes in light intensity. Calibrations were developed and implemented, which successfully compensated for the image distortion and nonlinear radiometric responses. Despite the camera responses being made linear, the radiometric resolution of the cameras remains poor at high-signal levels.

Future work should examine further calibration of the cameras to compensate for some of the other measured effects such as vignetting and image noise. Further validation of the calibrated images should also be performed, which ensures that the full dynamic range of the cameras is validated, rather than the limited coverage of low spectral reflectances found in this thesis. Finally, future comparisons should include the uncalibrated camera imagery as well to show to what extent the calibrations improve the images over their raw form.

This thesis contributed to the remote sensing literature by demonstrating methods for measuring key camera characteristics, as well as methods to calibrate camera data to be used in quantitative remote sensing applications. The research was also able to show that following calibration, digital cameras are capable of providing data which are comparable to commonly used professional-grade sensors.

5.1.2 Spatial Resolution Impact on Riparian LAI Modelling

This research demonstrated that the relationship between LAI and spectral vegetation indices was not scale invariant. SVI values calculated from the remotely sensed images became gradually diminished as resolution decreased. Consequently, LAI was progressively under predicted when the same model was applied at every spatial resolution.

While the relationship was found to change, differences in predicted LAI did not become evident until spatial resolution coarsened beyond 10 m, and moderate differences only manifested beyond 30 m. Based on these results, using any sensor with a spatial resolution of 30 m or higher would likely be appropriate. As there is an abundance of satellite sensors with resolutions of 30 m or higher, the selection of a sensor for riparian LAI monitoring should not be greatly limited by spatial resolution requirements. However, sensors with a very low spatial resolution should not be used for this application.

It may be possible to compensate for the reduction in MSR values at coarse spatial resolutions by using models which are developed at the same spatial resolution they are applied at, but the evidence for this is inconclusive based on the results from this thesis. Accurate LAI predictions were possible when models developed at low-spatial resolutions were used to predict LAI within the HSNC site; however, when the models were used in the River Transect site, LAI predictions progressively

increased as spatial resolution decreased. Taking care to train the models using rectangular training subsets taken from within larger riparian areas may lead to better models being created, allowing accurate LAI predictions using low-spatial resolution sensors. This possibility should be investigated in the future.

Several issues cast doubts on the results from this study. Firstly, the use of only six LAI measurements and corresponding image spectral measurements to create the LAI prediction models does not inspire great confidence in the model accuracy. The lack of data also prevented any validation of the models. Ground measurements of LAI were completely lacking in the River Transect site, preventing the LAI estimates in this site from being assessed for accuracy. Future studies would benefit from more robust model training and validation.

Another limiting factor was the presence of image boundaries, which contributed to the spectral mixture of pixels in some cases. This effect likely exacerbated the changes in predicted LAI that were observed with coarsening spatial resolution. This issue could be avoided by using satellite imagery offering full coverage of the river floodplain as well as adjacent areas.

This thesis contributed to the geographical and remote sensing literature in a number of ways. Firstly, there have been few studies which have attempted to estimate riparian LAI using remote sensing, a literature gap which this thesis has helped fill. The research also further demonstrated how remote sensing data are impacted by the modifiable areal unit problem by showing its effects within a specific application. Lastly, this research provides a framework for selecting an appropriate sensor spatial resolution for subsequent studies of riparian LAI.

Future studies should investigate the sensitivity of LAI modelling results to other sensor characteristics, such as the spectral resolution, number of spectral bands,

or the portions of the electromagnetic spectrum sampled by the sensor. If further investigation of spatial resolution are carried out, the causes of the variations in modelled LAI with decreasing spatial resolution should be investigated in greater detail. One possible avenue of investigation is quantifying the impact of spatial heterogeneity on LAI estimates as resolution decreases.

REFERENCES

Adams, J. B., Smith, M. O., & Gillespie, A. R. (1993). Imaging spectroscopy: Interpretation based on spectral mixture analysis. In C. M. Pieters & P. Englert (Eds.), *Remote geochemical analysis: elemental and mineralogical composition* (pp. 145 - 166). Cambridge, UK: Cambridge University Press.

Agriculture and Agrifood Canada. (1980). Soils of the Lethbridge Area 82-H. Retrieved January 07, 2016, from http://sis.agr.gc.ca/cansis/publications/surveys/ab/ab82h/index.html

Alberta Agriculture and Forestry. (2003). Agroclimatic Atlas of Alberta: Weather in Alberta. Retrieved January 8, 2016, from http://www1.agric.gov.ab.ca/$department/deptdocs.nsf/all/sag6295

AMEC. (2009). South Saskatchewan River Basin in Alberta Water Supply Study. Retrieved April 12, 2014, from http://www1.agric.gov.ab.ca/$Department/deptdocs.nsf/all/irr13053/$FILE/ssrb_main_report.pdf

Anbumozhi, V., Radhakrishnan, J., & Yamaji, E. (2005). Impact of riparian buffer zones on water quality and associated management considerations. *Ecological Engineering, 24*(5), 517-523. doi: http://dx.doi.org/10.1016/j.ecoleng.2004.01.007

Arbia, G., & Espa, G. (1996). Effects of the MAUP on image classification. *Geographical Systems*(3), 123-141.

Arias, D., Calvo-Alvarado, J., & Dohrenbusch, A. (2007). Calibration of LAI-2000 to estimate leaf area index (LAI) and assessment of its relationship with stand productivity in six native and introduced tree species in Costa Rica. *Forest Ecology and Management, 247*(1–3), 185-193. doi: http://dx.doi.org/10.1016/j.foreco.2007.04.039

ASD Inc. (2010). Fieldspec 3 User Manual. Retrieved January 16, 2014, from http://support.asdi.com/Document/Documents.aspx

Asner, G. P., Scurlock, J. M. O., & A. Hicke, J. (2003). Global synthesis of leaf area index observations: implications for ecological and remote sensing studies. *Global Ecology and Biogeography, 12*(3), 191-205. doi: 10.1046/j.1466-822X.2003.00026.x

Asrar, G., Fuchs, M., Kanemasu, E. T., & Hatfield, J. L. (1984). Estimating Absorbed Photosynthetic Radiation and Leaf Area Index from Spectral Reflectance in Wheat1. *Agron. J., 76*(2), 300-306. doi: 10.2134/agronj1984.00021962007600020029x

Asrar, G., Kanemasu, E. T., Miller, G. P., & Weiser, R. L. (1986). Light Interception and Leaf Area Estimates from Measurements of Grass Canopy Reflectance. *Geoscience and Remote Sensing, IEEE Transactions on, GE-24*(1), 76-82. doi: 10.1109/TGRS.1986.289590

Baret, F., & Guyot, G. (1991). Potentials and limits of vegetation indices for LAI and APAR assessment. *Remote Sensing of Environment, 35*(2–3), 161-173. doi: http://dx.doi.org/10.1016/0034-4257(91)90009-U

Baret, F., Guyot, G., & Major, D. J. (1989). *TSAVI: a vegetation index which minimizes soil brightness effects on LAI and APAR estimation.* Paper presented at the Geoscience and Remote Sensing Symposium, 1989. IGARSS'89. 12th Canadian Symposium on Remote Sensing., 1989 International.

Barnard, K., & Funt, B. (2002). Camera characterization for color research. *Color Research & Application, 27*(3), 152-163. doi: 10.1002/col.10050

Beaty, C. B. (1975). *The landscapes of southern Alberta: a regional geomorphology*: University of Lethbridge, Production Services.

Beck, P. S. A., Atzberger, C., Høgda, K. A., Johansen, B., & Skidmore, A. K. (2006). Improved monitoring of vegetation dynamics at very high latitudes: A new method using MODIS NDVI. *Remote Sensing of Environment, 100*(3), 321-334. doi: http://dx.doi.org/10.1016/j.rse.2005.10.021

Belsky, A. J., Matzke, A., & Uselman, S. (1999). Survey of livestock influences on stream and riparian ecosystems in the western United States. *Journal of Soil and Water Conservation, 54*(1), 419-431.

Bendea, H., Boccardo, P., Dequal, S., Giulio Tonolo, F., Marenchino, D., & Piras, M. (2008). Low cost UAV for post-disaster assessment. *The International Archives of the Photogrammetry, Remote Sensing and Spatial Information Sciences, 37*(Part B), 1373-1379.

Börner, A., Wiest, L., Keller, P., Reulke, R., Richter, R., Schaepman, M., & Schläpfer, D. (2001). SENSOR: a tool for the simulation of hyperspectral remote sensing systems. *ISPRS Journal of Photogrammetry and Remote Sensing, 55*(5), 299-312.

Bouguet, J. Camera Calibration Toolbox for Matlab. Retrieved April 01, 2014, from http://www.vision.caltech.edu/bouguetj/calib_doc/index.html

Braatne, J., Rood, S., Goater, L., & Blair, C. (2008). Analyzing the Impacts of Dams on Riparian Ecosystems: A Review of Research Strategies and Their Relevance to the Snake River Through Hells Canyon. *Environmental Management, 41*(2), 267-281. doi: 10.1007/s00267-007-9048-4

Braatne, J. H., Jamieson, R., Gill, K. M., & Rood, S. B. (2007). Instream flows and the decline of riparian cottonwoods along the Yakima River, Washington, USA. *River Research and Applications, 23*(3), 247-267.

Breuer, M., & Albertz, J. (2000). Geometric correction of airborne whiskbroom scanner imagery using hybrid auxiliary data. *International Archives of Photogrammetry and Remote Sensing, 33*(B3/1; PART 3), 93-100.

Brismar, A. (2002). River Systems as Providers of Goods and Services: A Basis for Comparing Desired and Undesired Effects of Large Dam Projects. *Environmental Management, 29*(5), 598-609. doi: 10.1007/s00267-001-0058-3

Broge, N. H., & Leblanc, E. (2001). Comparing prediction power and stability of broadband and hyperspectral vegetation indices for estimation of green leaf area index and canopy chlorophyll density. *Remote Sensing of Environment, 76*(2), 156-172. doi: http://dx.doi.org/10.1016/S0034-4257(00)00197-8

Brown, D. C. (1966). Decentering distortion of lenses. *Photometric Engineering, 32*(3), 444-462.

Bruegge, C. J., Stiegman, A. E., Rainen, R. A., & Springsteen, A. W. (1993). Use of Spectralon as a diffuse reflectance standard for in-flight calibration of earth-orbiting sensors. *Optical Engineering, 32*(4), 805-814.

Buermann, W., Dong, J., Zeng, X., Myneni, R. B., & Dickinson, R. E. (2001). Evaluation of the Utility of Satellite-Based Vegetation Leaf Area Index Data for Climate Simulations. *Journal of Climate, 14*(17), 3536-3550.

Carlson, T. N., & Ripley, D. A. (1997). On the relation between NDVI, fractional vegetation cover, and leaf area index. *Remote Sensing of Environment, 62*(3), 241-252. doi: http://dx.doi.org/10.1016/S0034-4257(97)00104-1

Catrysse, P. B., Liu, X., & El Gamal, A. (2000). *QE reduction due to pixel vignetting in CMOS image sensors.* Paper presented at the Electronic Imaging.

Chen, D., Stow, D. A., & Gong, P. (2004). Examining the effect of spatial resolution and texture window size on classification accuracy: an urban environment case. *International Journal of Remote Sensing, 25*(11), 2177-2192. doi: 10.1080/01431160310001618464

Chen, J. M. (1996a). Evaluation of vegetation indices and a modified simple ratio for boreal applications. *Canadian Journal of Remote Sensing, 22*(3), 229-242.

Chen, J. M. (1996b). Optically-based methods for measuring seasonal variation of leaf area index in boreal conifer stands. *Agricultural and Forest Meteorology, 80*(2), 135-163.

Chen, J. M. (1999). Spatial scaling of a remotely sensed surface parameter by contexture. *Remote Sensing of Environment, 69*(1), 30-42.

Chen, J. M., & Black, T. A. (1992). Defining leaf area index for non-flat leaves. *Plant, Cell & Environment, 15*(4), 421-429. doi: 10.1111/1365-3040.ep8115326

Chen, J. M., & Cihlar, J. (1995). Plant canopy gap-size analysis theory for improving optical measurements of leaf-area index. *Applied Optics, 34*(27), 6211-6222. doi: 10.1364/AO.34.006211

Chen, J. M., & Cihlar, J. (1996). Retrieving leaf area index of boreal conifer forests using Landsat TM images. *Remote Sensing of Environment, 55*(2), 153-162. doi: http://dx.doi.org/10.1016/0034-4257(95)00195-6

Chen, J. M., Govind, A., Sonnentag, O., Zhang, Y., Barr, A., & Amiro, B. (2006). Leaf area index measurements at Fluxnet-Canada forest sites. *Agricultural and Forest Meteorology, 140*(1–4), 257-268. doi: http://dx.doi.org/10.1016/j.agrformet.2006.08.005

Chen, J. M., Pavlic, G., Brown, L., Cihlar, J., Leblanc, S. G., White, H. P., . . . Pellikka, P. K. E. (2002). Derivation and validation of Canada-wide coarse-resolution leaf area index maps using high-resolution satellite imagery and ground measurements. *Remote Sensing of Environment, 80*(1), 165-184. doi: http://dx.doi.org/10.1016/S0034-4257(01)00300-5

Chen, T., Catrysse, P. B., El Gamal, A., & Wandell, B. A. (2000). *How small should pixel size be?* Paper presented at the SPIE 3965: Sensors and Camera Systems for Scientific, Industrial, and Digital Photography Applications.

Church, J. C., Yixin, C., & Rice, S. V. (2008, 3-6 April 2008). *A Spatial Median Filter for noise removal in digital images.* Paper presented at the Southeastcon, 2008. IEEE.

Clark, C. D. (1990). Remote sensing scales related to the frequency of natural variation-An example from paleo-ice-flow in Canada. *Ieee Transactions on Geoscience and Remote Sensing, 28*, 503-508.

Clayton, J. S., Ehrlic, W. A., & Cann, D. B. (1977). Soils of Canada Vol. 1: Soil Report. Retrieved January 08, 2016, from http://sis.agr.gc.ca/cansis/publications/manuals/1977-soc/index.html

Coburn, C., & Roberts, A. (2004). A multiscale texture analysis procedure for improved forest stand classification. *International Journal of Remote Sensing, 25*(20), 4287-4308.

Cocks, T., Jenssen, R., Stewart, A., Wilson, I., & Shields, T. (1998). *The HyMap airborne hyperspectral sensor: the system, calibration and performance.* Paper presented at the 1st EARSEL Workshop on Imaging Spectroscopy, Zurich, Switzerland.

Colombo, R., Bellingeri, D., Fasolini, D., & Marino, C. M. (2003). Retrieval of leaf area index in different vegetation types using high resolution satellite data. *Remote Sensing of Environment, 86*(1), 120-131. doi: http://dx.doi.org/10.1016/S0034-4257(03)00094-4

Cramer, M., Stallmann, D., & Haala, N. (2000). Direct georeferencing using GPS/inertial exterior orientations for photogrammetric applications. *International Archives of Photogrammetry and Remote Sensing, 33*(B3/1; PART 3), 198-205.

Cutini, A., Matteucci, G., & Mugnozza, G. S. (1998). Estimation of leaf area index with the Li-Cor LAI 2000 in deciduous forests. *Forest Ecology and Management, 105*(1–3), 55-65. doi: http://dx.doi.org/10.1016/S0378-1127(97)00269-7

Damuth, J. (2001). Scaling of growth: plants and animals are not so different. *Proceedings of the National Academy of Sciences, 98*(5), 2113-2114.

Dark, S. J., & Bram, D. (2007). The modifiable areal unit problem (MAUP) in physical geography. *Progress in Physical Geography, 31*(5), 471-479. doi: 10.1177/0309133307083294

Datt, B. (1998). Remote Sensing of Chlorophyll a, Chlorophyll b, Chlorophyll a+b, and Total Carotenoid Content in Eucalyptus Leaves. *Remote Sensing of Environment, 66*(2), 111-121. doi: http://dx.doi.org/10.1016/S0034-4257(98)00046-7

Deblonde, G., Penner, M., & Royer, A. (1994). Measuring leaf area index with the LI-COR LAI-2000 in pine stands. *Ecology*, 1507-1511.

Doraiswamy, P. C., Moulin, S., Cook, P. W., & Stern, A. (2003). Crop yield assessment from remote sensing. *Photogrammetric Engineering & Remote Sensing, 69*(6), 665-674.

Driggers, R. G. (2003). *Encyclopedia of Optical Engineering: Las-Pho, pages 1025-2048* (Vol. 2): CRC press.

Duchemin, B., Hadria, R., Erraki, S., Boulet, G., Maisongrande, P., Chehbouni, A., . . . Simonneaux, V. (2006). Monitoring wheat phenology and irrigation in Central Morocco: On the use of relationships between evapotranspiration, crops coefficients, leaf area index and remotely-sensed vegetation indices. *Agricultural Water Management, 79*(1), 1-27. doi: http://dx.doi.org/10.1016/j.agwat.2005.02.013

Ebner, M. (2007). *Estimating the spectral sensitivity of a digital sensor using calibration targets.* Paper presented at the Proceedings of the 9th annual conference on Genetic and evolutionary computation, London, England, UK.

Elvidge, C. D., & Chen, Z. (1995). Comparison of broad-band and narrow-band red and near-infrared vegetation indices. *Remote Sensing of Environment, 54*(1), 38-48.

Environment Canada. (2013). Canada Climate Normals: 1981 - 2010. Retrieved April 12, 2014, from http://climate.weather.gc.ca/climate_normals/

European Machine Vision Association. (2010). EMVA Standard 1288, Standard for Characterization of Image Sensors and Cameras. *Release, 3*, 29.

Fallavollita, P., Balsi, M., Esposito, S., Melis, M., Milanese, M., & Zappino, L. (2013). UAS for archaeology. New perspectives on aerial documentation. *ISPRS-International Archives of the Photogrammetry, Remote Sensing and Spatial Information Sciences, 1*(2), 131-135.

Fan, L., Gao, Y., Brück, H., & Bernhofer, C. (2009). Investigating the relationship between NDVI and LAI in semi-arid grassland in Inner Mongolia using in-situ measurements. *Theoretical and Applied Climatology, 95*(1-2), 151-156. doi: 10.1007/s00704-007-0369-2

Farrell, J., Okincha, M., & Parmar, M. (2008). *Sensor calibration and simulation.* Paper presented at the SPIE 6817, Digital Photography IV.

Fensholt, R., Sandholt, I., & Rasmussen, M. S. (2004). Evaluation of MODIS LAI, fAPAR and the relation between fAPAR and NDVI in a semi-arid environment using in situ measurements. *Remote Sensing of Environment, 91*(3), 490-507.

Fiete, R. D., & Tantalo, T. (2001). Comparison of SNR image quality metrics for remote sensing systems. *Optical Engineering, 40*(4), 574-585.

Floate, K. D. (2004). Extent and patterns of hybridization among the three species of Populus that constitute the riparian forest of southern Alberta, Canada. *Canadian Journal of Botany, 82*(2), 253-264.

Fotheringham, A. S., & Wong, D. W. (1991). The modifiable areal unit problem in multivariate statistical analysis. *Environment and planning A, 23*(7), 1025-1044.

Friedl, M. A., Davis, F. W., Michaelsen, J., & Moritz, M. A. (1995). Scaling and uncertainty in the relationship between the NDVI and land surface biophysical variables: An analysis using a scene simulation model and data from FIFE. *Remote Sensing of Environment, 54*(3), 233-246. doi: http://dx.doi.org/10.1016/0034-4257(95)00156-5

Garrigues, S., Shabanov, N., Swanson, K., Morisette, J., Baret, F., & Myneni, R. (2008). Intercomparison and sensitivity analysis of Leaf Area Index retrievals from LAI-2000, AccuPAR, and digital hemispherical photography over croplands. *Agricultural and Forest Meteorology, 148*(8), 1193-1209.

GCOS. (2010). Implementation Plan for the Global Observing System for Climate in Support of the UNFCCC. Retrieved February 19, 2014, from http://www.wmo.int/pages/prog/gcos/documents/GCOSIP-10_DRAFTv1.0_131109.pdf

Gehlke, C. E., & Biehl, K. (1934). Certain effects of grouping upon the size of the correlation coefficient in census tract material. *Journal of the American Statistical Association, 29*(185A), 169-170.

Gitelson, A. A., Kaufman, Y. J., & Merzlyak, M. N. (1996). Use of a green channel in remote sensing of global vegetation from EOS-MODIS. *Remote Sensing of Environment, 58*(3), 289-298. doi: http://dx.doi.org/10.1016/S0034-4257(96)00072-7

Gitelson, A. A., & Merzlyak, M. N. (1996). Signature Analysis of Leaf Reflectance Spectra: Algorithm Development for Remote Sensing of Chlorophyll. *Journal of Plant Physiology, 148*(3–4), 494-500. doi: http://dx.doi.org/10.1016/S0176-1617(96)80284-7

Glenn, E. P., Huete, A. R., Nagler, P. L., Hirschboeck, K. K., & Brown, P. (2007). Integrating Remote Sensing and Ground Methods to Estimate Evapotranspiration. *Critical Reviews in Plant Sciences, 26*(3), 139-168. doi: 10.1080/07352680701402503

Glenn, E. P., Huete, A. R., Nagler, P. L., & Nelson, S. G. (2008). Relationship between remotely-sensed vegetation indices, canopy attributes and plant physiological processes: what vegetation indices can and cannot tell us about the landscape. *Sensors, 8*(4), 2136-2160.

Goel, N. S., & Thompson, R. L. (1984). Inversion of vegetation canopy reflectance models for estimating agronomic variables. V. Estimation of leaf area index and average leaf angle using measured canopy reflectances. *Remote Sensing of Environment, 16*(1), 69-85. doi: http://dx.doi.org/10.1016/0034-4257(84)90028-2

Goetz, S. J., & Prince, S. D. (1996). Remote sensing of net primary production in boreal forest stands. *Agricultural and Forest Meteorology, 78*(3–4), 149-179. doi: http://dx.doi.org/10.1016/0168-1923(95)02268-6

Gom, L. A., & Rood, S. B. (1999). The discrimination of cottonwood clones in a mature grove along the Oldman River in southern Alberta. *Canadian Journal of Botany, 77*(8), 1084-1094.

Gonsamo, A., & Pellikka, P. (2012). The sensitivity based estimation of leaf area index from spectral vegetation indices. *ISPRS Journal of Photogrammetry and Remote Sensing, 70*(0), 15-25. doi: http://dx.doi.org/10.1016/j.isprsjprs.2012.03.009

Goodchild, M. F. (1979). The aggregation problem in location-allocation. *Geographical Analysis, 11*(3), 240-255.

Goward, S. N., Huemmrich, K. F., & Waring, R. H. (1994). Visible-near infrared spectral reflectance of landscape components in western Oregon. *Remote Sensing of Environment, 47*(2), 190-203.

Gower, S. T., Kucharik, C. J., & Norman, J. M. (1999). Direct and indirect estimation of leaf area index, f(APAR), and net primary production of terrestrial ecosystems. *Remote Sensing of Environment, 70*(1), 29-51. doi: 10.1016/s0034-4257(99)00056-5

Gray, J., & Song, C. (2012). Mapping leaf area index using spatial, spectral, and temporal information from multiple sensors. *Remote Sensing of Environment, 119*(0), 173-183. doi: http://dx.doi.org/10.1016/j.rse.2011.12.016

Gregory, S. V., Swanson, F. J., McKee, W. A., & Cummins, K. W. (1991). An ecosystem perspective of riparian zones. *Bioscience*, 540-551.

Greig-Smith, P. (1961). Data on pattern within plant communities: I. The analysis of pattern. *The Journal of Ecology*, 695-702.

Grossberg, M. D., & Nayar, S. K. (2004). Modeling the space of camera response functions. *Pattern Analysis and Machine Intelligence, IEEE Transactions on, 26*(10), 1272-1282. doi: 10.1109/tpami.2004.88

Guanter, L., Segl, K., & Kaufmann, H. (2009). Simulation of optical remote-sensing scenes with application to the enmap hyperspectral mission. *Geoscience and Remote Sensing, IEEE Transactions on, 47*(7), 2340-2351.

Haboudane, D., Miller, J. R., Pattey, E., Zarco-Tejada, P. J., & Strachan, I. B. (2004). Hyperspectral vegetation indices and novel algorithms for predicting green LAI of crop canopies: Modeling and validation in the context of precision agriculture. *Remote Sensing of Environment, 90*(3), 337-352. doi: 10.1016/j.rse.2003.12.013

Howe, W. H., & Knopf, F. L. (1991). On the imminent decline of Rio Grande cottonwoods in central New Mexico. *The Southwestern Naturalist*, 218-224.

Hu, B., Li, Q., & Smith, A. (2009). Noise reduction of hyperspectral data using singular spectral analysis. *International Journal of Remote Sensing, 30*(9), 2277-2296. doi: 10.1080/01431160802549344

Hu, B., Miller, J. R., Chen, J. M., & Hollinger, A. (2004). Retrieval of the canopy leaf area index in the BOREAS flux tower sites using linear spectral mixture analysis. *Remote Sensing of Environment, 89*(2), 176-188.

Hu, Z., & Islam, S. (1997). A framework for analyzing and designing scale invariant remote sensing algorithms. *Geoscience and Remote Sensing, IEEE Transactions on, 35*(3), 747-755. doi: 10.1109/36.581996

Huete, A., Didan, K., Miura, T., Rodriguez, E. P., Gao, X., & Ferreira, L. G. (2002). Overview of the radiometric and biophysical performance of the MODIS vegetation indices. *Remote Sensing of Environment, 83*(1–2), 195-213. doi: http://dx.doi.org/10.1016/S0034-4257(02)00096-2

Huete, A. R. (1988). A soil-adjusted vegetation index (SAVI). *Remote Sensing of Environment, 25*(3), 295-309. doi: http://dx.doi.org/10.1016/0034-4257(88)90106-X

Hunt, E., Hively, W. D., Daughtry, C., McCarty, G. W., Fujikawa, S. J., Ng, T., . . . Yoel, D. W. (2008). *Remote sensing of crop leaf area index using unmanned airborne vehicles.* Paper presented at the ASPRS Pecora 17 -The Future of Land Imaging...Going Operational, Denver, CO.

Hunt, E. R., Hively, W. D., Fujikawa, S., Linden, D., Daughtry, C. S., & McCarty, G. (2010). Acquisition of NIR-Green-Blue Digital Photographs from Unmanned Aircraft for Crop Monitoring. *Remote Sensing, 2*(1), 290-305.

Ide, R., & Oguma, H. (2010). Use of digital cameras for phenological observations. *Ecological Informatics, 5*(5), 339-347. doi: http://dx.doi.org/10.1016/j.ecoinf.2010.07.002

Irons, J. R., Dwyer, J. L., & Barsi, J. A. (2012). The next Landsat satellite: The Landsat data continuity mission. *Remote Sensing of Environment, 122*, 11-21.

Jacquemoud, S., Baret, F., Andrieu, B., Danson, F., & Jaggard, K. (1995). Extraction of vegetation biophysical parameters by inversion of the PROSPECT+ SAIL models on sugar beet canopy reflectance data. Application to TM and AVIRIS sensors. *Remote Sensing of Environment, 52*(3), 163-172.

Jacquemoud, S., Verhoef, W., Baret, F., Bacour, C., Zarco-Tejada, P. J., Asner, G. P., . . . Ustin, S. L. (2009). PROSPECT & SAIL models: A review of use for vegetation characterization. *Remote Sensing of Environment, 113, Supplement 1*(0), S56-S66. doi: http://dx.doi.org/10.1016/j.rse.2008.01.026

Jelinski, D. E., & Wu, J. (1996). The modifiable areal unit problem and implications for landscape ecology. *Landscape Ecology, 11*(3), 129-140. doi: 10.1007/BF02447512

Jensen, J. R. (2005). *Introductory Digital Image Processing: A Remote Sensing Perspective*. Upper Saddle River, NJ: Pearson Prentice Hall.

Jensen, J. R. (2007). *Remote Sensing Of The Environment: An Earth Resource Perspective*. Upper Saddle River, NJ: Pearson Prentice Hall.

Jensen, T., Apan, A., Young, F., & Zeller, L. (2007). Detecting the attributes of a wheat crop using digital imagery acquired from a low-altitude platform. *Computers and Electronics in Agriculture, 59*(1–2), 66-77. doi: http://dx.doi.org/10.1016/j.compag.2007.05.004

Jonckheere, I., Fleck, S., Nackaerts, K., Muys, B., Coppin, P., Weiss, M., & Baret, F. (2004). Review of methods for in situ leaf area index determination: Part I. Theories, sensors and hemispherical photography. *Agricultural and Forest Meteorology, 121*(1–2), 19-35. doi: http://dx.doi.org/10.1016/j.agrformet.2003.08.027

Jordan, C. F. (1969). Derivation of leaf-area index from quality of light on the forest floor. *Ecology, 50*(4), 663-669. doi: 10.2307/1936256

Jun, J., Dengyu, L., Jinwei, G., & Susstrunk, S. (2013, 15-17 Jan. 2013). *What is the space of spectral sensitivity functions for digital color cameras?* Paper presented at the Applications of Computer Vision (WACV), 2013 IEEE Workshop on.

Kavzoglu, T. (2004). Simulating Landsat ETM+ imagery using DAIS 7915 hyperspectral scanner data. *International Journal of Remote Sensing, 25*(22), 5049-5067.

Kim, S. J., & Pollefeys, M. (2008). Robust radiometric calibration and vignetting correction. *Pattern Analysis and Machine Intelligence, IEEE Transactions on, 30*(4), 562-576.

Laliberte, A. S., Herrick, J. E., Rango, A., & Winters, C. (2010). Acquisition, orthorectification, and object-based classification of unmanned aerial vehicle (UAV) imagery for rangeland monitoring. *Photogrammetric Engineering and Remote Sensing, 76*(6), 661-672.

Laliberte, A. S., Winters, C., & Rango, A. (2008, Apr 28 - May 2 2008). *A procedure for orthorectification of sub-decimeter resolution imagery obtained with an unmanned aerial vehicle (UAV).* Paper presented at the Proc. ASPRS Annual Conference, Portland, OR.

Landgrebe, D. A. (2005). *Signal theory methods in multispectral remote sensing* (Vol. 29). Hoboken, NJ: John Wiley & Sons.

Landsberg, J., & Sands, P. (2011). *Physiological Ecology of Forest Production: Principals, Processes and Models* (Vol. 4): Academic Press.

Lauziere, Y. B., Gingras, D., & Ferrie, F. P. (1999). Color camera characterization with an application to detection under daylight. *Vision Interface (VI)*, 280-287.

Leblanc, S. G., & Chen, J. M. (2001). A practical scheme for correcting multiple scattering effects on optical LAI measurements. *Agricultural and Forest Meteorology, 110*(2), 125-139.

Leblanc, S. G., Chen, J. M., & Kwong, M. (2002). Tracing Radiation and Architecture of Canopies TRAC MANUAL Version 2.1.3: Canada Centre for Remote Sensing.

Lee, J. B., Woodyatt, A. S., & Berman, M. (1990). Enhancement of high spectral resolution remote-sensing data by a noise-adjusted principal components transform. *Geoscience and Remote Sensing, IEEE Transactions on, 28*(3), 295-304. doi: 10.1109/36.54356

Lee, K.-S., Cohen, W. B., Kennedy, R. E., Maiersperger, T. K., & Gower, S. T. (2004). Hyperspectral versus multispectral data for estimating leaf area index in four different biomes. *Remote Sensing of Environment, 91*(3–4), 508-520. doi: http://dx.doi.org/10.1016/j.rse.2004.04.010

Li-Cor. (1992). LAI-2000 Plant Canopy Analyzer Manual. Lincoln, NE.

Li, X., Gunturk, B., & Zhang, L. (2008). *Image demosaicing: A systematic survey.* Paper presented at the SPIE 6822, Visual Communications and Image Processing.

Lowe, D. G. Demo Software: SIFT Keypoint Detector. Retrieved June 01, 2014, from http://www.cs.ubc.ca/~lowe/keypoints/

Lowe, D. G. (2004). Distinctive image features from scale-invariant keypoints. *International journal of computer vision, 60*(2), 91-110.

Mahoney, J., & Rood, S. (1998). Streamflow requirements for cottonwood seedling recruitment—An integrative model. *Wetlands, 18*(4), 634-645. doi: 10.1007/BF03161678

Manninen, T., Stenberg, P., Rautiainen, M., Voipio, P., & Smolander, H. (2005). Leaf area index estimation of boreal forest using ENVISAT ASAR. *Geoscience and Remote Sensing, IEEE Transactions on, 43*(11), 2627-2635. doi: 10.1109/TGRS.2005.857325

Marceau, D. J. (1999). The scale issue in the social and natural sciences. *Canadian Journal of Remote Sensing, 25*(4), 347-356.

Marceau, D. J., & Hay, G. J. (1999). Remote sensing contributions to the scale issue. *Canadian Journal of Remote Sensing, 25*(4), 357-366.

Marceau, D. J., Howarth, P. J., & Gratton, D. J. (1994). Remote sensing and the measurement of geographical entities in a forested environment. 1. The scale and spatial aggregation problem. *Remote Sensing of Environment, 49*(2), 93-104.

Martinez-Verdu, F., Pujol, J., & Capilla, P. (2002). Calculation of the color matching functions of digital cameras from their complete spectral sensitivities. *Journal of Imaging Science and Technology, 46*(1), 15-25.

Mitra, R., & Buliung, R. N. (2012). Built environment correlates of active school transportation: neighborhood and the modifiable areal unit problem. *Journal of Transport Geography, 20*(1), 51-61. doi: http://dx.doi.org/10.1016/j.jtrangeo.2011.07.009

Mitsunaga, T., & Nayar, S. K. (1999, 1999). *Radiometric self calibration.* Paper presented at the Computer Vision and Pattern Recognition, 1999. IEEE Computer Society Conference on.

Moran, M. S., Maas, S. J., & Pinter Jr, P. J. (1995). Combining remote sensing and modeling for estimating surface evaporation and biomass production. *Remote Sensing Reviews, 12*(3-4), 335-353.

Morsdorf, F., Kötz, B., Meier, E., Itten, K., & Allgöwer, B. (2006). Estimation of LAI and fractional cover from small footprint airborne laser scanning data based on gap fraction. *Remote Sensing of Environment, 104*(1), 50-61.

Myneni, R. B., Ramakrishna, R., Nemani, R., & Running, S. W. (1997). Estimation of global leaf area index and absorbed par using radiative transfer models. *Ieee Transactions on Geoscience and Remote Sensing, 35*(6), 1380-1393. doi: 10.1109/36.649788

Nagaraja Rao, C., & Chen, J. (1996). Post-launch calibration of the visible and near-infrared channels of the Advanced Very High Resolution Radiometer on the NOAA-14 spacecraft. *International Journal of Remote Sensing, 17*(14), 2743-2747.

Nagler, P. L., Cleverly, J., Glenn, E., Lampkin, D., Huete, A., & Wan, Z. (2005). Predicting riparian evapotranspiration from MODIS vegetation indices and meteorological data. *Remote Sensing of Environment, 94*(1), 17-30. doi: http://dx.doi.org/10.1016/j.rse.2004.08.009

Nagler, P. L., Glenn, E. P., & Huete, A. R. (2001). Assessment of spectral vegetation indices for riparian vegetation in the Colorado River delta, Mexico. *Journal of Arid Environments, 49*(1), 91-110. doi: http://dx.doi.org/10.1006/jare.2001.0844

Nagler, P. L., Glenn, E. P., Lewis Thompson, T., & Huete, A. (2004). Leaf area index and normalized difference vegetation index as predictors of canopy characteristics and light interception by riparian species on the Lower Colorado River. *Agricultural and Forest Meteorology, 125*(1–2), 1-17. doi: http://dx.doi.org/10.1016/j.agrformet.2004.03.008

Naiman, R. J., Decamps, H., & Pollock, M. (1993). The Role of Riparian Corridors in Maintaining Regional Biodiversity. *Ecological Applications, 3*(2), 209-212. doi: 10.2307/1941822

Nilsson, C., & Berggren, K. (2000). Alterations of Riparian Ecosystems Caused by River Regulation. *Bioscience, 50*(9), 783-792. doi: 10.1641/0006-3568(2000)050[0783:AORECB]2.0.CO;2

O'Keeffe, J., & Davies, B. (1991). Conservation and management of the rivers of the Kruger National Park: Suggested methods for calculating instream flow needs. *Aquatic Conservation: Marine and Freshwater Ecosystems, 1*(1), 55-71. doi: 10.1002/aqc.3270010105

Openshaw, S., & Taylor, P. J. (1979). A million or so correlation coefficients: three experiments on the modifiable areal unit problem. *Statistical applications in the spatial sciences, 21*, 127-144.

Orchard, T. (2015). *Water requirements of a Southern Alberta riparian cottonwood ecosystem.* (Master's Thesis), University of Lethbridge. Retrieved from https://www.uleth.ca/dspace/handle/10133/3748

Patten, D. (1998). Riparian ecosytems of semi-arid North America: Diversity and human impacts. *Wetlands, 18*(4), 498-512. doi: 10.1007/BF03161668

Peddle, D., & Johnson, R. (2000). Spectral mixture analysis of airborne remote sensing imagery for improved prediction of leaf area index in mountainous terrain, Kananaskis Alberta. *Canadian Journal of Remote Sensing, 26*(3), 177-188.

Peddle, D., & Smith, A. (2005). Spectral mixture analysis of agricultural crops: endmember validation and biophysical estimation in potato plots. *International Journal of Remote Sensing, 26*(22), 4959-4979.

Peddle, D. R., Hall, F. G., & LeDrew, E. F. (1999). Spectral mixture analysis and geometric-optical reflectance modeling of boreal forest biophysical structure. *Remote Sensing of Environment, 67*(3), 288-297.

Peddle, D. R., Johnson, R. L., Cihlar, J., & Latifovic, R. (2004). Large area forest classification and biophysical parameter estimation using the 5-Scale canopy reflectance model in Multiple-Forward-Mode. *Remote Sensing of Environment, 89*(2), 252-263. doi: 10.1016/j.rse.2002.08.001

Peddle, D. R., Teillet, P. M., & Wulder, M. A. (2003). Radiometric image processing *Remote Sensing of Forest Environments* (pp. 181-208): Springer US.

Peel, M. C., Finlayson, B. L., & McMahon, T. A. (2007). Updated world map of the Köppen-Geiger climate classification. *Hydrology and Earth System Sciences Discussions Discussions, 4*(2), 439-473.

Perry, C. R., & Lautenschlager, L. F. (1984). Functional equivalence of spectral vegetation indices. *Remote Sensing of Environment, 14*(1), 169-182.

Poff, N. L., Allan, J. D., Bain, M. B., Karr, J. R., Prestegaard, K. L., Richter, B. D., . . . Stromberg, J. C. (1997). The natural flow regime. *Bioscience, 47*(11), 769-784.

Propastin, P., & Panferov, O. (2013). Retrieval of remotely sensed LAI using Landsat ETM plus data and ground measurements of solar radiation and vegetation structure: Implication of leaf inclination angle. *International Journal of Applied Earth Observation and Geoinformation, 25*, 38-46. doi: 10.1016/j.jag.2013.02.006

Pryor, L. (2012). *Land-cover mapping in an agriculture zone using simulated Sentinel-2 data*. (Master's Thesis), University of Lethbridge. Retrieved from https://www.uleth.ca/dspace/handle/10133/3367

Putman, S., & Chung, S. (1989). Effects of spatial system design on spatial interaction models. 1: The spatial system definition problem. *Environment and planning A, 21*(1), 27-46.

Qi, J., Chehbouni, A., Huete, A., Kerr, Y., & Sorooshian, S. (1994). A modified soil adjusted vegetation index. *Remote Sensing of Environment, 48*(2), 119-126.

Quattrochi, D. A., & Goodchild, M. F. (1997). *Scale in remote sensing and GIS*. Boca Raton, FL: CRC Press LLC.

Rabie, T. (2004). Adaptive hybrid mean and median filtering of high-ISO long-exposure sensor noise for digital photography. *Journal of Electronic Imaging, 13*(2), 264-277.

Riaño, D., Valladares, F., Condés, S., & Chuvieco, E. (2004). Estimation of leaf area index and covered ground from airborne laser scanner (Lidar) in two contrasting forests. *Agricultural and Forest Meteorology, 124*(3), 269-275.

Richardson, A. D., Jenkins, J. P., Braswell, B. H., Hollinger, D. Y., Ollinger, S. V., & Smith, M.-L. (2007). Use of digital webcam images to track spring green-up in a deciduous broadleaf forest. *Oecologia, 152*(2), 323-334.

Richter, R., Bachmann, M., Dorigo, W., & Muller, A. (2006). Influence of the Adjacency Effect on Ground Reflectance Measurements. *IEEE Geoscience and Remote Sensing Letters, 3*(4), 565-569. doi: 10.1109/LGRS.2006.882146

Rogan, J., Franklin, J., & Roberts, D. A. (2002). A comparison of methods for monitoring multitemporal vegetation change using Thematic Mapper imagery. *Remote Sensing of Environment, 80*(1), 143-156. doi: http://dx.doi.org/10.1016/S0034-4257(01)00296-6

Rood, S., & Mahoney, J. (2000). Revised instream flow regulation enables cottonwood recruitment along the St. Mary River, Alberta, Canada. *Rivers, 7*(2), 109-125.

Rood, S. B., Braatne, J. H., & Hughes, F. M. R. (2003). Ecophysiology of riparian cottonwoods: stream flow dependency, water relations and restoration. *Tree Physiology, 23*(16), 1113-1124. doi: 10.1093/treephys/23.16.1113

Rood, S. B., Campbell, J. S., & Despins, T. (1986). Natural poplar hybrids from southern Alberta. I. Continuous variation for foliar characteristics. *Canadian Journal of Botany, 64*(7), 1382-1388. doi: 10.1139/b86-189

Rood, S. B., & Heinze-Milne, S. (1989). Abrupt downstream forest decline following river damming in southern Alberta. *Canadian Journal of Botany, 67*(6), 1744-1749. doi: 10.1139/b89-221

Rood, S. B., Kalischuk, A. R., & Mahoney, J. M. (1998). Initial cottonwood seedling recruitment following the flood of the century of the Oldman River, Alberta, Canada. *Wetlands, 18*(4), 557-570. doi: 10.1007/BF03161672

Rood, S. B., & Mahoney, J. M. (1990). Collapse of riparian poplar forests downstream from dams in western prairies: Probable causes and prospects for mitigation. *Environmental Management, 14*(4), 451-464. doi: 10.1007/BF02394134

Rood, S. B., Pan, J., Gill, K. M., Franks, C. G., Samuelson, G. M., & Shepherd, A. (2008). Declining summer flows of Rocky Mountain rivers: Changing seasonal hydrology and probable impacts on floodplain forests. *Journal of Hydrology, 349*(3–4), 397-410. doi: http://dx.doi.org/10.1016/j.jhydrol.2007.11.012

Rood, S. B., Samuelson, G. M., Braatne, J. H., Gourley, C. R., Hughes, F. M. R., & Mahoney, J. M. (2005). Managing river flows to restore floodplain forests. *Frontiers in Ecology and the Environment, 3*(4), 193-201. doi: 10.1890/1540-9295(2005)003[0193:MRFTRF]2.0.CO;2

Roujean, J.-L., & Breon, F.-M. (1995). Estimating PAR absorbed by vegetation from bidirectional reflectance measurements. *Remote Sensing of Environment, 51*(3), 375-384. doi: http://dx.doi.org/10.1016/0034-4257(94)00114-3

Rouse, J., Haas, R., Schell, J., & Deering, D. (1974). Monitoring vegetation systems in the Great Plains with ERTS. *NASA special publication, 351*, 309.

Roy, D. P., Lewis, P. E., & Justice, C. O. (2002). Burned area mapping using multi-temporal moderate spatial resolution data—A bi-directional reflectance model-based expectation approach. *Remote Sensing of Environment, 83*(1), 263-286.

Running, S. W., & Coughlan, J. C. (1988). A general model of forest ecosystem processes for regional applications. I. Hydrologic balance, canopy gas exchange and primary production processes. *Ecological modelling, 42*(2), 125-154.

Sakamoto, T., Shibayama, M., Kimura, A., & Takada, E. (2011). Assessment of digital camera-derived vegetation indices in quantitative monitoring of seasonal rice growth. *ISPRS Journal of Photogrammetry and Remote Sensing, 66*(6), 872-882. doi: http://dx.doi.org/10.1016/j.isprsjprs.2011.08.005

Sanz-Ablanedo, E., Rodríguez-Pérez, J. R., Armesto, J., & Taboada, M. F. Á. (2010). Geometric Stability and Lens Decentering in Compact Digital Cameras. *Sensors (Basel, Switzerland), 10*(3), 1553-1572. doi: 10.3390/s100301553

Sauer, C. O. (1918). Geography and the Gerrymander. *American Political Science Review, 12*(03), 403-426.

Schott, J. R. (2007). *Remote sensing: the image chain approach* (Vol. 2). New York, NY: Oxford University Press.

Schowengerdt, R. A. (2006). *Remote sensing: models and methods for image processing*. Burlington, MA: Academic press.

Scott, M. L., Shafroth, P. B., & Auble, G. T. (1999). Responses of Riparian Cottonwoods to Alluvial Water Table Declines. *Environmental Management, 23*(3), 347-358. doi: 10.1007/s002679900191

Sellers, P., Dickinson, R., Randall, D., Betts, A., Hall, F., Berry, J., . . . Nobre, C. (1997). Modeling the exchanges of energy, water, and carbon between continents and the atmosphere. *Science, 275*(5299), 502-509.

Serbin, S. P., Ahl, D. E., & Gower, S. T. (2013). Spatial and temporal validation of the MODIS LAI and FPAR products across a boreal forest wildfire chronosequence. *Remote Sensing of Environment, 133*(0), 71-84. doi: http://dx.doi.org/10.1016/j.rse.2013.01.022

Shafique, K., & Shah, M. (2004, 24-27 Oct. 2004). *Estimation of the radiometric response functions of a color camera from differently illuminated images.* Paper presented at the Image Processing, 2004. ICIP '04. 2004 International Conference on.

Shafroth, P. B., Stromberg, J. C., & Patten, D. T. (2002). Riparian vegetation response to altered disturbance and stress regimes. *Ecological Applications, 12*(1), 107-123.

Sheppard, E., & McMaster, R. B. (2008). *Scale and geographic inquiry: Nature, society, and method*. Hoboken, NJ: John Wiley & Sons.

Slater, P. N., Biggar, S. F., Palmer, J. M., & Thome, K. J. (1995). *Unified approach to pre-and in-flight satellite-sensor absolute radiometric calibration.* Paper presented at the SPIE 2583, Advanced and Next Generation Satellites, 130.

Smith, G. M., & Milton, E. J. (1999). The use of the empirical line method to calibrate remotely sensed data to reflectance. *International Journal of Remote Sensing, 20*(13), 2653-2662. doi: 10.1080/014311699211994

Smith, N., Chen, J., & Black, T. (1993). Effects of clumping on estimates of stand leaf area index using the LI-COR LAI-2000. *Canadian Journal of Forest Research, 23*(9), 1940-1943.

Soudani, K., François, C., le Maire, G., Le Dantec, V., & Dufrêne, E. (2006). Comparative analysis of IKONOS, SPOT, and ETM+ data for leaf area index estimation in temperate coniferous and deciduous forest stands. *Remote Sensing of Environment, 102*(1–2), 161-175. doi: http://dx.doi.org/10.1016/j.rse.2006.02.004

Sprintsin, M., Karnieli, A., Berliner, P., Rotenberg, E., Yakir, D., & Cohen, S. (2007). The effect of spatial resolution on the accuracy of leaf area index estimation for a forest planted in the desert transition zone. *Remote Sensing of Environment, 109*(4), 416-428. doi: http://dx.doi.org/10.1016/j.rse.2007.01.020

Stow, D., Hope, A., Nguyen, A. T., Phinn, S., & Benkelman, C. A. (1996). Monitoring detailed land surface changes using an airborne multispectral digital camera system. *Geoscience and Remote Sensing, IEEE Transactions on, 34*(5), 1191-1203. doi: 10.1109/36.536536

Stromberg, J. C., Lite, S. J., & Dixon, M. D. (2010). Effects of stream flow patterns on riparian vegetation of a semiarid river: Implications for a changing climate. *River Research and Applications, 26*(6), 712-729. doi: 10.1002/rra.1272

Teillet, P., Slater, P., Ding, Y., Santer, R., Jackson, R., & Moran, M. (1990). Three methods for the absolute calibration of the NOAA AVHRR sensors in-flight. *Remote Sensing of Environment, 31*(2), 105-120.

Teillet, P. M., Staenz, K., & William, D. J. (1997). Effects of spectral, spatial, and radiometric characteristics on remote sensing vegetation indices of forested regions. *Remote Sensing of Environment, 61*(1), 139-149. doi: http://dx.doi.org/10.1016/S0034-4257(96)00248-9

Thorne, K., Markharn, B., Barker, P. S., & Biggar, S. (1997). Radiometric calibration of Landsat. *Photogrammetric Engineering & Remote Sensing, 63*(7), 853-858.

Trishchenko, A. P., Cihlar, J., & Li, Z. (2002). Effects of spectral response function on surface reflectance and NDVI measured with moderate resolution satellite sensors. *Remote Sensing of Environment, 81*(1), 1-18. doi: http://dx.doi.org/10.1016/S0034-4257(01)00328-5

Tsai, F., & Philpot, W. (1998). Derivative analysis of hyperspectral data. *Remote Sensing of Environment, 66*(1), 41-51.

Turner, D. P., Cohen, W. B., Kennedy, R. E., Fassnacht, K. S., & Briggs, J. M. (1999). Relationships between Leaf Area Index and Landsat TM Spectral Vegetation Indices across Three Temperate Zone Sites. *Remote Sensing of Environment, 70*(1), 52-68. doi: http://dx.doi.org/10.1016/S0034-4257(99)00057-7

United States Geological Survey. Earth Explorer. Retrieved October 05, 2014, from http://earthexplorer.usgs.gov/

Verhoeven, G. J., Smet, P. F., Poelman, D., & Vermeulen, F. (2009). Spectral Characterization of a Digital Still Camera's NIR Modification to Enhance Archaeological Observation. *Geoscience and Remote Sensing, IEEE Transactions on, 47*(10), 3456-3468. doi: 10.1109/tgrs.2009.2021431

Vora, P. L., Farrell, J. E., Tietz, J. D., & Brainard, D. H. (1997a). Digital color cameras—1—Response models. *Hewlett-Packard Laboratory Technical Report, No. HPL-97-53*.

Vora, P. L., Farrell, J. E., Tietz, J. D., & Brainard, D. H. (1997b). Digital Color Cameras - 2 - Spectral Response. *Hewlett-Packard Laboratory Technical Report, No. HPL-97-54*.

Wang, T., Yan, L., & Mooney, P. (2011, June 29 2011-July 1 2011). *Dense point cloud extraction from UAV captured images in forest area.* Paper presented at the Spatial Data Mining and Geographical Knowledge Services (ICSDM), 2011 IEEE International Conference on.

Warner, T. A., Foody, G. M., & Nellis, M. D. (2009). *The SAGE handbook of remote sensing*. Thousand Oaks, CA: Sage Publications Inc.

Weiss, M., Baret, F., Smith, G. J., Jonckheere, I., & Coppin, P. (2004). Review of methods for in situ leaf area index (LAI) determination Part II. Estimation of LAI, errors and sampling. *Agricultural and Forest Meteorology, 121*(1-2), 37-53. doi: 10.1016/j.agrformet.2003.08.001

Welles, J. M., & Norman, J. (1991). Instrument for indirect measurement of canopy architecture. *Agronomy Journal, 83*(5), 818-825.

White, M. A., Asner, G. P., Nemani, R. R., Privette, J. L., & Running, S. W. (2000). Measuring Fractional Cover and Leaf Area Index in Arid Ecosystems - Digital Camera, Radiation Transmittance, and Laser Altimetry Methods. *Remote Sensing of Environment, 74*(1), 45-57. doi: 10.1016/s0034-4257(00)00119-x

Williams, C. A., & Cooper, D. J. (2005). Mechanisms of riparian cottonwood decline along regulated rivers. *Ecosystems, 8*(4), 382-395.

Wilson, K. B., Hanson, P. J., Mulholland, P. J., Baldocchi, D. D., & Wullschleger, S. D. (2001). A comparison of methods for determining forest evapotranspiration and its components: sap-flow, soil water budget, eddy covariance and catchment water balance. *Agricultural and Forest Meteorology, 106*(2), 153-168. doi: http://dx.doi.org/10.1016/S0168-1923(00)00199-4

Woodcock, C. E., & Strahler, A. H. (1987). The factor of scale in remote sensing. *Remote Sensing of Environment, 21*(3), 311-332. doi: http://dx.doi.org/10.1016/0034-4257(87)90015-0

Wüller, D., & Gabele, H. (2007). *The usage of digital cameras as luminance meters.* Paper presented at the SPIE 6502, Digital Photography III.

Xiao, J., & Moody, A. (2005). A comparison of methods for estimating fractional green vegetation cover within a desert-to-upland transition zone in central New Mexico, USA. *Remote Sensing of Environment, 98*(2–3), 237-250. doi: http://dx.doi.org/10.1016/j.rse.2005.07.011

Xiong, X., Chiang, K., Sun, J., Barnes, W. L., Guenther, B., & Salomonson, V. V. (2009). NASA EOS Terra and Aqua MODIS on-orbit performance. *Advances in Space Research, 43*(3), 413-422. doi: http://dx.doi.org/10.1016/j.asr.2008.04.008

Xu, H., Steven, M., & Jaggard, K. (1996). Monitoring leaf area of sugar beet using ERS-1 SAR data. *International Journal of Remote Sensing, 17*(17), 3401-3410.

Yoder, B. J., & Pettigrew-Crosby, R. E. (1995). Predicting nitrogen and chlorophyll content and concentrations from reflectance spectra (400–2500 nm) at leaf and canopy scales. *Remote Sensing of Environment, 53*(3), 199-211.

Yu, W. (2004). Practical anti-vignetting methods for digital cameras. *Consumer Electronics, IEEE Transactions on, 50*(4), 975-983.

Zhang, C., & Kovacs, J. M. (2012). The application of small unmanned aerial systems for precision agriculture: a review. *Precision Agriculture, 13*(6), 693-712.

Zhang, Z. (1999). *Flexible camera calibration by viewing a plane from unknown orientations.* Paper presented at the The Seventh IEEE International Conference on Computer Vision, 1999.

Zhang, Z. (2000). A flexible new technique for camera calibration. *Pattern Analysis and Machine Intelligence, IEEE Transactions on, 22*(11), 1330-1334.

Zheng, G., & Moskal, L. M. (2009). Retrieving leaf area index (LAI) using remote sensing: theories, methods and sensors. *Sensors, 9*(4), 2719-2745.